APPLIED COMPUTATIONAL ELECTROMAGNETICS SOCIETY JOURNAL

THE APPLIED COMPUTATIONAL ELECTROMAGNETICS SOCIETY

JOURNAL

TABLE OF CONTENTS

60 GHz Circular Patch-Fed High Gain Transparent Lens Antenna

Z. Briqech [1], A. R. Sebak [1], and T. Denidni [2]

[1] Electrical and Computer Engineering Department
Concordia University, 1455 de Maisonneuve West, EV005.127, Montréal, Québec, H3G 1M8, Canada
z_briqec@encs.concordia.ca, abdo@ece.concordia.ca

[2] Institut National De La Recherche Scientifique (INRS)
Place Bonaventure, 900 De la Gauchetière Ouest, Niveau C, Montréal, Québec, H5A 1C6, Canada
denidni@emt.inrs.ca

Abstract ─ A high gain, low cost and easy to fabricate millimeter-wave (MMW) antenna is presented. To focus the radiation into a very thin main beam, a concept based on employing a cylindrical air cavity with a convex front-end linking a microstrip patch radiator and a transparent dielectric lens is introduced. This principle is applied to enhance the coupling between the patch antenna and dielectric lens at 60 GHz. The design shows very directive and stable radiation patterns in both the E and H-planes. The proposed antenna exhibits a measured gain of 20 dB over the ISM-band, as well as high radiation efficiency (greater than 90%). The performance of the proposed antenna makes it a promising solution for various MMW applications, including short distance wireless communications and MMW imaging.

Index Terms ─ Dielectric lens, high gain, millimeter-wave antenna, unlicensed 60 GHz band.

I. INTRODUCTION

Due to the increasing demand for high data rate wireless communications, there has been considerable interest in the development of prototype systems for the 60 GHz unlicensed band. This band is free of charge and utilized in industrial, scientific and medical (ISM) applications. However, due to the resonance of the oxygen molecule absorption in the air, the attenuation loss at 60 GHz exceeds 13 dB/km [1]. This attenuation may limit wireless communication system's transmission range capability.

Recently, integrated lens antennas have been used successfully in millimeter and sub-millimeter wave applications, such as mm-wave imaging systems [6], traffic collision avoidance devices [7], radio astronomy [8], and satellite communications [9]. A lens works as a focusing system when fed by conventional elements, such as horns, waveguides or microstrip antenna. The lens antenna is thus a technique which can be implemented to increase the antenna gain by focusing the radiated energy [10,11]. Furthermore, there are alternative techniques for increasing the gain of an antenna [2,3,4,5], such as the leaky wave antenna presented as a hybrid microstrip antenna array [12] proposed to operate at MMW antenna. A discrete lens antenna is employed as linear and circular polarization transmit-arrays operating at 60GHz with an average gain of 20 dB presented in [13]. This antenna achieves a power efficiency of 50-61%, which is low compared for example to feed horn antennas. This drawback in efficiency is due to loss associated with discrete lens.

Various lens shapes for antenna applications have been investigated over the years. For instance, spherical, elliptical and extended hemispherical profiles are integrated with planar substrates, [11,12,14,21,22]. Lens designs are governed by geometrical optics (GO) laws [23]. A cylindrical air cavity integrated with a lens antenna operating at 28 GHz was introduced in 2012 [15]. It has a reduced lens size, although the flat end of this air cavity is less efficient in reducing internal reflections. In addition, from a fabrication point of view, certain lens shapes, such as hyper hemispherical or elliptical lenses, are more challenging and the

complexity of the fabrication procedure increases the cost.

High attenuation loss associated with millimeter-wave (MMW) propagation could be compensated for using high-gain antennas such as large-aperture antennas and array structures [20]. However, in MMW applications lens antennas are preferred for their small size and for the ease with which they can be mounted on and integrated with circuits and devices [7,8,22]. In addition, dielectric lenses have highly directive antenna patterns and thermal stability, and are compatible with suppressing surface-wave losses and capable of multiple-beam feeding. Furthermore, lens antennas have wideband capabilities depending on the feeding antenna's bandwidth.

In this paper, the proposed antenna consists of a full spherical dielectric lens, which is usually inexpensive and easier to manufacture than hyper hemispherical and elliptical lenses. The dielectric spherical lens is fed by a single element, a circular patch antenna, and supported by a cylindrical air cavity. To our best of knowledge, this work is the first one investigating the effect of a convex-shaped lens mounted on the top side of the air cavity as a key design parameter of the proposed antenna. This convex shape collimates the beam in order to obtain a more concentrated radiation from the patch antenna compared to those from an extended hemispherical lens with or without an air cavity [15]. Thus, the proposed design with a cylindrical air cavity increases the pencil beam directivity, enhances the antenna radiation characteristic, and improves antenna efficiency.

The proposed antenna achieved 20 dB gain while maintaining high efficiency by utilizing only one radiated element. Using arrays to increase the gain has a drawback in the overall antenna efficiency due to the losses caused by the feeding network [13]. In general, 60 GHz antennas are proposed for short range wireless applications [18]. For instance, this frequency band offers the opportunity of developing new industrial applications; short-range radar, high-resolution target detection, classification, miners wireless communications and tracking, and imaging detection systems. As demonstrated in [19] using real mining environment, 60 GHz antennas, including the proposed antenna, are adequate to

work in the mining industry.

II. ANTENNA GEOMETRY

A. Antenna element

The proposed geometry consists of three components: a lens, the air-cavity, and a microstrip patch antenna, as illustrated in Fig. 1. The spherical dielectric lens antenna is fed by a circular microstrip patch with radius $r_p = 0.78$ mm. The patch is etched on a thin Rogers RT Duroid 5880 ($h_p = 0.254$ mm, $\varepsilon_{rL} \approx 2.2$, $tan\delta \approx 0.0009$) substrate. It is aperture-coupled by a resonant slot with length $L_s = 0.835$ mm and × width $W_s = 0.1524$ mm. This rectangular radiating slot has an approximate length of $\lambda_g/4$, where λ_g is the guided wavelength at 60 GHz. The slot was drilled with offset from the center of the patch by $d = 0.3$ mm; this distance can be tuned to ensure that the optimum energy of TM_{010} excitation mode is passed through the feed line to the circular patch antenna. The microstrip feed line sits on the back side of the second thin layer composed of Rogers RT Duroid 6010 ($h_f = 0.254$ mm, $\varepsilon_{rf} \approx 10.2$, $tan\delta \approx 0.0023$), which excites the patch via a resonant slotted ground plane. The microstrip patch, feed line and ground plane are simulated as glossy copper sheets of thickness t = 0.035 mm with a conductivity of $\sigma = 5.80 \times 10^7$ S/m.

B. Lens configurations

Figure 1 (c) shows the dielectric lens model. The spherical lenses have the advantage of a multi-beam option, which gives them the ability to simultaneously collect signals from all directions. Another advantage is their ability to be manufactured with inexpensive dielectric materials and without the need for active elements. The spherical lens is a homogeneous dielectric sphere [23] which, for dielectric constants in the range $1 \leq \varepsilon_{rL} \leq 4$, focuses paraxial rays to a focal point (the radiated element) outside the sphere. The distance F of the focal point from the centre of a lens with radius r_L, and dielectric constant ε_{rL}, is approximately determined by geometrical optics (GO) and is given by:

$$F = \frac{r_L\sqrt{\varepsilon_{rL}}}{2(\sqrt{\varepsilon_{rL}}-1)}. \qquad (1)$$

The lens was selected with same characteristics as those of RO5880. The optimum diameter of the dielectric spherical lens antenna was chosen to be

$D_L = 2 \times r_L = 20$ mm $= 4 \times \lambda o$ (λ_o is the wavelength in free space) at the central frequency, 60 GHz.

C. Air cavity design

The cylindrical air cavity surrounding the circular patch antenna has important features for enhancing antenna performance. The proposed air cavity resonates at a slightly different frequency than that of the patch antenna, which increases the multi resonances surrounding the main resonance at 60 GHz. This leads to improving the antenna bandwidth as well as potential reduction of the surface-wave interactions in an array environment by isolating each antenna element. Furthermore, the cylindrical shape of the air cavity offers several advantages. One advantage is to guide the near-field propagating wave into the antenna lens, which enhances the directivity and increases the gain of the antenna without a loss in radiation efficiency. Another advantage is that the circular shape of the top of the cavity forms a perfect match to mount the spherical lens antenna. In addition, the top of the air-cavity is covered with the convex lens shape which creates more focusing of the radiated waves that come from the patch antenna, and the optimized dimension of the air cavity maintains the

patch antenna at the focal point.

The cylindrical hole of the proposed air cavity is drilled on a Rogers RT Duroid 5880 ($h_k = 1.575$ mm, $\varepsilon_{rL} \approx 2.2$, $tan\delta \approx 0.0009$) substrate with a size $W_k \times L_k = 10.5 \times 9.872$ mm^2. The starting design point for the radius (r_k) and height (h_k) of the cylindrical air cavity depends on the focal point distance (F) and the space between the lens end surface and the patch antenna, d_L. In Fig. 1 (c), the aperture angle to the air-cavity edge ($\emptyset_k$) is described by:

$$\emptyset_k = sin^{-1}(r_k/r_L). \tag{2}$$

The distance from the center of the lens to the edge of the cavity (d_o) is described by:

$$d_o = \sqrt{r_L^2 - r_k^2}. \tag{3}$$

This leads to determining the lens inset distance into the air-cavity, $d_k = r_L - d_o$, and $d_L = h_k - d_k - t$, where the copper thickness t is taken into account in particular at MMW frequencies. Thus, the focal point is determined as $F = r_L + d_L$ by substituting F in equation (1). d_L is expressed by equation (4), which considers the theoretical GO value as the initial value to determine the approximate focal point at the patch antenna level:

$$d_L = \frac{r_L\sqrt{\varepsilon_{rL}}}{2(\sqrt{\varepsilon_{rL}}-1)} - r_L. \tag{4}$$
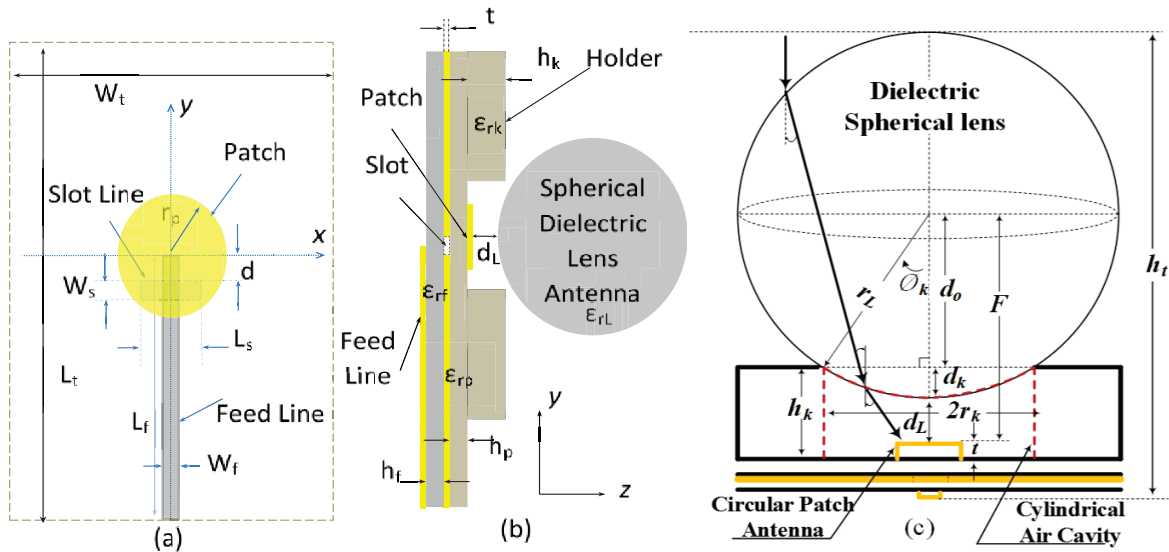
Fig. 1. Antenna geometry: (a) top view, (b), side view, and (c) side view of the proposed antenna.

III. SIMULATION RESULTS

The proposed antenna was studied numerically using the commercial electromagnetic simulator

CST Microwave Studio® (CST-MWS). The model was simulated to investigate the effect of different design parameters and their performance at

operating frequencies from 55 GHz to 65 GHz.

A. Parametric study
1. Cylindrical air cavity design effects

In this study, the aim is to increase the overall antenna gain while keeping a low antenna profile, which reduces the radius of the spherical lens without affecting the broadside directivity. This is accomplished by modeling an optimal combination of the radius and height of the air cavity. For this purpose, a CST model for the patch and air cavity is investigated. As shown in Fig. 2 (a), when the radius of the cavity (r_k) is increased from 1 mm to 4 mm, there are significant changes in the antenna gain, and the resonant frequency goes up. When the radius is close to that of the circular patch (1 mm), the reflected field caused by the cavity is very high

and causes drops in the antenna gain. Also, in form $r_k \geq \lambda_g$ the cavity has a close response to the patch antenna which adds to the overall gain.

The reflection coefficient and antenna gain results are shown in Fig. 2 (b) when the height of the cylindrical air cavity, h_k is changed. The return loss response shifted slightly upwards when the height of the cavity was increased. Furthermore, a higher antenna gain was obtained at $h_k = 1.575$-mm, with no major influence on the antenna impedance bandwidth. Therefore, $h_k \sim \lambda_g/2$ in the substrate and $r_k \sim \lambda_g$ were the values selected to obtain a good match between the patch and the lens, which is very important in order to optimize the plane-wave radiation of the lens. In addition, these values match the optimum focal point of this model's selected lens material.
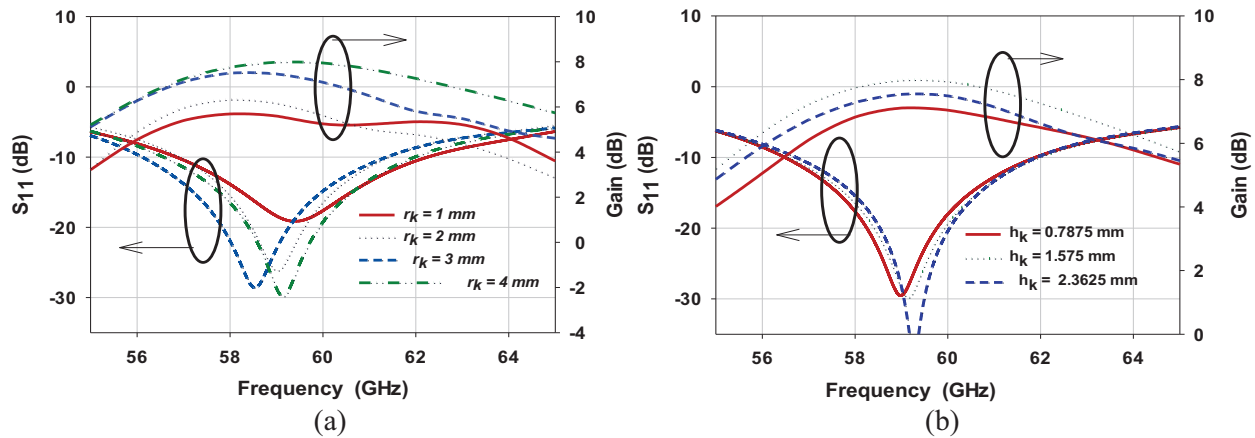
Fig. 2. The simulated antenna's gain and return loss $|S_{11}|$ of the patch antenna with air-cavity: (a) considering the effect of varying the radius of the air cavity (r_k), and (b) the height (h_k).

Figure 3 shows wave propagation comparison between an air cavity with a convex end lens as opposed to one with a flat end lens. The propagating wave of the patch antenna is more focused for the convex-end cavity. In other words, the diffraction angle θ_C of the convex end is less than the diffraction angle θ_F of the flat end. Furthermore, the convex shape of the lens provides the appropriate phase distribution to focus the radiating wave at the desired distance.

Figure 4 shows time snapshots of the electric field generated by CST. The snapshots show six travelling guided wavelengths (λ_{g2}) for three cases: (a) without an air cavity, (b) for a cylindrical air cavity with flat ends, and (c) for a cylindrical air cavity with a convex end. The snapshots show that

the combination of the spherical lens and cylindrical air cavity with convex end has increased the focus of the propagating wave caused by the convex shape of the lens. The cylindrical air cavity under the dielectric lens concentrates the planar wave into a narrow beam. The wave propagation illustrates inside the cavity with different phases are shown in Fig. 4. It can be noticed that the cavity with flat end is less efficient in wave concentration on the focal point (patch antennas) where the focus width $W_F > W_{NC} > W_C$. Therefore, the air cavity covered with the convex lens shape increases the focus of the radiated waves from the patch antenna. This convex shape also enhances the bandwidth of the antenna, as shown in Fig. 5.
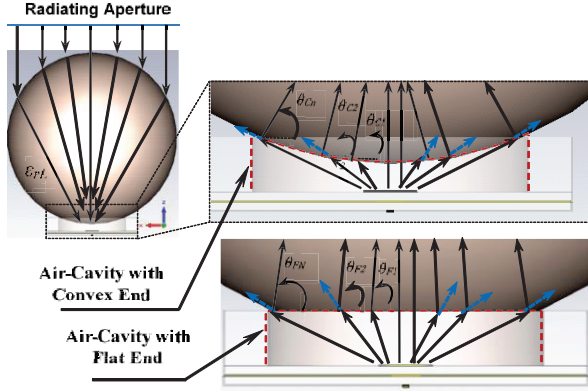
Fig. 3. Illustrates the wave distribution behavior comparison of the air-cavity with a convex end and with a flat end.
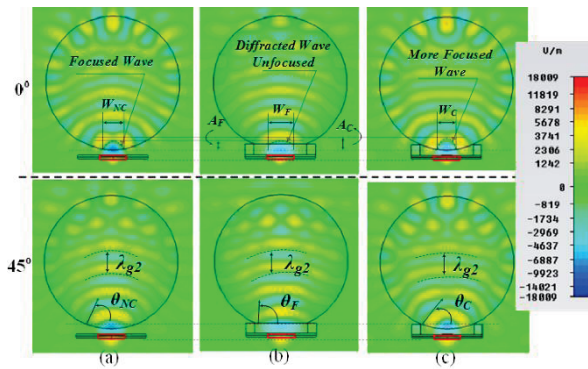
Fig. 4. A time snapshot of the electric field for three cases when the patch antenna fed the lens: (a) without an air cavity, (b) a cylindrical air cavity with flat ends, and (c) a cylindrical air cavity with a convex end.
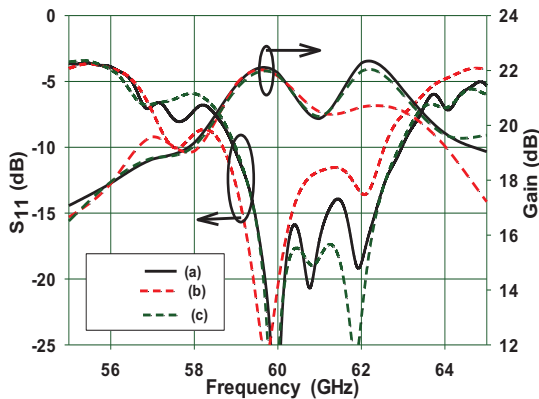
Fig. 5. The simulated antenna's gain, and the return loss $|S_{11}|$ of three cases: (a) without an air cavity, (b) a cylindrical air cavity with flat ends, and (c) a cylindrical air cavity with convex end.

2. Focal point distance dL

The space between the lens end surface and the patch antenna d_L is a distance associated with the height of the air cavity h_k. After calculating the value of d_L using equation (4) as a starting value, the optimized value has been obtained using CST. The value of d_L was selected to ensure that the focal spot appears on the patch antenna's level.

Figure 6 demonstrates the effect of variation in the d_L on the input reflection coefficient and the antenna gain. In Fig. 6, $|S_{11}|$ responses for the last two values of d_L, 1.75 mm and 2.25 mm, are almost identical and $d_L = 0.75$ mm is selected since it gives a higher average gain over the ISM band. The simulated radiation efficiency of the proposed antenna is 93 percent at 60 GHz, and 88 percent at 63 GHz.
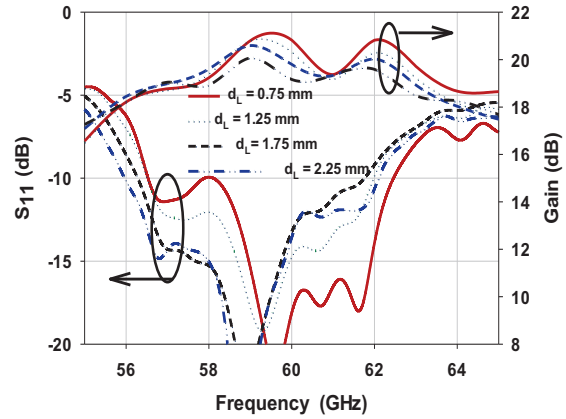
Fig. 6. The simulated reflection coefficient and gain of the proposed antenna, which results from varying the end surface of the lens and the patch (dL).

IV. EXPERIMENTAL RESULTS

A. Fabrication procedure for the proposed antenna

A standard milling machine with low-cost PCB processes was used to fabricate the two layers slot-coupled patch antenna as well the third layer cavity and the lens holder. The copper thickness of the substrate is 35µm with a conductivity $\sigma = 5.80 \times 10^7$ S/m. A photograph of the fabricated prototype is shown in Fig. 7. The antenna layers are manually attached using a thin film of bonding material and are correctly aligned to ensure that the feed line, the aperture slot, and the patch are in their positions.

As shown in Fig. 1, additional length from Ref1 to Ref2 was necessary to create a large enough ground plane for the SouthWest V-connector (1.85

mm connector). In addition, and as shown on the right side of Fig. 7, a circular shaped gap was drilled through the first layer to insert the screws of the V-connector. The 12.7 mm radius spherical dielectric lens is made of polymethyl methacrylate PMMA (Acrylic) material, a lightweight transparent thermoplastic with $\varepsilon_{rL} \approx 2.57$, $tan\delta \approx 0.0032$ at 24 GHz, and $\varepsilon_{rL} \approx 2.61$, $tan\delta \approx 0.002$ at 71 GHz [16]. According to the dielectric constant of the lens material given in [16], the interpolated value of the dielectric constant at 60 GHz is $\varepsilon_{rL} \approx 2.6$, $tan\delta \approx 0.0026$.
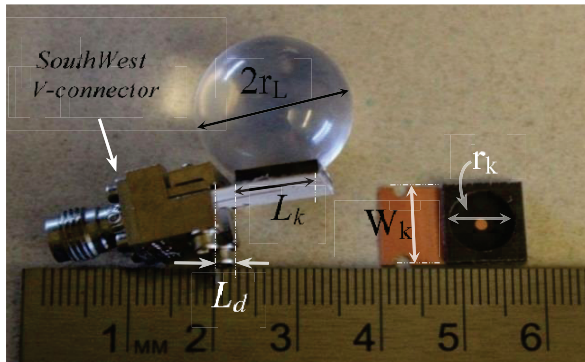
Fig. 7. Photographs of the lens antenna with the circular microstrip patch, fed with the holder substrate.

B. Measurement of the reflection coefficient

The measurements of the reflection coefficient (S_{11}) for the proposed antenna are done using Anritsu 37397C Vector Network Analyzer and Anritsu 3680V 60 GHz Universal Test Fixture. The reflection coefficient measurements were performed with the through-reflect-line (TRL) calibration kit, instead of the standard coaxial line calibration. The TRL calibration technique is a more accurate way to determine precise values for the reflection coefficient, especially for the MMW band, where any inaccurate connection during the measurements could cause inaccurate results for measured antenna parameters [17].

Figure 8 compares the measured reflection coefficient and antenna gain with CST results for two antenna configurations of the radiated element with and without the lens. The measured impedance bandwidth ($\leq$ -10 dB) is 3.5 GHz corresponds to 5.84% at 60 GHz. In the measured result of $|S_{11}|$, there is a shift in resonant frequency compared with CST results – this may be caused by inaccuracy in

the substrate material properties at 60 GHz and/or by the effects of etching and alignment tolerances in the fabrication process. The material used in the simulation for the microstrip feed line is RO6010, and the patch's substrate is RO5880. Dielectric constants of both substrates are slightly different at 60 GHz, from those specified by the manufacture at 10 GHz. As noted in Fig. 8, the measured and calculated reflection coefficient of the proposed antenna responses are fluctuating due to exciting multi-high order modes resonated in the air-cavity, which results in a 3-4 dB gain variation.
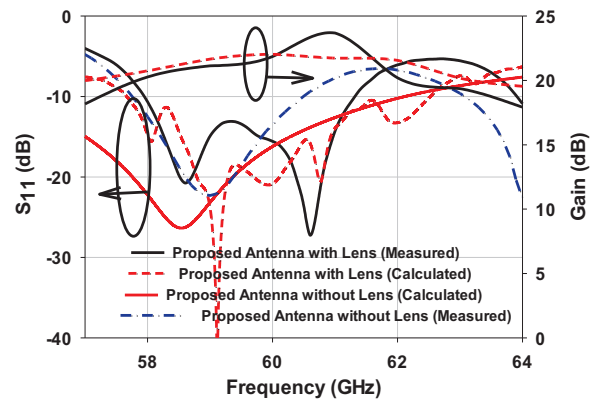
Fig. 8. Measured and calculated reflection coefficient of the proposed antenna.

C. Radiation pattern

The radiation patterns within the bandwidth range (from 58 GHz to 61 GHz) are measured in an anechoic chamber. As shown in Fig. 9, the E-plane is the yz-plane, and the H-plane is xy-plane. Two prototypes are measured: the first is the radiating element (a circular patch with cavity), and the second is the proposed antenna (a lens mounted on the radiating element). In both cases, the radiation pattern is measured with the antennas directly mounted by a 1.85 mm South-West Microwave connector.

The measured and calculated E- and H-planes radiation patterns for the patch antenna with the holder only (no lens) within the ISM frequency band at 58 GHz to 61 GHz are shown in Fig. 10. Both the CST and measured results agree well within the main lobe and HPBW range. In the results, the back lobe radiation of both the E- and H-planes was higher than expected due to the small ground plane and strong resonance. Furthermore, a higher side lobe level (SLL) within an angle range

of 150º to 270º, the side of the setup and the antenna's connector was observed for the measured E-plane pattern.
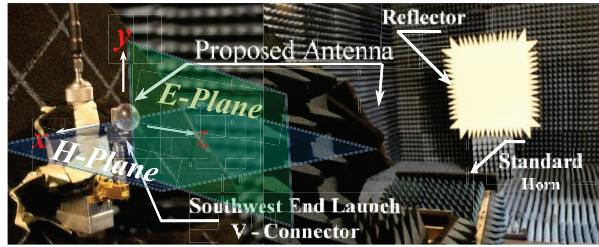
Fig. 9. Setup for radiation pattern measurements.
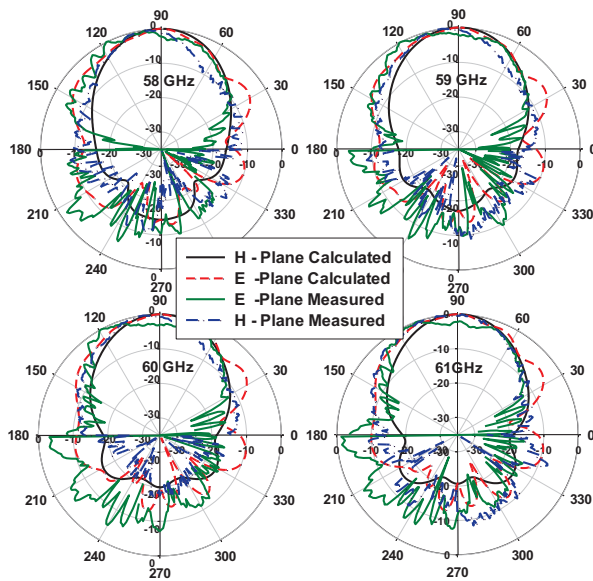
Fig. 10. The normalized E- and H-plane co-polarization patterns of the circular patch with holder for 58 GHz - 61 GHz.

In Fig. 11, the measured and the calculated results of the far-field patterns are presented for both the E- and H-planes of the proposed antenna, at 58 GHz to 61 GHz. The HPBW of the measured results agreed with the CST results for the entire ISM band. Moreover, the measured results of the H-plane agree quite well with the calculated results. However, the SLL in the measured results of the E-plane is higher than expected. This is mainly due to the effect the antenna's setup and the reflection from cable and connectors. The high reflection is caused by the Southwest connector, which is perpendicular to the E-plane, as seen in Fig. 9. A large reflection from the lab setup is also affecting

the side lobes in Fig. 11, especially from the feed line side. Meanwhile, the radiation pattern in the H-plane is far from the connectors, and thus the measured results of the radiation pattern agree well with CST results. Therefore, in a practical deployment of this antenna, this effect would not appear when mounted using a proper packaging system. This high gain hybrid antenna is a good alternative candidate to array structure for some applications such as mine wireless communications [19]. In addition, it could also be used as an array element taken into account the spacing between the elements and a proper lens diameter to fit in the array and avoid grating lobes. The estimated radiation efficiency from the measured gain and directivity is greater than 90 percent at 60 GHz, and it is 85 percent at 64 GHz.
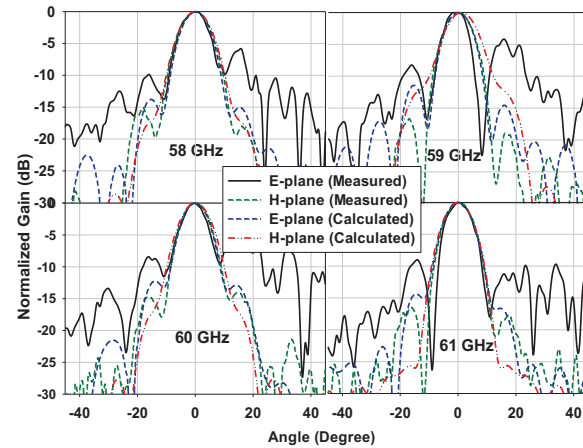
Fig. 11. Normalized E- and H-plane patterns of the proposed antenna at 58 GHz - 61 GHZ.

V. CONCLUSION

A circular patch slot-fed antenna loaded with a dielectric lens, optimized for operation at 60 GHz, is successfully implemented. An air cavity holder provides a noticeable enhancement, and makes the spherical dielectric lens simple to mount on the antenna. This prototype achieves a high measured gain of ~ 20 dB along the ISM band. The antenna impedance bandwidth is 3.5 GHz within the ISM unlicensed band. The proposed low cost antenna with a simple structure and a small size of $12.412 \times 10.5 \times 27.553$ mm^3 would be useful and suitable for millimeter-wave band applications, especially for imaging and mining applications. Moreover, the antenna can fit into portable devices.

REFERENCES

[1] E. E. Altshuler and R. A. Meir, "A comparison of experimental and theoretical values of atmospheric absorption at the longer millimeter wavelengths," *IEEE Trans. Antennas Propagat.*, vol. AP-36, no. 10, pp. 1471-1480, Oct. 1988.

[2] A. Perron, T. A. Denidni, and A. R. Sebak, "High-gain hybrid dielectric resonator antenna for millimeter-wave applications: design and implementation," *IEEE Trans. Antennas Propagat.*, vol. 57, no. 10, pp. 2882, 2009.

[3] E. Ayman and A. Sebak, "High-gain hybrid microstrip/conical horn antenna for MMW applications," *IEEE Antennas and Wireless Propagation Letters*, vol. 11, pp. 129-132, 2012.

[4] C. Karnfelt, P. Hallbjorner, H. Zirath, and A. Alping, "High gain active microstrip antenna for 60-GHz WLAN/WPAN applications," *IEEE Trans. Microw. Theory Tech.*, vol. 54 (6), pp. 2593-2603, 2006.

[5] X. Wu, G. V. Eleftheriades, and T. E. van Deventer-Perkins, "Design and characterization of single- and multiple-beam mm-wave circularly polarized substrate lens antennas for wireless communications," *IEEE Trans. Microw. Theory Tech.*, vol. 49, no. 3, pp. 431-441, 2001.

[6] Y. Larry, M. Shoucri, and P. Moffa, "Passive millimeter wave imaging," *IEEE Microwave Magazine*, vol. 4.3, pp. 39-50, 2003.

[7] J. Hasch, E. Topak, R. Schnabel, T. Zwick, R. Weigel, and C. Waldschmidt, "Millimeter-wave technology for automotive radar sensors in the 77 GHz frequency band," *IEEE Trans. Microw. Theory Tech.*, vol. 60, no. 3, pp. 845-860, 2012.

[8] T. H. Büttgenbach, "An improved solution for integrated array optics in quasioptical mm and submm receivers: the hybrid antenna," *IEEE Trans. Microw. Theory Tech.*, vol. 41, no. 10, pp. 1750-1761, 1993.

[9] D. Lemaire, C. A. Fernandes, P. Sobieski, and A. Barbosa, "A method to overcome the limitations of G.O. in axis-symmetric dielectric lens shaping," *Int. J. Infrared and MMW*, vol. 17, no. 8, pp. 1996.

[10] H. Kao-Cheng. "Millimeter wave lens antennas," *Modern Lens Antennas for Communications Engineering*, pp. 113-146, 2013.

[11] H. Kaouach, L. Dussopt, J. Lanteri, T. Koleck, and R. Sauleau, "Wideband low-loss linear and circular polarization transmit-arrays in V-band," *IEEE Trans. Antennas Propag.*, vol. 59, no. 7, pp. 2513-2523, 2011.

[12] A Henderson, A. E. England, and J. R. James, "New low-loss millimeter wave hybrid microstrip antenna array," *Eleventh European Microwave Conference*, Amsterdam, The Netherlands, 1981.

[13] M. Al Henawy and M. Schneider, "Planar antenna arrays at 60 GHz realized on a new thermoplastic polymer substrate," *Proceedings of the Fourth European Conference on Antennas and Propagation (EuCAP)*, pp. 1-5, 2010.

[14] L. Mall and R. B.Waterhouse, "Millimeter-wave proximity-coupled microstrip antenna on an extended hemispherical dielectric lens," *IEEE Trans. Antennas Propagat.*, vol. 49, no. 12, pp. 1738-1749, 2001.

[15] N. T. Nguyen, A. Rolland, A. V. Boriskin, G. Valerio, L. LeCoq, and R. Sauleau, "Size and weight reduction of integrated lens antennas using a cylindrical air cavity," *IEEE Trans. Antennas Propag.*, vol. 60, no. 12, pp. 5993-5998, 2012.

[16] W. J. Lamb, "Miscellaneous data on materials for millimeter and submillimetre optics," *Int. J. Infrared Millimeter Waves*, vol. 17, no. 12, 1996.

[17] R. B. Marks, et al., "Characteristic impedance determination using propagation constant measurement," *IEEE Microwave Guided Wave Let.*, vol. 1, pp. 141-143, 1991.

[18] E. Vilar and K. W. Wan, "Narrow and wide band estimates of field strength for indoor communications in the millimetre band," *Electronics Division Colloquium on Radiocommunications in the Range 30-60 GHz*, pp. 5/1-5/8, Jan. 17, 1991.

[19] I. Ben Mabrouk, J. Hautcoeur, L. Talbi, M. Nedil, and K. Hettak, "Feasibility of a millimeter-wave MIMO system for short-range wireless communications in an underground gold mine," *IEEE Trans. Antennas Propag.*, vol. 61 (8), pp. 4296-4305, 2013.

[20] H. Kaouach, L. Dussopt, J. Lanteri, T. Koleck, and R. Sauleau, "Wideband low-loss linear and circular polarization transmit-arrays in V-

band," *IEEE Trans. Antennas Propag.*, vol. 59, no. 7, pp. 2513-2523, 2011.

[21] S. Raman and G. M. Rebeiz, "Single and dual polarized millimeter wave slot ring antennas," *IEEE Trans. Antennas Propag.*, vol. 44, no. 11, pp. 1438-1444, Nov. 1996.

[22] T. H. Büttgenbach, "An improved solution for integrated array optics in quasioptical mm and submm receivers: the hybrid antenna," *IEEE Trans. Microw. Theory Tech.*, vol. 41, no. 10, pp. 1750-1761, Oct. 1993.

[23] J. J. Lee, *Lens Antennas, Microwave Passive and Antenna Components*, in Handbook of Microwave and Optical Components, K. Chang Ed., New York: Wiley, vol. 1, ch. 11.2, pp. 595-625, 1989.

Zouhair Briqech received the B.Sc. degree in Communications Engineering from High Institute of Electrical and Electronics Engineering, Bani-Walid, Libya, in 2003, and the M.Sc. degree in Communications and Microwave Engineering from Academy of Graduate studies, Tripoli, Libya, in 2007. In 2010, he joined to the Microwave group of Department of Electrical and Computer Engineering, Concordia University, as a Researcher Assistant and he is now working towards his Ph.D. degree.

Abdel-Razik Sebak received the B.Sc. degree in Electrical Engineering from Cairo University in 1976, and the M.Eng. and Ph.D. degrees from the University of Manitoba in 1982 and 1984, respectively. From 1984 to 1986, he was with the Canadian Marconi Company. From 1987 to 2002, he was a Professor of Electrical and Computer Engineering, University of Manitoba. He is currently a Professor of Electrical and Computer Engineering, Concordia University. His current research interests include phased array antennas, computational electromagnetics (EM), integrated antennas, EM theory, interaction of EM waves with new materials, and bio-EM. Sebak received the 1992 and 2000 University of Manitoba Merit Award for outstanding Teaching and Research, the 1994 Rh Award for Outstanding Contributions to Scholarship and Research in the Applied Sciences category, and the 1996 Faculty of Engineering Superior Academic Performance. He has served as Chair for the IEEE Canada Awards and Recognition Committee (2002-2004).

Tayeb A. Denidni received the B.Sc. degree in Electronic Engineering from the University of Setif, Setif, Algeria, in 1986, and the M.Sc. and Ph.D. degrees in Electrical Engineering from Laval University, Quebec, Canada, in 1990 and 1994, respectively. From 1994 to 2000, he was a Professor with the Engineering Department, Universite du Quebec, Rimouski, Quebec, Canada. Since August 2000, he has been a Professor with Institut National de la Recherche Scientifique (INRS), Universite du Quebec, Montreal, Canada. He is leading a large research group consisting of two research scientists, five Ph.D. students, and three M.S. students. Over the past 10 years, he has graduated numerous graduate students. His current research interests include planar microstrip filters, dielectric resonator antennas, EM-bandgap antennas, antenna arrays, and microwave and RF design for wireless applications. He has authored over 100 papers in refereed journals. He has also authored or co-authored over 140 conference papers.

Systematic Analysis on the Optical Properties of Chiral Metamaterial Slab for Microwave Polarization Control

I. Comez [1], M. Karaaslan [2], F. Dincer [3], F. Karadag [1], and C. Sabah [4]

[1] Department of Physics
Cukurova University, Adana, Turkey

[2] Department of Electrical and Electronics Engineering
[3] Department of Computer Engineering
Mustafa Kemal University, Iskenderun, Hatay, Turkey

[4] Department of Electrical and Electronics Engineering
Middle East Technical University ─ Northern Cyprus Campus
Kalkanli, Guzelyurt, TRNC/Mersin 10, Turkey
sabah@metu.edu.tr

Abstract ─ Theoretical and numerical of investigation of the chiral slab exhibiting polarization rotation is presented in detail. The effects of the chirality, thickness of medium, dielectric constant, and incident angle are analyzed in order to display the characteristic features of the chiral slab both for TE and TM incident waves. The chiral slab then is realized by using a full wave EM simulation software in order to validate the numerical results in which the numerical and simulation results are in good agreement with each other. Different than the other studies existing in literature, the proposed model shows optimum results for wide frequency band by using small chirality which is sufficient for polarization rotation. From the results, it is observed that the proposed system and its realization can be effectively used as a polarization converter and EM filters at some frequencies.

Index Terms ─ Chirality, EM filter metamaterial, polarization control.

I. INTRODUCTION

Chiral medium has received considerable attention in last decades due to their potential applications (such as filters, polarization rotators, antennas, and so on) in microwave and millimeter wave frequencies [1-5]. It can be realized using several methods [6-9] including metamaterials (MTMs) without mirror symmetry planes [10] to exhibit, for some desired aims, a controlled active, dynamical, and tunable EM response [11]. Chiral medium is characterized by the quantity of chirality, $\xi = (n_R - n_L)/2$, where n_R and n_L is the refractive index of the right- and left-handed circular polarized wave (RCP and LCP) [12,13]. Basically, chirality is defined as the lack of mirror image symmetry which refers to the ability of the polarization rotation. In this sense, it is always desirable to have full control of the polarization states of EM waves especially for filtering, data transmission, and sensing purposes. The polarization control can effectively be manipulated through the reflection/refraction using a chiral slab (CS) or chiral MTM (CMTM) owing to the strong polarization rotation ability due to lack of mirror symmetry. This is also known as optical activity and can be used in many fields as polarizers, diagnostic tool in spectroscopy and analytical chemistry, signature effect for the life detection in molecular biology [14-22]. Besides, oriented or randomly arranged man made metal helices was investigated as polarizer which exhibits large circular dichroism and huge polarization rotation as in the new-generation MTMs [21], [22]. Additionally, the reflection and transmission properties of multiple chiral layers are analyzed to

show the polarization conversion and EM filtering features of the conventional CSs [8], [9].

In this work, methodical investigation of a CS and its characteristic features are studied. First, the electromagnetic properties of the chiral medium are given. Then, theoretical equations for the CS are established. After that, the numerical analysis based on the theoretical formalism are provided by considering the effects of the different parameters such as chirality coefficients, thickness of medium, dielectric constant, and incident angle. Reflection and transmission coefficients through the CS are computed and presented for the incident wave of TE and TM cases. From the results, it can be seen that CS can be used as a polarization-convertor and EM filter (transmission and/or antireflection) at around the operation/central frequency. As a final investigation, the studied CS are constructed physically by a simulation software to be able to validate the numerical results and to show the feasibility of the proposed system. The constructed CS by the simulation software shows very good performance and can be fabricated for the experimental study to be used as EM filter or polarization-rotator [8], [9]. Commonly, these kinds of devices are generally realized using more than one-slab [4], [5], [8], [9]. However, the realization is accomplished using *only-one-slab* in the present study. Additionally, the new generation CMTMs have very large chirality values which creates some difficulties in the design and realization of mentioned devices. Keeping the chirality values small enough abolish the difficulties and makes the EM filter and polarization-rotator devices easily realizable. Those are main advantages of the present study and provide additional flexibilities to design and manufacturing processes.

II. THEORETICAL ANALYSIS

CS has interesting properties when it is embedded between two semi-infinite dielectrics. The configuration of the structure is shown in Fig. 1. TE and TM polarized monochromatic plane incident wave from free-space is applied to CS. In general, wave equation in a chiral media can be given as [8], [23]:

$$\vec{\nabla} \times \vec{\nabla} \times \vec{\varphi} - 2\omega\mu\xi\vec{\nabla} \times \vec{\varphi} - k^2\vec{\varphi} = 0, \quad (1)$$

where ξ is the chirality of CS; k is the wave number, and $\vec{\varphi}$ is the field. If the field $\vec{\varphi}$ is along p

direction and the field have two components along q and r orthogonal directions, it can be written as:

$$\vec{\varphi} = (q\vec{a_q} + r\vec{a_r})e^{kp}. \quad (2)$$

The left (LCP) and right (RCP) circularly polarized components of propagation $k_{LCP, \ RCP}$ are determined using of Eqs. (1) and (2) as [8], [23]:

$$k = -jk_{LCP, \ RCP} = -j\left[\omega\mu\xi \pm \sqrt{\omega^2\mu\hat{I} + (\omega\mu\xi)^2}\right]. \quad (3)$$

The relation between incidence, transmission and reflection angles is obtained by Snells Law [8], [23]:

$$k_i\sin\theta_i = k_R\sin\theta_R = k_L\sin\theta_L = k_t\sin\theta_t \ ; \theta_i = \theta_r, \quad (4)$$

where θ_i is the incidence angle, θ_r is the reflection angle; and θ_R and θ_L are the angles of right and left polarized components of the transmitted wave. The incident, reflected, and transmitted with respect to Fig. 1 can be determined as follows.
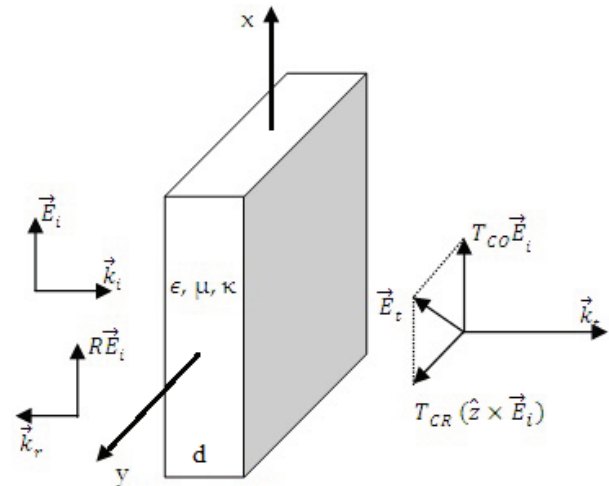
Fig. 1. Schematic diagram of CS with incident, reflected, and transmitted fields

According to Fig. 1, the incident electric field with arbitrary polarization composed of TE and TM components can be written as [8], [23]:

$$\boldsymbol{E}_i = (E_0^{TM}.\boldsymbol{u_{TM}} + E_0^{TE}.\boldsymbol{u_{TE}})e^{-jk_t r}.e^{-j\gamma p}, \quad (5)$$

where E_0^{TM} and E_0^{TE} are the components of incident electric field; $\boldsymbol{u_{TE}}$ and $\boldsymbol{u_{TM}}$ denotes direction vectors of TE and TM electric field components, and k_t represents the transverse component of wave vector. TE and TM refer to the parallel and perpendicular components of the electric field vector. Note that, the first region is selected as

vacuum. Then, the reflected electric (E_r) field can be written as [8], [23]:

$$E_r = (E_r^{TM} u_{TM} + j e_r^{TE} u_{TE}) e^{-jk_T r} e^{j\gamma p} +$$
$$(E_r^{TE} u_{TE} + j e_r^{TM} u_{TM}) e^{-jk_T r} . e^{j\gamma p}, \qquad (6)$$

where e_r^{TM} and e_r^{TE} are the components of the reflected electric field. The electric field is represented with RCP and LCP components in Eq. (6). As a next step, the fields in CS will be given. The electric field in CS has also two components (RCP and LCP) and they are propagating both in positive and negative directions. Therefore, in CS there are two waves, one propagating along the same direction with the incident wave and the other one propagating toward the opposite of the incident wave. Thus, the total electric field in CS can be expressed as [8], [23]:

$$E^+ = (A_L^{TM} u_{TM} + j A_L^{TE} u_{TE}) e^{-jk_T r} e^{-j\gamma_L p} +$$
$$(A_R^{TM} u_{TM} - j A_R^{TE} u_{TE}) e^{-jk_T r} e^{-j\gamma_R p} +$$
$$(j A_L^{TM} u_{TM} - j A_L^{TE} u_{TE}) e^{-jk_T r} e^{-j\gamma_L p} +$$
$$(j A_R^{TM} u_{TM} + A_R^{TE} u_{TE}) e^{-jk_T r} e^{-j\gamma_R p}, \qquad (7.a)$$

$$E^- = (B_L^{TM} u_{TM} - j B_L^{TE} u_{TE}) e^{-jk_T r} e^{j\gamma_L p} +$$
$$(B_R^{TM} u_{TM} - j B_R^{TE} u_{TE}) e^{-jk_T r} e^{j\gamma_R p} +$$
$$(-j B_L^{TM} u_{TM} - B_L^{TE} u_{TE}) e^{-jk_T r} e^{j\gamma_L p} +$$
$$(-j B_R^{TM} u_{TM} - B_R^{TE} u_{TE}) e^{-jk_T r} e^{j\gamma_R p}, \qquad (7.b)$$

where $A_L^{TM}, A_L^{TE}, A_R^{TM}, A_R^{TE}$ and $B_L^{TM}, B_L^{TE}, B_R^{TM}, B_R^{TE}$ are the amplitudes of the electric fields in CS. Note that, in all representations, the subscripts L, R, TM, and TE denotes the LCP, RCP, transverse electric, and transverse magnetic components of electric field, correspondingly. The electric fields in the last region can also be expressed in terms of both TE and TM components. Third region is also vacuum as in the first region. The transmitted electric field with any arbitrary polarization can be written as follows [8], [23]:

$$E_t = (E_t^{TM} u_{TM} + j e_t^{TE} u_{TE}) e^{-jk_T p} e^{-j\gamma(z-d)} +$$
$$(j E_t^{TM} u_{TM} + e_t^{TE} u_{TE}) e^{jk_T p} e^{-j\gamma(z-d)}, \qquad (8)$$

where E_t^{TM} and e_t^{TE} are TM and TE components of electric field and d is the thickness of CS. The corresponding magnetic fields for all regions can be found using Maxwell's equations [8], [23]. In order to analyze the proposed configuration, it is required to impose the boundary conditions at the interfaces of $z = 0$ and $z = d$. Therefore, the relationships between the fields in all regions can easily be determined by using the boundary conditions and Maxwell's equations. As a result, the reflection and

transmission coefficients can be found and computed [8], [23].

III. NUMERICAL RESULTS

In this section, co- (TE-TE or TM-TM) and cross-polarized (TE-TM or TM-TE) reflection and transmission coefficients are presented numerically to observe their behaviors using the theory of the previous section. Particularly, the effects of the chirality, thickness of the slab, dielectric constant, and incident angle will be investigated and analyzed in details by means of the numerical computations. In order to verify the computations, a particular case is simulated using a commercial full-wave software. Both processes give the same results, which means the numerical computations are verified.

A. Effect of the chirality on the reflection and transmission

One of the main parameters that affect the polarization state of the wave and provides polarization conversion is the chirality. Here, the effects of the chirality parameter on the reflection and transmission will be investigated. The incident and transmitted media are defined as free space ($\mu_i = \mu_t = \mu_0$, $\varepsilon_i = \varepsilon_t = \varepsilon_0$) and CS has the following parameters: $\varepsilon_c = 4\varepsilon_0$, $\mu_c = \mu_0$, $d = 3\ mm$. Note that, the selected chirality values are so small that its influence on the refractive index is negligible. However, it is carefully selected and its absolute value has to be lower than the upper bound resulting from maximum coupling and given by $|\xi_c| \leq \sqrt{\varepsilon/\mu}$ where ε and μ are permittivity and permeability of the medium [6], [8], [24], [25]. The optimum value is chosen for this study to provide sufficient coupling between the electric and magnetic fields. Note those Refs. [6,24] emphasize that even a small value of ξ_c can have a pronounced effect on the transmitted wave through rotation of the polarization. Note again, for the selected optimum chirality value, there exists a symmetry in the reflection and transmission with respect to the resonant frequency but the symmetry can be lost for different chirality values [8]. Figure 2 shows the reflection and transmission response with respect to frequency when the chirality varied. The increase in the chirality shifts the resonant frequency downward due to the inverse proportionality between the frequency and chirality (Eq. 3). Quasi-

reflection band-pass phenomenon is observed for all polarizations when the chirality parameter is varied. Thus, semi-band-pass EM filter for the reflected wave can be utilized using the proposed configuration. More importantly, the structure provides a wide-band polarization conversion in the transmitted wave at the resonant frequency for all chirality parameters. For example, parallel to perpendicular (TM to TE) polarization conversion occurs for the transmitted wave for $\xi_c = 0.003$ at the resonant frequency of 22.1 GHz, although the incident electric field has no perpendicular component at all (optical activity and polarization rotation with 100 % efficiency). The same observation are also scrutinized for the perpendicular to parallel (TE to TM) polarization conversion at the mentioned resonant frequency, since CS is a symmetric structure with respect to its front and back sides. Note that, similar polarization conversion cases (with ~100% efficiency for all cases) can also be seen for the other chirality parameters. Consequently, the small chirality leads to a polarization-rotated transmitted wave. At the resonant frequency, almost complete parallel-to-perpendicular or perpendicular-to-parallel conversions occur for the transmitted wave. Therefore, one can say that the proposed structure acts as a wide-band polarization-conversion transmission filter and antireflection (full-transmission) in some microwave frequency band.
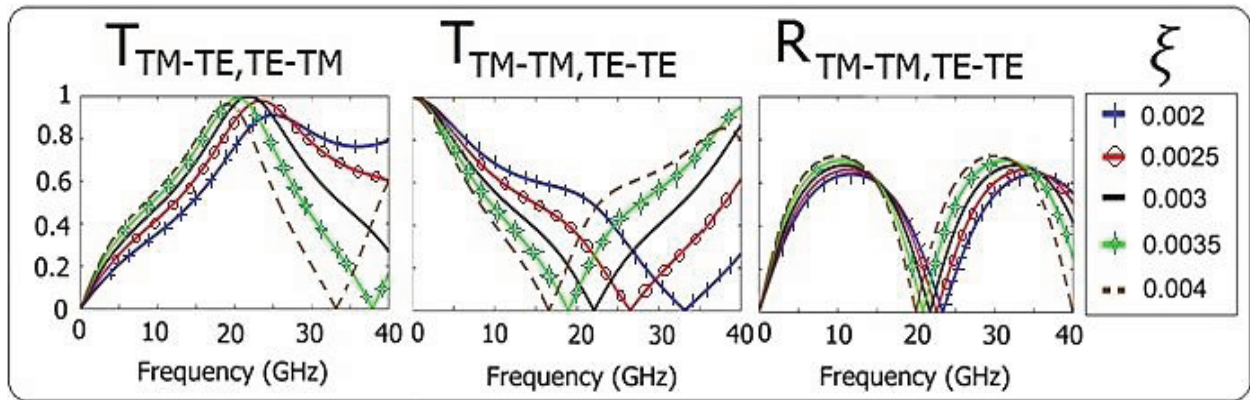
Fig. 2. Cross- and co-polarized transmission; and co-polarized reflection coefficients versus frequency with respect to the chirality variation.

B. Effect of the dielectric constant on the reflection and transmission

Another parameter that affect the reflection and transmission features of the system is the dielectric constant of CS. The incident and transmitted media are defined as free space. CS has the following parameters: $\mu_c = \mu_0$, $d = 3\ mm$ and $\xi_c = 0.003$. Figure 3 presents the reflection and transmission data. Quasi-reflection band-pass phenomenon (semi-bandpass EM filter property) for the reflected wave, as in the previous case, is also observed for both polarizations when the dielectric constant of CS is changed. The co-polarized (TE-TE or TM-TM) transmission is zero and the cross-polarized (TE-TM or TM-TE) transmission has a high peak (unity or close to unity) at the resonant frequency (~20 GHz) while the incident EM wave has no cross-polarized field component(s). It means that broad spacing of transmission peak is preserved and wide-band complete polarization conversion occurs at this frequency. Consequently, the proposed structure is insensitive to the variation of the dielectric constant of CS and this property can be regarded as an added value of the model which provides additional flexibility in the design, optimization, and fabrication processes.
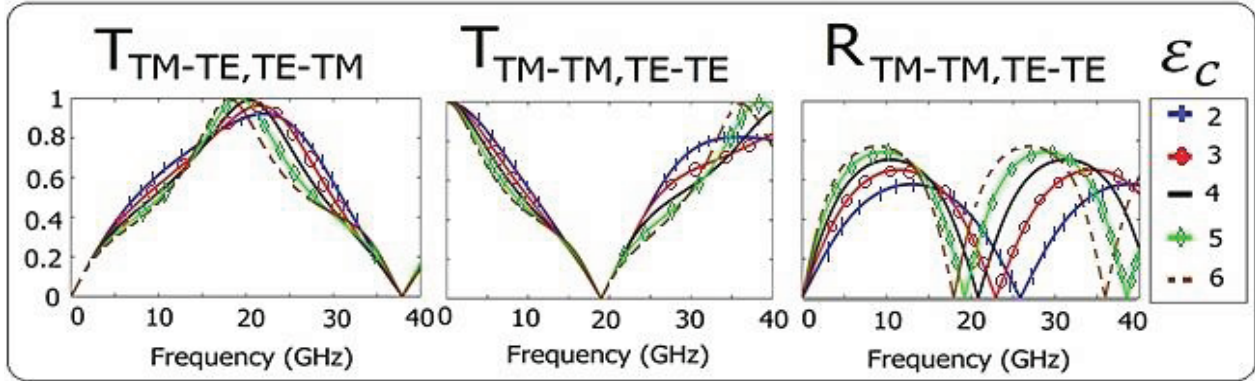
Fig. 3. Cross- and co-polarized transmission; and co-polarized reflection coefficients versus frequency with respect to the variation of the dielectric constant of CS.

C. Effect of the slab thickness on the reflection and transmission

In this section, the effect of the slab thickness on the character of the reflection and transmission will be analyzed. The incident and transmitted media are defined as free space as in the previous example. The CS has the following parameters: $\xi_c = 0.003$, $\mu_c = \mu_0$, and $\varepsilon_c = 4\varepsilon_0$. The results are shown in Fig. 4. Quasi-reflection band-pass for the reflected wave and polarization conversion for the transmitted wave occur (as in the previous two cases) regardless of the change in the thickness of CS. The increase in the thickness of CS yields a down-shift in the resonant frequency (and thus a down-shift in the cross-polarized transmission

peak). Complete polarization conversion (with fully anti-reflection property) for the transmitted wave occurs at the resonant frequency for the selected medium parameters for different thicknesses. The spectral location of the resonance is inversely proportional with the thickness of CS. Consequently, the proposed structure is independent from the change of the thickness of CS. This means that more flexible prototype can be designed and manufactured using the mentioned independency with the wide-band complete polarization conversion in the transmission and semi-reflection band-pass EM filter in some microwave frequency region.
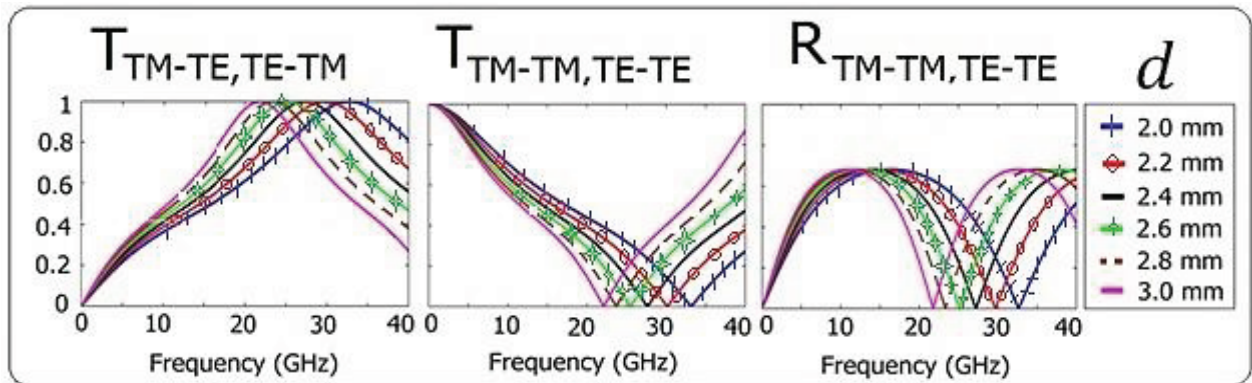
Fig. 4. Cross- and co-polarized transmission; and co-polarized reflection coefficients versus frequency with respect to the variation of the slab thickness.

D. Effect of the incident angle on the reflection and transmission

The last parameter to be investigated is the

incident angle of the EM wave. The incident and the transmitted media are assumed to be free-space and CS has the following medium parameters: $d =$

$0.3mm$, $\xi_c = 0.003$, $\mu_c = \mu_0$, and $\varepsilon_c = 3\varepsilon_0$. The results are shown in Fig. 5 and Fig. 6. Symmetric and asymmetric quasi-reflection band-pass for the reflected wave occurs for both polarizations when the angle of incidence is varied. The symmetry of the reflection is degraded with the increase of the incident angle. Polarization conversion still occurs for both polarization for the studied incident angles, but the level of the cross-polarized transmission peak strongly depends on the angle of incidence. For TE incidence case, this peak level is high compared to TM incidence case. The structure is more sensitive to the variation of the incident angle for TM incidence situation. This means that while an unstable polarization conversion with respect to the peak level occurs for TM incident wave, a significant (including complete) polarization conversion occurs for TE incident wave. As a result, complete polarization conversion for TM incident case can be achieved for only small incident angles. Therefore, the incident angle plays an important role for the polarization conversion using the proposed system and one should take care of the incident angle in the design and optimization processes before the fabrication.
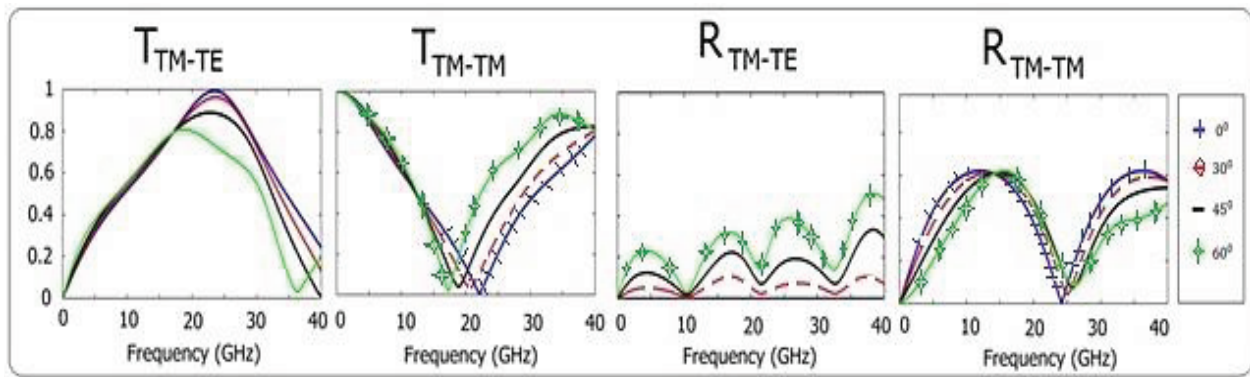
Fig. 5. Cross- and co-polarized transmission and reflection coefficients versus frequency with respect to the incident angle variation under TM incident wave.
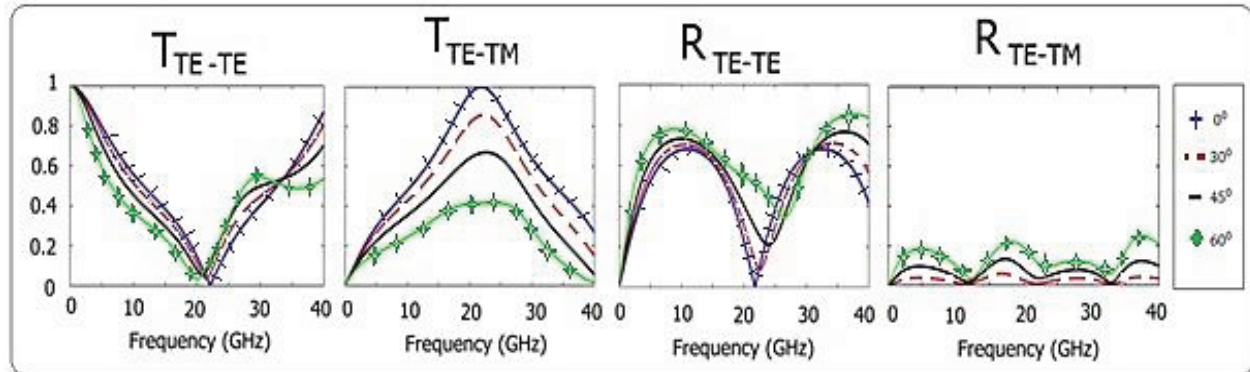
Fig. 6. Cross- and co-polarized transmission and reflection coefficients versus frequency with respect to the incident angle variation under TE incident wave.

IV. DESIGN AND OPTIMIZATION OF CHIRAL METAMATERIAL BASED ON SPLIT RECTANGULAR RESONATOR

In this part, the proposed structure given in the first section will be realized using full wave EM simulation software based on finite integration technique. The chirality parameter will be obtained and optimized to achieve a complete polarization conversion with wide-band transmission peak and antireflection property. The designed CMTM structure and its unit cell is shown in Fig. 7. The CMTM structure is formed by the periodic

arrangement of the unit cell based on split-rectangular-resonator (SRR). Commercial full wave EM simulation software is used in the simulation. FR4 is used as a substrate with the relative permittivity of 4.4, loss tangent of 0.002, and thickness of $0.28\ mm$. Copper is used for the metallic pattern with the conductivity of $5.8 \times 10^7\ S/m$ and thickness of $0.035\ mm$.
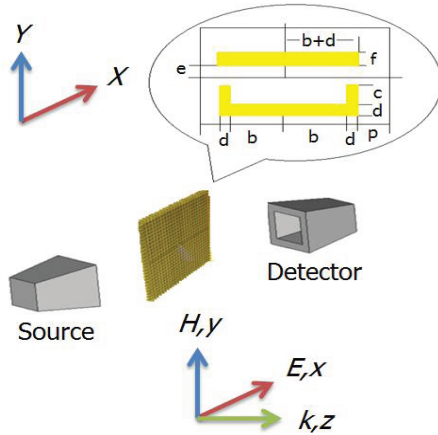
Fig. 7. Periodically arranged CMTM and its unit cell.

The optimized SRR dimensions are obtained using Interpolated Quasi Newton Approach in the simulation by setting them as parametric values. The augmentations can be realized by two different methods [26]; back tracking line-search and model-trust region methods. In the former method, step length is chosen to get satisfactory step, whereas a step is adjusted to reduce the norm of the local linear model in the latter method. Accuracy and S-parameter error threshold values are chosen as 10^{-6} and 0.01, respectively. The optimized dimensions are evaluated for different variables to provide polarization conversion and/or antireflection related to the results presented in the previous section. The computed optimized values are shown in Table 1 to Table 4. Table 1 shows the SRR dimensions when the chirality is changing which is related with the data of Section 3.1 (and Fig. 2). For example, there is a polarization conversion and antireflection phenomenon at the resonance frequency of 20.4 GHz when $\xi_c = 0.003$. The corresponding dimensions for SRR are given in Table 1 for the realization. Additionally, this is a

kind of verification for the spectral location of the cross-polarized transmission peak and polarization rotation.

Table 1: The optimized SRR dimensions when the chirality is changing (related to Fig. 2)

ξ	f(GHz)	b(mm)	c(mm)	d(mm)	e(mm)	f(mm)	p(mm)
0.002	25.1	0.538	0.733	0.069	0.081	0.073	0.285
0.0025	23.3	1.962	0.733	0.054	0.196	0.050	0.977
0.003	22.1	0.538	1.967	0.196	0.192	0.196	0.977
0.0035	20.4	1.23	0.900	0.111	0.084	0.061	0.215
0.004	19.1	0.538	0.733	0.050	0.0538	0.053	0.123

Table 2 shows the SRR dimensions when the permittivity of CS is changing which is related with the data of Section 3.2 (and Fig. 3). For each design, there is a polarization rotation and antireflection property. Note that, the results of the table and corresponding data of Section 3.2 are in good agreement with each other.

Table 2: The optimized SRR dimensions when the permittivity of CS is changing (related to Fig. 3)

ε	f(GHz)	b(mm)	c(mm)	d(mm)	e(mm)	f(mm)	p(mm)
2	24.7	0.538	0.733	0.054	0.058	0.054	0.123
3	23.5	0.538	1.967	0.192	0.196	0.054	0.977
4	21.8	1.269	1.333	0.123	0.123	0.127	0.123
5	20.3	0.538	1.966	0.200	0.1962	0.054	0.123
6	19.0	1.1538	0.733	0.196	0.0538	0.0538	0.977

Table 3 and Table 4 show the SRR dimensions for the variation of thickness of CS and incident angle which are related with the data of Section 3.3 (Fig. 4) and Section 3.4 (Fig. 5). Once again, there is a polarization rotation and antireflection property for each design parameters. Note again, the results of the tables and corresponding data of Section 3 are in good agreement with each other.

Table 3: The optimized SRR dimensions when the thickness of CS is changing (related to Fig. 4)

d(mm)	f(GHz)	b(mm)	c(mm)	d(mm)	e(mm)	f(mm)	p(mm)
2	32.7	1.985	0.713	0.198	0.200	0.199	0.990
2.2	29.8	0.515	0.726	0.198	0.052	0.198	0.109
2.4	27.3	1.984	1.985	0.043	0.297	0.295	0.101
2.6	25.2	0.515	0.713	0.124	0.126	0.0515	0.545
2.8	23.4	1.985	1.514	0.237	0.277	0.123	1.156
3	21.8	0.416	0.515	0.043	0.045	0.043	0.101

Table 4: The optimized SRR dimensions when the incident angle is changing (related to Fig. 5)

θ(in º)	f(GHz)	b(mm)	c(mm)	d(mm)	e(mm)	f(mm)	p(mm)
0º	23.4	0.426	0.624	0.043	0.042	0.043	0.104
30º	23.7	0.228	0.426	0.033	0.3	0.115	1.486
45º	22.7	0.228	0.327	0.040	0.794	0.843	1.226
60º	18.8	0.228	0.327	0.040	0.03	0.099	1.486

V. VALIDATION OF THE NUMERICAL AND SIMULATION RESULTS

As a last investigation, the numerical (related to Section 3) and simulation (related to Section 4) results are calculated and compared. In the numerical computation, the thickness, dielectric constant, and chirality of CS is $d = 0,28\ mm$, $\varepsilon_c = 4\varepsilon_0$, and $\xi_c = 0.003$, in order. In the simulation, FR4 and copper are used for the substrate and metallic pattern, respectively, as mentioned in the previous section. The unit cell has the following dimensions: $b = 1.985\ mm$, $c = 1.514\ mm$, $d = 0.237\ mm$, $e = 0.277\ mm$, $f = 0.123\ mm$, and $p = 1.155\ mm$. The results are shown in Fig. 8. As seen, polarization rotation and antireflection phenomenon are noticed. Complete polarization rotation are observed around 23 GHz. The numerical and simulation results are in good agreement. Consequently, the theory is validated by numerical and simulation results. Therefore, one can realize a microwave polarization rotator or antireflection filter using the proposed model.
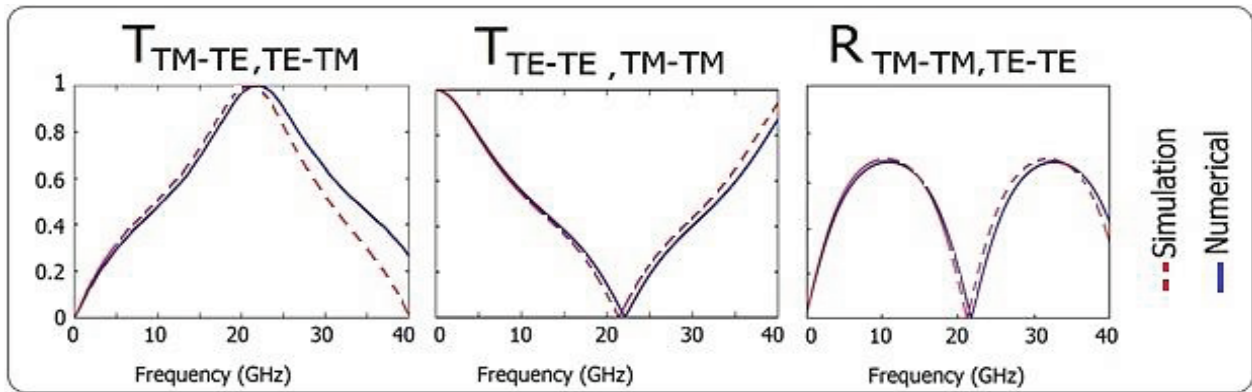
Fig. 8. Simulation and numerical results of CS and SRR based CMTM slab.

VI. CONCLUSION

The frequency response of CS is presented by theoretically and numerically. Then, a particular case is also studied by simulation, which means that the proposed CS is realized using full wave simulation software. The optical activity, EM filtering, and polarization rotation features of the structures with optimized parameters for the wide frequency region are presented via numerical and simulation results. The effects of the chirality, dielectric constant of CS, slab thickness, and incident angle are also investigated both for TE and TM cases. Complete polarization conversion and EM filtering are observed from the results of the parametric study. The mentioned properties are acquired using small chirality values. As known, new generation CMTMs existing in literature provide large/giant chirality values. Opposite to the existing studies, the proposed model (a kind of new generation CMTM) with small chirality shows optimum results within the wide frequency range. Additionally, this small chirality is sufficient for polarization rotation and EM filtering. According to the best of our knowledge, this kind of study (new generation CMTM with small chirality as a single slab and its application to the polarization conversion) is not studied in literature up to date. Consequently, the proposed structure can be utilized for EM filtering, and especially polarization conversion devices for wide range of microwave frequencies. As a result, this study paves the way towards the realization and fabrication of a polarization rotator and can be used for data transmission or sensing purposes.

REFERENCES

[1] A. Sihvola, "*Electromagnetic Emergence in Metamaterials*," Advances in Electromagnetics

of Complex Media and Metamaterials, S. Zouhdi, A. Sihvola, and M. Arsalane (eds.), vol. 89, NATO Science Series II: Mathematics, Physics, and Chemistry, Kluwer Academic, 2003.

[2] N. Engheta and R. W. Ziolkowski, *Metamaterials: Physics and Engineering Explorations*, Wiley-IEEE Press, Piscataway, NJ, 2006.

[3] L. Solymar and E. Shamonina, *Waves in Metamaterials*, Oxford University Press, New York, 2009.

[4] C. Sabah and S. Uckun, "Multilayer system of lorentz/drude type metamaterials with dielectric slabs and its application to electromagnetic filters," *Progress In Electromagnetics Research*, vol. 91, pp. 349-364, 2009.

[5] C. Sabah, H. T. Tastan, F. Dincer, K. Delihacioglu, M. Karaaslan, and E. Unal, "Transmission tunneling through the multi-layer double-negative and double-positive slabs," *Progress In Electromagnetics Research*, vol. 138, pp. 293-306, 2013.

[6] D. Jaggard, L. N. Engheta, M. W. Kowarz, P. Pelet, J. C. Liu, and Y. Kim, "Periodic chiral structures," *IEEE T. Antenn. Propag.*, vol. 37, pp. 1447-1452, 1989.

[7] J. Lekner, "Optical properties of isotropic chiral media," *Pure Appl. Opt.*, vol. 5, pp. 417-443, 1996.

[8] C. Sabah and S. Uckun, "Mirrors with chiral slabs," *J. Optoelectronics and Advanced Materials*, vol. 8, pp. 1918-1924, 2006.

[9] C. Sabah and H. G. Roskos, "Design of a terahertz polarization rotator based on a periodic sequence of chiral – metamaterial and dielectric slabs," *Progress In Electromagnetics Research*, vol. 124, pp. 301-317, 2012.

[10] J. Zhou, J. Dong, B. Wang, T. Koschny, M. Kafesaki, and C. M. Soukoulis, "Negative refractive index due to chirality," *Phys. Rev. B*, vol. 79, pp. 121104-4, 2009.

[11] W. Padilla, A. J. Taylor, C. Highstrete, M. Lee, and R. D. Averitt, "Dynamical electric and magnetic metamaterial response at terahertz frequencies," *Phys. Rev. Lett.*, vol. 96, pp. 107401-4, 2006.

[12] Z. Li, R. Zhao, T. Koschny, M. Kafesaki, K. Alici, E. Colak, H. Caglayan, E. Ozbay, and C. M. Soukoulis, "Chiral metamaterials with negative refractive index based on four "U" split ring resonators," *Appl. Phys. Lett.*, vol. 97, pp. 081901-3, 2010.

[13] R. Zhao, L. Zhang, J. Zhou, T. Koschny, and C. M. Soukoulis, "Conjugated gammadion chiral metamaterial with uniaxial optical activity and negative refractive index," *Phys. Rev. B*, vol. 83, pp. 035105-4, 2011.

[14] R. Zhao, T. Koschny, and C. M. Soukoulis, "Chiral metamaterials: retrieval of the effective parameters with and without substrate," *Opt. Express*, vol. 18, pp. 14553-67, 2010.

[15] U. C. Hasar, J. J. Barroso, M. Ertugrul, C. Sabah, and B. Cavusoglu, "Application of a useful uncertainty analysis as a metric tool for assessing the performance of electromagnetic properties retrieval methods of bianisotropic metamaterials," *Progress In Electromagnetics Research*, vol. 128, pp. 365-80, 2012.

[16] D. Jaggard, L. N. Engheta, M. W. Kowarz, P. Pelet, J. C. Liu, and Y. Kim, "Periodic chiral structures," *IEEE T. Antenn. Propag.*, vol. 37, pp. 1447-1452, 1989.

[17] C. Zhangand and T. J. Cui, "Negative reflections of electromagnetic waves in a strong chiral medium," *Appl. Phys. Lett.*, vol. 91, pp. 194101, 2007.

[18] J. C. Bose, "On the rotation of plane of polarization of electric waves by a twisted structure," *J. Proceedings of the Royal Society of London*, vol. 63, pp. 146-152, 1898.

[19] I. Tinoco and M. P. Freeman, "The optical activity of oriented copper helices, I. experimental," *J. Phys. Chem.*, vol. 61, pp. 1196-1200, 1957.

[20] C. Guerin, "Energy dissipation and absorption in resiprocal bi-isotropic media described by different formalism," *Progress In Electromagnetics Research*, vol. 9, pp. 31-44, 1994.

[21] F. Dincer, C. Sabah, M. Karaaslan, E. Unal, M. Bakir, and U. Erdiven, "Asymmetric transmission of linearly polarized waves and dynamically wave rotation using chiral metamaterial," *Progress In Electromagnetics Research*, vol. 140, pp. 227-239, 2013.

[22] Y. Cheng, Y. Nie, L. Wu, and R. Gong, "Giant circular dichroism and negative refractive index of chiral metamaterial based on split-ring resonators," *Progress In Electromagnetics Research*, vol. 138, pp. 421-432, 2013.

[23] S. J. Orfanidis, *Electromagnetic Waves and Antennas*, online text book, Rutgers University, 2004 (ece.rutgers.edu/~orfanidi/ewa/).

[24] D. L. Jaggard, A. R. Mickelson, and C. H. Papas, "On electromagnetic waves in chiral media," *Appl. Physics*, vol. 18, pp. 211-216, 1979.

[25] N. Engheta and D. L. Jaggard, "Electromagnetic chirality and its applications," *IEEE AP-S Newsletter*, vol. 30, pp. 6-12, 1988.

[26] J. E. Dennis and J. J. More, "Quasi-Newton methods, motivation and theory," *SIAM Review*, vol. 19, pp. 46-89, 1977.

Ibrahim Comez received the M.S. degree in Physics Department from the University of Cukurova, Adana, Turkey. He is currently studying Metamaterials and Chiral Media as a Ph.D. student. His research interests are metamaterials, solid state physics, cihral, and anisotropic media.

Muharrem Karaaslan received the Ph.D. degree in Physics Department from the University of Cukurova, Adana, Turkey, in 2009. He is the co-author of about 20 scientific contributions published in journals and conference proceedings. His research interest are applications of metamaterials, analysis and synthesis of antennas, and waveguides.

Furkan Dincer received the B.Sc., M.Sc., and Ph.D. degrees in Electrical and Electronics Engineering from Sutcu Imam, Yuzuncu Yil and Mustafa Kemal Universities, Turkey. His research interests are related with the functional microwave structures and metamaterials.

Faruk Karadag received the Ph.D. degree in Physics Department from the University of Çukurova, Adana, Turkey, in 2002. He is the co-author of about 25 scientific contributions published in international journals and conference proceedings. His research interest includes the applications of metamaterials, solid state physics, and anisotropic media.

Cumali Sabah received the B.Sc., M.Sc., and Ph.D. degrees in Electrical and Electronics Engineering from the University of Gaziantep, Turkey. He is currently with Middle East Technical University ─ Northern Cyprus Campus. His research interests include the microwave and electromagnetic investigation of unconventional materials and structures, wave propagation, scattering, complex media, metamaterials and their applications.

A Fourth Order FDFD Approach for the Analysis of Sectorial Elliptic Waveguides

Alessandro Fanti, Luisa Deias, Giovanni Andrea Casula, and Giorgio Montisci

Department of Electrical and Electronic Engineering
University of Cagliari, 09123, Piazza d'Armi, Cagliari, Italy
{alessandro.fanti, luisa.deias, a.casula, giorgiom}@diee.unica.it

Abstract ─ We present a fourth order frequency domain finite difference approach (FDFD) in curvilinear coordinates for the computation of the modes of sectorial and ridged elliptic waveguides. The use of an elliptic mesh allows to avoid usual the staircase approximations of the boundary, providing a very effective and accurate procedure.

Index Terms ─ Cutoff frequency, elliptical ridged waveguide analysis, finite difference frequency domain, microwave components, microwave filters, ridged waveguides, waveguide modes.

I. INTRODUCTION

Application of sectorial and ridged circular and elliptic waveguides [1] can be found in many components like filters, matching networks, orthomode transducers, polarizers and circulators that are widely used in satellite and terrestrial communication systems [2-6]. Low-cost design, small size, and optimal performance of these components are essential to satisfy today's stringent payload requirements. Analysis and design of such structures requires the solution of waveguide problems, which can be faced both with general-purpose software and with specialized numerical techniques, such as methods of moments (MoM) [7-9] and mode-matching (MM) [10-11]. However, MM requires an accurate knowledge of the waveguide modes to be implemented. The same type of information is also required in the analysis, using MoM, of thick-walled apertures [12] and slots [13-14]. Indeed, these apertures can be considered as stub waveguides, and the modes of these guides are the natural basis functions for the MoM [15].

Apart from some simple geometries, where analytical evaluation of such modes is possible, the mode computation cannot be done in closed form (or the closed-form solution is unsuitable for effective use). In particular, for a circular waveguide, the analytic computation of the modes is simple, since the mode distribution can be expressed in terms of Bessel functions and the eigenvalues are the zeroes of these functions, which are well-known [16]. An analytical, closed form solution exists also for elliptic waveguides and has been found by Chu [17] since the 30's. Unfortunately, the field distribution is described by the Mathieu functions [18], whose numerical evaluation is very cumbersome. The best approach seems the expansion of those functions in a series of (more tractable) Bessel functions [19]. These series are not quickly converging, so the evaluation of these series are computationally heavy, above all when a high accuracy is required. In the literature, there are many different approximate or numerical techniques for the solution the Helmholtz equation. In particular, the frequency-domain finite-difference approach (FDFD) [20], namely the direct discretization of the differential eigenvalue problem is the simplest strategy however, and can be applied to both scalar [21-22] and vector [23] problems. Despite of its simplicity, in many cases it is accurate and computationally effective, too, since at variance of, e.g., [24] it leads to matrices which are highly sparse. However, accuracy or effectiveness (or both) are lost for guides with curved boundary, since the most popular FDFD implementation amount to replace the correct boundary geometry with a staircase approximation a solution which strongly affects the accuracy or the computational load (or both). Nevertheless, it is still adopted also in sophisticated numerical techniques [25].

Aim of this work is to devise a FDFD approach for sectorial (SEW) and ridged (REW) homogeneous elliptic waveguides, tailored to the structure, but as simple as the standard one in the formulation. Use of a suitable elliptical grid (which perfectly fits the waveguide boundary) allows to evaluate the SEW and REW modes with the required accuracy using order of magnitude less sampling points than the standard approach. For each grid point, a fourth-order Taylor approximations allow to replace the continuous eigenfunction problem with a discrete one. This work is therefore an extension of work presented in [26], where a second-order approximation has been used.

The proposed approach has been validated by comparison with some analytical results found in literature [27].

II. DESCRIPTION OF TECNIQUE

Let us consider an empty elliptic waveguide. Both TE and TM modes can be found from a suitable scalar eigenfunction, solution of the Helmholtz equation:

$$\nabla_t^2 \phi + k_t^2 \phi = 0,$$

(1)

with the boundary conditions (BC):

$$\begin{array}{ll}\dfrac{\partial \phi}{\partial n} = 0 & (TE \text{ modes}) \\ \phi = 0 & (TM \text{ modes})\end{array},$$

(2)

at the boundary of the ridged waveguide. Both the equation (1) and the BC (2) can be replaced by a discretized version, looking for the eigenvalues and eigenfunction defined on a suitable set of sampling points, and therefore replacing derivatives with finite approximations. The standard solution is to use a rectangular set of sampling points [22], but this forces to replace the curved boundary with a staircase approximation. This approximation results in a low accuracy (using a course grid), or in a heavy computational load (using a very fine grid). Since we are interested in elliptic boundaries, our propose here is to select a set of sampling points located on the elliptic coordinates framework (see Fig. 1).

We choose a regular spacing on the elliptic coordinate lines, with step $\Delta u, \Delta v$. Letting $\phi_{pq} = \phi(p\Delta u, q\Delta v)$, the eigenvalues equation (1) should be:

$$\frac{1}{a^2\left(\sinh^2 p\Delta u + \sin^2 q\Delta v\right)} \cdot \left[\frac{\partial^2 \phi}{\partial u^2} + \frac{\partial^2 \phi}{\partial v^2}\right]_{pq} = -k_t^2 \phi_{pq}. \quad (3)$$

For each internal point P (see Fig. 2) is simpler to discretize the term in brackets (3) using a fourth-order Taylor expansion:

$$\begin{aligned}\phi_B = \phi_P + \left.\frac{\partial \phi}{\partial u}\right|_P \cdot (-\Delta u) + \frac{1}{2}\left.\frac{\partial^2 \phi}{\partial u^2}\right|_P \cdot (-\Delta u)^2 + \\ + \frac{1}{6}\left.\frac{\partial^3 \phi}{\partial u^3}\right|_P \cdot (-\Delta u)^3 + \frac{1}{24}\left.\frac{\partial^4 \phi}{\partial u^4}\right|_P \cdot (-\Delta u)^4\end{aligned}, \quad (4)$$

$$\begin{aligned}\phi_N = \phi_P + \left.\frac{\partial \phi}{\partial u}\right|_P \cdot (-2\Delta u) + \frac{1}{2}\left.\frac{\partial^2 \phi}{\partial u^2}\right|_P \cdot (-2\Delta u)^2 + \\ + \frac{1}{6}\left.\frac{\partial^3 \phi}{\partial u^3}\right|_P \cdot (-2\Delta u)^3 + \frac{1}{24}\left.\frac{\partial^4 \phi}{\partial u^4}\right|_P \cdot (-2\Delta u)^4\end{aligned}, \quad (5)$$

$$\begin{aligned}\phi_D = \phi_P + \left.\frac{\partial \phi}{\partial u}\right|_P \cdot (\Delta u) + \frac{1}{2}\left.\frac{\partial^2 \phi}{\partial u^2}\right|_P \cdot (\Delta u)^2 + \\ + \frac{1}{6}\left.\frac{\partial^3 \phi}{\partial u^3}\right|_P \cdot (\Delta u)^3 + \frac{1}{24}\left.\frac{\partial^4 \phi}{\partial u^4}\right|_P \cdot (\Delta u)^4\end{aligned}, \quad (6)$$

$$\begin{aligned}\phi_Q = \phi_P + \left.\frac{\partial \phi}{\partial u}\right|_P \cdot (2\Delta u) + \frac{1}{2}\left.\frac{\partial^2 \phi}{\partial u^2}\right|_P \cdot (2\Delta u)^2 + \\ + \frac{1}{6}\left.\frac{\partial^3 \phi}{\partial u^3}\right|_P \cdot (2\Delta u)^3 + \frac{1}{24}\left.\frac{\partial^4 \phi}{\partial u^4}\right|_P \cdot (2\Delta u)^4\end{aligned}. \quad (7)$$

By combining the four last equations we find:

$$\left.\frac{\partial^2 \phi}{\partial u^2}\right|_P = \frac{1}{12\Delta u^2} \cdot \left(16\phi_B + 16\phi_D - \phi_N - \phi_Q - 30\phi_P\right). \quad (8)$$

Likely in v direction:

$$\left.\frac{\partial^2 \phi}{\partial v^2}\right|_P = \frac{1}{\Delta v^2} \cdot \left(16\phi_H + 16\phi_G - \phi_A - \phi_C - 30\phi_P\right). \quad (9)$$

Expression (8,9) are the substituted in the term in brackets (3) to get:

$$\left[\frac{\partial^2 \phi}{\partial u^2} + \frac{\partial^2 \phi}{\partial v^2}\right] =$$

$$\begin{aligned}&\frac{16}{12\Delta v^2}\cdot\phi_H + \frac{16}{12\Delta v^2}\cdot\phi_G - \frac{1}{12\Delta v^2}\cdot\phi_A - \frac{1}{12\Delta v^2}\cdot\phi_C \\ &\frac{16}{12\Delta u^2}\cdot\phi_B + \frac{16}{12\Delta u^2}\cdot\phi_D - \frac{1}{12\Delta u^2}\cdot\phi_N - \frac{1}{12\Delta u^2}\cdot\phi_Q \\ &-\frac{30}{12}\left(\frac{1}{\Delta u^2} + \frac{1}{\Delta v^2}\right)\cdot\phi_P\end{aligned}, \quad (10)$$

which easily leads to the FDFD approximation of (1).

Equation (10) cannot be used for the two foci, for points between them and for external points. For a point P lying on the segment joining the two foci

we can integrate (1):

$$\int \nabla_t^2 \phi \, dS = -k_t^2 \int \phi \, dS\theta \;, \tag{11}$$

and apply the Gauss theorem to obtain:

$$\int_{\Gamma_F} \frac{\partial \phi}{\partial n} \cdot dl = -k_t^2 \int_{S_F} \phi \, dS, \tag{12}$$

wherein S_F is the cell surface, and Γ_F is the cell boundary.
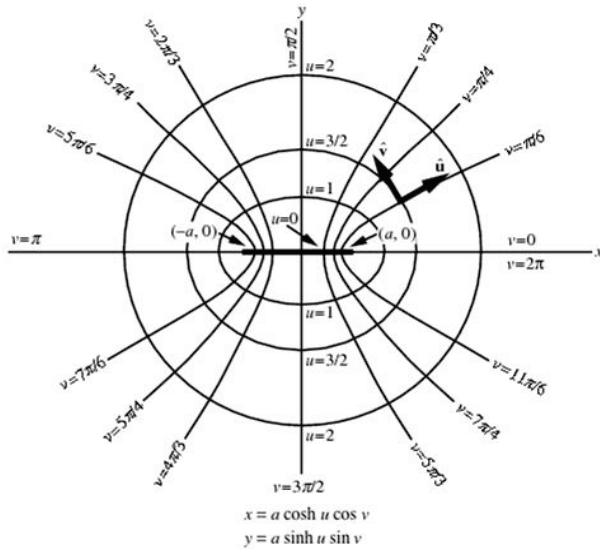
Fig. 1. Geometry of the elliptic coordinates [28].
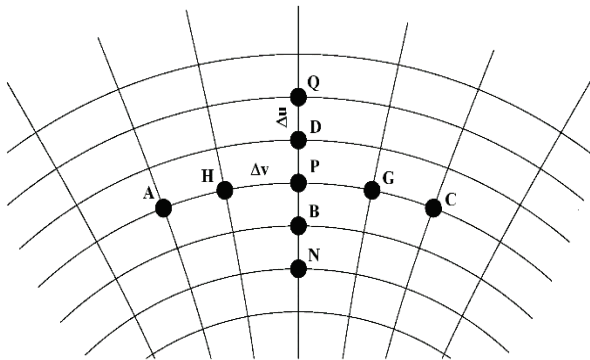
Fig. 2. Internal point of the elliptic coordinates grid TE and TM.

In the elliptic grid used for a SEW or REW, we have two types of boundary points: the radial ones (P in Fig. 3 (a)) and the angular ones (P in Fig. 3 (b)).

The TE boundary condition can be enforced in the same way for both types of boundary points, so we describe it only for an elliptic one (Fig. 3). The

boundary point X in Fig. 2 (a) is not a discretization point. Therefore, use of the Taylor expansion would require an extrapolation of $\phi(u)$ outside the sampling region, using either ϕ_X to enforce the boundary condition $\frac{\partial \phi}{\partial n} = 0$.
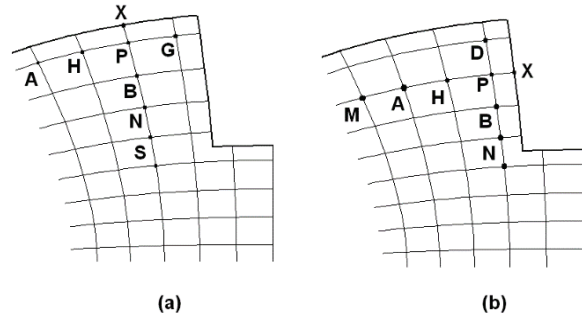
Fig. 3. (a) Geometry pertinent to the first type of boundary point P, and (b) geometry pertinent to the second type of boundary point P.

Let us consider an edge point P (Fig. 3 (a)), we can write the second derivative in u, as:

$$\frac{\partial^2 \phi}{\partial u^2} \cong \sum_{i=B}^{np} A_i \left(\phi_i - \phi_P \right) =$$

$$= \left[B_1 \frac{\partial \phi}{\partial u}\bigg|_P + B_2 \frac{\partial^2 \phi}{\partial u^2}\bigg|_P + B_3 \frac{\partial^3 \phi}{\partial u^3}\bigg|_P + B_4 \frac{\partial^4 \phi}{\partial u^4}\bigg|_P \right], \tag{13}$$

where:

$$B_1 = \sum_{i=1}^{np} A_i \cdot \Delta u_i \;, \quad B_2 = \sum_{i=1}^{np} A_i \cdot \Delta u_i^2 \;,$$

$$B_3 = \sum_{i=1}^{np} A_i \cdot \Delta u_i^3 \;, \quad B_4 = \sum_{i=1}^{np} A_i \cdot \Delta u_i^4 \;,$$

are linear combinations of the unknown coefficient A_i, and $np = 3$ is the number of the points used in the expression $(i = B, N, S)$.

Now can be expressed $\partial \phi / \partial u = 0$ using Taylor series:

$$\frac{\partial \phi}{\partial u}\bigg|_X \simeq \frac{\partial \phi}{\partial u}\bigg|_P + \frac{\partial^2 \phi}{\partial u^2}\bigg|_P \cdot \left(\frac{\Delta u}{2} \right) +$$

$$+ \frac{1}{2} \frac{\partial^3 \phi}{\partial u^3}\bigg|_P \cdot \left(\frac{\Delta u}{2} \right)^2 + \frac{1}{6} \frac{\partial^4 \phi}{\partial u^4}\bigg|_P \cdot \left(\frac{\Delta u}{2} \right)^3 = 0 \tag{14}$$

which can be solved for $\frac{\partial \phi}{\partial u}\bigg|_P$. Its expression is used to and can be used for replace of the terms in the bracket on the r.h.s. of equation (13):

$$\left(B_2 - B_1 \frac{\Delta u}{2}\right) \cdot \frac{\partial^2 \phi}{\partial u^2}\bigg|_P + \left(B_3 - B_1 \frac{\Delta u^2}{8}\right) \cdot \frac{\partial^3 \phi}{\partial u^3}\bigg|_P +$$
$$+ \left(B_4 - B_1 \frac{\Delta u^3}{48}\right) \frac{\partial^4 \phi}{\partial u^4}\bigg|_P \qquad . \text{(15)}$$

Eq. (15) is an approximation of $\dfrac{\partial^2 \phi}{\partial u^2}$ if:

$$B_2 - B_1 \frac{\Delta u}{2} = 1, \quad B_3 - B_1 \frac{\Delta u^2}{8} = 0, \quad B_4 - B_1 \frac{\Delta u^3}{48} = 0, \text{ and}$$

coefficients A_i are given by the solution of the linear system (15) so (8) is replaced by:

$$\frac{\partial^2 \phi}{\partial u^2}\bigg|_P = \frac{1}{24\Delta u^2} \cdot \left(21\phi_B + 3\phi_N - \phi_S - 23\phi_P\right). \quad \text{(16)}$$

In the same way, we can replace (9) by:

$$\frac{\partial^2 \phi}{\partial v^2}\bigg|_P = \frac{1}{264\Delta v^2} \cdot \left(357\phi_H + 335\phi_G - 23\phi_A - 792\phi_P\right), \text{(17)}$$

and the equation (10) becomes:

$$\frac{21}{24\Delta u^2}\phi_B + \frac{3}{24\Delta u^2}\phi_N - \frac{1}{24\Delta u^2}\phi_S +$$
$$\frac{357}{264\Delta v^2}\phi_H + \frac{335}{264\Delta v^2}\phi_G - \frac{23}{264\Delta v^2}\phi_A + . \quad \text{(18)}$$
$$-\left(\frac{23}{24\Delta u^2} + \frac{792}{264\Delta v^2}\right)\phi_P \cong -k_t^2\phi_P$$

A significant advantage of the present approach is that TM modes can be computed on the same TE grid, at variance of the standard approach [22], which calls for two different sets of sampling points, to cope with the different BC (2). To get the TM modes on the same grid, we express the potential in X through a Taylor approximation:

$$\phi_X = \phi_P + \frac{\partial \phi}{\partial u}\bigg|_P \cdot \left(\frac{\Delta u}{2}\right) + \frac{1}{2}\frac{\partial^2 \phi}{\partial u^2}\bigg|_P \cdot \left(\frac{\Delta u}{2}\right)^2 +$$
$$+ \frac{1}{6}\frac{\partial^3 \phi}{\partial u^3}\bigg|_P \cdot \left(\frac{\Delta u}{2}\right)^3 + \frac{1}{24}\frac{\partial^4 \phi}{\partial u^4}\bigg|_P \cdot \left(\frac{\Delta u}{2}\right)^4 \qquad , \text{(19)}$$

and set $\phi_X = 0$. By adding the last equation with (13) and solving the linear system (8) we get:

$$\frac{\partial^2 \phi}{\partial u^2}\bigg|_P = \frac{7}{3\Delta u^2}\phi_B - \frac{2}{5\Delta u^2}\phi_N + \frac{1}{21\Delta u^2}\phi_S - \frac{16}{3\Delta u^2}\phi_P. \text{(20)}$$

Likely in v direction:

$$\frac{\partial^2 \phi}{\partial v^2}\bigg|_P = \frac{1}{3\Delta v^2}\phi_G + \frac{5}{3\Delta v^2}\phi_H - \frac{2}{15\Delta v^2}\phi_A - \frac{4}{\Delta v^2}\phi_P, \text{(21)}$$

combining the equations (20) and (21) into (10) we find the final expression:

$$\frac{7}{3\Delta u^2}\phi_B - \frac{2}{5\Delta u^2}\phi_N + \frac{1}{21\Delta u^2}\phi_S +$$
$$\frac{1}{3\Delta v^2}\phi_G + \frac{5}{3\Delta v^2}\phi_H - \frac{2}{15\Delta v^2}\phi_A + . \quad \text{(22)}$$
$$-\left(\frac{4}{\Delta v^2} + \frac{16}{3\Delta u^2}\right)\phi_P \cong -k_t^2\phi_P$$

In the point in Fig. 3 (b), we use the same procedure to calculate the approximation of laplace operator for TE and TM modes.

III. RESULTS

The fourth-order FDFD for elliptic ridge waveguide described in the previous sections has been extensively validated, to evaluate its accuracy and effectiveness. In the simulations presented in this section, we will consider first a sector of elliptic ridged waveguide (see Fig. 4) and then a ridged sector. All dimensions have been normalized to the minor semi-axis of the ellipse.

Our FDFD procedure has been assessed against the analytical results of [27]. The resulting eigenvalue problem has been solved using standard MATLAB routines, on a PC with two Intel Xeon E5504 CPUs@2.00 GHz, 48 GB RAM, OS: MS Windows 7 Professional.
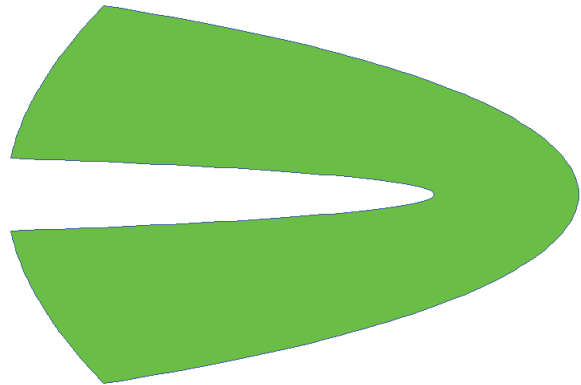
Fig. 4. Elliptic sectorial guide with $u_1 = 0.1$, $u_2 = 0.5$, and $v_1 = -50°$, $v_2 = 50°$.

The main results of our validation are collected in the next tables $u \in (u_1, u_2)$, $v \in (v_1, v_2)$. From them it appears that our FDFD approach is able to give a very high accuracy, with a difference (with respect to the accurate data of [27]), which is smaller than 0.02% in most cases.

The computation time of the FDFD approach is the sum of the matrix filling time and the time needed to extract eigenvalue and eigenvectors of the sparse matrix. For example, for a grid with $\Delta u = 0.0040$, $\Delta v = 0.0009$ and 1010000 points, the filling matrix time is 2,07 sec and the time to extract eigenvalue and eigenvectors is 93.02 sec.

Table 1: Relative error on normalized TE cut-off wavelengths, with respect to [27], for the guide of Fig. 4, $\Delta u = 0.0078$, $\Delta v = 0.01755$

TE	λ_c/a [27]	λ_c/a Our Code	Relative Error %
1	2.656401	2.656343	0.0022
2	6.836981	6.835793	0.0174
3	9.544562	9.540887	0.0385

Table 2: Relative error on normalized TM cut-off wavelengths, with respect to [27], for the guide of Fig. 4, $\Delta u = 0.0078$, $\Delta v = 0.01755$

TM	λ_c/a [27]	λ_c/a Our Code	Relative Error %
1	14.283213	14.280411	0.0196
2	14.299466	14.297190	0.0159
3	19.561598	19.545863	0.0804

Table 3: Relative error on normalized TE cut-off wavelengths, with respect to [27], for the guide of Fig. 4, $\Delta u = 0.004$, $\Delta v = 0.0017$

TE	λ_c/a [27]	λ_c/a Our Code	Relative Error %
1	2.656401	2.656366	0.0013
2	6.836981	6.836941	0.0006
3	9.544562	9.544720	0.0017

Table 4: Relative error on normalized TM cut-off wavelengths, with respect to [27], for the guide of Fig. 4, $\Delta u = 0.004$, $\Delta v = 0.0017$

TM	λ_c/a [27]	λ_c/a Our Code	Relative Error %
1	14.283213	14.283476	0.0018
2	14.299466	14.300252	0.0055
3	19.561598	19.558674	0.0150

In Fig. 5, left, we show the potential eigenfunctions for the first three TE modes (corresponding to the data of Table 1).

In order to show the flexibility of our approach, a different, ridged, sector has been considered. Only

the eigenfunctions has been reported, since no analytic data is available. In Figs. 6 and 7 report a convergence analysis, with respect to the side of the discretization step. It appears that a fourfold reduction in Δv allows an accuracy increase of more than an order of magnitude. The behavior respect to Δu is different, since the structure is quite slender.
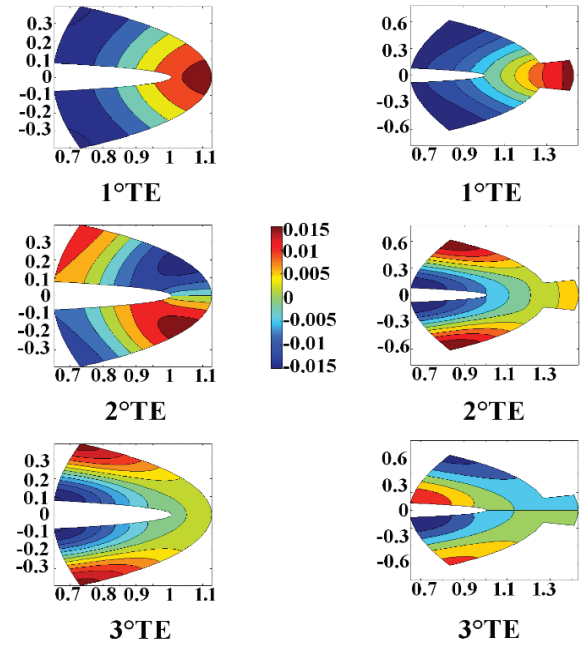
Fig. 5. Lowest-order eigenvectors for the examples presented. Left: structure of Fig. 4. Right: ridged sectorial guide with $u_1 = 0.1$, $u_2 = 0.74$, $v_1 = -50°$, $v_2 = 50°$, and $u_3 = 0.1$, $u_4 = 0.9$, $v_3 = -10°$, $v_4 = 10°$.
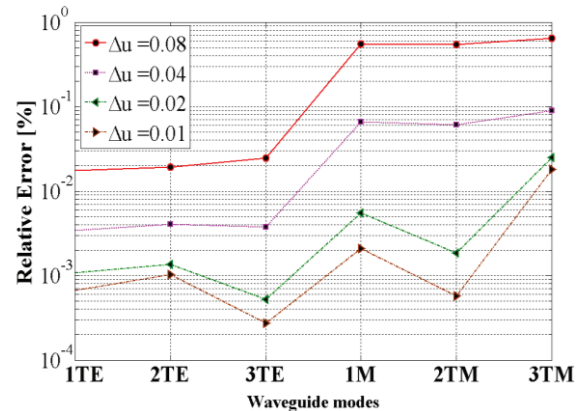
Fig. 6. Relative error on the cut-off frequency of the first modes of an elliptic sector waveguide with $\Delta v = 0.0017$.
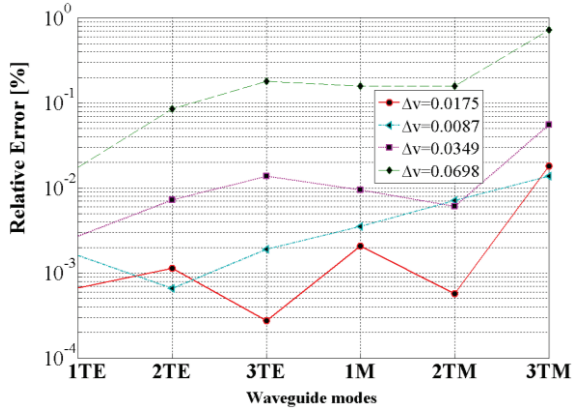
Fig. 7. Relative error on the cut-off frequency of the first modes of an elliptic sector waveguide with $\Delta u = 0.01$.

Finally in Fig. 8, we compare the present fourth-order FDFD with a lively second order one, with different discretization steps. Figure 8 shows clearly that the accuracy of a fourth order approach can be reached using a second-order one, but with at least four times the discretization points, and therefore a computational load larger by nurse than an order of magnitude. Therefore, the proposed use of a fourth-order approximation is a significant improvement with respect to [26].
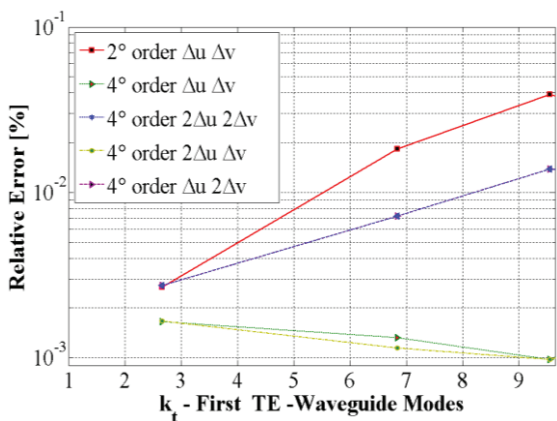
Fig. 8. Comparison of fourth and second order FDFD for the comparison of the k_t of the first TE modes for the structure of Fig. 4, for different discretization steps, $\left(\Delta u = 0.004, \Delta v = 0.0017 \right)$.

IV. CONCLUSION

An approach to the FDFD computation of modes of an elliptic ridged waveguide has been presented. We describe here a fourth order finite difference frequency domain approach to the mode computation for both TE and TM modes. An elliptic mesh has been used in order to avoid staircase approximations of the boundary. The presented results show both the flexibility of the method, as well as its simplicity for the computation for TE and TM modes in an elliptic ridged waveguide.

REFERENCES
[1] A. A. El-Sherbiny, "Cutoff wavelengths of ridged, circular, and elliptic guides," *IEEE Trans. Microwave Theory Tech.*, vol. 21, pp. 7-12, Jan. 1973.

[2] A. E. Williams and A. E. Atia, "Dual-mode canonical waveguide filters," *IEEE Transactions on Microwave Theory & Techniques*, vol. 25, no. 12, pp. 1021-1026, Dec. 1977.

[3] R. Behe and P. Brachat, "Compact duplexer-polarizer with semicircular waveguide," *IEEE Trans. Antennas Propagat.*, vol. 39, pp. 1222-1224, Aug. 1991.

[4] B. V. de la Filolie and R. Vahldieck, "Coaxial and circular waveguide band-pass filters using printed metal inserts," *IEEE MTT-S Int. Microwave Symp. Dig.*, pp. 905-908, 1992.

[5] J. Huang, R. Vahldieck, and H. Jin, "Computer-aided design of circular ridged waveguide evanescent-mode bandpass filters using the FDTLM method," *IEEE MTT-S Int. Microwave Symp. Dig.*, pp. 459-462, 1993.

[6] U. Balaji and R. Vahldieck, "Mode matching analysis of circular-ridged waveguide discontinuities," *IEEE Trans. Microwave Theory Tech.*, vol. 46, pp. 191-195, Feb. 1998.

[7] G. Mazzarella and G. Montisci, "Wideband equivalent circuit of a centered-inclined waveguide slot coupler," *Journal of Electromagnetic Waves and Applications*, vol.

14, pp. 133-151, 2000.

[8] H. P. Zhao and Z. X. Shen, "Efficient modeling of three-dimensional reverberation chambers using hybrid discrete singular convolution-method of moments," *IEEE Transactions on Antennas and Propagation*, vol. 59, issue: 8, pp. 2943-2953, Aug. 2011.

[9] G. Mazzarella and G. Montisci, "Accurate characterization of the interaction between coupling slots and waveguide bends in waveguide slot arrays," *IEEE Trans. Microw. Theory Tech.*, vol. MTT-48, pp. 1154-1157, Sept. 2000.

[10] L. Prkna, M. Hubalek, and J. Ctyroky, "Vectorial eigenmode solver for bent waveguides based on mode matching," *Photonics Technology Letters, IEEE*, vol. 16, issue (9), pp. 2057-2059, Sept. 2004.

[11] M. Mongiardo and C. Tomassoni, "Modal analysis of discontinuities between elliptical waveguides," *IEEE Trans. Microw. Theory Tech.*, vol. MTT-48, pp. 597-605, Apr. 2000.

[12] G. Mazzarella and G. Montisci, "A rigorous analysis of dielectric-covered narrow longitudinal shunt slots with finite wall thickness," *Electromagnetics*, vol. 19, pp. 407-418, 1999.

[13] G. Montisci, M. Musa, and G. Mazzarella, "Waveguide slot antennas for circularly polarized radiated field," *IEEE Transactions on Antennas and Propagation*, vol. 52, pp. 619-623, 2004.

[14] S. R. Rengarajan, "Compound radiating slot in a broad wall of a rectangular waveguide," *IEEE Transactions on Antennas Propagation*, vol. 37, pp. 1116-1124, 1989.

[15] G. Montisci, G. Mazzarella, and G. A. Casula, "Effective analysis of a waveguide longitudinal slot with cavity," *IEEE Transactions on Antennas and Propagation*, vol. 60, pp. 3104-3110, 2012.

[16] M. Abramowitz and I. A. Stegun, *Handbook of Mathematical Functions*, 1972: National Bureau of Standards.

[17] L. J. Chu, "Electromagnetic waves in elliptic hollow pipes of metal," *J. Appl. Phys.*, vol. 9, 583-591, 1938.

[18] N. Marcuvitz, *Waveguide Handbook*, Peregrinus, London, 1986.

[19] J. G. Kretzschmar, "Wave propagation in hollow conducting elliptical waveguides," *IEEE Trans. Microwave Theory Techniques*, vol. 18, pp. 547-554, 1970.

[20] T. Weiland, "Three dimensional resonator mode computation by finite difference method," *IEEE Trans. Magn.*, vol. 21, pp. 2340-2343, 1985.

[21] A. Fanti, G. Mazzarella, G. Montisci, and G. A. Casula, "Computation of the modes of elliptic waveguides with a curvilinear 2D frequency-domain finite-difference approach," *Progress In Electromagnetics Research M*, vol. 26, 69-84, 2012.

[22] A. Fanti and G. Mazzarella, "A finite difference polar-cartesian grid approach for mode computation in rounded-end waveguides," *ACES Journal*, vol. 26, no. 9, Sept. 2011.

[23] A. Fanti, G. Montisci, G. Mazzarella, and G. A. Casula, "VFD approach to the computation TE and TM modes in elliptic waveguide on TM grid," *ACES Journal*, vol. 28, no. 12, Dec. 2013.

[24] Y. Shunchuan, C. Zhizhang, Y. Yiqiang, and S. Ponomarenko, "A divergence-free meshless method based on the vector basis function for transient electromagnetic analysis," *Microwave Theory and Techniques, IEEE Transactions on*, vol. 62, issue 7, pp. 1409-1416, Jul. 2014.

[25] M. Chai, T. Xiao, G. Zhao, and Q. H. Liu, "A hybrid PSTD/ADI-CFDTD method for mixed-scale electromagnetic problems," *IEEE Transactions on Antennas and Propagation*, vol. 55, issue 5, pp. 1398-1406, 2007.

[26] A. Fanti and L. Deias, "A new approach the analysis of sectorial elliptic waveguides," 30th *International Review of Progress in Applied Computational Electromagnetics*, Jacksonville, Florida, Mar. 23-27, 2014.

[27] G. Amendola, G. Di Massa, and G. Angiulli, "Elliptic-hyperbolical waveguides," *Journal of Electromagnetic Waves and Applications*, vol. 14, issue 11, pp. 1473-1487, 2000.

[28] http://mathworld.wolfram.com/EllipticCylindricalCoordinates.html.

Alessandro Fanti received the Laurea degree in Electronic Engineering and Ph.D. degree in Electronic Engineering and Computer Science from the University of Cagliari, Cagliari, Italy, in 2006 and 2012, respectively. He currently holds a Post-Doc scholarship for Design of Microwave Components. His research activity involves the use of numerical techniques for modes computation of guiding structures, optimization techniques, analysis and design of waveguide slot arrays, analysis and design of patch antennas.

Luisa Deias received the Laurea degree in Electronic Engineering and Ph.D. degree in Electronic Engineering and Computer Science from the University of Cagliari, Cagliari, Italy, in 2002 and 2006, respectively. She worked as Post-Doctoral Fellow in the Electromagnetic Group at the University of Cagliari from 2006 to 2013. Her research interests include numerical techniques in electromagnetism, metamaterial analysis and optimization, microwave components and antennas analysis and design.

Giovanni Andrea Casula received the Laurea degree (summa cum laude) in Electronic Engineering and Ph.D. degree in Electronic Engineering and Computer Science from the University di Cagliari, Cagliari, Italy, in 2000 and 2004, respectively. Since March 2006, he is Assistant Professor of Electromagnetic Field and Microwave Engineering at the Dipartimento di Ingegneria Elettrica ed Elettronica, University of Cagliari. His current research interests are in the field of synthesis, analysis and design of wire, patch, and slot antennas. Casula serves as Reviewer for several international journals and is a member of the Italian Electromagnetic Society (SIEm).

Giorgio Montisci received the Laurea degree (summa cum laude) in Electronic Engineering and Ph.D. degree in Electronic Engineering and Computer Science from the University of Cagliari, Cagliari, Italy, in 1997 and 2000, respectively. Since November 2000, he is Assistant Professor of Electromagnetic Field at the Dipartimento di Ingegneria Elettrica ed Elettronica, University of Cagliari, teaching courses in electromagnetics and microwave engineering. His research activity is mainly focused on analysis and design of waveguide slot arrays, microwave holographic techniques for the diagnostic of large reflector antennas, numerical methods in electromagnetics, and printed antennas. He is author or co-author of about 40 papers in international journals and Reviewer for EM Journals.

A Vector Parabolic Equation Method Combined with MLFMM for Scattering from a Cavity

Z. He, Z. H. Fan, D. Z. Ding, and R. S. Chen

Department of Communication Engineering
Nanjing University of Science and Technology, Nanjing, 210094, China
eerschen@njust.edu.cn

Abstract ─ The three-dimensional vector parabolic equation (PE) method was used for the fast analysis of the electromagnetic scattering with reasonable accuracy. The algorithm was marched from plane to plane along some preferred directions so that the computational load could be reduced significantly. However, large errors will be introduced for cavities with the multiple scattering. In this paper, the vector parabolic equation method combined with the multilevel fast multipole method (MLFMM) is presented for the analysis of the electromagnetic scattering from a cavity. Numerical results demonstrate that the proposed technique can efficiently give reasonably accurate results for the cavities when compared with the conventional PE method.

Index Terms ─ Cavity, electromagnetic scattering, MLFMM, vector parabolic equation method.

I. INTRODUCTION

The parabolic equation (PE) method provides an approximate solution for the wave equation with the energy propagating along the paraxial direction [1]. The calculation of the PE is taken to march gradually from one plane to another plane along the paraxial direction so that the 3D problem can be converted into a series of 2D problems to be solved by the PE method. Therefore, the electromagnetic scattering from electrically large objects can be analyzed efficiently. However, the PE is applicable only to the object which does not have large changes in direction, because large errors will be introduced for both nonconvex objects and cavities with the multiple scattering. The electromagnetic scattering from cavities has been paid more and more attention due to its wide range of applications in both the industry and the military. Many numerical methods, including the method of moment (MoM) [2-3], the finite difference method (FDM) [4], and the finite element method (FEM) [5-6] have been used to analyze the electromagnetic scattering from cavities. The error of each solution is large unless fine discretization is used for the scatterers. But a fine mesh will bring a large system of equations which may be computationally prohibitive. Therefore, fast and accurate calculation of the electromagnetic scattering from cavities becomes significant problem to be solved.

The MoM accelerated by the multilevel fast multipole method (MLFMM) can be used to analyze the electromagnetic scattering from cavities accurately [2]. However, a large number of computations are required for the very electrically large three-dimensional PEC objects. In this paper, the PE method is combined with MLFMM for the analysis of electromagnetic scattering from electrically large PEC objects with cavities. Firstly, the scattered electric fields in the aperture can be obtained by calculating the current density on the inner sides of the cavity with the MLFMM. Then, the PE method can be applied to analyze the scattered electric fields of other parts with the corresponding boundary conditions on the PEC objects. By this way, both the accuracy and the efficiency for electromagnetic scattering from electrically large PEC cavities can be assured.

This paper is organized as follows. Section 2 gives a brief introduction to the traditional vector parabolic equation method. At the same time, the vector parabolic equation method combined with the multilevel fast multipole method is explained in detail. A slant cavity embedded in a block is analyzed as the numerical example to show the

validity and the efficiency of the proposed method in Section 3. Section 4 gives some conclusions and comments.

II. THEORY AND FORMULATIONS

A. Vector parabolic equation method for electromagnetic scattering problems

The three-dimensional vector wave equation can be used as an efficient tool to analyze the electromagnetic scattering problems. The scattered field components E_x^s, E_y^s, E_z^s satisfy scalar wave equation in the Cartesian coordinate as follows:

$$\frac{\partial^2 E_\xi^s}{\partial x^2} + \frac{\partial^2 E_\xi^s}{\partial y^2} + \frac{\partial^2 E_\xi^s}{\partial z^2} + k^2 E_\xi^s = 0 \tag{1}$$

$$\xi = x, y, z,$$

where k is the wave number.

The reduced scattered fields u_x^s, u_y^s, u_z^s are defined as:

$$u_\xi^s(x, y, z) = e^{-jkx} E_\xi^s(x, y, z) \tag{2}$$

$$\xi = x, y, z.$$

Substitute equation (1) with equation (2), the vector parabolic equations can be gotten in air domain:

$$\frac{\partial u_\xi^s}{\partial x}(x, y, z) = \frac{j}{2k}\left(\frac{\partial^2 u_\zeta^s}{\partial y^2}(x, y, z) + \frac{\partial^2 u_\xi^s}{\partial z^2}(x, y, z)\right) \tag{3}$$

$$\xi = x, y, z.$$

It should be noted that the first order Taylor expansions of the square root and the exponential are used in this paper. And it can be seen from the equation (3) that the solutions at $(x + \Delta x)$ plane can be calculated from those at x plane. As shown in Fig. 1, the computation can start in the plane before the object and stop in the plane beyond the object.

When the FD scheme of the Crank-Nicolson type is applied to the equation (3), the computational format for the vector parabolic equations can be written as follows:

$$\frac{\Delta x}{2jk(\Delta y)^2} u_\xi^s(x + \Delta x, y + \Delta y, z)$$

$$+ \frac{\Delta x}{2jk(\Delta z)^2} u_\xi^s(x + \Delta x, y, z + \Delta z)$$

$$+ (1 - \frac{\Delta x}{jk(\Delta y)^2} - \frac{\Delta x}{jk(\Delta z)^2}) u_\xi^s(x + \Delta x, y, z) \tag{4}$$

$$+ \frac{\Delta x}{2jk(\Delta y)^2} u_\xi^s(x + \Delta x, y - \Delta y, z)$$

$$+ \frac{\Delta x}{2jk(\Delta z)^2} u_\xi^s(x + \Delta x, y, z - \Delta z) = u_\xi^s(x, y, z)$$

$$\xi = x, y, z.$$

The incident field is taken into account by the boundary conditions on the scatterer in each transverse plane. Perfect matching layers (PML) are placed around the object to truncate an infinite space to a finite computation domain. For PML domain, the following coordinate transformation is introduced [7-9]:

$$\hat{y} = y - i\int_0^y \sigma(\xi)d\xi,$$

$$\hat{z} = z - i\int_0^z \sigma(\xi)d\xi. \tag{5}$$

In equation (5), $\sigma(\xi) = \frac{3}{2\delta} \times \frac{1}{\eta} \times \log(\frac{1}{10^{-3}}) \times (\frac{\xi}{\delta})^2$, δ is the thickness of the PML and η is the wave impedance. As in air domain, the FD scheme of the Crank-Nicolson type is used. Therefore, the equation (6) can be replaced with equation (4) for the computation in the PML domain:

$$\frac{\Delta x e_i e_{i-1/2}}{2ik\Delta y^2} u_\xi^s(x + \Delta x, y - \Delta y, z) +$$

$$\frac{\Delta x e_j e_{j-1/2}}{2ik\Delta z^2} u_\xi^s(x + \Delta x, y, z - \Delta z) +$$

$$(1 - \frac{\Delta x e_j(e_{j+1/2} + e_{j-1/2})}{2ik\Delta z^2} -$$

$$\frac{\Delta x e_i(e_{i+1/2} + e_{i-1/2})}{2ik\Delta y^2}) u_\xi^s(x + \Delta x, y, z) + \tag{6}$$

$$\frac{\Delta x e_i e_{i+1/2}}{2ik\Delta y^2} u_\xi^s(x + \Delta x, y + \Delta y, z) +$$

$$\frac{\Delta x e_j e_{j+1/2}}{2ik\Delta z^2} u_\xi^s(x + \Delta x, y, z + \Delta z) = u_\xi^s(x, y, z)$$

$$\xi = x, y, z,$$

where

$$e_i = \frac{1}{1 - i\sigma(y_i)}, \tag{7}$$

$$\sigma(y_i) = \frac{1}{\Delta z} \int_{y_{i-1/2}}^{y_{i+1/2}} \sigma(\xi)d\xi, \tag{8}$$

$$e_j = \frac{1}{1 - i\sigma(z_j)}, \tag{9}$$

$$\sigma(z_j) = \frac{1}{\Delta z} \int_{z_{j-1/2}}^{z_{j+1/2}} \sigma(\xi)d\xi. \tag{10}$$

The narrow-angle approximation is only accurate when energy does not have large changes along the paraxial direction. As a result, the traditional parabolic equation method cannot be used to analyze the scattering from cavities.
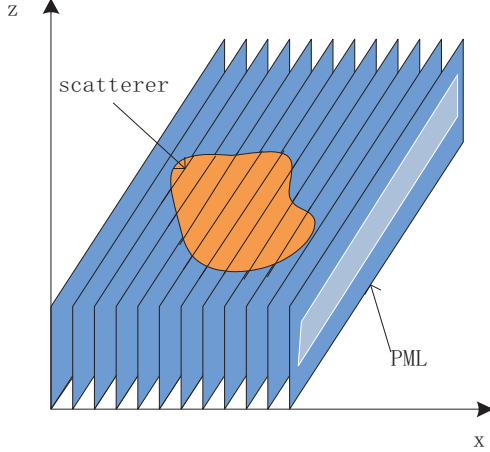
Fig. 1. Transverse planes for PE marching.

B. Vector parabolic equation method combined with the MLFMM for scattering from a cavity

As shown in Fig. 2, a PEC object with cavity in free space is illuminated by a plane wave e^{ikx} propagating along $-x$ direction with wave number k.

The scattering by 3-D arbitrary conducting objects can be formulated by the electrical-field integral equation (EFIE). As shown in Fig. 2, the current density on the inner sides of the cavity can be calculated with the equation (11) by the MLFMM

$$-ik\mathbf{n}(\mathbf{r})\times \int_{S_{inner}} G(\mathbf{r},\mathbf{r}')\mathbf{J}(\mathbf{r}')dS'$$

$$+\frac{1}{ik}\mathbf{n}(\mathbf{r})\times\nabla \int_{S_{inner}} G(\mathbf{r},\mathbf{r}')\nabla\Box\mathbf{J}(\mathbf{r}')dS' \qquad (11)$$

$$= -\mathbf{n}(\mathbf{r})\times\mathbf{E}^{\mathbf{i}}(\mathbf{r}) \qquad \forall\mathbf{r}\in S_{inner},$$

where S_{inner} denotes the surface of the inner sides in the cavity, μ_0 and ε_0 are the free-space permittivity and permeability, $k=\omega\sqrt{\mu_0\varepsilon_0}$ is the wave number, $\mathbf{J}$ is the current density in the inner sides of the cavity, $\mathbf{E}^{\mathbf{i}}(\mathbf{r})$ is the incident plane wave, $\mathbf{n}$ denotes the surface outward pointing unit normal and $G(\mathbf{r},\mathbf{r}')$ is the Green's function in free space [2].

For the aperture, the scattered electric fields on S_2 can be obtained by the integration of the electric current on the inner sides S_{inner} of the cavity, as written in equation (12).

$$\mathbf{E^s}(\mathbf{r}) =$$

$$-\frac{i\omega\mu_0}{4\pi}\int_{S_{inner}}\left(I-\frac{1}{k^2}\nabla\nabla'\right)G(\mathbf{r},\mathbf{r}')\cdot\mathbf{J}(\mathbf{r}')dS' \quad (12)$$

$$\forall\mathbf{r}\in S_2.$$

To efficiently analyze the electromagnetic scattering from PEC objects with cavities, the vector PE method is introduced to calculate the scattered electric fields from the surface S_1 and the aperture surface S_2 with equation (3).

The FD scheme of the Crank-Nicolson type is used to the equation (3), as shown in equation (4). Therefore, the $u^s_\xi(x+\Delta x, y, z)$ at $(x+\Delta x)$ plane can be calculated from $u^s_\xi(x,y,z)$ at x plane [1]. The tangential electric field must be zero on the scatterer for a PEC object. To guarantee the unicity of the solution, the reduced scattered fields in equation (3) are coupled through both the boundary conditions on the surface S_1 and the divergence-free condition [1], as shown in equation (13):

$$\begin{cases} n_x u^s_y(P) - n_y u^s_x(P) = \\ \qquad -e^{-ikx}\left(n_x E^i_y(P) - n_y E^i_x(P)\right) \\ n_x u^s_z(P) - n_z u^s_x(P) = \\ \qquad -e^{-ikx}\left(n_x E^i_z(P) - n_z E^i_x(P)\right) \\ n_y u^s_z(P) - n_z u^s_y(P) = \\ \qquad -e^{-ikx}\left(n_y E^i_z(P) - n_z E^i_y(P)\right) \\ \frac{i}{2k}\left(\frac{\partial^2 u^s_x(P)}{\partial y^2} + \frac{\partial^2 u^s_x(P)}{\partial z^2}\right) + \\ \qquad iku^s_x(P) + \frac{\partial u^s_y(P)}{\partial y} + \frac{\partial u^s_z(P)}{\partial z} = 0 \end{cases} \qquad (13)$$

$$\forall P \in S_1,$$

where p is a point on the surface of the scatterer, $\left(E^i_x, E^i_y, E^i_z\right)$ is the field components of the incident wave and (n_x, n_y, n_z) is the outer normal to the surface at p.

For the last transverse (y-z) plane, the boundary

conditions for the equation (3) on both the PEC surface S_1 and the aperture S_2 are obtained by equation (13) and (12), respectively. The computation for equation (3) is taken from one plane to another, which begins just before the PEC scattering object and stops beyond it. Once the scattered electric fields are obtained in the last transverse plane, the RCS can be calculated by Fourier transform of them [1].
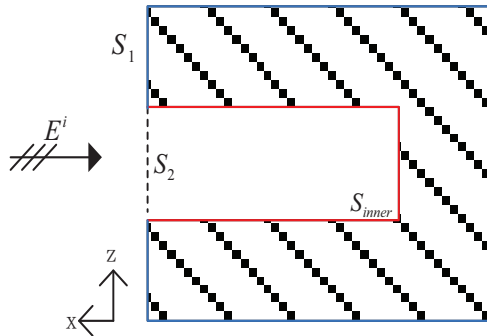
Fig. 2. A PEC object with cavity in free space.

III. NUMERICAL RESULTS

As shown in Fig. 3, a slant cavity nested in a block is presented to demonstrate the efficiency of the proposed method. The incident field is a plane wave, vertical polarized and propagating along -x direction. The RCS curves are compared between the proposed method and the MLFMM in Fig. 4 for a wide band from 200 to 600 MHz. It can be observed that the proposed method is in good agreement with the MLFMM. As shown in Fig. 5, the bi-static RCS results at the frequency of 300 MHz are compared among the proposed method, the conventional PE method and the MLFMM. Moreover, the amplitude and the phase of the scattering electric fields for the cavity's middle line paralleled to the y axis in the last transverse plane are given in Fig. 6. It can be found that the proposed method is more accurate than the conventional PE method when compared with the MLFMM. As listed in Table 1, both the CPU time and the memory requirement are compared between the proposed method and the MLFMM at the frequency

of 300 MHz. It can be found that memory requirement and CPU time can be reduced 71.9% and 43.6% for the proposed method, respectively.

(a)

(b)
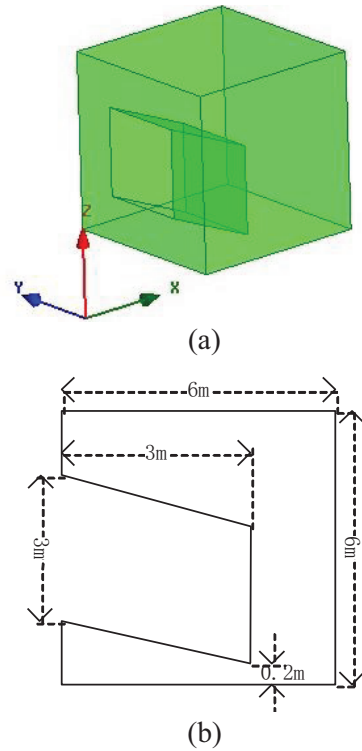
Fig. 3. The model of the slant cavity nested in a block: (a) stereogram, and (b) side view.
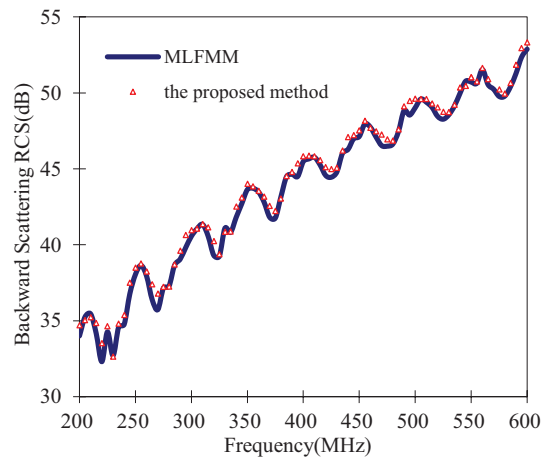
Fig. 4. The RCS from 200 MHz to 600 MHz.
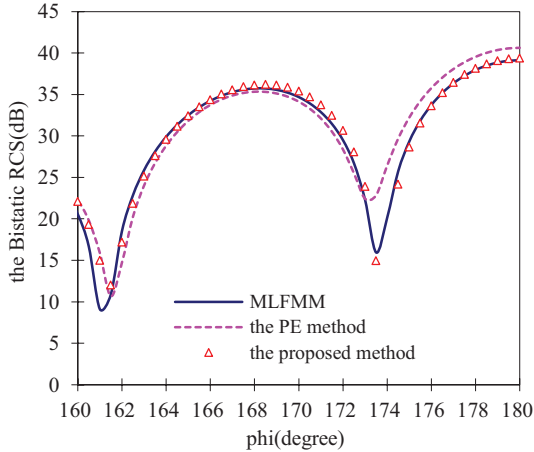
Fig. 5. The bi-static RCS of the cavity at 300 MHz.

(a)

(b)
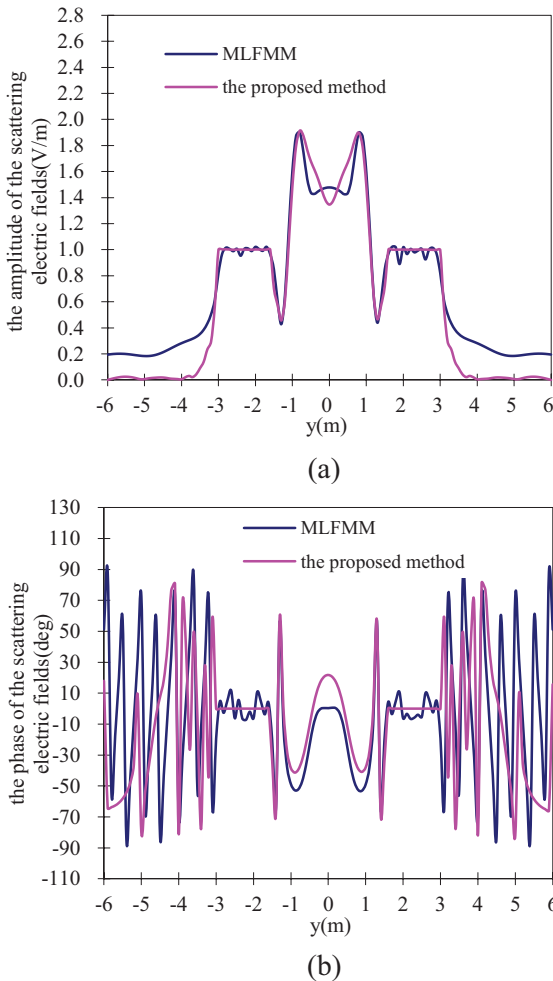
Fig. 6. (a) The amplitude of the scattering electric fields for the cavity's middle line, and (b) the phase of the scattering electric fields for the cavity's middle line.

Table 1: Comparison for the CPU time and the memory requirement between the proposed method and the MLFMM at the frequency of 300 MHz

	CPU Time (s)	Memory Requirement (MB)
MLFMM	1184	448
The proposed method	668	126

IV. CONCLUSION

In this paper, a vector parabolic equation method combined with the MLFMM has been proposed to analyze the electromagnetic scattering from a PEC cavity. The MLFMM is introduced to compute the scattered currents on the inner side of the cavity and the electric fields in the aperture induced by these scattered currents are obtained. The scattered fields from the cavity are calculated by the vector PE method with the corresponding boundary conditions. It can be found that both the CPU time and the memory requirement are significantly reduced when compared with the MLFMM.

ACKNOWLEDGMENT

REFERENCES

[1] A. A. Zaporozhets and M. F. Levy, "Bistatic RCS calculations with the vector parabolic equation method," *IEEE Trans. Antennas and Propagation*, vol. 47, pp. 1688-1696, 1999.

[2] Z. Nie, H. Wang, and J. Wang, "A combined field solution with single operator for electromagnetic scattering from conductive targets with open cavities," *IEEE Trans. Antennas and Propagation*, vol. 56, pp. 1734-1741, 2008.

[3] C. F. Wang and Y. B. Gan, "2-D cavity modeling using method of moments and iterative solvers," *J. Electromagn. Waves*

Appl., vol. 17, no. 12, pp. 1739-1741, 2003.

[4] T.-T. Chia, R. J. Burkholder, and R. Lee, "The application of FDTD in hybrid methods for cavity scattering analysis," *IEEE Trans. Antennas and Propagation*, vol. 43, 1082-1090, 1995.

[5] J.-M. Jin and K. Donepudi, "Electromagnetic scattering from large, deep, and arbitrarily-shaped open cavities," *Antennas and Propagation Society International Symposium*, vol. 4, 2186-2189, 1998.

[6] J. Liu and J. Jin, "A special higher order finite-element method for scattering by deep cavities," *IEEE Trans. Antennas and Propagation*, vol. 48, 694-703, 2000.

[7] J. P. Bergener, "Three-dimensional perfectly matched layer for the absorption of electromagnetic waves," *J. Comp. Phys*., no. 127, pp. 363-379, 1996.

[8] F. Collino, "Perfectly matched absorbing layers for the paraxial equations," *J. Comp. Phys*., 94:1-29, 1991.

[9] J. P. Bergener, "A perfectly matched layer for the absorption of electromagnetic waves," *J. Comp. Phys*., 114:185-200, 1994.
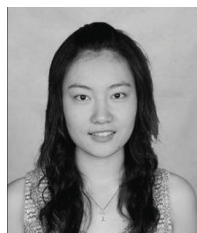
Zi He received the B.Sc. degree in Electronic Information Engineering from the School of Electrical Engineering and Optical Technique, Nanjing University of Science and Technology, Nanjing, China, in 2011. She is currently working towards the Ph.D. degree in Electromagnetic Fields and Microwave Technology at the School of Electrical Engineering and Optical Technique, Nanjing University of Science and Technology. Her research interests include antenna, RF-integrated circuits, and computational electromagnetics.

Zhenhong Fan was born in Jiangsu, China, in 1978. He received the M.Sc. and Ph.D. degrees in Electromagnetic Field and Microwave Technique from Nanjing University of Science and Technology (NJUST), Nanjing, China, in 2003 and 2007, respectively.

During 2006, he was with the Center of wireless Communication in the City University of Hong Kong, Kowloon, as a Research Assistant. He is currently an Associate Professor with the Electronic Engineering of NJUST. He is the author or co-author of over 20 technical papers. His current research interests include computational electromagnetics, electromagnetic scattering and radiation.

Dazhi Ding was born in Jiangsu, China, in 1979. He received the B.S. and Ph.D. degrees in Electromagnetic Field and Microwave Technique from Nanjing University of Science and Technology (NUST), Nanjing, China, in 2002 and 2007, respectively.

During 2005, he was with the Center of Wireless Communication in the City University of Hong Kong, Kowloon, as a Research Assistant. He is currently an Associate Professor with the Electronic Engineering of NJUST. He is the author or co-author of over 30 technical papers. His current research interests include computational electromagnetics, electromagnetic scattering, and radiation.

Rushan Chen (M'01) was born in Jiangsu, China. He received the B.Sc. and M.Sc. degrees from the Department of Radio Engineering, Southeast University, China, in 1987 and 1990, respectively, and the Ph.D. degree from the Department of Electronic Engineering, City University of Hong Kong, in 2001.

He joined the Department of Electrical Engineering, Nanjing University of Science and Technology (NJUST), China, where he became a Teaching Assistant in 1990 and a Lecturer in 1992. Since September 1996, he has been a Visiting Scholar with the Department of Electronic Engineering, City University of Hong Kong, first as Research Associate, then as a Senior Research Associate in July 1997, a Research Fellow in April 1998, and a Senior Research Fellow in 1999. From June to September 1999, he was also a Visiting Scholar at Montreal University, Canada. In September 1999, he was promoted to Full Professor

and Associate Director of the Microwave and Communication Research Center in NJUST, and in 2007, he was appointed Head of the Department of Communication Engineering, NJUST. He was appointed as the Dean in the School of Communication and Information Engineering, Nanjing Post and Communications University in 2009. And in 2011, he was appointed as Vice Dean of the School of Electrical Engineering and Optical Technique, Nanjing University of Science and Technology. His research interests mainly include microwave/millimeter-wave systems, measurements, antenna, RF-integrated circuits, and computational electromagnetics. He has authored or co-authored more than 200 papers, including over 140 papers in international journals.

Chen received the 1992 third-class science and technology advance prize given by the National Military Industry Department of China, the 1993 third-class science and technology advance prize given by the National Education Committee of China, the 1996 second-class science and technology advance prize given by the National Education Committee of China, and the 1999 first-class science and technology advance prize given by Jiangsu Province, as well as the 2001 second-class science and technology advance prize. He is the recipient of the Foundation for China Distinguished Young Investigators presented by the National Science Foundation (NSF) of China in 2003. In 2008, he became a Chang-Jiang Professor under the Cheung Kong Scholar Program awarded by the Ministry of Education, China. Besides, he was selected as a Member of Electronic Science and Technology Group by Academic Degree Commission of the State Council in 2009. Chen is a Senior Member of the Chinese Institute of Electronics (CIE), Vice-Presidents of Microwave Society of CIE and IEEE MTT/APS/EMC Nanjing Chapter. He serves as the Reviewer for many technical journals such as IEEE Trans. on AP and MTT, Chinese Physics etc., and now serves as an Associate Editor for the International Journal of Electronics.

Scattering from an Arbitrarily Incident Plane Wave by a PEMC Elliptic Cylinder Confocally Coated with a Chiral Material

A-K. Hamid

Department of Electrical and Computer Engineering
University of Sharjah, P. O. Box 27272, Sharjah, United Arab Emirates
akhamid@sharjah.ac.ae

Abstract ─ An analytic solution to the problem of scattering of a plane electromagnetic wave by a chirally coated elliptic cylinder defined by PECM boundary condition has been obtained by expanding the different electromagnetic fields in terms of appropriate elliptic wave functions and a set of expansion coefficients. The expansion coefficients associated with the transmitted field inside the coating as well as the scattered field outside the coating are unknown and will be obtained by applying the boundary conditions at various layers. Numerical results have been presented graphically to show the effects of chiral and PEMC materials simultaneously on the bistatic width of scattering from coated elliptic cylinder.

Index Terms ─ Bistatic, chiral, elliptic cylinder, Mathieu functions, PEMC.

I. INTRODUCTION

Since the introduction of PEMC materials in 2005 [1], there has been a lot of research into scattering from different types of both two- and three-dimensional PEMC objects [2-12]. This has recently led to an interest on research involving coated PEMC objects [13-14]. As described in [1], a PEMC medium is a generalized form of a perfect electric conducting (PEC) and a perfect magnetic conducting (PMC) medium in which certain linear combinations of electromagnetic fields become extinct [15], and is definable by a single real-valued parameter known as the PEMC admittance. A null admittance corresponds to a PMC medium and an admittance of infinity corresponds to a PEC medium, when the field magnitudes are finite [16]. A PEMC material acts as a perfect reflector of electromagnetic waves, but differs from PEC and PMC materials due to the fact that it produces a reflected wave with a cross-polarized field component [17-22].

The elliptic cylinder is a geometry that has been extensively analyzed in the literature due to its ability to produce cylinders of different cross sectional shapes, by changing the axial ratio of the ellipse. Moreover, since the elliptic cylindrical coordinate system is one of the coordinate systems in which the wave equation is separable, solutions to problems involving elliptic cylinders can be obtained in closed form.

In this paper, we present the analysis corresponding to the scattering from a chiral coated PEMC elliptic cylinder of arbitrary axial ratio, when it is excited by either a plane wave of arbitrary polarization and angle of incidence. Such solution is valuable, since it can be used for validating solutions obtained using other methods. The analysis and the software used for obtaining the results have been validated by calculating the normalized scattering widths for a PEMC coated elliptic [22] when it is illuminated by a plane wave. It was shown graphically that these results are in very good agreement with the corresponding results obtained using various values of admittances for coated PEMC elliptic cylinder.

II. FORMULATION

Consider a linearly polarized uniform plane electromagnetic wave arbitrarily incident on an infinitely long PEMC elliptic cylinder confocally coated with a chiral material. The semi-major and semi-minor axis lengths of the uncoated cylinder are denoted by a_0 and b_0, and those of the coated cylinder are denoted by a_c and b_c, respectively. The coated cylinder is assumed to be located in free space, with the incident wave making an angle φ_i with the negative x-axis of a Cartesian coordinate system as shown in Fig. 1. It is beneficial to define the *x* and *y* coordinates of the Cartesian coordinate system in terms *u, v, z* of an elliptical coordinate system where $x = F \cosh u \cos v$, $y = F \sinh u \sin v$, with F being the semi-focal length of the ellipse. A time dependence of $\exp(j\omega t)$ with ω being the angular frequency, is assumed throughout the analysis, but suppressed for convenience. The analysis is conducted for an incident uniform plane wave of transverse magnetic (TM) polarization. The analysis corresponding to a plane wave

of transverse electric (TE) polarization can be obtained from that for a plane wave of TM polarization, using duality.
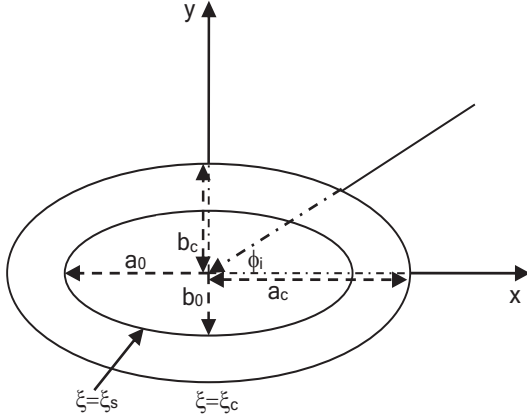
Fig. 1. Geometry of the chiral coated PEMC elliptic cylinder.

Considering a TM polarized arbitrarily incident plane wave of unit amplitude, we can expand the incident electric field component as [23]:

$$E_z^{inc} = \sum_{q,n} A_{qn} R_{qn}^{(1)}(c,\xi) S_{qn}(c,\eta), \qquad (1)$$

where $R_{qn}^{(i)}(c,\xi)$ and $S_{qn}(c,\eta)$ are the i-th order of the radial and angular Mathieu functions respectively, where $q = e,o$ stands for even and odd solution, and

$$A_{qn} = j^n \frac{\sqrt{8\pi}}{N_{qn}(c)} S_{qn}(c,\cos\phi_i), \qquad (2)$$

in which $c = kF$ with k being the wavenumber of the medium outside the cylinder and $N_{qn}(c)$ is the normalization constant associated with $S_{qn}(c,\eta)$. Using Maxwell's equations we can expand the incident magnetic field component as:

$$H_v^{inc} = \frac{1}{jkZh} \sum_{q,n} A_{qn} R_{qn}^{(1)'}(c,\xi) S_{qn}(c,\eta), \qquad (3)$$

where $h = F\sqrt{\cosh^2 u - \cos^2 v}$, with $\xi = \cosh u$, $\eta = \cos v$, Z is the wave impedance of the medium outside the cylinder, and the prime denoting the differentiation with respect to u.

Since the cylinder comprises of a PEMC material, the scattered field consists of both co- and cross-polar components. These can be expanded as:

$$E_z^s = \sum_{q,n} B_{qn} R_{qn}^{(4)}(c,\xi) S_{qn}(c,\eta), \qquad (4)$$

$$E_v^s = -\frac{1}{kh} \sum_{q,n} C_{qn} R_{qn}^{(4)'}(c,\xi) S_{qn}(c,\eta), \qquad (5)$$

$$H_z^s = \frac{j}{Z} \sum_{q,n} C_{qn} R_{qn}^{(4)}(c,\xi) S_{qn}(c,\eta), \qquad (6)$$

$$H_v^s = \frac{1}{jkZh} \sum_{q,n} B_{qn} R_{qn}^{(4)'}(c,\xi) S_{qn}(c,\eta), \qquad (7)$$

in which C_{qn} and B_{qn} are the unknown co- and cross-scattered field expansion coefficients.

The fields within the chiral coating also have both co- and cross-polar components, comprising of left- and right-handed parts. These can be expanded as:

$$E_z^c = \sum_{q,n} \{[D_{qn} R_{qn}^{(1)}(c_R,\xi) + P_{qn} R_{qn}^{(2)}(c_R,\xi)] S_{qn}(c_R,\eta) \\ + [F_{qn} R_{qn}^{(1)}(c_L,\xi) + Q_{qn} R_{qn}^{(2)}(c_L,\xi)] S_{qn}(c_L,\eta)\}, \qquad (8)$$

$$E_v^c = \sum_{q,n} \{-\frac{1}{k_R h}[D_{qn} R_{qn}^{(1)'}(c_R,\xi) + P_{qn} R_{qn}^{(2)'}(c_R,\xi)] S_{qn}(c_R,\eta) \\ + \frac{1}{k_L h}[F_{qn} R_{qn}^{(1)'}(c_L,\xi) + Q_{qn} R_{qn}^{(2)'}(c_L,\xi)] S_{qn}(c_L,\eta)\}, \qquad (9)$$

$$H_z^c = \frac{j}{Z_c} \sum_{q,n} \{[D_{qn} R_{qn}^{(1)}(c_R,\xi) + P_{qn} R_{qn}^{(2)}(c_R,\xi)] S_{qn}(c_R,\eta) \\ - [F_{qn} R_{qn}^{(1)}(c_L,\xi) + Q_{qn} R_{qn}^{(2)}(c_L,\xi)] S_{qn}(c_L,\eta)\}, \qquad (10)$$

$$H_v^c = \frac{j}{Z_c} \sum_{q,n} \{-\frac{1}{k_R h}[D_{qn} R_{qn}^{(1)'}(c_R,\xi) + P_{qn} R_{qn}^{(2)'}(c_R,\xi)] S_{qn}(c_R,\eta) \\ - \frac{1}{k_L h}[F_{qn} R_{qn}^{(1)'}(c_L,\xi) + Q_{qn} R_{qn}^{(2)'}(c_L,\xi)] S_{qn}(c_L,\eta)\}, \qquad (11)$$

where $D_{qn}, F_{qn}, P_{qn}, Q_{qn}$ are the unknown field expansion coefficients, $c_R = k_R F$, $c_L = k_L F$, with the wavenumbers k_R and k_L corresponding to the right- and left-handed waves inside the chiral medium given by $k_{R,L} = \omega\sqrt{\mu\varepsilon_c} \pm \omega\mu\zeta_c$, in which ζ_c is the chirality admittance and ε_c is the effective permittivity defined by $\varepsilon_c = \mu + \varepsilon\zeta_c^2$ with ε and μ being the permittivity and permeability of the chiral medium, and Z_c is the wave impedance in the chiral medium, given by $Z_c = \sqrt{\mu/\varepsilon_c}$.

The boundary conditions at the surface $\xi = \xi_c$ of the coating require the continuity of the tangential components of the electric and magnetic fields across the boundary. These can be written mathematically as:

$$E_z^c = E_z^i + E_z^s, \qquad (12)$$

$$E_v^c = E_v^i + E_v^s, \qquad (13)$$

$$H_z^c = H_z^i + H_z^s, \qquad (14)$$

$$H_v^c = H_v^i + H_v^s. \qquad (15)$$

Similarly, the boundary conditions at the surface $\xi = \xi_s$ of the PEMC elliptic cylinder can be written using the PEMC admittance M as:

$$H_z^c + ME_z^c = 0, \tag{16}$$

$$H_v^c + ME_v^c = 0. \tag{17}$$

Substituting for the electric field components in (12)-(13) in terms of their respective expansions, we get:

$$\sum_{q,n}\{[D_{qn}R_{qn}^{(1)}(c_R,\xi_c)+P_{qn}R_{qn}^{(2)}(c_R,\xi_c)]S_{qn}(c_R,\eta)$$

$$+[F_{qn}R_{qn}^{(1)}(c_L,\xi_c)+Q_{qn}R_{qn}^{(2)}(c_L,\xi_c)]S_{qn}(c_L,\eta)\} \tag{18}$$

$$=\sum_{q,n}[A_{qn}R_{qn}^{(1)}(c,\xi_c)+B_{qn}R_{qn}^{(4)}(c,\xi_c)]S_{qn}(c,\eta),$$

$$\sum_{q,n}\{-\frac{1}{k_R h}[D_{qn}R_{qn}^{(1)'}(c_R,\xi_c)+P_{qn}R_{qn}^{(2)'}(c_R,\xi_c)]S_{qn}(c_R,\eta)$$

$$+\frac{1}{k_L h}[F_{qn}R_{qn}^{(1)'}(c_L,\xi_c)+Q_{qn}R_{qn}^{(2)'}(c_L,\xi_c)]S_{qn}(c_L,\eta)\} \tag{19}$$

$$=-\frac{1}{kh}\sum_{q,n}C_{qn}R_{qn}^{(4)'}(c,\xi_c)S_{qn}(c,\eta).$$

Substituting for the magnetic field components in (14)-(15) in terms of their respective expansions yields:

$$\frac{j}{Z_c}\sum_{q,n}\{[D_{qn}R_{qn}^{(1)}(c_R,\xi_c)+P_{qn}R_{qn}^{(2)}(c_R,\xi_c)]S_{qn}(c_R,\eta)$$

$$-[F_{qn}R_{qn}^{(1)}(c_L,\xi_c)+Q_{qn}R_{qn}^{(2)}(c_L,\xi_c)]S_{qn}(c_L,\eta)\} \tag{20}$$

$$=\frac{j}{Z}\sum_{q,n}C_{qn}R_{qn}^{(4)}(c,\xi_c)S_{qn}(c,\eta),$$

$$\sum_{q,n}\{\frac{1}{jk_R hZ_c}[D_{qn}R_{qn}^{(1)'}(c_R,\xi_c)+P_{qn}R_{qn}^{(2)'}(c_R,\xi_c)]S_{qn}(c_R,\eta)$$

$$+\frac{1}{jk_L hZ_c}[F_{qn}R_{qn}^{(1)'}(c_L,\xi_c)+Q_{qn}R_{qn}^{(2)'}(c_L,\xi_c)]S_{qn}(c_L,\eta)\} \tag{21}$$

$$=\sum_{q,n}\frac{1}{jkhZ}[A_{qn}R_{qn}^{(1)'}(c,\xi_c)+B_{qn}R_{qn}^{(4)'}(c,\xi_c)]S_{qn}(c,\eta).$$

Substituting for the field components in (17) and (18) in terms of their expansions, we get:

$$\frac{j}{Z_c}\sum_{q,n}\{[D_{qn}R_{qn}^{(1)}(c_R,\xi_s)+P_{qn}R_{qn}^{(2)}(c_R,\xi_s)]S_{qn}(c_R,\eta)$$

$$-[F_{qn}R_{qn}^{(1)}(c_L,\xi_s)+Q_{qn}R_{qn}^{(2)}(c_L,\xi_s)]S_{qn}(c_L,\eta)\}$$

$$+M\sum_{q,n}D_{qn}R_{qn}^{(1)}(c_R,\xi_s)+P_{qn}R_{qn}^{(2)}(c_R,\xi_s)]S_{qn}(c_R,\eta) \tag{22}$$

$$+[F_{qn}R_{qn}^{(1)}(c_L,\xi_s)+Q_{qn}R_{qn}^{(2)}(c_L,\xi_s)]S_{qn}(c_L,\eta)=0,$$

$$\sum_{q,n}\{\frac{1}{jk_R hZ_c}[D_{qn}R_{qn}^{(1)'}(c_R,\xi_s)+P_{qn}R_{qn}^{(2)'}(c_R,\xi_s)]S_{qn}(c_R,\eta)$$

$$+\frac{1}{jk_L hZ_c}[F_{qn}R_{qn}^{(1)'}(c_L,\xi_s)+Q_{qn}R_{qn}^{(2)'}(c_L,\xi_s)]S_{qn}(c_L,\eta)\}$$

$$+M\sum_{q,n}-\frac{1}{k_R h}[D_{qn}R_{qn}^{(1)'}(c_R,\xi_s)+P_{qn}R_{qn}^{(2)'}(c_R,\xi_s)]S_{qn}(c_R,\eta) \tag{23}$$

$$+\frac{1}{k_L h}[F_{qn}R_{qn}^{(1)'}(c_L,\xi_s)+Q_{qn}R_{qn}^{(2)'}(c_L,\xi_s)]S_{qn}(c_L,\eta)=0.$$

If both sides of equations (18)-(23) are multiplied by $S_{qn}(c,\eta)$ and integrated over η from -1 to 1, then considering the orthogonality of the angular Mathieu functions, we can write these equations after a rearrangement as:

$$[D_{qn}R_{qn}^{(1)}(c_R,\xi_c)+P_{qn}R_{qn}^{(2)}(c_R,\xi_c)]M_{qn}^R(c_R,c)$$

$$+[F_{qn}R_{qn}^{(1)}(c_L,\xi_c)+Q_{qn}R_{qn}^{(2)}(c_L,\xi_c)]M_{qn}^L(c_L,c)= \tag{24}$$

$$[A_{qn}R_{qn}^{(1)}(c,\xi_c)+B_{qn}R_{qn}^{(4)}(c,\xi_c)]N_{qn}(c),$$

$$\frac{k}{k_R}[D_{qn}R_{qn}^{(1)'}(c_R,\xi_c)+P_{qn}R_{qn}^{(2)'}(c_R,\xi_c)]M_{qn}^R(c_R,c)$$

$$-\frac{k}{k_L}[F_{qn}R_{qn}^{(1)'}(c_L,\xi_c)+Q_{qn}R_{qn}^{(2)'}(c_L,\xi_c)]M_{qn}^L(c_L,\eta)= \tag{25}$$

$$C_{qn}R_{qn}^{(4)'}(c,\xi_c)N_{qn}(c),$$

$$D_{qn}R_{qn}^{(1)}(c_R,\xi_c)+P_{qn}R_{qn}^{(2)}(c_R,\xi_c)]M_{qn}^R(c_R,c)$$

$$-[F_{qn}R_{qn}^{(1)}(c_L,\xi_c)+Q_{qn}R_{qn}^{(2)}(c_L,\xi_c)]M_{qn}^L(c_L,c)= \tag{26}$$

$$\frac{Z_c}{Z}C_{qn}R_{qn}^{(4)}(c,\xi_c)N_{qn}(c),$$

$$\left(\frac{kZ}{k_R Z_c}\right)[R_{qn}^{(1)'}(c_R,\xi_c)+P_{qn}R_{qn}^{(2)'}(c_R,\xi_c)]M_{qn}^R(c_R,c)$$

$$+\left(\frac{kZ}{k_L Z_c}\right)[F_{qn}R_{qn}^{(1)'}(c_L,\xi_c)+Q_{qn}R_{qn}^{(2)'}(c_L,\xi_c)]M_{qn}^L(c_L,c) \tag{27}$$

$$=[A_{qn}R_{qn}^{(1)'}(c,\xi_c)+B_{qn}R_{qn}^{(4)'}(c,\xi_c)]N_{qn}(c),$$

$$(1-jMZ_c)[D_{qn}R_{qn}^{(1)}(c_R,\xi_s)+P_{qn}R_{qn}^{(2)}(c_R,\xi_s)]M_{qn}^R(c_R,c)$$

$$-(1+jMZ_c)[F_{qn}R_{qn}^{(1)}(c_L,\xi_s)+Q_{qn}R_{qn}^{(2)}(c_L,\xi_s)]M_{qn}^L(c_L,c)=0, \tag{28}$$

$$(1-jMZ_c)\left(\frac{k}{k_R}\right)[D_{qn}R_{qn}^{(1)'}(c_R,\xi_s)+P_{qn}R_{qn}^{(2)'}(c_R,\xi_s)]M_{qn}^R(c_R,c)$$

$$+(1+jMZ_c)\left(\frac{k}{k_L}\right)[F_{qn}R_{qn}^{(1)'}(c_L,\xi_s)+Q_{qn}R_{qn}^{(2)'}(c_L,\xi_s)]M_{qn}^L(c_L,c)=0, \tag{29}$$

where

$$M_{qn}^\alpha(c_\alpha,c)=\int_{-1}^{1}S_{qn}(c_\alpha,\eta)S_{qn}(c,\eta)\,d\eta, \tag{30}$$

for $\alpha=R,L$. Writing the system of equations (24)-(29) in matrix form and the solution by matrix inversion yields the unknown coefficients associated with the scattered and transmitted fields.

III. NUMERICAL RESULTS

In the limit $\xi\to\infty$, since $c\xi\to k\rho$ with ρ being the radial cylindrical coordinate, using asymptotic expressions, the radial Mathieu function of the fourth kind and its first derivative with respect to argument can be written as:

$$\lim_{\xi\to\infty}R_{qn}^{(4)}(c,\xi)\approx j^n\sqrt{\frac{j}{k\rho}}e^{-jk\rho},$$

$$\lim_{\xi \to \infty} R_{qn}^{(4)'}(c,\xi) \approx j^{n-1}k\rho\sqrt{\frac{j}{k\rho}}e^{-jk\rho}. \qquad (31)$$

Using (31) and the fact that in the limit $\xi \to \infty$, $kh \to kF\cosh u \approx k\rho$, we can write expressions for the scattered electric field components in the far zone as:

$$E_z^s = \sqrt{\frac{j}{k\rho}}e^{-jk\rho}\left[\begin{array}{c}\sum_{n=0}^{\infty}j^n B_{en}S_{en}(c,\cos\varphi)+\\ \sum_{n=1}^{\infty}j^n B_{on}S_{on}(c,\cos\varphi)\end{array}\right], \qquad (32)$$

$$E_\varphi^s = j\sqrt{\frac{j}{k\rho}}e^{-jk\rho}\left[\begin{array}{c}\sum_{n=0}^{\infty}j^n C_{en}S_{en}(c,\cos\varphi)+\\ \sum_{n=1}^{\infty}j^n C_{on}S_{on}(c,\cos\varphi)\end{array}\right], \qquad (33)$$

and the scattered magnetic field components as $H_z^s = E_\varphi^s/Z$ and $H_\varphi^s = -E_z^s/Z$.

The bistatic scattering cross section is defined as:

$$\sigma = \lim_{\rho \to \infty}2\pi\rho\frac{\text{Re}[\mathbf{E}_s \times \mathbf{H}_s^* \cdot \hat{\boldsymbol{\rho}}]}{\text{Re}[\mathbf{E}_i \times \mathbf{H}_i^* \cdot \hat{\boldsymbol{\rho}}]}, \qquad (34)$$

with $\text{Re}[w]$ denoting the real part of the complex number w, the asterisk denoting the complex conjugate, and $\hat{\boldsymbol{\rho}}$ denoting the unit vector in the increasing radial direction. Substituting for the far zone scattered fields in (34), and recalling that the incident field is of unit amplitude, an expression for the normalized bistatic width can be written as:

$$\frac{\sigma(\varphi)}{\lambda} = \left|\sum_{q=e,o}\sum_{n=0}^{\infty}j^n B_{qn}S_{qn}(c,\cos\varphi)\right|^2 + \\ \left|\sum_{q=e,o}\sum_{n=0}^{\infty}j^n C_{qn}S_{qn}(c,\cos\varphi)\right|^2. \qquad (35)$$

It can be seen from equation (35) that the uniqueness of PEMC material over PEC and PMC materials it has both co and cross-polarized field components.

Results obtained are presented graphically as normalized bistatic width for chiral coated PEMC elliptic cylinders of different sizes, PEMC admittances, and chiral coatings, with all coated cylinders assumed to be located in free space. For convenience, the PEMC admittance M is expressed in terms of the dimensionless quantity MZ1, using the formula MZ1=tan(υ), so that υ=0º and υ=90º correspond to the PMC and PEC cases, respectively.

Normalized bistatic widths of chiral coated PEMC elliptic cylinders obtained for different scattering angles, when they are illuminated by a plane wave incident at 0º, are shown in Fig. 2. The geometrical parameters of the

scatterer are a=0.4λ, b=0.2λ, a_c=0.56λ, b_c=0.44λ, and the coating values are ε_{rc}=2.5 and μ_{rc}=1.0. The admittances of the PEMC cylinders are specified by the parameter υ, which varies from 0º to 90º, in steps of 15º and chiral admittance is ζ_c=0.0.
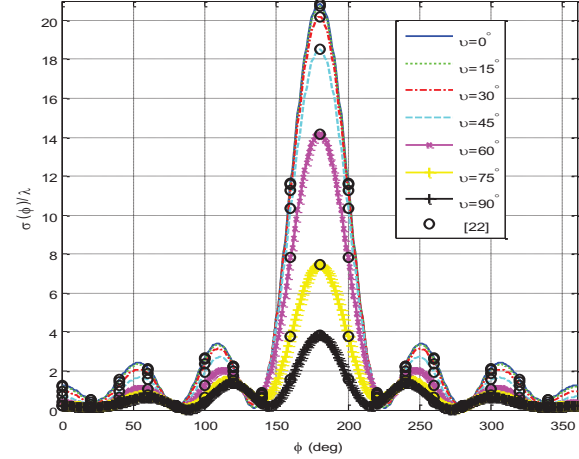
Fig. 2. Normalized bistatic width versus scattering angle for PEMC elliptic cylinders of different admittances coated with ε_{rc}=2.5, μ_{rc}=1.0, ϕ_i=0º, and ζ_c=0.0.

The plots are symmetric around φ=180º as expected. The normalized bistatic width for a given scattering angle decreases as the value of υ increases, with the magnitude for each angle being a maximum for υ=0º (PMC), a minimum for υ=90º (PEC), and the differences for two values of υ becoming a maximum at φ=180º, corresponding to forward scattering. The normalized bistatic widths are compared with the corresponding values obtained for a conventional coated PEMC elliptic cylinder in [22], presented by circles, and are in very good agreement, validating the calculations for an elliptic cylinder in general.

Figure 3 (a) is similar to Fig. 2, except that the chiral admittance is taken to be ζ_c=0.002. This figure shows the effect of both PEMC and chiral coating on the bistatic of coated elliptic cylinder. There is a drop in the bistatic width by approximately of 50% at υ=0º and υ=90º, and no change in the location of the maximum values for other values of υ. It is worth mentioning that the value of the bistatic widths for υ=75º and 90º are the same at φ=180º. Figure 3 (b) is similar to Fig. 3 (a), except ζ_c is reduced to 0.0015. It can be seen that the bistatic width is higher and the maximum is back at υ=0º and the minimum at υ=90º. The variation of the bistatic widths is due to the presence of the cross-polarized fields of

PEMC and chiral materials.

Figure 4 is similar to Fig. 3, except that the incident angle is 90º. Figure 4 (a) shows that the magnitude of the bistatic width has maxima at υ=90º and minima at υ=0º and φ=90º, while the opposite is happening at the scattering angle of φ=270º. Figure 4 (b) is for the case of ζ_c =0.0015.

(a)

(b)
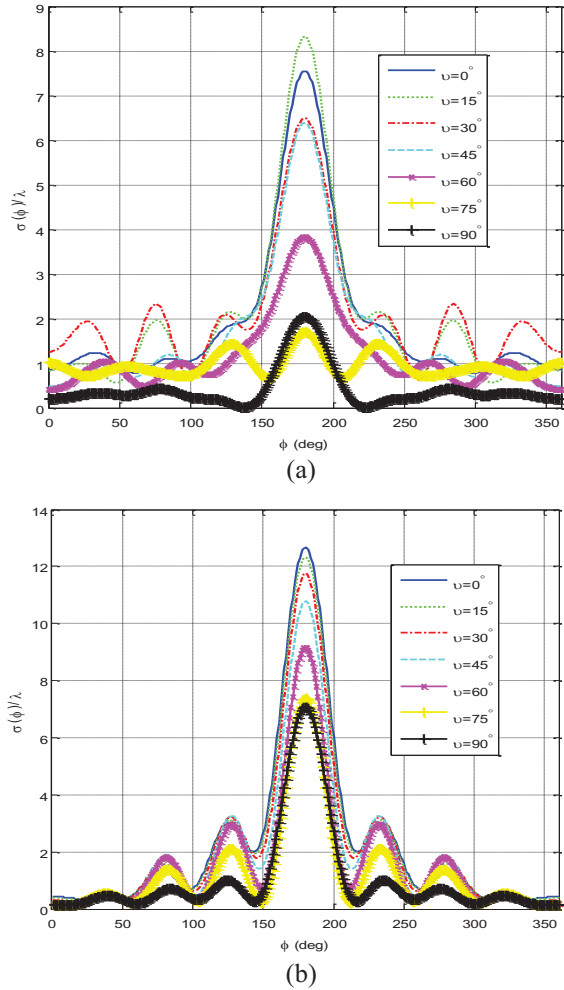
Fig. 3. Normalized bistatic width versus scattering angle for PEMC elliptic cylinders of different admittances coated with ε_{rc}=2.5, μ_{rc}=1.0, ϕ_i =0º: (a) ζ_c =0.002, and (b) ζ_c =0.0015.

It can be seen that Fig. 5 is similar to 4, except by increasing ε_{rc} from 2.5 to 3.0. Figure 6 shows the bistatic widths versus the major axis of the dielectric coating for υ=45º and 75º and ζ_c =0.002 and 0.0025. The presence of chiral material effects the magnitude but not the pattern of the bistatic width. More results and analysis on chiral coated or PEMC conventional coated elliptic cylinder can be found in [22,24].

(a)

(b)
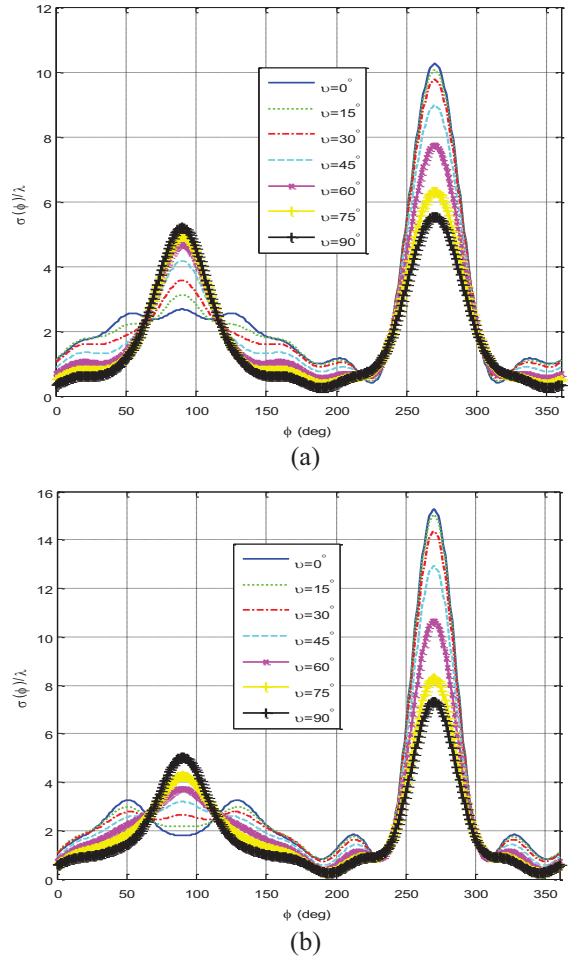
Fig. 4. Normalized bistatic width versus scattering angle for PEMC elliptic cylinders of different admittances coated with ε_{rc}=2.5, μ_{rc}=1.0, ϕ_i =90º: (a) ζ_c =0.002, and (b) ζ_c =0.0015.
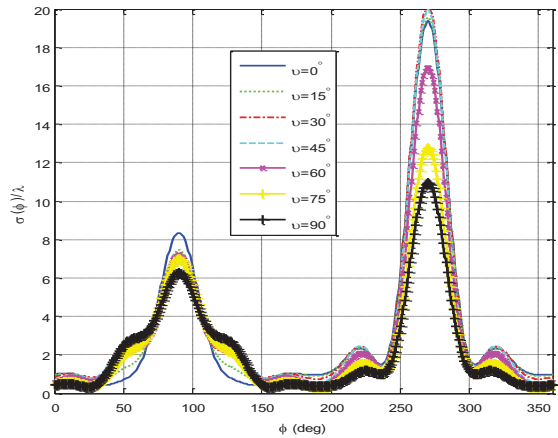
Fig. 5. Normalized bistatic width versus scattering angle for PEMC elliptic cylinders of different admittances coated with ε_{rc}=3.0, μ_{rc}=1.0, ϕ_i =90º and ζ_c =0.002.

(a)

(b)
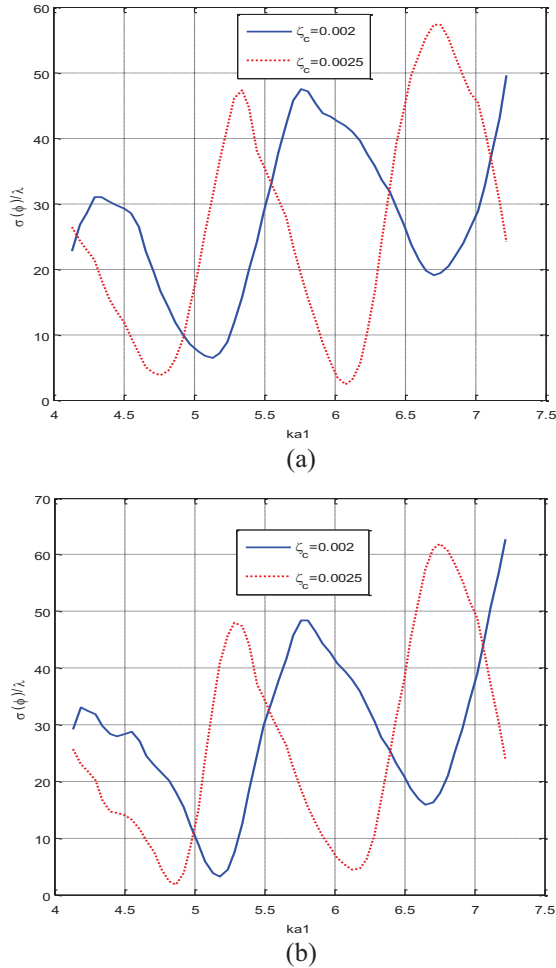
Fig. 6. Normalized bistatic width versus ka$_1$ for PEMC elliptic cylinders of different admittances coated with ε_{rc}=3.0, μ_{rc}=1.0, ϕ_i=0.0$^\text{o}$, a=0.4λ, b=0.2λ: (a) υ=45$^\text{o}$, and (b) υ=75$^\text{o}$.

IV. CONCLUSION

Analytic solution has been obtained to the problem of scattering from a chirally coated PEMC elliptic cylinder, when it is excited by a uniform plane wave. The solution is general since it also can provide the solution to the scattering by PEMC circular or strip chiral coated geometries. The results obtained show that the admittances as well as the constitutive parameters of the chiral coating material can be used to control (enhancing or reducing) the scattering width of a coated PEMC elliptic cylinder. Thus, the solution provides the designer with two degree of freedom to control the bistatic width. The new results obtained in this paper are important, since they can be used to validate similar results obtained using other methods, and provide an insight into how the changing of various parameters associated with a chirally coated PEMC elliptic cylinder changes the scattering widths that could be obtained from it.

REFERENCES

[1] I. V. Lindell and A. H. Sihvola, "Perfect electromagnetic conductor," *J. Electromag. Waves Appl.*, vol. 19, no. 7, pp. 861-869, 2005.

[2] R. Ruppin, "Scattering of electromagnetic radiation by a perfect electromagnetic conductor cylinder," *J. Electromag. Waves Appl.*, vol. 20, no. 13, pp. 1853-1860, 2006.

[3] S. Ahmed and Q. A. Naqvi, "Electromagnetic scattering from a perfect electromagnetic conductor cylinder buried in a dielectric half-space," *PIER 78*, pp. 25-38, 2008.

[4] S. Ahmed and Q. A. Naqvi, "Electromagnetic scattering from parallel perfect electromagnetic conductor cylinders of circular cross-sections using an iterative procedure," *J. Electromag. Waves Appl.*, vol. 22, pp. 987-1003, 2008.

[5] A. Illahi, M. Afzaal, and Q. A. Naqvi, "Scattering of dipole field by a perfect electromagnetic conductor cylinder," *PIER L 4*, pp. 43-53, 2008.

[6] S. Ahmed and Q. A. Naqvi, "Electromagnetic scattering from a two dimensional perfect electromagnetic conductor (PEMC) rectangular strip and PEMC rectangular strip grating simulated by circular cylinders," *Optics Comm.*, vol. 281, pp. 4211-4218, 2008.

[7] S. Ahmed and Q. A. Naqvi, "Electromagnetic scattering of two or more incident plane waves by a perfect electromagnetic conductor cylinder coated with a metamaterial," *PIER B*, vol. 10, pp. 75-90, 2008.

[8] A. Illahi and Q. A. Naqvi, "Scattering of an arbitrarily oriented dipole field by an infinite and a finite length PEMC circular cylinder," *CEJP*, vol. 7, no. 4, pp. 829-853, 2009.

[9] S. Ahmed and Q. A. Naqvi, "Directive EM radiation of a line source in the presence of a coated PEMC circular cylinder," *PIER 92*, pp. 91-102, 2009.

[10] A. Sihvola, P. Ylä-Oijala, and I. V. Lindell, "Bistatic scattering from a PEMC (perfect electromagnetic conducting) sphere: surface integral equation approach," *Symp. Digest IEEE/ACES Int. Conf. Wireless Comm. Appl. Comp. Electromag.*, pp. 317-320, 2005.

[11] R. Ruppin, "Scattering of electromagnetic radiation by a perfect electromagnetic conductor sphere," *J. Electromag. Waves Appl.*, vol. 20, no. 12, pp. 1569-1576, 2006.

[12] A-K. Hamid and F. R. Cooray, "Scattering of electromagnetic waves by a perfect electromagnetic conducting spheroid," *IET Proc. Microwaves Antennas Propagat.*, vol. 2, no. 7, pp. 686-695, 2008.

[13] Q. Naqvi and S. Ahmed, "Electromagnetic scattering from a perfect electromagnetic

conductor circular cylinder coated with a metamaterial having negative permittivity and/or permeability," *Optics Comm.*, vol. 281, pp. 5664-5670, 2008.

[14] R. Ruppin, "Scattering of electromagnetic radiation by a coated perfect electromagnetic conductor sphere," *PIER L*, vol. 8, pp. 53-62, 2009.

[15] I. V. Lindell and A. H. Sihvola, "Perfect electromagnetic conductor," *J. Electromag. Waves Appl.*, vol. 19, no. 7, pp. 861-869, 2005.

[16] A. Sihvola, I. V. Lindell, and P. Ylä-Oijala, "Scattering properties of PEMC (perfect electromagnetic conducting) materials," *Symp. Digest PIERS*, Hangzhou, China, Aug. 2005.

[17] I. V. Lindell and A. H. Sihvola, "Perfect electromagnetic conductor (PEMC) in electromagnetics," *Symp. Digest PIERS*, Hangzhou, China, Aug. 2005.

[18] I. V. Lindell and A. H. Sihvola, "Transformation method for problems involving perfect electromagnetic conductor (PEMC) structures," *IEEE Trans. Antennas Propag.*, vol. 53, no. 9, pp. 3005-3011, 2005.

[19] H. A. Ragheb and L. Shafai, "Electromagnetic scattering from a dielectric-coated elliptic cylinder," *Can. J. Phys.*, vol. 66, no. 12, pp. 1115-1122, 1988.

[20] S. Ahmed, F. Manan, A. Shahzad, and Q. A. Naqvi, "Electromagnetic scattering from a chiral-coated PEMC cylinder," *Progress In Electromagnetics Research M*, vol. 19, pp. 239-250, 2011.

[21] M. Khalid, A. A. Syed, and Q. A. Naqvi, "Circular cylinder with D'B, DB' and D'B' boundary conditions placed in chiral and chiral nihility media," *International Journal of Applied Electromagnetics and Mechanics*, vol. 44, pp. 59-68, 2014.

[22] F. Cooray and A-K. Hamid, "Scattering from a coated perfect electromagnetic conducting elliptic cylinder," *International Journal of Electronics and Communications, AEUE*, vol. 66, pp. 472-479, 2012.

[23] P. M. Morse and H. Feshbach, *Methods of Theoretical Physics, Part II*, McGraw Hill, New York, 1953.

[24] A-K. Hamid and F. Cooray, "Scattering from a chirally coated DB elliptic cylinder," *International Journal of Electronics and Communications, AEUE*, vol. 68, pp. 1106-1111, 2014.

A-K. Hamid received the B.Sc. degree in Electrical Engineering from West Virginia Institute of Technology and University, West Virginia, U.S.A. in 1985, the M.Sc. and Ph.D. degrees from the University of Manitoba, Winnipeg, Manitoba, Canada in 1988 and 1991, respectively, both in Electrical Engineering. From 1991-1993, he was with Quantic Laboratories Inc., Winnipeg, Manitoba, Canada, developing two and three dimensional electromagnetic field solvers using boundary integral method. From 1994-2000 he was with the Faculty of Electrical Engineering at King Fahd University of Petroleum and Minerals, Dhahran, Saudi Arabia. Since Sept. 2000, he has been with the Electrical and Computer Engineering Department at the University of Sharjah, Sharjah, United Arab Emirates. His research interest includes EM wave scattering from two and three dimensional bodies, propagation along waveguides with discontinuities, FDTD simulation of cellular phones, and inverse scattering using neural networks.

Design of Compact and Wideband Suppression Low Pass Elliptic Filter by n-Segment Step Impedance Transmission Line

M. Hayati [1], M. Amiri [1], and S. H. Sedighy [2]

[1] Department of Electrical Engineering
Razi University, Kermanshah, Iran
hayati@razi.ac.ir, mozhgan.amiri@gmail.com

[2] School of New Technologies
Iran University of Science and Technology, Tehran, Iran
sedighy@iust.ac.ir

Abstract ─ In this paper, the invasive weed optimization technique for compacting a microstrip elliptic low pass filter is proposed and validated. At the first step, the invasive weed optimization (IWO) technique is used to replace the shunt resonators transmission lines of the conventional filter with arbitrary n-segments Step Impedance Transmission Lines (SITLs) for compacting it. To validate the proposed method, the shunt resonator transmission lines of a seventh-order elliptic lowpass filter are replaced with proper SITLs which cause more than 30% compactness in this step. Then the IWO technique is applied on the general filter configuration to design a wideband harmonic suppression and compact elliptic low pass filter. This method extends the stop band bandwidth more than 8.5 f0 and also increases the compactness to 47%. The measurement results of the final optimized fabricated filter are in good agreement with the simulation ones.

Index Terms ─ Elliptic low pass filter, harmonic suppression, Invasive Weed Optimization (IWO), microstrip, miniaturization, wideband.

I. INTRODUCTION

A microstrip lowpass filter with small size, sharp transition band and wide stopband is frequently used in the modern microwave and millimeter wave communication system to suppress harmonics and unwanted signals. There are several techniques for designing low pass filters such as Butterworth, Chebyshev, elliptic function, all pass, and Gaussian response. In the elliptic filters, the response has equal-ripple in both the pass band and stopband, which means that the elliptic function design is superior to both the Butterworth and Chebyshev designs. Moreover, these filters have sharp cutoff skirts and low in-band insertion loss [1-5].

The elliptic function low pass filters show the advantages of high performance, low cost, capability of implementation with microstrip technology and easy fabrication [1,2]. Also elliptic filters achieve the smallest filter order for the same specifications and the narrowest transition width for the same filter order compared to other filter design techniques. The microstrip realization of elliptic filter can be implemented with several configurations of microstrip transmission lines such as shunt stubs and stepped impedances [1,2]. Due to the rapid development of wireless communication technology, miniaturization receives a high demand in the designing of microwave devices, especially filters [6]. The conventional microstrip low pass filters techniques such as shunt stubs or high–low impedance transmission lines have been widely used in microwave systems for their remarkable characteristics [3]. However, it is hard to achieve compact size and high performance simultaneously with these implementation methods [3]. Also, the conventional low pass filters (LPFs) can only provide a gradual transition and a narrow stopband [1]. Moreover, raising the filter's order can improve its performance which enlarges the overall filter size and increases the insertion loss.

To reduce the physical size of microstrip filters, many approaches have been investigated and commonly used in the circuit designs such as stepped-impedance resonator (SIR) [7], defected ground structure (DGS) [8], photonic band gap structure (PBG) [9,10], metamaterial [11], quasi-lumped element [12], and dual-mode/half-mode resonator [6]. Photonic bandgap and defected ground structures can provide sharp and extended stopband in the LPF [13-15]. However, these techniques cause many disadvantages such as complex configuration and fabrication difficulties [13]. The LPFs using defected ground structures have been proposed in [16] and [17]. In [16], a quarter-circle defected ground

structure shape was introduced, despite its wide stopband with very good insertion and return losses, it suffers the large size and gradual transition band. A quasi-elliptic LPF using three DGS units and a compensated microstrip line has been designed and implemented in [17], which has high insertion loss and narrow stopband. A lowpass filter using stepped impedance compact microstrip resonator cell (SICMRC) has been proposed in [18]. The SICMRC has been embedded in the structure of double arrow shaped microstrip cell (DASMC) to obtain a sharp response. Although it is compact LPF with wide stopband, it isn't sharp adequately. A compact elliptic-function low-pass filter by etching stepped impedance resonators (SIR) in the back substrate side has been presented in [19], which it suffers the narrow stop bandwidth. A microstrip lowpass filter with a novel patch resonator consisting of a semi-circle and semi-ellipse loaded by delta stub and rhomboid structures has been studied in [20], which has the gradual transition band with large size. In [21], a compact microstrip stepped impedance lowpass filter using back-to-back C-shaped and triple C-shaped thin slots has been presented which has wide stopband, but its frequency response is not sharp sufficiently in the transition band and does not have good passband performance due to its significant insertion loss. A LPF using circular hairpin resonator has been designed in [22] which has a compact size, but it doesn't have good insertion loss, sharp roll off and wide stop band.

In [23], the uniform transmission line segments of a low pass filter have been replaced by step impedance transmission lines optimized by invasive weed optimization (IWO) technique. In this paper, the IWO algorithm is used to compact the conventional elliptic low pass filter and increase the harmonic suppression bandwidth. For this purpose, the shunt resonators which have m-segments transmission lines are replaced with proper compact arbitrary n-segments step impedance transmission lines in a seventh-order lowpass elliptic filter configuration. The simulation results show more than 30% compactness compared with the conventional one. Then, the IWO technique is applied on the general filter structure to design a compact wideband harmonic suppression elliptic low pass filter. The designed filter has 3 dB cut off frequency at 3.2 GHz. Moreover, the optimized filter has area reduction about 47% and the harmonic suppression about $8.5f_0$. Finally, the optimized filter is fabricated. The measurement results are in good agreement with the simulation ones.

II. COMPACT SITL ELLIPTIC LPF

In this section, replacing method of m-segments step impedance transmission lines with n-segments SITLs by using the IWO technique is discussed. Then, this technique is applied in a seventh-order lowpass elliptic filter to miniaturize the overall filter size. This section is

organized as follows. At first, the formulation of an arbitrary n-segment SITLs is presented and equaled with m-segments SITLs to extract the problem equations. Then, the IWO is used to find the best responses which satisfy the equations with the most compact size. Finally, the proposed optimized SITLs method is used to compact a conventional seventh order elliptic LPF.

A. Formulation of an arbitrary SITL

Step impedance transmission line (SITL) is a non-uniform transmission line which can be used in the microstrip circuits to reduce its overall size, shift the spurious pass band to the higher frequency, and even to suppress the multiple spurious pass bands [23,24]. Figure 1 illustrates the non-uniform m-segments transmission lines with the electrical length and characteristic impedance of the θ_i and Z_i for the i-th segment which should be equal to non-uniform transmission lines with arbitrary n-segments at the design frequency, f_0. As depicted in Fig. 1, the compact SITL configuration is constructed from the n transmission line segment with the electrical length and characteristic impedance of the θ_i' and Z_i' for the i-th segment.
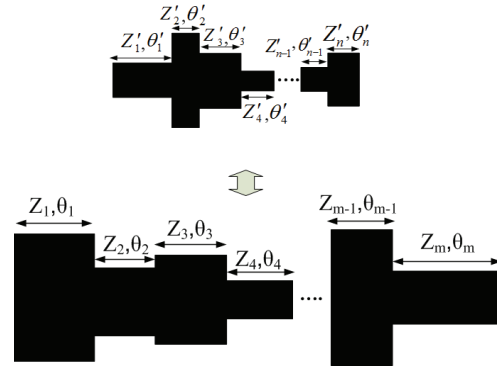
Fig. 1. Equivalent of m-segments step impedance transmission lines with arbitrary n-segments SITLs.

The ABCD matrix of the SITLs is obtained by multiplying the ABCD matrixes of all m or n-segments. Therefore, to equate these two mentioned structures, the ABCD matrixes of them should be equal with each other at the design frequency, f_0, as follows:

$$\left[ABCD^{mSITL} \right] =$$

$$\begin{bmatrix} \cos\theta_1 & jZ_1\sin\theta_1 \\ j\sin\theta_1/Z_1 & \cos\theta_1 \end{bmatrix} \times \begin{bmatrix} \cos\theta_2 & jZ_2\sin\theta_2 \\ j\sin\theta_2/Z_2 & \cos\theta_2 \end{bmatrix} \times$$

$$.... \times \begin{bmatrix} \cos\theta_m & jZ_m\sin\theta_m \\ j\sin\theta_m/Z_m & \cos\theta_m \end{bmatrix} = \begin{bmatrix} \cos\theta_1' & jZ_1'\sin\theta_1' \\ j\sin\theta_1'/Z_1' & \cos\theta_1' \end{bmatrix} , (1)$$

$$\times \begin{bmatrix} \cos\theta_2' & jZ_2'\sin\theta_2' \\ j\sin\theta_2'/Z_2' & \cos\theta_2' \end{bmatrix} \times .... \times \begin{bmatrix} \cos\theta_n' & jZ_n'\sin\theta_n' \\ j\sin\theta_n'/Z_n' & \cos\theta_n' \end{bmatrix}$$

$$= \left[ABCD_n^{nSITL} \right]$$

where "mSITL" and "nSITL" stand for m-step and n-step impedance transmission lines, respectively. As it can be seen, there are 3 equations with $2n$-unknown variables in (1) which are $Z_1' \sim Z_n'$ and $\theta_1' \sim \theta_n'$. Therefore, there are a lot of response groups which can satisfy the equations. Notice that since the structure is reciprocal, there are only three independent equations [1]. To achieve the most compact equivalent SITLs, the invasive weed optimization can be used which is described in the next section.

B. Invasive weed optimization

IWO is a simple numerical stochastic search algorithm that mimics the natural behavior of weed colonizing in the opportunity spaces for optimizing the function. However, it has been shown to be effective in converging to an optimal solution by employing basic properties such as seeding, growth, and competition in a weed colony. Some basic properties of the process are as follows [24]:

1) *Initialization:* A population of initial seeds (*N0*) is randomly being dispread over the search area.
2) *Reproduction*: The individuals, after growing, are allowed to reproduce new seeds linearly based on their fitness, the lowest and the highest fitness of the colony (all of plants). Note that maximum (*Smax*) and minimum (*Smin*) number of seeds are predefined parameters of the algorithm and fitted according to structure of problem. The procedure is demonstrated in Fig. 2 [25].
3) *Spatial Dispersal*: The generated seeds are being randomly spread with a normal distribution over the search area.
4) *Competitive Exclusion*: When the maximum number of plants in a colony is obtained (*Pmax*), each weed is allowed to produce seeds and scatter them according to its fitness. Then, new seeds with their parents are categorized together with respect to their fitness. Next, weeds with lower fitness are eliminated to reach the maximum determined population size in a colony.
5) *Termination Condition*: The whole process continues until the maximum number of iterations has been obtained, the plant with the best fitness is the closest one to the optimal solution [26].

In this section, the optimization goal is the equalization of the non-uniform m-segments transmission lines with a n-segment step transmission lines. For this purpose, the ABCD matrixes of m-segments transmission lines are compared with n-segment step transmission lines as described in Sec. II.A and construct the error function as:

$$error = \sqrt{e_A^2 + e_B^2 + e_C^2}, \qquad (2)$$

where

$$e_A = A^{mSITL} - A^{nSITL}, \qquad (3)$$

$$e_B = B^{mSITL} - B^{nSITL}, \qquad (4)$$

$$e_C = C^{mSITL} - C^{nSITL}. \qquad (5)$$

The goal of the design is to minimize the error in (2) with the smallest electrical length. The fitness function of this objective can be expressed as:

$$f = w_1 e - w_2 \theta_T, \qquad (6)$$

where θ_T is the total electrical length of the m-segments SITL and w_1 and w_2 are the weighting coefficients. By choosing the weighting coefficients, one can decide the importance of the m-segments SITL and n-segments SITL equalization against the compactness. In other words, choosing the $w_1 / w_2 > 1$ puts the goal of optimization on the compacting of the transmission line rather than the equalization of m-segments SITL with n-segments SITL. Notice that the equalization importance of m-segments SITL and n-segments SITL is related to the structure that the transmission line wants to be employed on it.
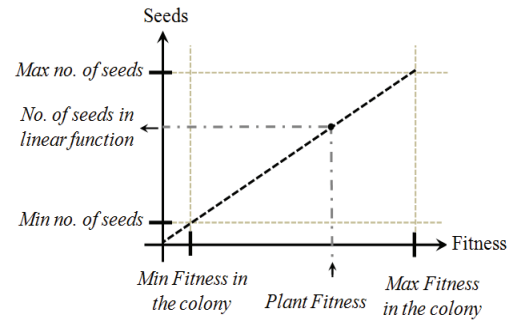
Fig. 2. Seed production procedure in a colony of weeds versus the fitness.

C. Simulation and results

In this section, a compact seventh-order lowpass elliptic filter is designed and simulated by using the n-SITLs. For this purpose, a conventional elliptic low pass filter is designed firstly. Then, the three 2-segments resonators of the conventional elliptic filter are replaced with the SITLs to validate the proposed technique in a practical miniaturization. An elliptic lowpass prototype filter with pass band ripple L_{Ar}=0.1 dB and a minimum stop band attenuation L_{As}=86.9778 dB at Ω_s=1.8182 for the Ω_c=1.8182 is chosen, where element values are g_0=g_8=1, g_1=1.141, g_2=1.369, g_2'=0.0479, g_3=1.9472, g_4=1.4033, g_4'=0.1408, g_5=1.8107, g_6=1.1316, g_6'=0.1408, g_7=0.9616 [1]. The microstrip LPF is designed to have a 3 dB cut off frequency at 3.2 GHz and source/load impedance Z_0=50 Ω. The microstrip realization is performed by using RT/Duroid 5880 substrate with the dielectric constant of 2.2 and a thickness of 20 mil. Also, all of the inductors are realized by using high-impedance lines with characteristic

impedance of ZOL=164 Ω, whereas the all capacitors are realized by using low-impedance lines with characteristic impedance Z_{OC}=19 Ω. Figure 3 (a) shows the layout of the designed LPF, which all the electrical lengths are denoted in Table 1. Notice that the superscript "P" stands for the "prototype" in the indexes. Also, the overall prototype LPF size is 25.2 mm × 10.3 mm. Moreover, as demonstrated in Fig. 3 (a), two shunt resonant branches are realized with two high and low impedance microstrip lines segments in the both sides of the filter structure.

Figure 3 (b) illustrates the elliptic LPF which its shunt resonators with two SITLs segments are replaced with 3 or 4 segments SITLs. Notice that here the superscript "O" is stand for the "optimized" in the indexes. The optimized values of the SITLs are computed by the IWO method based on the formula presented in Sec. II.B. Moreover, the IWO algorithm parameters are shown in Table 2. As exhibited in the Table 3, 13 Ω and 164 Ω are chosen as the lower and higher limitation of the impedances research area. Also, the 1 and 90 degrees are selected as the interval of the electrical length variables. This interval guarantees the global optimum finding of the problem. Since the run time of the algorithm is very low, the number of initial population and maximum number of plant population are selected as high as 80 to achieve more accuracy in the method. Moreover, by choosing σ_{final}=0.01, the error level can be decreased and more precise results may be achieved. The equivalents SITLs for each shunt resonant branch are obtained based on the resonance frequency of it. The resonance frequencies of the three shunt resonators of the designed prototype filter are f_{r1}=12.49 GHz, f_{r2}=7.19 GHz and f_{r3}=8.02 GHz. The final values of the optimized electrical lengths and characteristic impedances of the transmission lines at the design frequency, f_0, are specified in Table 3.

Figure 4 shows the comparison between full wave simulation of the prototype and optimized LPF done by commercial microwave circuit simulator Agilent Advance Design System (ADS). As it can be seen, there is a good agreement between the prototype and compact design filters. The physical size of the optimized LPF is 22×8.1 mm². It implies that the IWO technique decreases the circuit size of the filter about 30%. Although this size reduction is good, it is possible to achieve more compactness. We discussed about it in the next section.

(a)

(b)

Fig. 3. (a) Prototype elliptic LPF, and (b) elliptic LPF with SITL.

Table 2: IWO parameters

Symbols	Quantity	Value
N	Number of initial population	80
$iter_{max}$	Maximum number of iterations	72
D	Problem dimension	6, 8
P_{max}	Maximum number of plant population	80
S_{max}	Maximum number of seeds	10
S_{min}	Minimum number of seeds	2
n	Nonlinear modulation index	3
$\sigma_{initial}$	Initial value of standard deviation	1
σ_{final}	Final value of standard deviation	0.01
Z_i	Impedance of the lines	19<Z_i<164
θ_i	Electrical length of the lines	0.5<θ_i<190

Table 3: Values of the proposed compact SITL LPF

Parameter	Z_1^O	Z_2^O	Z_3^O	Z_4^O	Z_5^O
Value (Ω)	130.989	17.003	55.5374	46.6154	125.957
Parameter	Z_6^O	Z_7^O	Z_8^O	Z_9^O	Z_{10}^O
Value (Ω)	13.0077	133.241	163.929	13.0665	56.104
Parameter	θ_1^O	θ_2^O	θ_3^O	θ_4^O	θ_5^O
Value (rad)	0.1751	0.845	0.0821	0.1634	0.0411
Parameter	θ_6^O	θ_7^O	θ_8^O	θ_9^O	θ_{10}^O
Value (rad)	0.6982	0.0707	0.2358	0.344	0.0642

Table 1: Values of prototype LPF electrical lengths

Parameter	θ_1^P	θ_2^P	θ_3^P	θ_4^P	θ_5^P
Value (rad)	0.355	0.113	1.105	0.632	0.095
Parameter	θ_6^P	θ_7^P	θ_8^P	θ_9^P	θ_{10}^P
Value (rad)	1.325	0.589	0.215	0.565	0.303
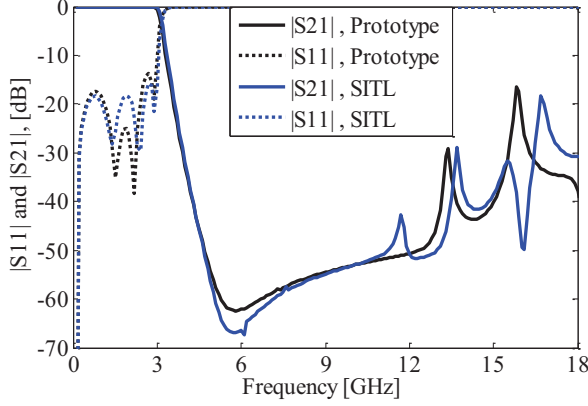
Fig. 4. Full wave simulation results of the prototype LPF and SITL LPF.

Fig. 5. Finding the input impedance of the shunt SITLs resonators.

III. OPTIMZATION OF WIDEBAND HARMONIC SUPPRESSION ELLIPTIC LOW PASS FILTER

In this section, we aim to achieve much more compactness and wideband harmonic suppression in the elliptic low pass filter by using IWO technique. For this purpose, first the ABCD matrix of the general compact filter shown in Fig. 3 (b) is extracted. Then the scattering parameters of it are calculated by using the ABCD matrix technique.

A. Formulation of the ABCD matrix of the general filter structure

From the ABCD matrix point of view, the filter layout in Fig. 3 (b) is composed of 4 cascaded high impedance transmission lines with 3 shunt impedance between them which its circuit is shown in Fig. 5. In more details, the resonant branches can be considered as shunt impedance which is located between two transmission line segments. To find these shunt impedances, the end open transmission line segment of them can be considered as the load of the previous line as depicted in Fig. 5. As an example, this calculation is done for the first shunt resonator of the filter. The impedance of an open end step can be calculated by:

$$Z_{in1}^{SH1} = \frac{Z_3^F}{j \tan \theta_3^F}, \tag{7}$$

where Z_3^F and θ_3^F are the characteristic impedance and the electrical length of the open end transmission line, respectively. Also the whole impedance of the each open end step transmission line with previous segment can be calculated by:

$$Z_{in2}^{SH2} = Z_2^F \frac{Z_{in1}^{SH1} + jZ_2^F \tan \theta_2^F}{Z_2^F + jZ_{in1}^{SH1} \tan \theta_2^F}, \tag{8}$$

where Z_2^F and θ_2^F are the characteristic impedance and the electrical length of the second segment, respectively.

Similarly, the other transmission line steps can be considered as the load impedance for previous one. Therefore, the impedance of the 3 sequential steps can be calculated as follows:

$$Z_{in3}^{SH3} = Z_3^F \frac{Z_{in2}^{SH2} + jZ_3^F \tan \theta_3^F}{Z_3^F + jZ_{in2}^{SH2} \tan \theta_3^F}, \tag{9}$$

where Z_3^F and θ_3^F are the characteristic impedance and the electrical length of the third transmission line. Notice that, the first and the last shunt resonators are placed on the both sides of the filter layout and therefore we consider them divided by two in the circuit and formulation. This process is iterated to achieve all the input impedance of the shunt SITLs resonators. Then each of these resonator branches is considered between the cascaded transmissions lines with the ABCD matrix as follows [1]:

$$\begin{bmatrix} A & B \\ C & D \end{bmatrix} = \begin{bmatrix} 1 & 0 \\ 1/Z_{ini}^{SH} & 1 \end{bmatrix}. \tag{10}$$

Notice that, to decrease the number of the variables, the filter configuration is considered as a symmetrical structure. Therefore, we have two different shunt resonators, the first one with 3 segments (6 variables) and the middle one with the 4 segments (8 variables), and two different horizontal line (4 variables). Now, the ABCD matrix of the general structure can be obtained by multiplying the ABCD matrix of all cascaded parts which are computed as:

$$ABCD^{LPF} = \begin{bmatrix} \cos\theta_8^F & jZ_8^F \sin\theta_8^F \\ \dfrac{j \sin\theta_8^F}{Z_8^F} & \cos\theta_8^F \end{bmatrix} \times \begin{bmatrix} 1 & 0 \\ \dfrac{2}{Z_{in1}^{SH3}} & 1 \end{bmatrix} \times$$
$$\times \begin{bmatrix} \cos\theta_9^F & jZ_9^F \sin\theta_9^F \\ \dfrac{j \sin\theta_9^F}{Z_9^F} & \cos\theta_9^F \end{bmatrix} \times \begin{bmatrix} 1 & 0 \\ \dfrac{1}{Z_{in2}^{SH4}} & 1 \end{bmatrix} \times$$
$$\times \begin{bmatrix} \cos\theta_9^F & jZ_9^F \sin\theta_9^F \\ \dfrac{j \sin\theta_9^F}{Z_9^F} & \cos\theta_9^F \end{bmatrix} \times \begin{bmatrix} 1 & 0 \\ \dfrac{2}{Z_{in1}^{SH3}} & 1 \end{bmatrix} \times$$
$$\times \begin{bmatrix} \cos\theta_8^F & jZ_8^F \sin\theta_8^F \\ \dfrac{j \sin\theta_8^F}{Z_8^F} & \cos\theta_8^F \end{bmatrix} \tag{11}$$

where Z_8^F, Z_9^F and θ_8^F, θ_9^F are the characteristic impedances and the electrical lengths of the 4 cascaded high impedance transmission lines and $Z_{in1}^{SH3}, Z_{in2}^{SH4}$ are the input impedance of the series-resonant branches. According to (12) and (13), the S-Parameters of the filter are given in the terms of SITLs electrical lengths and characteristic impedances as follows [1]:

$$S_{21} = \frac{2}{A + B/Z_0 + CZ_0 + D}, \quad (12)$$

$$S_{11} = \frac{A + B/Z_0 - CZ_0 - D}{A + B/Z_0 + CZ_0 + D}. \quad (13)$$

Since the electrical length of a transmission line changes versus frequency linearly, the electrical length θ_t in a different frequency (f_t), can be calculated as:

$$\theta_t = \theta_0 \frac{f_t}{f_{3dB}}, \quad (14)$$

where θ_0 is the electrical length in the 3 dB cut off frequency (f_{3dB}). This relation can be used to achieve the ABCD matrix of the filter versus frequencies.

B. IWO description

The IWO algorithm has been explained in the previous section. Here we want to use the IWO to achieve a compact and high order suppression filter presented in Sec. III.A. For this purpose, the scattering matrix of the general proposed filter structure introduced in the previous section should compare with the desired low pass filter response. The desired lowpass filter response shown in Fig. 6 with blue color. As it can be seen, the desired response has very high order suppression. The IWO tries to adapt the response of the general filter structure with the desired one. In other words, the IWO should minimize the error function of this adaption which can be expressed as:

$$error = \sqrt{\left(\left|S_{11}^{design}\right| - \left|S_{11}^{desired}\right|\right)^2 + \left(\left|S_{12}^{design}\right| - \left|S_{11}^{desired}\right|\right)^2}, \quad (15)$$

where the $|S_{11}|$ and $|S_{12}|$ are the vector of the sampled data. Notice that the -20 dB in $f < f_{3dB}$ and -15 dB in $f > f_{3dB}$ in Fig. 6 are chosen as thresholds for $|S_{11}|$ and $|S_{12}|$, respectively. In other words, $|S_{11}|$ and $|S_{12}|$ below these values in the corresponding regions don't make any change in the error value. The IWO parameters are tabulated in Table 4.

The final results of the optimized electrical lengths and characteristic impedances for the compact and wideband suppression SITL LPF are tabulated in Table 5. The full wave simulation results of the final optimized SITL LPF are demonstrated in the Fig. 6 with black color. As it can be seen, the simulation results of the optimized SITL LPF has good compatibility with the desired response in the pass band and stop band areas.

Table 4: IWO parameters

Symbols	Quantity	Value
N	Number of initial population	80
$iter_{max}$	Maximum number of iterations	72
D	Problem dimension	18
P_{max}	Maximum number of plant population	80
S_{max}	Maximum number of seeds	10
S_{min}	Minimum number of seeds	2
n	Nonlinear modulation index	3
$\sigma_{initial}$	Initial value of standard deviation	1
σ_{final}	Final value of standard deviation	0.01
Z_i	Impedance of the lines, Ohm	$19<Z_i<164$
θ_i	Electrical length of the lines, degree	$0.5<\theta_i<90$
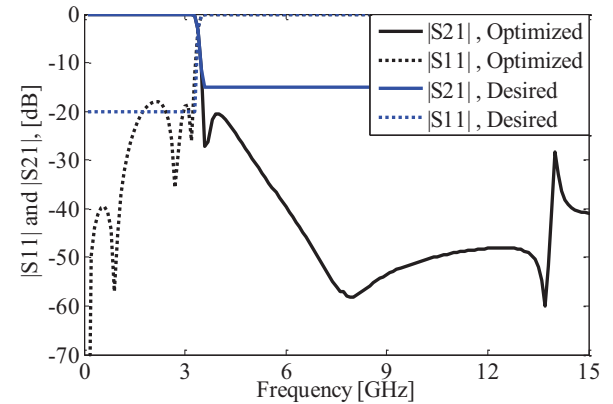
Fig. 6. The desired response for elliptic low pass filter and full wave simulation result of the optimized SITL LPF.

Table 5: Values of wideband SITL LPF

Parameter	Z_1^F	Z_2^F	Z_3^F	Z_4^F	Z_5^F
Value (Ω)	164.004	62.1178	19.6982	164.004	58.9093
Parameter	Z_6^F	Z_7^F	Z_8^F	Z_9^F	-
Value (Ω)	27.0067	58.9093	164.004	164.004	-
Parameter	θ_1^F	θ_2^F	θ_3^F	θ_4^F	θ_5^F
Value (rad)	0.026	0.01819	0.25759	0.59803	0.33738
Parameter	θ_6^F	θ_7^F	θ_8^F	θ_9^F	-
Value (rad)	0.11323	0.09118	0.25135	0.31202	-

C. Fabrication and measurement

Figure 7 illustrates the fabricated compact and wideband suppression elliptic optimized LPF. As it can be seen, the meandering techniques have been applied to the middle high-impedance section of the proposed LPF to reduce the overall circuit size. The optimized SITL LPF is fabricated on RT/Duroid 5880 substrate with the relative dielectric constant of 2.2, thickness of 20 mil and loss tangent of 0.0009. The measurements were performed by the HP 8757A network analyzer. The EM simulation and measured S-Parameters of the proposed LPF are shown in Fig. 8 (a), which indicates a good agreement between them. The final physical size of the designed LPF is 13.3 mm × 10.3 mm, which is 47% less than the prototype LPF. The maximum insertion loss is only 0.1dB in the passband and the rejection band extends from 3.34 GHz to 27 GHz with the attenuation level better than 15 dB, whereas the prototype LPF rejection band is only 12.8 GHz. In other words, the proposed filter has about 23.66 GHz reject bandwidth compared with the traditional LPF which has 12 GHz reject bandwidth. The transition band of the proposed LPF is only 0.16 GHz from 3.2 GHz to 3.36 GHz with corresponding attenuation levels of -3 dB and -20 dB, respectively while the prototype LPF transition band is 0.47 GHz. In other words, the optimized filter has a sharp roll off response. Also, the insertion loss is less than 0.1 dB from DC to 3.14 GHz (98.12% of the passband region). The group delay of the designed LPF in the pass band region is shown in Fig. 8 (b). It can be seen that the maximum variation is less than 0.85 ns which is negligible.
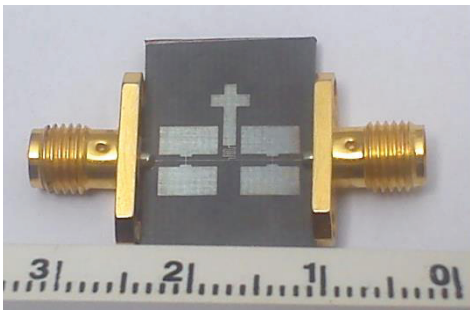
Fig. 7. Fabricated wide band suppression elliptic LPF.

The performance of the proposed LPF is compared with some other published works in Table 6, where f_c is 3 dB cut off frequency and ζ is the roll-off rate that is used to evaluate the sharpness of transition band, which is defined as [27]:

$$\xi = \frac{\alpha_{max} - \alpha_{min}}{f_s - f_c}, \qquad (16)$$

where α_{max} is the -20 dB attenuation point, α_{min} is the -3 dB attenuation point, f_s is the -20 dB stopband frequency

and f_c is the -3 dB cutoff frequency. The relative stopband bandwidth (RSB) is calculated by [28]:

$$RSB = \frac{stopband(-20dB)}{stopband\ center\ frequency}. \qquad (17)$$

The suppression factor (SF) is dependent upon the stopband suppression. A higher suppression degree in the stopband leads to a greater SF. For example, if the stopband bandwidth is calculated under -40 dB limitation, then the SF is considered as 4. Also, the normalized circuit size (NCS) is formulated as [27]:

$$NCS = \frac{physical\ size\ (length \times width)}{\lambda_g^2}. \qquad (18)$$

This is used to obtain the degree of miniaturization of a filter, where λg is the guided wavelength at -3 dB cutoff frequency. The architecture factor (AF) can be identified as the circuit complexity factor, which is signed as 1 when the design is 2D and as 2 when the design is 3D. Eventually, the figure-of-merit (FOM) of a filter is defined as [28]:

$$FOM = \frac{\xi \times RSB \times SF}{NCS \times AF}. \qquad (19)$$
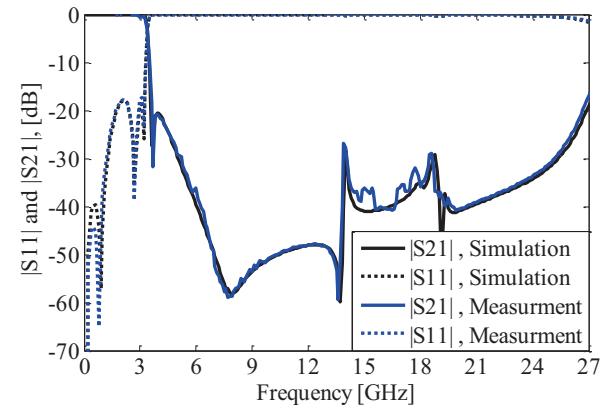
(a)
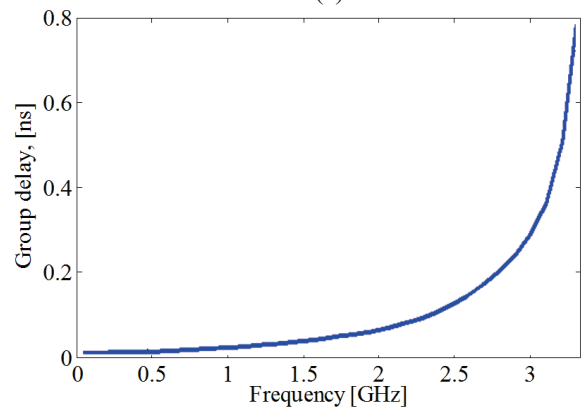
(b)

Fig. 8. (a) EM simulation and measurement results of the fabricated filter, and (b) the group delay of the fabricated filter.

Table 6: Performance comparison of the proposed LPF with other published works

Ref.	f_c (GHz)	ζ	RSB	NCS	FOM
[16]	2.95	12.1	1.28	0.093	500
[17]	1.87	130	1.16	0.0827	3775
[18]	5.8	23	1.45	0.07	1100
[19]	1	130	0.98	0.0042	6010
[20]	3.12	35.7	1.351	0.0508	1900
[21]	2	28.3	1.3	0.0128	5754
[22]	2.5	27.4	0.6	0.0148	2518
This Work	3.2	106	1.54	0.0295	12500

According to Table 6, the proposed lowpass filter has good compactness and excellent RSB as well as higher roll-off rate and FOM among the published works.

IV. CONCLUSION

The invasive weed optimization was applied on the non-uniform *m*-segments transmission line to compact it, by replacing with *n*-segments step impedance transmission lines. Then the proposed method was implied on transmission lines of a seventh-order lowpass elliptic filter to reduce the circuit size. The results showed about 30% compactness. In the next step, the IWO technique was used to design a wideband harmonic suppression elliptic low pass filter based on the extracted layout in the previous section. The proposed filter was simulated, fabricated and measured. The measurement results were in good agreement with the simulation results and showed the stop band bandwidth more than 8.5 f_0 and about 47% compactness. Also, this technique can be use in the design of other microwave devices.

REFERENCES

[1] J. S. Hong and M. J. Lancaster, *Microstrip Filters for RF/Microwave Applications*, Wiley, New York, 2001.

[2] G. D. Vendelin, A. M. Pavio, and U. L. Rohde, *Microwave Circuit Design Using Linear and Nonlinear Techniques*, 2nd ed., Wiley, New Jersey, 2005.

[3] D. M. Pozar, *Microwave Engineering*, 3rd ed., Wiley, New York, 2005.

[4] P. P. Roberts and G. E. Town, "Design of microwave filters by inverse scattering," *IEEE Trans. Micro. Theory and Tech*., vol. 43, no. 4, pp. 739-743, Apr. 1995.

[5] M. L. Roy, A. Perennec, S. Toutain, and C. Calvez, "The continuously varying transmission-line technique – application to filter design," *IEEE Trans. Micro. Theory and Tech*., vol. 47, no. 9, pp. 1680-1687, Sep. 1999.

[6] S. Y. Shi, W. J. Feng, W. Q. Che, and Q. Xue, "Novel miniaturization method for wideband filter design with enhanced upper stopband," *IEEE Microwave Theory and Techniques*, vol. 61, no. 2, pp. 817-826, Feb. 2013.

[7] L.-H. Hsieh and K. Chang, "Compact elliptic-function low-pass filters using microstrip stepped-impedance hairpin resonators," *IEEE Trans. Microw. Theory Tech*., vol. 51, no. 1, pp. 193-199, Jan. 2003.

[8] A. S. Mohra, "Compact lowpass filter with sharp transition using defected ground structure," *Prog. Electromagnetic Res. Lett*., vol. 8, pp. 83-92, 2009.

[9] J.-I. Park, C.-S. Kim, J. Kim, and J.-S. Park, "Photonic bandgap structure for low-pass filter of wide stopband," vol. 10, no. 1, pp. 13-15, Jan. 2000.

[10] H. Liu, Z. Li, X. Sun, and J. Mao, "A novel photonic band-gap microstrip structures for low-pass filters of wide stop-band," vol. 37, no. 6, pp. 470-472, Jun. 2003.

[11] A. Ali. and Z. Hu, "Negative permittivity meta-material microstrip binomial low-pass filter with sharper cut-off and reduced size," *Microwaves, Antennas & Propagation, IET*, vol. 2, no. 1, pp. 15-18, Feb. 2008.

[12] C. Miao, J. Xu, and W. Wu, "Compact wide stopband quasi-elliptic function lowpass filter using quasi-lumped elements," *Progress In Electromagnetics Research Letters*, vol. 39, pp. 151-159, 2013.

[13] L. Li, Z.-F. Li, and J.-F. Mao, "Compact lowpass filters with sharp and expanded stopband using stepped impedance hairpin units," *IEEE Microw. Wireless Compon. Lett*., vol. 20, no. 6, pp. 310-312, Jun. 2010.

[14] I. Rumsey, M. Piket-May, and P. K.Kelly, "Photonic bandgap structure used as filters in microstrip circuits," *IEEE Microw. Guided Wave Lett*., vol. 8, no. 10, pp. 336-338, Oct. 1998.

[15] D. Ahn, J. S. Park, C. S. Kim, J. Kim, Y. Qian, and T. Itoh, "A design of the low-pass filter using the novel microstrip defected ground structure," *IEEE Trans. Microw. Theory Tech*., vol. 49, no. 1, pp. 86-93, Jan. 2001.

[16] M. Challal, A. Boutejdar, M. Dehmas, A. Azrar, and A. Omar, "Compact microstrip low-pass filter design with ultra-wide reject band using a novel quarter-circle DGS shape," *ACES Journal*, vol. 27, no. 10, pp. 808-815, Oct. 2012.

[17] J.-M. Zhou, L.-H. Zhou, H. Tang, Y.-J. Yang, J.-X. Chen, and Z.-H. Bao, "Novel compact microstrip lowpass filters with wide stopband using defected ground structure," *J. of Electromagn. Waves and Appl*., vol. 25, pp. 1009-1019, 2011.

[18] M. Hayati and H. Abbasi, "Compact microstrip stepped-impedance lowpass filter with wide stopband using SICMRC," *IEICE Electronics Express*, vol. 9, no. 22, pp. 1742-1747, Nov. 2012.

[19] M. Durán-Sindreu, J. Bonache, and F. Martín, "Compact elliptic-function coplanar waveguide low-pass filters using backside metallic patterns," *IEEE Microwave and Wireless Components Letters*, vol. 20, no. 11, pp. 1507-1509, Nov. 2010.

[20] M. Hayati, A. Sheikhi, and A. Lotfi, "Compact lowpass filter with wide stopband using modified semi-elliptic and semi-circular microstrip patch resonator," *Electronics Letters*, vol. 46, no. 22, pp. 601-603, Oct. 2010.

[21] J.-Y. Wu, Y.-H. Tseng, and W.-H. Tu, "Design of compact lowpass filter with ultra-wide stopband using thin slots," *Progress In Electromagnetics Research C*, vol. 31, pp. 137-151, Jul. 2012.

[22] M. H. Yang, J. Xu, Q. Zhao, L. Peng, and G. P. Li, "Compact, broad-stopband lowpass filters using sirs-loaded circular hairpin resonators," *Progress In Electromagnetics Research*, 102, 95-106, 2010.

[23] H. R. Khakzad, S. H. Sedighy, and M. K. Amirhosseini, "Design of compact SITLs low pass filter by using invasive weed optimization (IWO) technique," *Applied Computational Electromagnetics Society (ACES) Journal*, vol. 28, no. 3, pp. 228-233, Mar. 2013.

[24] S. H. Sedighy, A. R. Mallahzadeh, M. Soleimani, and J. Rashed-Mohassel, "Optimization of printed Yagi antenna using invasive weed optimization (IWO)," *IEEE Antennas and Wireless Propagation Letters*, vol. 9, pp. 1275-1278, Jan. 2010.

[25] A. R. Mehrabian and C. Lucas, "A novel numerical optimization algorithm inspired from invasive weed colonization," *Ecological Informatics*, vol. 1, pp. 355-366, 2006.

[26] M. R. Ghalenoei, H. Hajimirsadeghi, and C. Lucas, "Discrete invasive weed optimization algorithm: application to cooperative multiple task assignment of UAVs, *Presented at Joint 48th IEEE Conference on Decision and Control and 28th Chinese Control Conference Shanghai*, available, Dec. 2009.

[27] J. Wang, L.-J. Xu, S. Zhao, Y.-X. Guo, and W. Wu, "Compact quasi-elliptic microstrip lowpass filter with wide stopband," *Electronics Letters*, vol. 46, no. 20, pp. 1384-1385, Sep. 2010.

[28] J.-K. Lee, D.-H. Lee, and Y.-S. Kim, "A compact lowpass filter with double step impedance shunt stub and defected ground structure for wideband rejection," *Microwave Opt. Technol. Lett.*, vol. 52, pp. 132-134, Jan. 2010.

Multi-Objective Optimal Design of Surface-Mounted Permanent Magnet Motor Using NSGA-II

S. Mendaci [1], H. Allag [2], and M. R. Mekideche [2]

[1] Laboratory of Automatics and Informatics of Guelma-LAIG
University of Guelma, Guelma, 24000, Algeria
mendaci.sofiane@yahoo.fr

[2] Department of Electrical Engineering
University of Jijel, 18000, Algeria
allag_hic@yahoo.fr, mek_moh@yahoo.fr

Abstract ─ This paper presents a highly structured procedure for multi-objective optimal design of radial surface Permanent-Magnet Synchronous Motor (PMSM). Firstly, a detailed analytical model based on the resolution of Maxwell's equations using the separation of variables method is presented. From the same model, analytical expressions of four constraint functions dedicated for the optimal design of the PMSM are developed. These constraints are: electromagnetic torque, back electromotive force (back-EMF), flux density saturation in stator/rotor yoke and saturation in stator tooth. Then, the Non-dominated Sorting Genetic Algorithm-II (NSGA-II) is employed to optimize the multi-objective problem formed by two objective functions (weight and power loss of the motor) and different constraints. Finally, the finite element method is used to validate the designed 30 kW PMSM.

Index Terms ─ Analytical model, finite elements, NSGA-II, optimal design, permanent magnet synchronous motor.

I. INTRODUCTION

In recent years, the manufacturers of electrical machines have shown a growing interest for permanent magnet synchronous machines (PMSMs). This interest is mainly due to the high efficiency, high reliability, high power density, small size and decreasing cost of magnets. Different topologies of PM machines are available; e.g., radial flux machines, axial flux machines and transversal flux machines [1]. However, the performances of PMSMs are greatly depends on their optimal design and control.

The design and dimensioning of an electromechanical actuator calls into play a great number of parameters which are subject to the laws which describe physical phenomena on the one hand and to the specifications of the schedule of conditions on the other hand. In the practice, many electromagnetic optimization problems are solved by means of highly accurate models (e.g., finite element model) with different optimization algorithms. However, these approaches are computationally expensive, especially when stochastic optimization algorithms are used [2]. As an alternative, very simplified analytical models are useful tools for first evaluation and design optimization. They are proved fast, but not very accurate [3].

In this paper, the authors attempt to provide helpful tools for the fast analysis and multi-objective optimal design of PMSMs. Prior to the optimization, an analytical model, sufficiently accurate and fast, based on the resolution of Maxwell's equations using the separation of variables method is presented. Then, the design processes was formulated as a multi-objective optimization problem and solved by NSGA-II method. Finally, validity of the proposed methodology is confirmed through the finite element analysis of the designed 30 kW PMSM.

II. DEVELOPMENT OF THE ANALYTICAL MODEL

The general configuration of a slotted surface-mounted permanent magnet motor considered in the present work is shown in Fig. 1.

The analytical method used in this paper is based on analysis of 2-D model in polar coordinates. The following assumptions are made [4-7]:
- The stator and rotor cores are assumed to be infinitely permeable.
- End effect and saturation are neglected.
- Permanent magnets have a linear demagnetization characteristic.
- Eddy current effects are neglected (no eddy current loss in the magnets or armature windings).

- Stator current source is represented by a current sheet distributed over the stator inner radius.
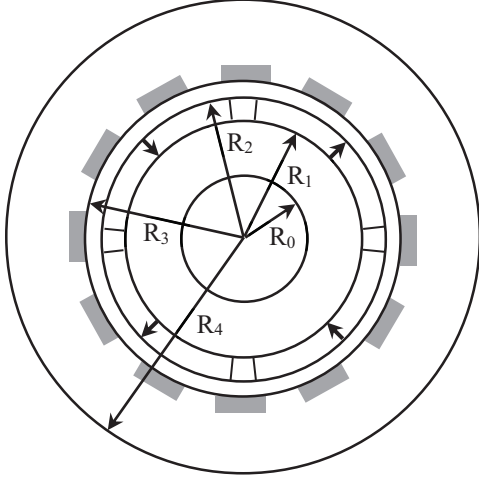
Fig. 1. Cross sectional view of the studied PMSM.

In the above considerations, the calculation region can be classified into two parts: PMs (Region I), and air-gap (Region II). The flux density and field intensity are expressed as:

In Region I: $\vec{B} = \mu_0 \vec{H}.$ (1)

In Region II: $\vec{B} = \mu_0 \mu_r \vec{H} + \mu_0 \vec{M},$ (2)

where μ_r is the relative recoil permeability, $\vec{M}$ is the magnetization vector of permanent magnets. The direction of $\vec{M}$ depends on the orientation and magnetization of permanent magnets. In polar coordinates, the magnetization vector $\vec{M}$ is expressed as:

$$\vec{M} = M_r \vec{e}_r + M_\theta \vec{e}_\theta.$$ (3)

The governing field equations are, in terms of the Coulomb gauge, $\nabla \vec{A} = 0$, as follows:

In Region I: $\nabla^2 \vec{A} = -\mu_0 \nabla \times \vec{M}.$ (4)

In Region II: $\nabla^2 \vec{A} = 0.$ (5)

$\vec{A}$ (the magnetic vector potential) only has A_z component which is independent of z (infinitely long machine in axial direction).

By using the method of separating variables, the general solution of (4) and (5) can be expressed as:

$$A_z^I = \sum_{g=-\infty}^{+\infty} \left(C_1 r^{gp} + C_2 r^{-gp} + A_p \right) e^{jgp\theta},$$ (6)

$$A_z^{II} = \sum_{g=-\infty}^{+\infty} \left(C_3 r^{gp} + C_4 r^{-gp} \right) e^{jgp\theta},$$ (7)

where A_p is the particular solution of (4) for the permanent magnets region, given by:

$$A_p(r) = \begin{cases} \mu_o \dfrac{jgp M_{r,g} - M_{\theta,g}}{1-(gp)^2} r & \text{if } gp \neq 1 \\ \mu_o \dfrac{jgp M_{r,g} - M_{\theta,g}}{2} r \ln(r) & \text{if } gp = 1 \end{cases},$$ (8)

where $M_{r,g}$ and $M_{\theta,g}$ are the complex Fourier coefficients of the two components $M_r(\theta)$ and $M_\theta(\theta)$ of the magnetization vector $\vec{M}$.

$$M_r(\theta) = \sum_{g=-\infty}^{+\infty} M_{r,g} e^{jgp(\theta - \Omega t)}.$$ (9)

$$M_\theta(\theta) = \sum_{g=-\infty}^{+\infty} M_{\theta,g} e^{jgp(\theta - \Omega t)},$$ (10)

where p is the pole pair number and Ω is the rotor speed.

In (6) and (7), C_1, C_2, C_3, and C_4 are constants to be determined by applying the boundary conditions on the interface between rotor and PMs (i.e., $r=R_1$), PMs and air gap (i.e., $r=R_2$) and between the air-gap and stator (i.e., $r=R_3$). These conditions can be defined as:

$$\begin{cases} H_\theta^I(R_1, \theta) = 0. \\ H_\theta^I(R_2, \theta) = H_\theta^{II}(R_2, \theta). \\ B_r^I(R_2, \theta) = B_r^{II}(R_2, \theta). \\ H_\theta^{II}(R_3, \theta) = -\mu_0 J. \end{cases}$$ (11)

J is the total current density vector given by:

$$J(\theta, t) = \sum_{n=1}^{m} J_n = \sum_{n=1}^{m} I_n C_n,$$ (12)

where m is the number of phase windings and J_n is the current density for phase n given by the product of the conductor density $C_n(\theta)$ and the stator current I_n, with:

$$C_n(\theta) = \sum_{g=-\infty}^{+\infty} \frac{S_g}{2j} e^{jgp\left(\theta - \frac{(n-1)}{p}\frac{2\pi}{m}\right)}.$$ (13)

The Fourier coefficient S_g is determined by taking into account the windings characteristics. In the case of diametric winding, S_g is given by:

$$S_g = 2\gamma \sum_{k=1}^{\frac{N_{spp}}{2}} \cos\left((2k-1)gp\frac{P_t}{2}\right). \quad N_{spp} \text{ is even}$$ (14)

$$S_g = \gamma\left(1 + 2\sum_{k=1}^{\frac{N_{spp}-1}{2}} \cos(kgpP_t)\right), \quad N_{spp} \text{ is odd}$$ (15)

where N_{spp} is the number of slots per pole and per phase, P_t is the stator tooth-pitch and γ given by:

$$\gamma = \frac{4N_c}{R_3 b_s} \sin\left(g\frac{\pi}{2}\right) \sin\left(gp\frac{b_s}{2}\right),$$ (16)

where N_c is the number of conductors in one slot and b_s is the slot width.

In the general case, the total stator current density can be written as a Fourier series:

$$J(\theta,t) = \sum_{g=-\infty}^{+\infty} J_g(t)e^{jgp\theta}, \tag{17}$$

where J_g is the complex Fourier coefficient given by:

$$J_g(t) = \frac{S_g}{2j} \sum_{n=1}^{m} I_n(t)e^{-jg(n-1)\frac{2\pi}{m}}. \tag{18}$$

The resolution of the above system (11) gives the constants C_1, C_2, C_3, and C_4. They can be expressed as:

$$C_1 = \mu_0 \left(P_2 M_{r,g} + P_3 M_{\theta,g}\right)e^{-j(gp\Omega t - \frac{\pi}{2})} \\ + P_1 S_g \sum_{n=1}^{m} I_n(t)e^{-j(g(n-1)\frac{2\pi}{m} + \frac{\pi}{2})}. \tag{19}$$

$$C_2 = \mu_0 \left(D_2 M_{r,g} + D_3 M_{\theta,g}\right)e^{-j(gp\Omega t - \frac{\pi}{2})} \\ + D_1 S_g \sum_{n=1}^{m} I_n(t)e^{-j(g(n-1)\frac{2\pi}{m} + \frac{\pi}{2})}. \tag{20}$$

$$C_3 = \mu_0 \left(E_2 M_{r,g} + E_3 M_{\theta,g}\right)e^{-j(gp\Omega t - \frac{\pi}{2})} \\ + E_1 S_g \sum_{n=1}^{m} I_n(t)e^{-j(g(n-1)\frac{2\pi}{m} + \frac{\pi}{2})}. \tag{21}$$

$$C_4 = \mu_0 \left(F_2 M_{r,g} + F_3 M_{\theta,g}\right)e^{-j(gp\Omega t - \frac{\pi}{2})} \\ + E_1 S_g \sum_{n=1}^{m} I_n(t)e^{-j(g(n-1)\frac{2\pi}{m} + \frac{\pi}{2})}, \tag{22}$$

where

$$P_1 = \mu_0 R_3^{1-gp} L_1. \tag{23}$$

$$P_2 = gp\frac{L_1}{2}\left[\frac{df(R_1)}{dr}L_2 + \frac{df(R_2)}{dr}L_3 + f(R_2)L_4\right]. \tag{24}$$

$$P_3 = \frac{L_1}{2}\left[\left(\frac{df(R_1)}{dr}-1\right)L_2 + \left(\frac{df(R_2)}{dr}-1\right)L_3 + f(R_2)L_4\right]. \tag{25}$$

$$D_1 = P_1 R_1^{2gp}. \tag{26}$$

$$D_2 = P_2 R_1^{2gp} + \frac{df(R_1)}{dr}\frac{R_1^{1+gp}}{2}. \tag{27}$$

$$D_3 = P_3 R_1^{2gp} + \left(\frac{df(R_1)}{dr}-1\right)\frac{R_1^{1+gp}}{2gp}. \tag{28}$$

$$E_1 = P_1. \tag{29}$$

$$E_2 = P_2 + \frac{gpR_2^{-gp}}{4}f(R_2) + \frac{df(R_2)}{dr}\frac{R_2^{1-gp}}{4}. \tag{30}$$

$$E_3 = P_3 + \frac{R_2^{-gp}}{4}f(R_2) + \left(\frac{df(R_2)}{dr}-1\right)\frac{R_2^{1-gp}}{4gp}. \tag{31}$$

$$F_1 = D_1. \tag{32}$$

$$F_2 = D_2 + \frac{gpR_2^{gp}}{4}f(R_2) - \frac{df(R_2)}{dr}\frac{R_2^{1+gp}}{4}. \tag{33}$$

$$F_3 = D_3 + \frac{R_2^{gp}}{4}f(R_2) - \left(\frac{df(R_2)}{dr}-1\right)\frac{R_2^{1+gp}}{4gp}, \tag{34}$$

with

$$L_1 = \frac{1}{2gp\left(1 - R_1^{2gp}R_3^{-2gp}\right)}. \tag{35}$$

$$L_2 = 2R_1^{1+gp}R_3^{-2gp}. \tag{36}$$

$$L_3 = -\left(R_2^{1-gp} + R_2^{1+gp}R_3^{-2gp}\right). \tag{37}$$

$$L_4 = gp\left(R_2^{gp}R_3^{-2gp} - R_2^{-gp}\right). \tag{38}$$

$$f(r) = \begin{cases} \dfrac{r}{1-(gp)^2} & \text{if } gp \neq 1 \\[2mm] \dfrac{r}{2}\ln(r) & \text{if } gp = 1 \end{cases}. \tag{39}$$

Hence, the magnetic vector potential is completely defined in the two regions by (6) and (7). Therefore, the flux density in the air-gap and PMs is given by:

$$B_r^i(r,\theta,t) = \\ 2\sum_{g=1}^{\infty}\left[\begin{array}{l} \mu_0\left(N_{2,r}^i M_{r,g} + N_{3,r}^i M_{\theta,g}\right)\cos(gp(\Omega t - \theta)) \\ -N_{1,r}^i S_g \sum_{n=1}^{m} I_n(t)\cos\left(g\left(p\theta - (n-1)\frac{2\pi}{m}\right)\right) \end{array}\right]. \tag{40}$$

$$B_\theta^i(r,\theta,t) = \\ 2\sum_{g=1}^{\infty}\left[\begin{array}{l} \mu_0\left(T_{2,r}^i M_{r,g} + T_{3,r}^i M_{\theta,g}\right)\sin(gp(\Omega t - \theta)) \\ +T_{1,r}^i S_g \sum_{n=1}^{m} I_n(t)\sin\left(g\left(p\theta - (n-1)\frac{2\pi}{m}\right)\right) \end{array}\right], \tag{41}$$

where $i=I,II$ design the concerned region.

$$N_{l,r}^i = \frac{-gp}{r}P_{l,r}^i. \tag{42}$$

$$T_{l,r}^i = -\frac{dP_{l,r}^i}{dr}, \quad \text{with} \quad l=1,2,3 \tag{43}$$

and

$$P_{1,r}^1 = P_1 r^{gp} + D_1 r^{-gp}. \tag{44}$$

$$P_{2,r}^1 = P_2 r^{gp} + D_2 r^{-gp} + \frac{gp}{2}f(r). \tag{45}$$

$$P_{3,r}^1 = P_3 r^{gp} + D_3 r^{-gp} + \frac{1}{2}f(r). \tag{46}$$

$$P_{1,r}^2 = E_1 r^{gp} + F_1 r^{-gp}. \tag{47}$$

$$P_{2,r}^2 = E_2 r^{gp} + F_2 r^{-gp}. \tag{48}$$

$$P_{3,r}^2 = E_3 r^{gp} + F_3 r^{-gp}. \tag{49}$$

To improve the precision of this analytical model, Carter's coefficient K_c is applied to compensate the slots

effects. In this case, a new air gap length e_c is defined by [8]:

$$e_c = K_c e, \qquad (50)$$

where

$$K_c \approx \frac{P_t}{\left(P_t - \dfrac{b_s^2}{5e+b_s}\right)}, \quad \text{and} \quad P_t = \frac{2\pi R_s}{2pmN_{spp}}. \qquad (51)$$

III. CONSTRAINTS DEDUCED FROM THE PROPOSED MODEL

A. Torque constraint

The torque developed on the motor can be obtained by calculating the Maxwell stress tensors in the air-gap [4,6,7]:

$$T_m = \frac{LR_2^2}{\mu_o} \int_0^{2\pi} B_r^{II} B_\theta^{II} \, d\theta, \qquad (52)$$

where L is the axial length.

Incorporating (40) and (41) in (52) and integrating on the tangential direction yields to the final expression of the torque in terms of field sources ($M_{r,g}$, $M_{\theta,g}$ and I_n):

$$T_m = \frac{8\pi L p^2}{\mu_o} \left[\begin{array}{c} \displaystyle\sum_{g=1}^{\infty} g^2 N_g S_g \\ \times \left(\displaystyle\sum_{n=1}^{m} I_n(t) \sin\left(gp\left(\Omega t - \frac{(n-1)}{p} \frac{2\pi}{m} \right) \right) \right) \end{array} \right], \qquad (53)$$

where

$$N_g = \mu_o \left(E_1 F_2 - E_2 F_1 \right) M_{r,g} + \mu_o \left(E_1 F_3 - E_3 F_1 \right) M_{\theta,g}. \qquad (54)$$

The torque expression (53) depends on the design parameters. Therefore, this expression can be used as objective function or as constraint in the preliminary PM motor design.

B. Back electromotive force constraint

The back-EMF created by the permanent magnet can be obtained by Faraday's law:

$$E_n(t) = -\frac{\partial \Phi_{n0}(t)}{\partial t}, \qquad (55)$$

where $\Phi_{n0}(t)$ is the phase n flux linkage created by PMs.

Based on Stokes theorem, the flux linkage $\Phi_{n0}(t)$ is calculated by:

$$\Phi_{n0}(t) = \int_s B ds = \int_\Gamma A dl = LR_3 \int_0^{2\pi} A_z^{II}(R_3,\theta,t) C_n(\theta) d\theta. \qquad (56)$$

After the substitution and the simplification, the final expression of $\Phi_{n0}(t)$ is given by:

$$\Phi_{n0}(t) = 2\pi R_3 L \sum_{g=1}^{\infty} \Phi_{AP}(R_3) \cos\left(g\left(p\Omega t - (n-1)\frac{2\pi}{m} \right) \right), \qquad (57)$$

with

$$\Phi_{AP}(R_3) = -\mu_0 S_g \left[P_{2,r}^2(R_3) M_{r,g} + P_{3,r}^2(R_3) M_{\theta,g} \right]. \qquad (58)$$

From the equations (55) and (57), the back-EMF created by PMs is given by:

$$E_n(t) = 2\pi R_3 L p \Omega \times \sum_{g=1}^{\infty} g\Phi_{AP}(R_3) \sin\left(g\left(p\Omega t - (n-1)\frac{2\pi}{m} \right) \right). \qquad (59)$$

C. Stator and rotor yoke saturation constraint

The definition of the no saturation constraint of rotor/stator yoke needs the acknowledgement of the flux density in these regions.

The Fig. 2 shows that the magnetic flux in rotor yoke $\Phi_r(t)$ is equal to the flux in a half PM pole $\Phi_{hp}(t)$:

$$\Phi_r(t) = \Phi_{hp}(t). \qquad (60)$$
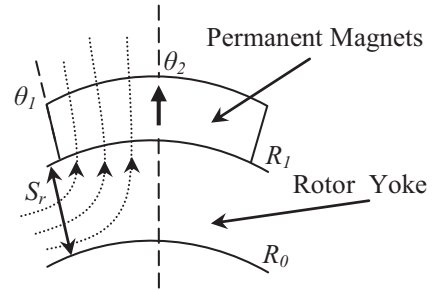
Fig. 2. Flux density trajectory in rotor yoke.

From the Fig. 2, the rotor flux yoke is given by:

$$\Phi_r(t) = B_r(t) S_r = L(R_1 - R_0) B_r(t), \qquad (61)$$

where $B_r(t)$ is the tangential component of flux density in the rotor and S_r is the cross section area of the rotor yoke.

In other hand, the magnetic flux in half PM pole at R_1 is given by:

$$\Phi_{hp}(t) = \int A_z^I(R_1) dl = L\left[A_z^I(R_1,\theta_2,t) - A_z^I(R_1,\theta_1,t) \right]. \qquad (62)$$

By using (60), (61) and (62) we obtain the analytical expression of the flux density in the rotor/stator yoke (supposed to have the same dimensions):

$$B_r(t) = \frac{\left[A_z^I(R_1,\theta_2,t) - A_z^I(R_1,\theta_1,t) \right]}{(R_1 - R_0)}. \qquad (63)$$

Usually, to avoid excessive saturation, the maximum flux density of iron core is limited to the range 1.6-1.9 T [3].

D. Stator tooth saturation constraint

In the case of slotted motor, we can introduce a constraint for no stator tooth saturation.

If we neglecting the flux leakage, the flux in the stator tooth $\Phi_{tooth}(t)$ is given by:

$$\Phi_{tooth}(t) = \frac{2\Phi_{hp}(t)}{mN_{spp}}. \qquad (64)$$

The stator tooth flux can be also expressed as:

$$\Phi_{tooth}(t) = B_{st}(t)S_{st}, \tag{65}$$

where $B_{st}(t)$ and S_{st} are the flux density and the small cross section area of stator tooth respectively.

By using (62), (64) and (65) we obtain the expression of the flux density in the stator tooth as:

$$B_{st}(t) = \frac{2L\left[A_z^I(R_1,\theta_2,t) - A_z^I(R_1,\theta_1,t)\right]}{S_{st}mN_{spp}}. \tag{66}$$

IV. DESIGN OPTIMIZATION PROCEDURE

A. Optimization problem definition

In order to present the design optimization procedure of surface mounted PMSM, based on the above analytical model, we designed a 30 kw PMSM with the following assumptions: 10 poles, 30 slots, one slot per pole and per phase (N_{spp}=1), based speed w_{base}=1500 rpm, maximal speed w_{max}=4500 rpm, current density J=7 A/mm², NdFeB magnets with a remanent flux density of 1.2 and a relative permeability of 1.

The objective functions fixed for this optimization are:

- *Minimizing the weight of the motor (M).*
- *Maximizing the efficiency by minimizing the power loss (PL).*

The mass M of the active part is given by:

$$M = M_C + M_{PM} + M_S + M_R, \tag{67}$$

where M_C, M_{PM}, M_S and M_R are respectively the weight of: the copper, the permanent magnet, the stator iron and the rotor iron. These masses are given by the following expressions:

$$M_C = 2\,pmN_{spp}S_s\left(L + 1.6\left(\frac{2\pi R_3}{2p}\right)\right)\rho_{copper}. \tag{68}$$

$$M_{PM} = \pi\left(R_2^2 - R_1^2\right)LK_{PM}\rho_{PM}. \tag{69}$$

$$M_S = \left(\pi\left(R_4^2 - R_3^2\right) - 2\,pmN_{spp}P_s b_s\right)L\rho_{iron}. \tag{70}$$

$$M_R = \pi\left(R_1^2 - R_0^2\right)L\rho_{iron}, \tag{71}$$

where S_s is the section of copper in slot, K_{PM} is the magnet-arc to pole-pitch ratio and P_s is the slot depth. Also, ρ_{copper}, ρ_{PM} and ρ_{iron} are respectively the density of: copper, permanent magnet and iron.

The power loss in the PMSM is given by the sum of the loss in the stator winding (P_{Lcop}) and the core loss (hysteresis P_{Lhys} and eddy current loss P_{Leddy}) [3]:

$$P_L(W) = P_{Lcop} + (P_{Lhys} + P_{Leddy})V_{volume\_iron}, \tag{72}$$

with

$$P_{Lcop}(W) = 3R_s I_{neff}^2. \tag{73}$$

$$P_{Lhys}(W.m^{-3}) = K_{hys}B^\beta w_s. \tag{74}$$

$$P_{Leddy}(W.m^{-3}) = \frac{2}{T}\int_0^T K_{eddy}\left(\frac{dB}{dt}\right)^2 dt, \tag{75}$$

where K_{hys} and K_{eddy} are the classical eddy and hysteresis loss coefficients which can be calculated at various frequencies and flux densities from curve fitting of manufacturer data sheets.

Finally, the multi-objective constrained optimization problem is defined as:

Minimize: **weight** and **power loss** (76)
Subject to the following constraints:
- *Electromagnetic torque, T = 191 Nm*
- *Back-EMF at maximum speed, Emax ≤ 500 V*
- *Tator/rotor yoke flux density, Byoke ≤ 1.6 T*
- *Tator tooth flux density, Btooth ≤ 1.6 T*

Firstly, before solving the above problem (76), we have dimensioning our PMSM by using the direct method proposed in [3]. From the obtained initial dimensioning, we have chosen seven variables, given in Table 1 with their exploration domain, to solve the final problem (76).

Table 1: The exploration domain for each variable

Variable	Symbol	Min	Max
Inner radius of the rotor yoke (m)	R_0	0.07	0.13
Axial length (m)	L	0.06	0.12
Thickness of magnet (m)	L_{PM}	0.003	0.006
Radius of the rotor yoke surface (m)	R_1	0.13	0.2
Magnet-arc to pole-pitch ratio	K_{PM}	0.6	0.9
Slot-opening to slot-pitch ratio	K_{So}	0.3	0.6
Slot depth (m)	P_s	0.02	0.03

B. Non-dominated sorting genetic algorithm

To optimize the constrained multi-objective problem (76), the Non-dominated Sorting Genetic Algorithm II (NSGA-II) is applied.

The NSGA-II is one of the most widely used algorithms in various engineering optimization processes due to its simplicity, parameter less-niching, better convergence near the true Pareto-optimal front, better spread of solutions and low computational requirements [9-11].

The main NSGA-II procedure is given below:
- Create a random population P_0 (of size N).
- Sort P_0 according to non-domination. Each solution is assigned a new fitness equal to its non-domination rank (1 is the best level). Then, use selection, recombination, and mutation to create the offspring population Q_0 (of size N) from P_0.
- While generation count is not reached, combine parent and offspring population to form the combined population R_t (of size 2N).

- Perform non-dominated sort on the population R_t. Then, calculate the crowding-distance for each solution. It is calculated by the size of the largest cuboid enclosing each solution without including any other point [9,10].
- Construct the next parent population P_{t+1} by choosing only the best N solutions from R_t. Each solution is evaluated by using its front rank as primary criteria and crowding-distance as secondary if it belongs to the last selected front.
- Use the new parent population P_{t+1} (of size N) for selection, crossover, and mutation to create a new population Q_{t+1} (of size N). We note that the selection criterion between two solutions is now based on the crowded-comparison operator (If the two solutions are from different fronts, we select the solution with lowest front rank. But, if they are from the same front, we select the individual with the highest crowding distance).

In this paper, the following parameters are used: population size N=200, maximum number of generations is 4000, mutation probability is 0.1, and crossover probability is 0.9. The variables are treated as real numbers and the Breeder Genetic Crossover (BGX) and the real-parameter mutation operator are used [12].

C. Results

The multi-objective optimization takes 70 minutes with NSGA-II method. The Pareto-optimal front for motor weight versus total loss is obtained as shown in Fig. 3.

The variables and the performances of the initial (MI) and two optimized PMSMs (MW: minimum weight and MP: minimum power loss) are presented in Table 2. As shown, the optimized motors characteristics are significantly better than the initial motor. The mass and the total power loss are minimized and are smaller than that of the initial motor. Also, the four optimization constraints are respected, especially the value of the electromagnetic torque.
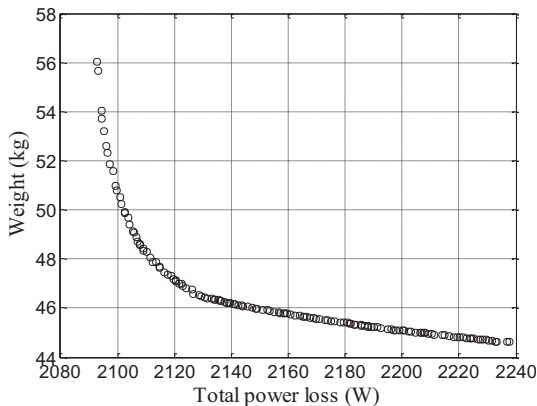
Table 2: Comparison between the initial and optimized PMSMs

Variables and Performances	MI	MW	MP
R_0 (m)	0.0955	0.1147	0.113
L (m)	0.0955	0.06	0.0695
L_{PM} (m)	0.0077	0.006	0.006
R_1 (m)	0.1251	0.1428	0.1439
K_{PM}	0.833	0.6	0.6
K_{So}	0.5	0.4027	0.3042
P_s	0.0239	0.0272	0.03
Number of conductors in slot	8	12	10
Current (A)	100	105	105
Electromagnetic torque (Nm)	177.7	191	191
Back-EMF at maximum speed (V)	448.9	464.3	461.5
Maximum yoke flux density (T)	1.9	1.6	1.5
Maximum tooth flux density (T)	1.4	1.6	1.4
Mass (kg)	61.3	44.6	56
Total power loss (W)	3955	2237.7	2092.5
Efficiency	0.8835	0.9306	0.9348

In order to validate the proposed design procedure, the performances of MW designed machine have been compared with 2D finite element simulations (2D FE). Figures 4 and 5 show respectively the electromagnetic torque and the back-EMF. We can observe that the mean torque and the maximum value of the back-EMF obtained by FE simulations are in good agreement with analytical results. However, the small error between the two models and the ripples in the torque and in the back-EMF are due to the effect of stator slots, considered in implicit way in the analytical model by Carter's coefficient.

Fig. 3. Pareto-optimal front.
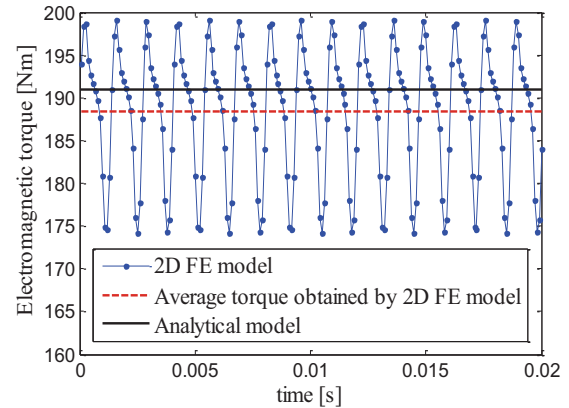
Fig. 4. Electromagnetic torque obtained for w=1500 rpm (the base speed).
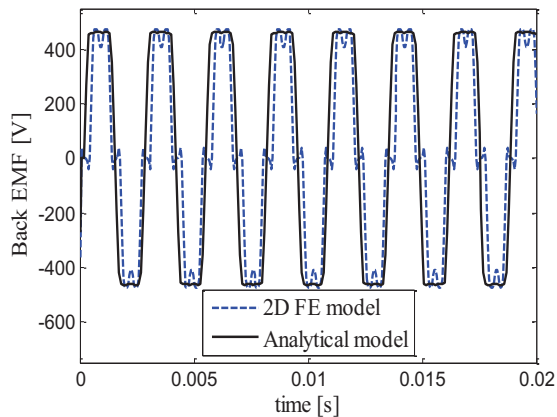
Fig. 5. Back-EMF obtained for *w*=4500 rpm (the maximum speed).

V. CONCLUSION

In this paper, an optimal design procedure of surface mounted PMSM is investigated. Firstly, an analytical model of PMSM is presented. This model is sufficiently accurate and fast to be used in the design optimization with stochastic methods like genetic algorithms. Then, the NSGA-II method is proposed to solve the highly nonlinear constrained multi-objective problem formed by two objectives (motor weight and total power loss) and four important constraints (demanded value of electromagnetic torque, maximum limit of back EMF, flux density saturation in stator/rotor yoke and saturation in stator tooth).

Finally, this design procedure, based on the proposed analytical model and NSGA-II algorithm, has been successfully applied for optimal design of 30 kW/1500 rpm PMSM. The obtained results show that the proposed methodology has a good accuracy and requires a reasonable computation time. Also, the Pareto fronts obtained from this procedure allows the designer to consider a good compromise between efficiency and weight of the motor in an effective manner. Moreover, this method can be used to design another types of machine, such as PMSM with external rotor.

REFERENCES

[1] A. Cavagnino, M. Lazzari, F. Profumo, and A. Tenconi, "A comparison between the axial flux and the radial flux structures for PM motors," *IEEE Trans. Ind. Applicat.*, vol. 38, pp. 1517-1524, Nov. 2002.

[2] S. Sonoda, Y. Takahashi, K. Kawagishi, N. Nishida, and S. Wakao, "Application of stepwise multiple regression to design optimization of electric machine," *IEEE Trans. Magn.*, vol. 43, pp. 1609-1612, Apr. 2007.

[3] G. R. Slemon and X. Liu, "Modeling and design optimization of permanent magnet motors,"

Electric Machines & Power systems, vol. 20, pp. 71-92, 1992.

[4] B. Nogarede, A. D. Kone, and M. Lajoie, "Modeling and simulation of inverter fed slotless permanent magnet machines," *in IMACS'91-13th World Congress on Computation and Applied Mathematics*, vol. 4, pp. 1529-1531, Jul. 1991.

[5] Z. Q. Zhu, D. Howe, E. Bolte, and B. Ackermann, "Instantaneous magnetic field distribution in brushless permanent magnet dc motors, part I: open-circuit field," *IEEE Trans. Magn.*, vol. 29, pp. 124-135, Jan. 1993.

[6] A. Chebak, P. Viarouge, and J. Cos, "Analytical model for design of high-speed slotless brushless machines with SMC stators," *IEEE Electric Machines & Drives Conference IEMDC '07*, vol. 1, pp. 159-164, May 2007.

[7] S. Mendaci, M. R. Mekideche, and H. Allag, "Instantaneous analytical model of radial surface permanent magnet synchronous motor dedicated to optimal design," *IREMOS*, vol. 4, pp. 1542-1549, Aug. 2011.

[8] Z. Q. Zhu and D. Howe, "Instantaneous magnetic field distribution in brushless permanent magnet dc motors, part III: effect of stator slotting," *IEEE Trans. Magn.*, vol. 29, pp. 143-151, Jan. 1993.

[9] K. Deb, *Multi-Objective Optimization Using Evolutionary Algorithm*, Wiley, Chichester, 2001.

[10] K. Deb, A. Pratap, S. Agarwal, and T. Meyarivan, "A fast and elitist multiobjective genetic algorithm: NSGA-II," *IEEE Trans. On Evolutionary Computation*, vol. 6, pp. 182-197, Apr. 2002.

[11] M. T. Jensen, "Reducing the run-time complexity of multiobjective EAs: the NSGA-II and other algorithms," *IEEE Trans. On Evolutionary Computation*, vol. 7, pp. 503-515, Oct. 2003.

[12] B. Sareni, J. Regnier, and X. Roboam, "A recombination and self-adaptation in multi-objective genetic algorithms," *Lectures Notes in Computer Science*, vol. 2936, pp. 115-127, 2004.

Sofiane Mendaci was born in Jijel, Algeria, in 1976. He received the B.S. degree from Jijel University, Algeria, in 2000, the M.S. degree from Paris XI University, France, in 2004, and the Ph.D. degree from Jijel University, Algeria, in 2013, all in Electrical Engineering. His research interests include design, modeling, and control of electrical machines.

He is currently an Assistant Professor in the Department of Electrical Engineering at the University of Guelma, Algeria.

Hicham Allag was born in Jijel, Algeria, in 1978. He received the B.S. degree from Jijel University, Algeria, in 2000, the M.S. degree from University of Constantine, Algeria, in 2004, and the Ph.D. degree from Grenoble University, France, in 2010, all in Electrical Engineering. His research interests include magnetic levitation and electromagnetic forces calculation.

He is an Associate Professor in the Department of Electrical Engineering at Jijel University, Algeria.

Mohamed Rachid Mekideche was born in Jijel, Algeria in 1957. He received the M.S. degree from the National Polytechnic School of Algiers, Algeria, in 1986, and the Ph.D. degree from Nantes University, France, in 1994, all in Electrical engineering. His research interests include analytical modeling and analysis of electrical machines.

He is now at the University of Jijel, as a Professor and Dean of the Engineering Faculty.

On the Properties of Loop-Flower Basis Functions

Yibei Hou [1], Gaobiao Xiao [1], and Jinpeng Fang [2]

[1] Key Laboratory of Ministry of Education
Design and Electromagnetic Compatibility of High-Speed Electronic Systems
Shanghai Jiao Tong University, Shanghai, 200240, China
yibhou@sjtu.edu.cn, gaobiaoxiao@sjtu.edu.cn

[2] Shanghai Key Laboratory
Electromagnetic Environmental Effects for Aerospace Vehicle
Shanghai, China
jpfang1129@sina.com

Abstract ─ This paper presents a mathematical analysis of loop-flower basis functions which are adopted to cure low frequency breakdown in integral equations for solving electromagnetic scattering problems. Flower basis functions will be analyzed based on RWG-connected graph generated according to RWG basis functions. This paper will also explore the conditioning behavior of loop-flower Gram matrices which greatly contributes to the whole conditioning of electric field integral equation. The performance of loop-flower basis functions is confirmed by numerical results that show fast convergence rate of iteration solvers, which are better than those of loop-star basis functions.

Index Terms ─ Conditioning behavior, electromagnetic scattering, Gram matrices, loop-flower basis functions, low frequency breakdown.

I. INTRODUCTION

Electric field integral equations (EFIEs) are usually discretized by using Method of Moment (MoM), which is widely adopted to analyze electromagnetic problems in computational electromagnetics community. To numerically solve EFIE, the surface of the object is often discretized as simple elements such as triangles and quadrilaterals. Rao-Wilton-Glisson (RWG) basis functions are popular to expand surface electric and magnetic currents among all divergence-conforming vector basis functions. However, the use of RWG basis functions for the EFIE exhibits low frequency breakdown, that is to say, at very low frequencies the discretized EFIE matrix system is highly ill-conditioned, and hence is difficult to be solved accurately and efficiently [1,2]. In addition, when the EFIE is discretized with boundary elements of average geometry diameter h, the resulting matrix has a condition number growing as $(kh)^{-2}$, where k is the wavenumber. Moreover,

the impedance matrices resulting from EFIE tend to be ill-conditioned when derived from dense meshes whose average lengths are much smaller than the wavelength of the excitation [1,3].

Performing quasi-Helmholtz decomposition can cure the low frequency breakdown effectively. Various quasi-Helmholtz decompositions such as loop-star (LS) basis functions, loop-tree (LT) basis functions and so on, have been proposed in the past few years [4-8]. These quasi-Helmholtz decompositions forcibly separate the surface currents into the solenoidal part and the irrotational one properly at low frequencies. Moreover, a frequency scaling scheme is also implemented to obtain stable systems. Hence, both two parts of the currents can be handled correctly. Even though the quasi-Helmholtz decomposition is an efficient method to overcome low frequency breakdown, it cannot improve the conditioning of the EFIE operator when meshes are dense. Recently, an efficient Calderón multiplicative preconditioner [9] has been proposed to solve the above problems and introduce the Buffa-Christiansen (BC) basis functions [10] to avoid the singular Gram matrix. BC basis functions can be expressed by the linear combinations of the RWG basis functions defined on the barycentric refined triangular mesh, and thus additional memory is required. Furthermore, the Calderón preconditioner with BC basis functions may fail at very low frequencies without other special treatments [11].

Loop-flower (LF) basis functions are proposed to implement Calderón preconditioner directly in [11]. The left and right EFIE operators are both discretized by using loop-flower basis functions. Consequently, there is no need to refine the original mesh to generate BC basis functions. Besides, loop and flower basis functions are both defined on nodes, which compress the degrees of freedom (DoF) compared with RWG basis functions. When the loop-flower basis functions are implemented

in EFIE, the convergence rate of iterations can be estimated by analyzing the conditioning of EFIE system, in which the conditioning of loop-flower Gram matrix is the sole cause of the overall condition number of the decomposed equation. Preliminary results of the conditioning properties of loop-flower Gram matrices are presented in [12].

In this paper, we present an analysis of flower basis functions from a perspective of graph theory. Hereafter, we will use the terminology 'RWG-connected' to denote the relationship between two nodes which are free vertexes of a RWG basis function, as is defined in [11]. The graph generated according to RWG-connected relations has a similar behavior compared with the edge-connected graph. In addition, Gram matrices associated with the loop-flower basis functions are analyzed using graph Laplacian matrices as auxiliary tools. The performance of loop-flower basis functions in comparison with loop-star basis functions is also presented in this work.

II. LOOP-FLOWER BASIS FUNCTIONS

Loop-flower basis functions arise from the need to perform quasi-Helmholtz decomposition. In this method, loop basis functions are used to expand the solenoidal currents, while flower basis functions are for the irrotational parts [11-13]. A loop basis function is defined on each interior vertex v_j, which is shown in the left one of Fig. 1. Loop basis functions can be written as:

$$f_j^L(r) = \sum_{i=1}^N \Lambda_{i,j} f_i'(r), \qquad (1)$$

where N represents the number of RWG basis functions, $\bar{\bar{\Lambda}} = [\Lambda_{ij}]$ is the loop to RWG transformation matrix and $f'(r)$ means the standard RWG basis function divided by the common edge length.

A loop basis function maintains a direct relationship with the piecewise linear Lagrange basis function [12] (or the nodal basis function) associated with vertex in the FEM community. Consequently, loop basis function can be also rewritten by:

$$f_p^L(r) = \nabla \times \hat{n}_r \lambda_p(\mathbf{r}) = \hat{n}_r \times \nabla \lambda_p(r), \qquad (2)$$

in which, $\hat{n}_r$ denotes the outward normal unit vector and $\lambda_p(r)$ is piecewise linear Lagrange basis function. It is easy to verify that the gradient of $\lambda_p(r)$ is divergence-conforming, while $\hat{n}_r \times \nabla \lambda_p(r)$ is curl-conforming.

A flower basis function is also defined on the node v_j, like a loop basis function, as depicted in the right one of Fig. 1. Its support covers all the RWG bases that share the reference node v_j as one free vertex. It can be explicitly expressed by:

$$f_j^F(r) = \sum_{i=1}^N F_{i,j} f_i(r), \qquad (3)$$

where $\bar{\bar{F}} = [F_{ij}]$ stands for the flower to RWG transformation matrix. The reference direction of flower basis function points away from the reference node.

Since the space spanned by flower basis functions is a subspace of the space spanned by star basis functions, the accuracy of the EFIE solver using loop-flower bases can be affected by the mesh quality. To improve the accuracy, the flower basis function is slightly modified and constructed by using RWG bases without normalization directly.
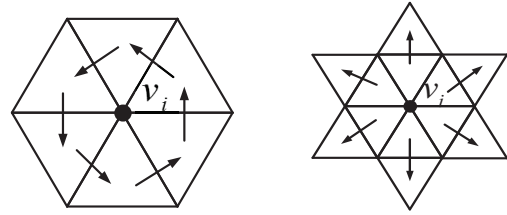
Fig. 1. Loop and flower basis function.

In order to proceed, we need to summarize a number of preliminary facts. Recall that the Laplacian matrix of the graph G is the $N \times N$ symmetric matrix $\bar{\bar{L}}$:

$$\bar{\bar{L}} = \bar{\bar{D}} - \bar{\bar{A}}, \qquad (4)$$

in which, $\bar{\bar{A}}$ is the adjacency matrix of the graph G and $\bar{\bar{D}}$ stands for the diagonal matrix diag(d_1, d_2, …, d_m) whose diagonal entries are the degree of the corresponding vertices [14-16]. Since all the sums of rows in $\bar{\bar{L}}$ equal to zero, the matrix $\bar{\bar{L}}$ has a zero eigenvalue with the corresponding eigenvector $\bar{1}$ containing all ones. In other words, the Laplacian matrix $\bar{\bar{L}}$ has a one-dimensional null-space spanned by vector $\bar{1}$. We can denote eigenvalues of the Graph G by $\sigma_1(G)$, $\sigma_2(G)$, …, $\sigma_N(G)$ with the following assumption:

$$\sigma_1(G) \geq \sigma_2(G) \geq ... \geq \sigma_N(G) = 0. \qquad (5)$$

As for a connected graph without isolated vertices or components, $\sigma_{N-1}(G)$ is the smallest nonzero eigenvalue [15,16]. Here, we call the $(N-1) \times (N-1)$ submatrix, obtained by deleting row i and column i of the Laplacian matrix, principal submatrix. It is easy to prove that the principal submatrix is of full rank when the graph is connected.

The number of loop basis functions has been explicitly investigated in [5]. It is obvious that the matrix $\bar{\bar{\Lambda}}^T \bar{\bar{\Lambda}}$ is the principal submatrix of the Laplacian matrix associated with the graph constituted by nodes and edges

of the mesh in the closed structure.

The RWG-connected graph can also be analyzed in a similar manner. By deleting edges between two nodes and drawing lines between RWG-connected vertices, a companion graph can be obtained. As shown in Fig. 2 (b), where three subgraphs are drawn with solid lines using different colors in the RWG-connected graph which is the companion one of the edge-connected graph in Fig. 2 (a). In the companion graph, there are at most three isolated subgraphs [11], while vertices are connected in every subgraph. Assume that the number of the subgraph is N_s and the flower to RWG base transformation matrices in every subgraphs are denoted by $\bar{\bar{\mathbf{F}}}_i$, then it follows:

$$\bar{\bar{\mathbf{F}}}_i^T \bar{\bar{\mathbf{F}}}_j = \bar{\bar{\mathbf{0}}} \quad (i, j = 1,...,N_s;\ i \neq j) . \tag{6}$$

The matrix $\bar{\bar{\mathbf{F}}}_i^T \bar{\bar{\mathbf{F}}}_i$ is the principal submatrix of the Laplacian matrix $\bar{\bar{\mathbf{L}}}_i$ corresponding to the i-th subgraph. Given that every subgraph is connected, the smallest eigenvalue of the Laplacian matrix is zero, while the second smallest eigenvalue is positive. In result, the multiplicity of zero eigenvalues of the Laplacian matrix associated with the total RWG-connected graph equals to the number of the subgraph. In order to make sure that flower basis functions are linearly independent, one node should be dropped in every subgraph, consequently, N_s nodes must be dropped in total.

(a)   (b)
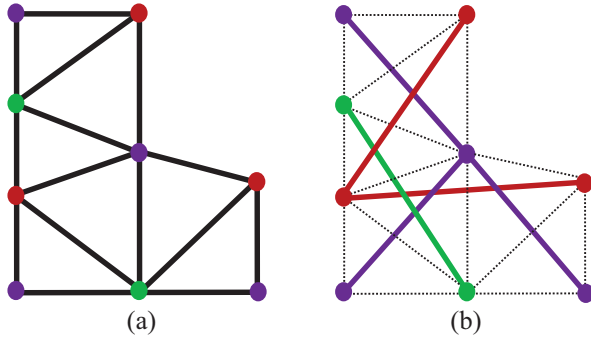
Fig. 2. Graphs generated using the same mesh nodes: (a) edge-connected graph, and (b) RWG-connected graph.

III. ELECTRIC FIELD INTEGRAL EQUATION WITH LOOP-FLOWER BASIS FUNCTIONS

Consider the problem of electromagnetic wave scattering by three dimensional perfectly conducting surface Ω. The scatter fields (E^s, H^s) are generated by surface current $J(r)$. The EFIE can be written by:

$$\mathcal{T}(\boldsymbol{J}) = -\hat{\boldsymbol{n}} \times \boldsymbol{E}^{inc} , \tag{7}$$

where $\boldsymbol{E}^{inc}$ is the incident electric field and the EFIE operator $\mathcal{T}$ is defined by:

$$\mathcal{T}(\boldsymbol{J}) = -j\omega\mu\hat{\boldsymbol{n}} \times \int_{\Omega} \boldsymbol{J}(\boldsymbol{r}')g(\boldsymbol{r},\boldsymbol{r}')\,\mathrm{d}\Omega$$
$$+ \frac{1}{j\omega\varepsilon}\hat{\boldsymbol{n}} \times \int_{\Omega} \nabla' \cdot \boldsymbol{J}(\boldsymbol{r}')\nabla g(\boldsymbol{r},\boldsymbol{r}')\,\mathrm{d}\Omega , \tag{8}$$

in which, ω is the angular frequency, μ and ε denote the permeability and the permittivity respectively. By expanding the surface current $\boldsymbol{J}$ using RWG basis functions and applying Galerkin's method to the EFIE, we can obtain the following linear system:

$$\bar{\bar{\mathbf{Z}}} \cdot \bar{\mathbf{I}} = \bar{\mathbf{V}} . \tag{9}$$

When the loop-flower decomposition is performed, the surface current satisfies:

$$\boldsymbol{J} = \boldsymbol{J}^L + \boldsymbol{J}^F , \tag{10}$$

in which, the two currents satisfy that $\nabla \cdot \boldsymbol{J}^L = 0$, $\nabla \times \boldsymbol{J}^L \neq 0$, $\nabla \cdot \boldsymbol{J}^F \neq 0$ and $\nabla \times \boldsymbol{J}^L \approx 0$, consequently the EFIE (9) can be rewritten by:

$$\begin{bmatrix} \bar{\bar{\mathbf{Z}}}^{LL} & \bar{\bar{\mathbf{Z}}}^{LF} \\ \bar{\bar{\mathbf{Z}}}^{FL} & \bar{\bar{\mathbf{Z}}}^{FF} \end{bmatrix} \begin{bmatrix} \bar{\mathbf{I}}^L \\ \bar{\mathbf{I}}^F \end{bmatrix} = \begin{bmatrix} \bar{\mathbf{V}}^L \\ \bar{\mathbf{V}}^F \end{bmatrix} . \tag{11}$$

In order to obtain stable system, a frequency scaling is adopted as follows:

$$\begin{bmatrix} k^{-1}\bar{\bar{\mathbf{Z}}}^{LL} & \bar{\bar{\mathbf{Z}}}^{LF} \\ \bar{\bar{\mathbf{Z}}}^{FL} & k\bar{\bar{\mathbf{Z}}}^{FF} \end{bmatrix} \begin{bmatrix} \bar{\mathbf{I}}^L \\ k^{-1}\bar{\mathbf{I}}^F \end{bmatrix} = \begin{bmatrix} k^{-1}\bar{\mathbf{V}}^L \\ \bar{\mathbf{V}}^F \end{bmatrix} . \tag{12}$$

After the treatment, the low-frequency breakdown can be overcome, and the conditioning of the impendence matrix can be improved significantly, hence the linear equation system is now solvable even at very low frequencies. From another point of view, loop-flower basis functions can be easily integrated into existing EFIE-MoM codes as if they construct an algebraic preconditioner. Consequently, (9) can be rewritten by:

$$\bar{\bar{\mathbf{P}}}_{PR}\left(\bar{\bar{\mathbf{H}}}_{LF}^T \bar{\bar{\mathbf{Z}}}^{RWG} \bar{\bar{\mathbf{H}}}_{LF}\right)\bar{\bar{\mathbf{P}}}_{PO}\left(\bar{\bar{\mathbf{P}}}_{PO}^{-1}\bar{\mathbf{I}}^{LF}\right) = \bar{\bar{\mathbf{P}}}_{PR}\bar{\bar{\mathbf{H}}}_{LF}^T \bar{\mathbf{V}}^{RWG} , \tag{13}$$

where

$$\bar{\bar{\mathbf{P}}}_{PR} = \begin{bmatrix} k^{-1}\bar{\bar{\mathbf{U}}} & \bar{\bar{\mathbf{0}}} \\ \bar{\bar{\mathbf{0}}} & \bar{\bar{\mathbf{U}}} \end{bmatrix} , \tag{14}$$

and

$$\bar{\bar{\mathbf{P}}}_{PO} = \begin{bmatrix} \bar{\bar{\mathbf{U}}} & \bar{\bar{\mathbf{0}}} \\ \bar{\bar{\mathbf{0}}} & k\bar{\bar{\mathbf{U}}} \end{bmatrix} , \tag{15}$$

in which, $\bar{\bar{\mathbf{U}}}$ is the identity matrix, and $\bar{\bar{\mathbf{H}}}^{LF} = [\bar{\bar{\mathbf{\Lambda}}}, \bar{\bar{\mathbf{F}}}]$ denotes loop-flower to RWG basis functions transformation matrix. Finally, the coefficients of RWG basis functions can be obtained by:

$$\bar{\mathbf{I}}^{RWG} = \bar{\bar{\mathbf{H}}}^{LF}\bar{\mathbf{I}}^{LF} . \tag{16}$$

IV. LOOP-FLOWER GRAM MATRIX

It can be found in [17] that the Gram matrix of RWG basis functions:

$$(\bar{\bar{\mathbf{G}}})_{i,j} = <\boldsymbol{f}_i, \boldsymbol{f}_j>, \tag{17}$$

is well-conditioned. Here, the inner product is defined by $<\boldsymbol{a}, \boldsymbol{b}> = \int_\Gamma \boldsymbol{a} \cdot \boldsymbol{b} \, d\Gamma$. The Gram matrix of RWG basis functions has the same conditioning property as the identity matrix [12,17].

Since loop and star coefficient matrices are orthogonal [5], in addition, flower basis functions are actually the linear combinations of star basis functions surrounding their reference nodes, it can be validated that loop and flower coefficient matrices are also orthogonal between each other. Loop and flower Gram matrices can be written by:

$$\{\bar{\bar{\mathbf{G}}}^L\}_{i,j} = \{\bar{\bar{\mathbf{\Lambda}}}^T\bar{\bar{\mathbf{G}}}\bar{\bar{\mathbf{\Lambda}}}\}_{i,j} = <\boldsymbol{f}_i^L, \boldsymbol{f}_j^L>, \tag{18}$$

$$\{\bar{\bar{\mathbf{G}}}^F\}_{i,j} = \{\bar{\bar{\mathbf{F}}}^T\bar{\bar{\mathbf{G}}}\bar{\bar{\mathbf{F}}}\}_{i,j} = <\boldsymbol{f}_i^F, \boldsymbol{f}_j^F>, \tag{19}$$

respectively, here $\{\bar{\bar{\mathbf{G}}}^L\}_{i,j}$ means the (i,j) element of matrix $\bar{\bar{\mathbf{G}}}^L$. According to above discussion, the Gram matrix of loop-flower basis functions has the following relationship:

$$\bar{\bar{\mathbf{G}}}^{LF} = \bar{\bar{\mathbf{H}}}_{LF}^T\bar{\bar{\mathbf{G}}}\bar{\bar{\mathbf{H}}}_{LF} \asymp \bar{\bar{\mathbf{H}}}_{LF}^T\bar{\bar{\mathbf{H}}}_{LF} = \begin{pmatrix} \bar{\bar{\mathbf{\Lambda}}}^T\bar{\bar{\mathbf{\Lambda}}} & \bar{\bar{\mathbf{0}}} \\ \bar{\bar{\mathbf{0}}} & \bar{\bar{\mathbf{F}}}^T\bar{\bar{\mathbf{F}}} \end{pmatrix}$$
$$\asymp \begin{pmatrix} \bar{\bar{\mathbf{\Lambda}}}^T\bar{\bar{\mathbf{G}}}\bar{\bar{\mathbf{\Lambda}}} & \bar{\bar{\mathbf{0}}} \\ \bar{\bar{\mathbf{0}}} & \bar{\bar{\mathbf{F}}}^T\bar{\bar{\mathbf{G}}}\bar{\bar{\mathbf{F}}} \end{pmatrix} = \begin{pmatrix} \bar{\bar{\mathbf{G}}}^L & \bar{\bar{\mathbf{0}}} \\ \bar{\bar{\mathbf{0}}} & \bar{\bar{\mathbf{G}}}^F \end{pmatrix}. \tag{20}$$

The notation $\bar{\bar{\mathbf{A}}} \asymp \bar{\bar{\mathbf{B}}}$ denotes that there exist two constant numbers C_1 and C_2 such that $C_1\bar{\mathbf{v}}^T\bar{\bar{\mathbf{B}}}\bar{\mathbf{v}} \le \bar{\mathbf{v}}^T\bar{\bar{\mathbf{A}}}\bar{\mathbf{v}} \le C_2\bar{\mathbf{v}}^T\bar{\bar{\mathbf{B}}}\bar{\mathbf{v}}$ holds true for every arbitrary vector $\bar{\mathbf{v}}$, which means that spectral properties between matrix $\bar{\bar{\mathbf{A}}}$ and $\bar{\bar{\mathbf{B}}}$ are equivalent. After investigating (20), we can find that the Gram matrix of loop-flower basis functions has the equivalent conditioning behavior of the block diagonal matrix with two block elements which are Gram matrices of loop basis functions and flower basis functions. So we can analyze the two block elements separately to obtain the total conditioning property of the Gram matrix of loop-flower basis functions. Assume that the surface of a concerned object is discretized using uniform triangular mesh with average edge length h, it has been presented in [17] that:

$$\mathrm{cond}(\bar{\bar{\mathbf{G}}}^L) \asymp \frac{1}{h^2}, \tag{21}$$

holds true for both closed and open objects. In addition, $\mathrm{cond}(\bar{\bar{\mathbf{G}}}^L)$ should be interpreted as the reduced condition number $\sigma_1(\bar{\bar{\mathbf{G}}}^L)/\sigma_{Nl-1}(\bar{\bar{\mathbf{G}}}^L)$ when the closed structure is analyzed and meshed with Nl loop basis

functions. Since the number of the triangular mesh is subject to $N_h \asymp 1/h^2$, we can also find that $\mathrm{cond}(\bar{\bar{\mathbf{G}}}^L) \asymp N_h$. For more details associated with the conditioning of loop Gram matrix, the reader should refer to [17,18] and references therein.

From (18), (20) and (21), it follows that:

$$\mathrm{cond}(\bar{\bar{\mathbf{\Lambda}}}^T\bar{\bar{\mathbf{\Lambda}}}) \asymp \frac{1}{h^2}, \tag{22}$$

where $\bar{\bar{\mathbf{\Lambda}}}^T\bar{\bar{\mathbf{\Lambda}}}$ is the principal submatrix of the Laplacian matrix. We can also obtain that:

$$\sigma_1(\bar{\bar{\mathbf{\Lambda}}}^T\bar{\bar{\mathbf{\Lambda}}}) \asymp 1 \text{ and } \sigma_{Nl-1}(\bar{\bar{\mathbf{\Lambda}}}^T\bar{\bar{\mathbf{\Lambda}}}) \asymp h^2. \tag{23}$$

The analysis of $\bar{\bar{\mathbf{G}}}^F$ can be traced to the analysis of $\bar{\bar{\mathbf{G}}}^L$. Given that the RWG Gram matrix is well-conditioned, the matrix $\bar{\bar{\mathbf{G}}}^F$ maintains the following equivalences:

$$\bar{\bar{\mathbf{G}}}^F = \bar{\bar{\mathbf{F}}}^T\bar{\bar{\mathbf{G}}}\bar{\bar{\mathbf{F}}} \asymp \bar{\bar{\mathbf{F}}}^T\bar{\bar{\mathbf{F}}}, \tag{24}$$

so that we can analyze the principal submatrix $\bar{\bar{\mathbf{F}}}^T\bar{\bar{\mathbf{F}}}$ of the Laplacian matrix $\bar{\bar{\mathbf{L}}}$ of the RWG-connected graph instead. For the sake of brevity, here we assume that there are three RWG-connected subgraphs in the mesh structure. According to the discussion in the previous section, the flower coefficient matrix $\bar{\bar{\mathbf{F}}}$ can be expressed by:

$$\bar{\bar{\mathbf{F}}} = [\bar{\bar{\mathbf{F}}}_1, \bar{\bar{\mathbf{F}}}_2, \bar{\bar{\mathbf{F}}}_3], \tag{25}$$

and the principal submatrix $\bar{\bar{\mathbf{F}}}^T\bar{\bar{\mathbf{F}}}$ turns to be:

$$\bar{\bar{\mathbf{F}}}^T\bar{\bar{\mathbf{F}}} = \begin{pmatrix} \bar{\bar{\mathbf{F}}}_1^T\bar{\bar{\mathbf{F}}}_1 & \bar{\bar{\mathbf{0}}} & \bar{\bar{\mathbf{0}}} \\ \bar{\bar{\mathbf{0}}} & \bar{\bar{\mathbf{F}}}_2^T\bar{\bar{\mathbf{F}}}_2 & \bar{\bar{\mathbf{0}}} \\ \bar{\bar{\mathbf{0}}} & \bar{\bar{\mathbf{0}}} & \bar{\bar{\mathbf{F}}}_3^T\bar{\bar{\mathbf{F}}}_3 \end{pmatrix}, \tag{26}$$

where $\bar{\bar{\mathbf{F}}}_i^T\bar{\bar{\mathbf{F}}}_i$ is the principal submatrix of the Laplacian matrix $\bar{\bar{\mathbf{L}}}_i$ corresponding to the subgraph G_i that is connected. According to Cauchy interlacing theorem in [16,19], we can get the following spectral inequality:

$$\sigma_1(\bar{\bar{\mathbf{L}}}_i) \ge \sigma_1(\bar{\bar{\mathbf{F}}}_i^T\bar{\bar{\mathbf{F}}}_i) \ge \sigma_2(\bar{\bar{\mathbf{L}}}_i) \ge \sigma_2(\bar{\bar{\mathbf{F}}}_i^T\bar{\bar{\mathbf{F}}}_i) \ge \dots$$
$$\ge \sigma_{N_1-1}(\bar{\bar{\mathbf{L}}}_i) \ge \sigma_{N_1-1}(\bar{\bar{\mathbf{F}}}_i^T\bar{\bar{\mathbf{F}}}_i) \ge \sigma_{N_1}(\bar{\bar{\mathbf{L}}}_i) = 0. \tag{27}$$

Since the maximum singular value of the Laplacian matrix $\bar{\bar{\mathbf{L}}}_i$ is bounded by:

$$d(u)+1 \le \sigma_1(\bar{\bar{\mathbf{L}}}_i)$$
$$\le \max\{d(u)+d(v) \,|\, (u,v) \in E(G_i)\}, \tag{28}$$

where u and v are two vertices of arbitrary edges in the graph G_i, and $d(u)$ means the degree associated with the vertex u [15], so that the maximum singular value of $\bar{\bar{\mathbf{F}}}_i^T\bar{\bar{\mathbf{F}}}_i$ is also bounded. From the inequality (27), it is

obvious that the smallest eigenvalue is rather small and becomes an isolated singular value from the perspective of quantity. The isolated singular value is irrelevant for iterative solution [17], so that we can use the reduced condition number, which is the ratio between the maximum singular value and second smallest one, to estimate the global convergence.

Consider that RWG-connected relation behaves similarly to edge-connected relation in the analysis of loop basis functions, we can also obtain that:

$$\sigma_1(\overline{\overline{\mathbf{F}}}_i^T \overline{\overline{\mathbf{F}}}_i) \asymp 1 \ \text{and} \ \sigma_{Nfi-1}(\overline{\overline{\mathbf{F}}}_i^T \overline{\overline{\mathbf{F}}}_i) \asymp h^2, \quad (29)$$

so that,

$$\text{cond}(\overline{\overline{\mathbf{F}}}^T \overline{\overline{\mathbf{F}}}) \asymp \frac{1}{h^2}. \quad (30)$$

From (24) and (30), it follows that:

$$\text{cond}(\overline{\overline{\mathbf{G}}}^F) \asymp \frac{1}{h^2}. \quad (31)$$

In result, from (20), (21) and (31),

$$\text{cond}(\overline{\overline{\mathbf{G}}}^{LF}) \asymp \frac{1}{h^2}. \quad (32)$$

In fact, the transformation matrix $\overline{\overline{\mathbf{F}}}$ is defined on the total nodes in the mesh except no more than three discarded nodes and the number of the discarded nodes equals to the multiplicity of zero eigenvalue of the Laplacian matrix associated with the RWG-connected graph. Furthermore, the discarded nodes can be selected and dropped according to the algorithm in [11].

V. NUMERICAL RESULTS

This section presents numerical tests that corroborate the theory developed in the previous sections. The efficiency and accuracy of loop-flower basis functions have been validated by a scattering example. Unless otherwise specified, the simulations are run on a personal computer equipped with four Core Intel(R) Core(TM) i5-4440 CPU at 3.10 GHz and 8 GB of RAM.

A. Conditioning of loop-flower Gram matrices

The first test illustrates the validity of spectral properties of the principal submatrix corresponding to the Laplacian matrix associated with the RWG-connected graph. The test is conducted with a 1m×1m PEC square plate discretized by using different uniform meshes. It is obvious in Fig. 3 that the maximum singular value is bounded and the upper bound is about 10, while the second smallest singular value decays in the same order of h^2. In addition, the smallest value is vanishingly small.

Figure 4 shows the reduced condition numbers for loop-flower Gram matrices in both closed and open structures. In Fig. 4 (a), the reduced condition number of the loop-flower Gram matrix corresponding to the above square plate is presented. The results indicates that the

reduced condition number of the loop-flower Gram matrix has a predicted growth of h^{-2}. Additionally, the loop-flower Gram matrix associated with a PEC sphere discretized with several uniform meshes is also investigated. Figure 4 (b) shows that the reduced condition number of the loop-flower Gram matrix associated with a sphere also grows theoretically as h^{-2}.
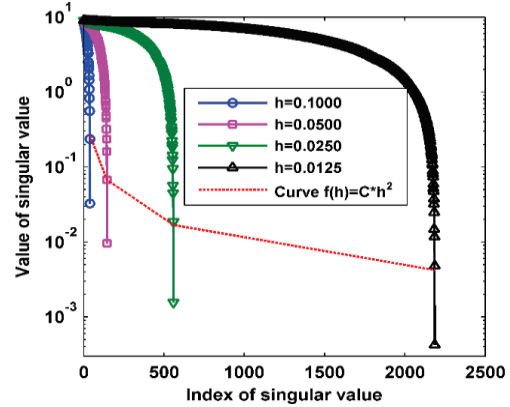
Fig. 3. Singular value of principal submatrix.

(a)

(b)
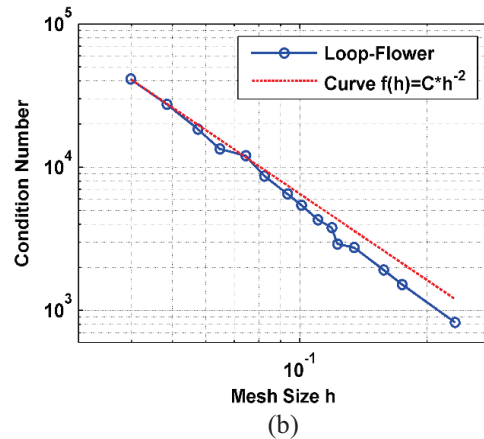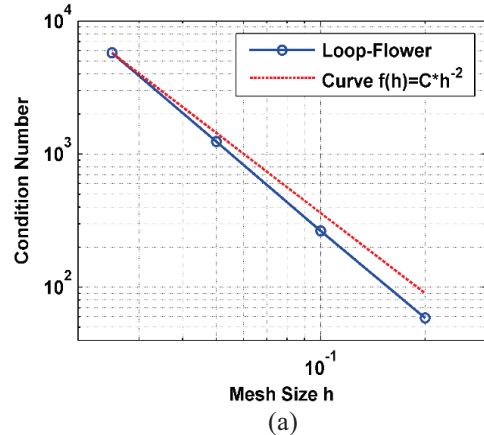
Fig. 4. Reduced condition number of loop-flower Gram matrix: (a) square plate, and (b) sphere.

B. Performance of loop flower basis functions

In this part, the structures are under the excitation of x-polarized plane waves with amplitude of 1 V/m and frequency of 300 Hz, traveling along $-z$ axis.

A PEC cylinder is analyzed in this part. The radius of the cylinder is 0.5 m and the height is 2 m. The surface mesh contains 3372 triangles, 5058 edges and 1688 nodes. Figure 5 shows the RCS calculated by LS bases, LF bases. The result obtained by LF bases agrees well with LS bases.

Convergence results for LS bases and LF basis functions are given in Fig. 6 with conjugate gradient (CG) iteration. It can be seen that iteration associated with LF bases converge fast compared with LS basis functions. It took the LS bases 154920 times of iterations to achieve a relative residual error of 10^{-6}, while LF bases 4203 times of iterations.

Furthermore, the total CPU time of LS solver is 13350 seconds, which is about 30 times more than LF with the CPU time of 453 seconds only.
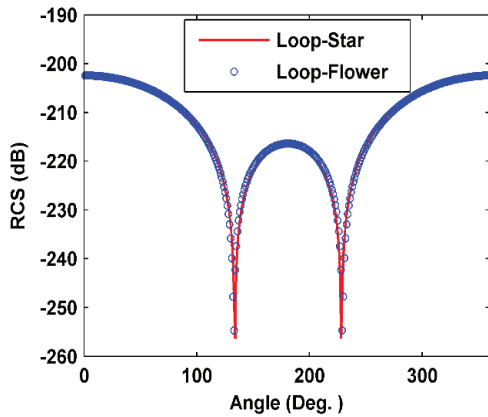
Fig. 5. BiRCS solutions for a PEC cylinder when the frequency equals to 300 Hz.
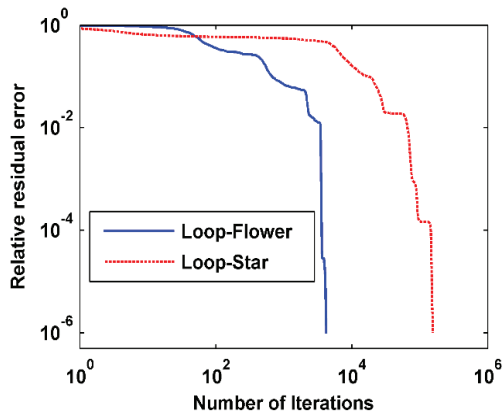
Fig. 6. Relative residual error versus number of iterations for a PEC cylinder scattering problems when frequency is 300 Hz.

VI. CONCLUSION

We have analyzed flower basis functions based on RWG-connected graphs which are generated according to RWG basis functions. The number of zero eigenvalues of the Laplacian matrix associated with the RWG-connected graph equals to the number of redundant nodes of flower basis functions. In addition, the maximum singular value of flower Gram matrix is bounded, and the reduced condition number of flower Gram matrix grows as h^{-2}. Furthermore, the reduced condition number of loop-flower basis functions also has a growth as h^{-2} and the condition behavior of the Gram matrix becomes worse with increase of the mesh density.

Loop-flower basis functions are efficient to overcome the low frequency breakdown. Compared with loop-star basis functions, the linear EFIE system with loop-flower basis functions has a better conditioning. The numerical results demonstrate the excellent performance of loop-flower basis functions.

ACKNOWLEDGMENT

REFERENCES

[1] F. P. Andriulli, A. Tabacco, and G. Vecchi, "Solving the EFIE at low frequencies with a conditioning that grows only logarithmically with the number of unknowns," *IEEE Trans. Antennas Propagat.*, vol. 58, no. 5, pp. 1614-1624, May 2010.

[2] S. B. Adrian, F. P. Andriulli, and T. F. Eibert, "Hierarchical bases preconditioners for the electric filed integral equation on multiply connected geometries," *IEEE Trans. Antennas Propagat.*, vol. 62, no. 11, pp. 5856-5861, Nov. 2014.

[3] F. P. Andriulli, K. Cools, I. Bogaert, and E. Michielssen, "On a well-conditioned electric field integral operator for multiply connected geometries," *IEEE Trans. Antennas Propagat.*, vol. 61, no. 4, pp. 2077-2087, Apr. 2013.

[4] M. Burton and S. Kashyap, "A study of a recent, moment-method algorithm that is accurate to very low frequencies," *Appl. Computat. Electromagn. Soc. J.*, vol. 10, no. 3, pp. 58-68, Nov. 1995.

[5] G. Vecchi, "Loop-star decomposition of basis functions in the discretization of the EFIE," *IEEE Trans. Antennas Propagat.*, vol. 47, no. 2, pp. 339-346, Feb. 1999.

[6] J.-F. Lee and R. J. Burkholder, "Loop star basis functions and a robust preconditioner for EFIE scattering problems," *IEEE Trans. Antennas Propagat.*, vol. 51, no. 8, pp. 1855-1863, Aug. 2003.

[7] J.-S. Zhao and W. C. Chew, "Integral equation solution of Maxwell's equations from zero

frequency to microwave frequencies," *IEEE Trans. Antennas Propagat.*, vol. 48, no. 10, pp. 1635-1645, Oct. 2000.

[8] T. F. Eibert, "Iterative-solver convergence for loop-star and loop-tree decompositions in method-of-moments solutions of the electric-field integral equation," *IEEE Antennas Propagation Magazine*, vol. 46, no. 3, pp. 80-85, Jun. 2004.

[9] F. P. Andriulli, K. Cools, H. Bagci, F. Olyslager, A. Buffa, S. Christiansen, and E. Michielssen, "A multiplicative Calderon preconditioner for the electric field integral equation,". *IEEE Trans. Antennas Propagat.*, vol. 56, no. 8, pp. 2398-2412, Aug. 2008.

[10] A. Buffa and S. H. Christiansen, "A dual finite element complex on the barycentric refinement," *Mathematics of Computation*, vol. 76, no. 260, pp. 1743-1769, Oct. 2007.

[11] G. Xiao, "Applying loop-flower basis functions to analyze electromagnetic scattering problems of PEC scatterers," *Int. J. Antennas Propag.*, vol. 2014, pp. 9, article ID 905925, 2014.

[12] Y. Hou and G. Xiao, "Properties of the Gram matrices associated with loop-flower basis functions," *PIERS Proceedings*, Guangzhou, China, pp. 2316-2321, Aug. 2014.

[13] X. Tian, G. Xiao, and J. Fang, "Application of loop-flower basis functions in the time-domain electric field integral equation," *IEEE Trans. Antennas Propagat.*, vol. 63, no. 3, pp. 1178-1181, Mar. 2015.

[14] A. Brualdi Richard, *The Mutually Beneficial Relationship of Graphs and Matrices*, vol. 115, American Mathematical Soc., 2011.

[15] R. Grone, R. Merris, and V. S. Sunder, "The Laplacian spectrum of a graph," *SIAM Journal on Matrix Analysis and Applications*, vol. 11, no. 2, pp. 218-238, 1990.

[16] X. D. Zhang, "The Laplacian eigenvalues of graphs: a survey," *arXiv preprint arXiv: 1111.2897*, 2011.

[17] F. P. Andriulli, "Loop-star and loop-tree decompositions: analysis and efficient algorithms," *IEEE Trans. Antennas Propagat.*, vol. 60, no. 5, pp. 2347-2356, May 2012.

[18] A. Quarteroni and A. Valli, *Numerical Approximation of Partial Differential Equations*, Berlin: Springer, 1997.

[19] D. Carlson, "Minimax and interlacing theorems for matrices," *Linear Algebra and its Applications*, vol. 54, pp. 153-172, 1983.

Yibei Hou received the B.S. degree from University of Electronic Science and Technology of China (UESTC), Chengdu, China, in 2014, and is currently pursuing the Ph.D. degree in Electronic Engineering at Shanghai Jiao Tong University, Shanghai, China. His research interests include computational electromagnetics and its application in scattering and radiation problems.

Gaobiao Xiao received the M.S. degree from Huazhong University of Science and Technology, Wuhan, China, in 1988, the B.S. degree from the National University of Defense Technology, Changsha, China, in 1991, and the Ph.D. degree from Chiba University, Chiba, Japan, in 2002. He worked in Hunan University, Changsha, China, from 1991 to 1997. Since April 2004, he has been a Faculty Member in the Department of Electronic Engineering, Shanghai Jiao Tong University, Shanghai, China. His research interests are numerical methods in electromagnetic fields, coupled thermo-electromagnetic analysis, microwave filter designs, fiber-optic filter designs, and inverse scattering problems.

Jinpeng Fang received his M.E. from Shanghai Jiao Tong University, Shanghai, China, in 2010. From 2010 on, he's worked as a RF Engineer of Shanghai Key Laboratory of Electromagnetic Environmental Effects for Aerospace Vehicle. His main research interests include simulation and measurement of the effect of electromagnetic environment, electromagnetic scattering properties of objects.

A Solution of One-Dimensional Stationary Schrödinger Equation by the Fourier Transform

V. M. Fitio [1], I. Y. Yaremchuk [1], V. V. Romakh [1], and Y. V. Bobitski [1,2]

[1] Department of Photonics
Lviv Polytechnic National University, Lviv, 79013, Ukraine
polyana@polynet.lviv.ua, yaremchuk@polynet.lviv.ua, vladykv@gmail.com

[2] Institute of Technology
University of Rzeszów, Rzeszów, 35959, Poland
bobitski@polynet.lviv.ua

Abstract ─ In this paper, a new numerical method for solving of one-dimensional stationary Schrödinger equation has been presented. The method is based on the Fourier transform of a wave equation. It is shown that, as a result we obtain an integral equation where integral is replaced by sum. A main problem is transformed in the eigenvalue/eigenvector problem which corresponds to discrete energy levels as well as the Fourier transform of wave functions. Wave function is obtained by usage of the inverse Fourier transform. Discrete energy levels are split and form the forbidden and permitted zones for the one-dimensional finite crystal. The method is tested in many examples, and it is characterized by high accuracy and stability of search of the discrete energy levels.

Index Terms ─ Convolution, energy levels, Fourier transform, Schrödinger equation.

I. INTRODUCTION

Quantum wells [1] emerging in semiconductor heterostructures have recently become the subject of significant scientific interest. They are often studied since their physical effects can be seen at room temperature and can be exploited in real devices [2]; for example, as a primary component of a number of optoelectronic devices such as: photo-detectors in infrared spectral range [3], quantum cascade lasers [4] and other optoelectronic devices [5]. A detailed theory of optoelectronic devices based on quantum wells is offered by Bastard in [6].

An analysis of devices based on quantum wells requires a solution of the stationary Schrödinger equation solution is reduced to the transcendental equation if a potential well has a rectangular form. In case of two or more rectangular wells, the obtained transcendental equation becomes much more complicated. In addition, a solution becomes more difficult if the potential well hasn't a rectangular barrier. Precise solutions of one-dimensional stationary Schrödinger equation [7] have been obtained only for a small number of functional dependencies of a well potential. For this reason, search of solutions of one-dimensional Schrödinger stationary equation continues; moreover, there are attempts to form potential energy in such a way to obtain a precise analytical solution of the corresponding equation [8-10].

A similar problem exists at the finding of propagation constants of waveguide modes in the gradient planar waveguides [11-16]. The methods described in [12-16] can be used for solving the Schrödinger equation as a structure of the wave equation is identical to the one-dimensional stationary Schrödinger equation for planar waveguides. On the other hand, the approaches developed in quantum mechanics, for instance, the WKB approximation [11], can be used to search propagation constants of gradient planar waveguides.

The current state of computer technologies and the sophistication of software allow applied numerical methods to solve equations of the various types. The numerical method ensures high accuracy, and it is relatively simple. It enables its application in quantum mechanics and waveguide technologies. A well-known numerical method to find propagation constants of waveguide modes [16] is based on replacing the second derivative of the wave equation by the difference operator. The solution is reduced to the eigenvalue/eigenvector problem in this method. This method also can be used to search discrete energy levels of the stationary Schrödinger equation. However, it doesn't offer high accuracy. In addition, the evidence of

numerical differentiation is found as a source of noise due to approximation in the numerical process.

It should be noted that, the known methods of searching the discrete levels of energy (searching of propagation constants of waveguide modes) are based on the solution of a wave equation in a coordinate domain. The relevant wave functions and the primary derivatives of coordinate x at $\pm\infty$ are zero for discrete levels of energy. Therefore, there is the Fourier transform [17] of a wave function, and the appropriate wave equation can be transformed into a frequency domain by the Fourier transform. At the same time, integral equation will be obtained and also can be solved by numerical methods.

The aim of this study is to develop a new numerical method to solve the Schrödinger one-dimensional stationary equation using the Fourier transform, and demonstrate some advantages in comparison with the known methods. The second section of this paper is devoted to numerical implementation of the method proposed. The third section presents the results of the numerical analysis of the stationary Schrödinger equation for certain functional dependencies of the potential energy. The fourth section presents the results of the solution of the Schrödinger one-dimensional stationary equation in accordance with the method proposed for the one-dimensional crystal which has several periods.

II. ONE-DIMENSIONAL SCHRÖDINGER WAVE EQUATION AND ITS FOURIER TRANSFORM

The one-dimensional stationary Schrödinger equation is:

$$-\frac{\hbar^2}{2m}\frac{d^2\psi(x)}{dx^2}+U(x)\psi(x)=E\psi(x),\qquad(1)$$

where $U(x)$ is a potential energy of particle which has only discrete values, $\psi(x)$ is a wave function.

Dimensionless equation is used [7] frequently in quantum mechanics, which is obtained by replacing the variables. The dimensionless equation (1) can be presented as:

$$-\frac{d^2\psi(x)}{dx^2}+U(x)\psi(x)=E\psi(x).\qquad(2)$$

Function $\psi(x)$ is a solution of the stationary Schrödinger equation, which corresponds to discrete levels of energy, and their primary derivatives tend to zero at $x \to \pm\infty$. Therefore, the Fourier transform for these functions as well as for their primary and secondary derivatives exists. Let's write the appropriate proportions for $\psi(x)$. Thus, the Fourier transform of $\psi(x)$ and its primary and secondary derivatives are zero [17], and it can be written as follows:

$$\psi(u)=\int_{-\infty}^{\infty}\psi(x)\exp(-i2\pi ux)dx,\qquad(3)$$

$$i2\pi u\psi(u)=\int_{-\infty}^{\infty}\frac{d\psi(x)}{dx}\exp(-i2\pi ux)dx,\qquad(4)$$

$$-(2\pi u)^2\psi(u)=\int_{-\infty}^{\infty}\frac{d^2\psi(x)}{dx^2}\exp(-i2ux)dx.\qquad(5)$$

In addition, for functions for which a Fourier transform exists, the next conditions are satisfied [17]:

$$F\{g(x)\}=G(u),\ F\{h(x)\}=H(u),$$
$$F\{g(x)h(x)\}=\int_{-\infty}^{\infty}G(u-v)H(v)dv,\qquad(6)$$

where $F\{...\}$ is the Fourier transform. Expression (6) describes the content of the convolution theorem.

Let's execute the Fourier transform of left and right parts of equation (2) by using equations (3), (5) and (6). As a result we obtain:

$$4\pi^2u^2\psi(u)+\int_{-\infty}^{\infty}U(u-v)\psi(v)dv=E\psi(u).\qquad(7)$$

Therefore, we have moved from the differential equation (2) for eigenfunctions and eigenvalues to the integral one equation (7). In the last equation we can replace integral by sum, so the continuous values u and v can be replaced by discrete ones:

$$4\pi^2(s\Delta)^2\psi(s\Delta)+\sum_{p=-(N-1)/2}^{(N-1)/2}U(s\Delta-p\Delta)\psi(p\Delta)\Delta=E\psi(s\Delta),(8)$$

where $\Delta=u_{max}/N$, $u_s=s\Delta$, $v_p=p\Delta$, $-(N-1)/2\le s$, $p\le(N-1)/2$, s and p are integers; $|u|\ge u_{max}/2$; values of $\psi(x)$ are almost equal to zero. Value of N must be large and preferably unpaired. Obviously, sum in equation (8) should have N elements.

Let's write the last equation for all discrete spatial frequencies $u_s=s\Delta$, where s changes between $-(N-1)/2$ and $(N-1)/2$. Then a set of equations in the amount of N can be written in a matrix form, where E is common for all values of s:

$$(\mathbf{P}+\mathbf{U})\psi=E\psi,\qquad(9)$$

where $\mathbf{P}$ is a diagonal matrix with elements $4(\pi s\Delta)^2$, $\mathbf{U}$ is a square symmetric matrix with elements $U(s\Delta-k\Delta)$, ψ is a vector-column with elements $\psi(s\Delta)$.

Therefore in the last case, the problem is reduced to the problem of eigenvalues (energy) and eigenvectors (the discrete Fourier transform of $\psi(x)$) which corresponds to the given value of energy. We can have many eigenvalues and its corresponding eigenvectors. By carrying out the inverse discrete Fourier transform of eigenvector, we obtain the eigenfunction $\psi(x)$. All eigenvalues (discrete levels of energy) are determined

inside the potential well for quantum-mechanical problems. If, the potential well has finite depth, then the precision is determined by N and Δ. If, the potential energy varies from zero to infinity (for example $U = x^2$), then in this method the potential energy is limited; i.e., it serves up to a certain value as $U(x)$, and further acquires a constant value. Obviously, in this case, the lowest levels of energy can be determined with the highest accuracy. In our numerical calculations whose results are presented below, we used the simplest way to replace integral by sum.

III. EXAMPLES OF NUMERICAL SIMULATION

Example 1. Schrödinger equation according to equation (2), for which potential energy is:

$$U = \begin{cases} x^2, & |x| \le a, \\ a^2, & |x| > a = 7 \end{cases}.$$

Numerical process parameters are: sampling number $N = 1001$, maximum frequency $u_{max} = 8.0$. The 25 eigenvalues of energy are obtained by numerical calculations. There are 13 lowest energy levels which have next values: $E_0 = 1.0000000025$, ..., $E_6 = 13.00000000025$, ..., $E_{12} = 24.999999971$, and they accurately fit the data of [7], where $E_n = 2n + 1$. However, error is large enough at potential energy $U(x) = x^2$ for $E_{24} = 48.64036656$, which is sufficiently accurate for our model potential. Figure 1 shows the wave functions (not normalized) for the three lowest values of energy. One can see well that points fit with continuous curves.

Example 2. Schrödinger equation according to equation (2) where potential energy is:

$$U = \begin{cases} x^4, & |x| \le a, \\ a^4, & |x| > a = 3 \end{cases}.$$

Numerical process parameters are next: $N = 1001$, $u_{max} = 25$. The 11 smallest eigenvalues E_n are found at these data, there are: $E_0 = 1.0603646$, ..., $E_5 = 21.238375$, ..., $E_{10} = 50.256257$. This quantum problem is not solved precisely by analytical methods, therefore the value of the lowest level of energy is found by approximation at which $E_0 \approx 1.156194$ [7]. In other words, the approximate value is found with a large error. In addition, this problem can be solved by the numerical difference method [16], however, it offers solutions with low accuracy: $E_0 = 1.0603593$, ..., $E_5 = 21.237897$, ..., $E_{10} = 50.253695$.
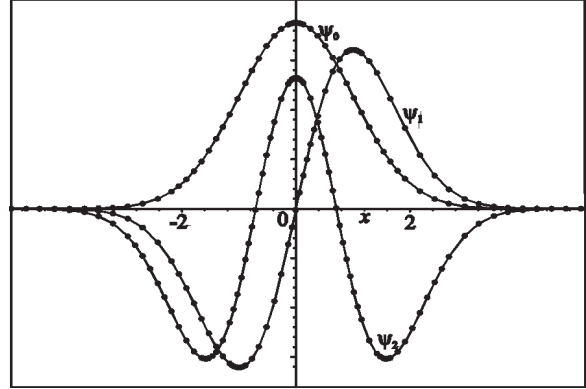
Fig. 1. Wave functions of the three lowest energy levels. The continuous curves correspond to exact wave functions, while the points correspond to the results of calculation obtained by the method proposed in this study.

IV. NUMERICAL SIMULATION OF ONE-DIMENSIONAL CRYSTAL

One-dimensional crystal consists of periodic placement of potential wells, which are described by the following analytical function:

$$U(x) = a - a \exp(-\pi x^2), \qquad (10)$$

where a is a certain positive number determining the depth of a potential well.

The Fourier transform of this function is:

$$F\{U(x)\} = a\delta(u) - a \exp(-\pi u^2). \qquad (11)$$

If we have N_1 number of periodically placed (N_1 is unpaired) potential wells on a distance Λ from each other, we will receive one-dimensional crystal, whose potential energy will be described as following expression:

$$U(x)_{kr} = a - a \sum_{n=(N_1-1)/2}^{(N_1-1)/2} \exp\left[-\pi(x - n\Lambda)^2\right]. \qquad (12)$$

After simple mathematical transformations we obtain the Fourier transform of equation (12):

$$F\{U(x)_{kr}\} = a\delta(u) - a \exp(-\pi u^2)\frac{\sin[\pi N_1 \Lambda u]}{\sin(\pi \Lambda u)}. \qquad (13)$$

The five energy levels are found ($a = 100$): $E_0 = 16.539595$, $E_1 = 47.036248$, $E_2 = 72.011285$, $E_3 = 90.446940$, $E_4 = 99.832730$ for the potential energy according to equation (10) at parameters of the numerical process $N = 1001$ and $u_{max} = 10 \div 20$.

A more detailed dependence of the calculated energy levels as function on u_{max} is presented in Table 1. Table 2 shows the dependence of the calculated energy levels on N at $u_{max} = 15$. Analysis of Table 1 indicates

that there is a frequency range at sufficiently large N in which values of energy are constant (these values of energy in the Tables are shown in bold).

Four levels are split into 11 sublevels and form the permitted zones, but level E_4 splits only into two

sublevels: $E_{4,0} = 99.041696$ and $E_{4,1} = 99.551008$.

The widths of permitted zones increase with the increase of energy. The fact that the fourth level splits into two sublevels only can be understood from Fig. 2.

Table 1: The dependence of the calculated energy levels on u_{max} at $N = 1001$

u_{max}	4	6	10	14	20	24	28
E_0	16.54607358	16.53959718	16.53959510	16.53959509	16.53959509	16.53959509	16.53959510
E_1	47.08219239	47.03626733	47.03624767	47.03624767	47.03624767	47.03624767	47.03624768
E_2	72.15044578	72.01136385	72.01128540	72.01128540	72.01128540	72.01128540	72.01128541
E_3	90.66025796	90.44709161	90.44693968	90.44693968	90.44693968	90.44693968	90.44693969
E_4	99.88445912	99.83277513	99.83272955	99.83272955	99.83272955	99.83272950	99.832729002

Table 2: The dependence of the calculated energy levels on N at $u_{max} = 15$

N	101	201	401	601	801	1001	1501
E_0	16.53959512	16.53959510	16.53959511	16.53959509	16.53959509	16.53959509	16.53959509
E_1	47.03624768	47.03624766	47.03624768	47.03624767	47.03624767	47.03624767	47.03624767
E_2	72.01128540	72.01128539	72.01128542	72.01128540	72.01128540	72.01128540	72.01128540
E_3	90.44694122	90.44693968	90.44693970	90.44693968	90.44693968	90.44693968	90.44693968
E_4	99.76898968	99.82787662	99.83270759	99.83272945	99.83272955	99.83272955	99.83272955
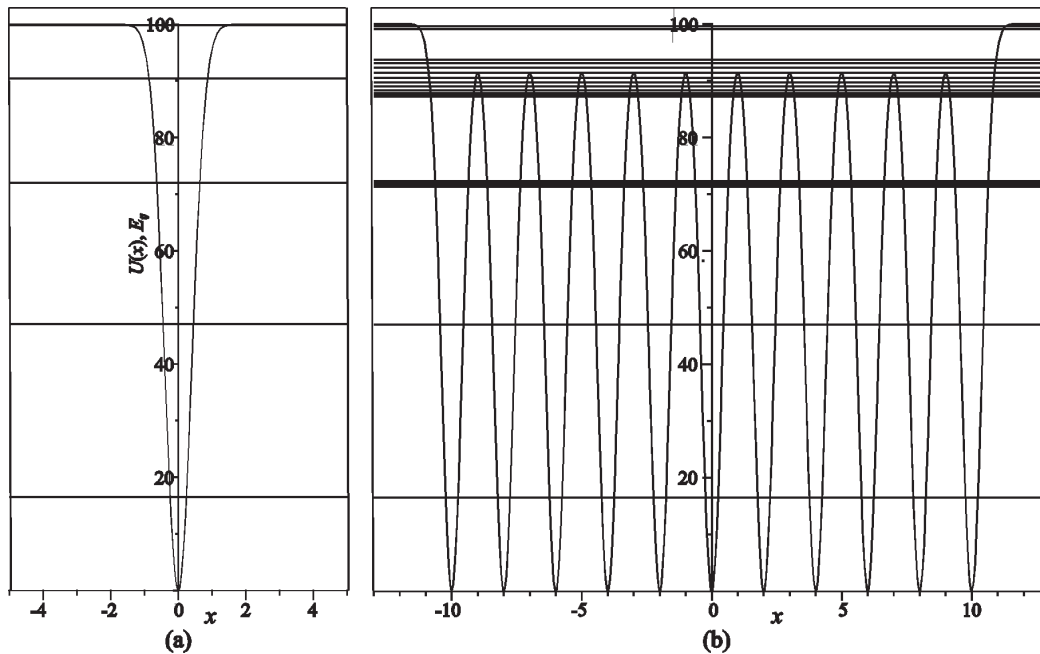
Fig. 2. Dependence of potential energy on the coordinate and energy level (horizontal line): (a) single potential well, and (b) one-dimensional crystal.

The numerical analysis of one-dimensional crystal was carried out at the following parameters: $N = 1001$, $u_{max} = 25$, $\Lambda = 2$.

Figure 2 demonstrates the potential energies and energy levels for single potential well and one-dimensional crystal. The scales of Figs. 2 (a) and 2 (b)

are vertically the same; the starting point of the coordinates for both pictures is combined. The lowest level is split to the least degree: $E_{0,10} = 16.533261$. Level E_3 is split at most: $E_{3,0} = 87.157709$, $E_{3,10} = 93.704412$.

Table 2 leads to a conclusion that the calculated energy tends toward a certain value at increase of N for certain frequencies.

V. CONCLUSION

The new numerical method for solving stationary Schrödinger equation based on the Fourier transform is developed. The integral equation is obtained as a result of mathematical manipulations. The next step is to obtain the eigenvalue/eigenvector problem by replacing integral by sum and to write the corresponding equation for a set of discrete frequencies, where the eigenvalues correspond to energy levels and eigenvectors do to the discrete Fourier transforms of wave functions. Carrying out the inverse Fourier transform of the eigenvector, the wave function in a coordinate domain is obtained. The method is tested on a number of examples, and it shows high accuracy of the energy levels for a single potential energy. The method is characterized by numerical stability.

The discrete levels of energy have been determined for one-dimensional crystal, consisting of 11 regularly placed potential wells. It demonstrates that discrete levels are split and form permitted zones during the formation of one-dimensional crystal, and the multiplicity of splitting equals to a number of potential wells that form one-dimensional crystal. The energy width of the permitted zone expands at the increase of energy of corresponding discrete level of a single potential well. This conclusion is consistent with the data of [18].

ACKNOWLEDGMENT

REFERENCES

[1] L. C. West and S. J. Eglash, "First observation of an extremely large dipole infrared band of a GaAs quantum well," *Appl. Phys. Lett.*, vol. 46, pp. 1156-1158, 1985.

[2] J. Faist, F. Capasso, A. L. Hutchnson, L. Pfeiffer, and K. W. West, "Suppression of optical absorption by electric-field-induced quantum interference in coupled potential wells," *Phys. Rev. Lett.*, vol. 71, pp. 3573-3576, 1993.

[3] B. F. Levine, "Quantum-well infrared photodetectors," *J. Appl. Phys.*, vol. 74, pp. R1-R81, 1993.

[4] J. Faist, P. Capasso, D. L. Sivco, C. Sirtori, A. L. Hutchnson, and A. Y. Cho, "Quantum cascade laser," *Science*, vol. 264, pp. 553-556, 1994.

[5] S. Noda, T. Yamashita, M. Ohya, Y. Muromoto, and A. Sasaki, "All-optical modulation for semiconductor lasers by using three energy levels in n-doped quantum wells," *IEEE J. Quantum Electron.*, vol. 29, no. 6, pp. 1640-1647, 1993.

[6] G. Bastard, *Wave Mechanics Applied to Semiconductor Heterostructures*, Les editions de physique, Les Ulis, France, 1988.

[7] I. O. Vakarchuk, *Quantum Mechanics*, Second edition, Ivan Franko Lviv National University, Lviv, 2004.

[8] A. Caticha, "Construction of exactly soluble double-well potentials," *Physical Review A*, vol. 51, pp. 4264-4267, 1995.

[9] A. S. Dutra, "Conditionally exactly soluble class of quantum potentials," *Physical Review A*, vol. 47, pp. R2435-2437, 1993.

[10] V. M. Tkachuk and T. V. Fityo, "Multidimensional quasi-exactly solvable potentials with two known eigenstates," *Phys. Lett. A*, vol. 309, pp. 351-356, 2003.

[11] A. Gedeon, "Comparison between rigorous theory and WKB-analysis of modes in graded-index waveguides," *Opt. Commun.*, vol. 12, no. 3, pp. 329-332, 1974.

[12] R. E. Smith, S. N. Houde-Walter, and G. W. Forbes, "Mode determination for planar waveguide using the four-sheeted dispersion relation," *J. Quantum Electronics*, vol. 26, no. 4, pp. 627-630, 1990.

[13] E. Anemogiannis and E. N. Glytsis, "Multilayer waveguides: efficient numerical analysis of general structures," *J. Lightwave Technol.*, vol. 10, no. 10, pp. 1344-1351, 1992.

[14] A. K. Chatak, K. Thyaagarajan, and M. R. Shenoy, "Numerical analysis of planar optical waveguides using matrix approach," *J. Lightwave Technol.*, vol. 5, no. 5, pp. 660-667, 1987.

[15] T. Baba and Y. Kokubun, "Dispersion radiation loss characteristics of antiresonant reflecting optical waveguides-numerical results and analytical expressions," *J. Quantum Electronics*, vol. 28, no. 7, pp. 1689-1700, 1992.

[16] A. G. Rganov and S. E. Grigas, "Numerical algorithm for waveguide and leaky modes determination in multilayer optical waveguides," *Technical Physics*, vol. 55, pp. 1614-1618, 2010.

[17] J. W. Goodman, *Introduction to Fourier Optics*, McGraw-Hill Book Company, 1968.

[18] C. Kittel, *Introduction to Solid State Physics*, Fourth edition, John Wiley and Sons, Inc., 1978.

Fitio Volodymyr was born in Lviv, Ukraine, in 1950. He graduated from the Department of Radiophysics and Radioelectronics, Ivan Franko National University of Lviv in 1974, and received the both Ph.D degree in 1998 and Doctor habilitation in Optics and Laser Techniques from the Institute of Physics of NAS of Ukraine in 2009.

His research interests include holography, diffraction by periodical and chaotic structures, distribution light by waveguide, feedback lasers and the application of numerical methods for the analysis and design of optic elements and devices. He has more than 150 papers in international journals and proceedings of international and national symposia.

Yaremchuk Iryna was born in Lviv, Ukraine, in 1980. She graduated from the Department of Semiconductors, Ivan Franko National University of Lviv in 2004, and received the Ph.D degree in Optoelectronics Systems from the Institute of Semiconductors Physics of NAS of Ukraine in 2009.

Her research interests include diffraction by periodical structures, plasmonics and the numerical methods for the analysis and design elements to some engineering optical applications. She has more than 50 papers in international journals and proceedings of international and national symposia.

Romakh Volodymyr was born in Lviv, Ukraine in 1991. He received the M.Sc. in Laser and Optoelectronics Engineering from the Lviv Polytechnic National University, Ukraine. He is currently working towards his PhD Degrees at the Photonics Department.

His research interests include design and analysis of distribution of electromagnetic wave in active and passive waveguides.

Yaroslav Bobitski was born in Lviv, Ukraine, in 1951. He graduated from the Department of Automated Control Systems, Lviv Polytechnic National University in 1974, and received the both Ph.D degree in 1980 and Professor Habilitation in Technology of materials for electronic devices from the Lviv Polytechnic National University in 1991. He is the head of the Photonics Department.

His research interests include distribution light by nanostructured systems, interaction laser irradiation with layered media. He has more than 150 papers in international journals and proceedings of international and national symposia.

Compact Microwave Impedance Matching Using Patterned Conducting Planes

A. Ghajar and H. Ghorbaninejad

[1] Department of Electrical Engineering
University of Guilan, Rasht, Iran
alighajar1990@gmail.com

[2] Department of Electrical Engineering
University of Guilan, Rasht, Iran
ghorbaninejad@guilan.ac.ir

Abstract ─ In this paper, a novel structure for impedance matching in microwave frequency range is introduced. The proposed structure utilizes one or more patterned conducting planes, which are placed transversely in a waveguide. The patterned conducting planes act as frequency selective surfaces for impedance matching purposes. The Green's function of one or more desired patterned planes, considering coupling effects between them, is obtained. Then magnetic field integral equations, in terms of unknown magnetic currents of patterned planes, are calculated and solved using method of moment. The suitable pattern of a patterned plane is obtained using optimization by genetic algorithm, so that the return loss of whole structure, in the desired frequency range vanishes.

The proposed structure, compared with traditional impedance matching structures, is very compact and wideband. It has been shown that its length, in comparison with another compact and wideband microwave impedance matcher, is fifty times shorter.

The usefulness of the proposed structure and its performance is verified in some examples, and the response of designed impedance matchers are compared with the results of simulations.

Index Terms ─ Frequency selective surfaces, genetic algorithm, impedance matching, magnetic field integral equation, patterned conducting planes.

I. INTRODUCTION

Impedance matching structures are very important parts of microwave systems. Impedance matching is necessary in the input of waveguide type power dividers and antennas [1-3]. The most important goal of impedance matching is maximum power delivery from the source to the load.

Some considerations in the design of impedance matching structures are complexity of implementation,

adjustability, compactness and depending on the application, matching may be required over a band of frequencies, such that the bandwidth of the matching network is an important design parameter. Many approaches has been investigated for impedance matching in microwave devices such as using irises, rods, apertures, posts, and lumped microwave elements [1-4]; which could be used only for narrow band matching, i.e., a few percent. Other approaches are multi-section quarter-wave transformers, tapered homogeneous dielectrics filled waveguide [5,6], longitudinally inhomogeneous waveguides (LIWs) [7], and tapered or stepped transformer [8], whose length often is long; besides, construction of LIWs is not such practical.

In this article, we proposed patterned dielectric backed conducting planes as an impedance matcher, which is located transversely in a waveguide. Conducting plane of suitable pattern, supported by a dielectric layer acts as a frequency selective surface (FSS), which has many applications in microwave and antenna engineering. FSS improves the gain and return loss of antennas [9,10], it can also shift the phase of incident electromagnetic waves, and this characteristic could be used for beam steering of antenna [11], increases antenna gain, even for ultra-wide frequency band [12], transforms linear polarization to circular [13]. Also, it has been used as spatial microwave filter [14], and it has capability of switching between reflection and transmission for incident waves that was used for modifying the electromagnetic architecture of buildings [15].

Frequency response of a dielectric backed conducting plane such as its bandwidth, depends on the pattern of the plane, thickness and electric permittivity of the supported layer. So, using dielectric backed conducting planes in the structure of an impedance matcher, makes it possible to achieve compact

impedance matching devices. In addition, according to the frequency selectivity of such planes, wide band or multiband impedance matcher can be designed. Design procedure is based on deriving magnetic field integral equations in terms of unknown magnetic currents of patterned conducting plane which can be solved using the method of moment. Suitable pattern for a desired specification can be extracted by genetic algorithm optimization.

II. DESIGN METHOD

Figure 1 (a) shows three dimensional view of the proposed impedance matcher, consisting of one dielectric backed patterned conducting plane which is located transversely in a waveguide. This structure is a two dimensional symmetric structure. Relative permittivity of dielectric layer is ε_r with thickness of d. Figure 1 (b) illustrates side view of the structure.

According to equivalence theorem, the equivalent magnetic current of the proposed structure in two regions has been shown in Fig. 1 (c). Using spectral domain immitance approach [16,17], one can derive magnetic type dyadic Green's functions in two side of conducting plane.

As it has been shown in Fig. 1 (c), the electric and magnetic fields in region of z<0 is due to induced magnetic current on the aperture parts of patterned plane and incident wave, which is TE_{10} mode, while fields in region of z>0 is only due to induced magnetic current on the aperture parts of patterned plane.

Then magnetic fields, in two side of the conducting plane, in terms of their spectral Green's function and magnetic current, were obtained. Then boundary condition of transverse magnetic fields across the aperture parts of the patterned plane must be satisfied. A coupled set of magnetic field integral equations is obtained by enforcing continuity of tangential component of magnetic fields at z=0.

Expressing the magnetic fields, in term of their spectral magnetic type Green's function, makes it possible to use the method of moment with traditional x- and y-directed piece-wise linear or triangle basis and testing functions. So, integral equations are converted into linear equations.

To derive linear equations, unknown magnetic currents can be considered as follows:

$$\mathbf{M}_x = \sum_{l=1}^{C(R-1)} \mathbf{C}_x B_l^x, \tag{1}$$

$$\mathbf{M}_y = \sum_{l=1}^{R(C-1)} \mathbf{C}_y B_l^y, \tag{2}$$

where B_l^x, and B_l^y are the x-directed and y-directed triangular sub-domain basis functions for $\mathbf{M}_x$ and $\mathbf{M}_y$ representation, and R and C are the number of subsections at x direction and y direction, respectively.

By applying Galerkin's method, the following matrix equations are obtained:

$$\mathbf{Z}_1\mathbf{C}_x + \mathbf{Z}_2\mathbf{C}_y = \mathbf{U}_x^{inc}, \tag{3}$$

$$\mathbf{Z}_3\mathbf{C}_x + \mathbf{Z}_4\mathbf{C}_y = \mathbf{U}_y^{inc}. \tag{4}$$

Each of above matrices has been given in the appendix. $\mathbf{C}_x$ and $\mathbf{C}_y$ are obtained by solving equations, and then x-directed and y-directed magnetic currents can be achieved.
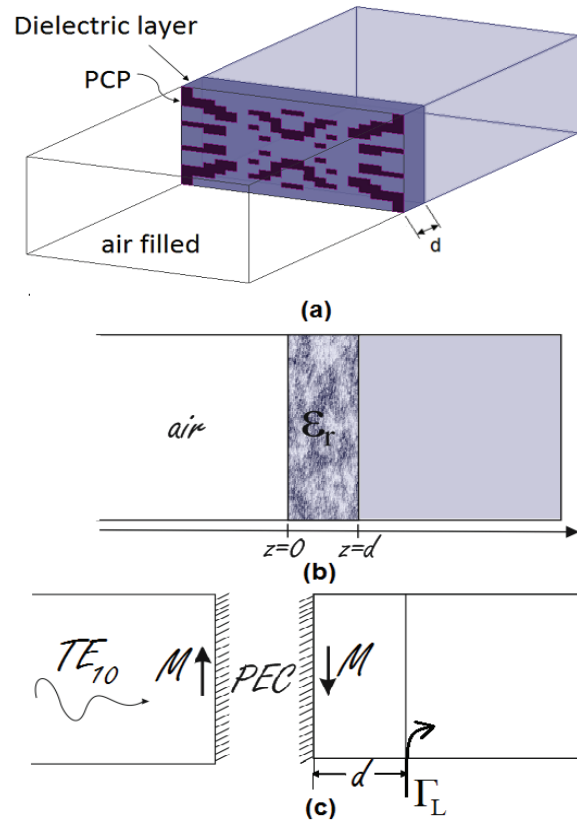
Fig. 1. The structure of proposed impedance matcher: (a) three dimensional view, (b) side view, and (c) equivalent structure of Fig. 1 (a).

The amplitude of reflected wave at z=0, is calculated by the following equation:

$$A^- = \frac{1}{P}\int_v \mathbf{H}_{inc}^+ \cdot \mathbf{M}_x \, dv, \tag{5}$$

where P is the total incident power, and $\mathbf{H}_{inc}$ is the magnetic field of dominant mode. So, reflection coefficient can be obtained from the following equation:

$$S_{11} = \frac{-\left|\mathbf{H}_{inc}^x\right| + A^-}{\left|\mathbf{H}_{inc}^x\right|}. \tag{6}$$

It is aimed to achieve a specific pattern for patterned conducting plane, so that a desired reflection coefficient for the impedance matcher, in a given frequency range,

can be obtained. This procedure is performed with MATLAB GA tool.

For this purpose, the cross-section area of waveguide is divided into $R \times C$ subsections. Non-metalized parts and metalized parts are presented in terms of 1 s and 0 s in the GA, respectively. Also, GA population type is set to bit string, consisting of 0 and 1 binary digits. Also, those are produced with uniform creation function.

Here, based on the symmetry excitation requirements (incident plane wave), it is assumed that the pattern of the patterned conducting plane is symmetric respect to horizontal and vertical axes of the waveguide cross-section. Consequently, GA operated only on one quarter region of cross-section [14].

The designing method is based on the optimization of a suitable fitness function so that, return loss of the structure can be adjusted to the desired return loss in the frequency range. The following fitness function is defined here:

$$ fitness = \sqrt{\frac{1}{M}\sum_{m=1}^{M}\left|20\log\left|S_{11}\left(f_m\right)\right| - (\text{desired RL})\right|^2}, \quad (7) $$

where $S_{11}\left(f_m\right)$ are reflection coefficient of the structure at frequency samples, calculated with mentioned manner and M is the number of frequency samples in the frequency range.

III. EXAMPLES AND RESULTS

A. Example I

In the first example, an impedance matching network in a frequency range from 8 to 12 GHz (X-band) using a waveguide with dimensions of 0.9 and 0.4 (in), WR-90, and one dielectric backed patterned conducting plane with the relative electric permittivity of 3.55 and thickness of 0.4 mm is designed. Three dimensional view of this structure is shown in Fig. 1 (a).

We consider the right medium of the network has been connected to a frequency dependent load impedance, whose reflection coefficient is varying from 0.48×exp (1.91i) to 0.28×exp (1.45i) in the frequency range. We also considered 10×10 subsections for the quarter of conductive plane and M=17 frequency samples with equal distance of 250 MHz.

Figure 2 illustrates the designed geometry of conductive plane. Figure 3 compares the return loss of the designed impedance matching structure with the simulated one, which is obtained by HFSS. It is obvious that there is a good agreement between two curves in the frequency range.

Also, an impedance matcher using a waveguide filled by inhomogeneous dielectrics for the same load is presented in [7]. Figure 4 compares the return loss of the proposed impedance matcher in this example and that in [7]. This impedance matcher is fifty times as short as that

impedance matcher; besides, the constructing of inhomogeneous dielectrics is not such practical, while constructing of the proposed structure is quite practical.
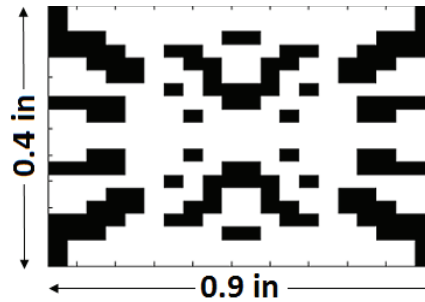
Fig. 2. The designed geometry of patterned conducting plane of impedance matching structure.
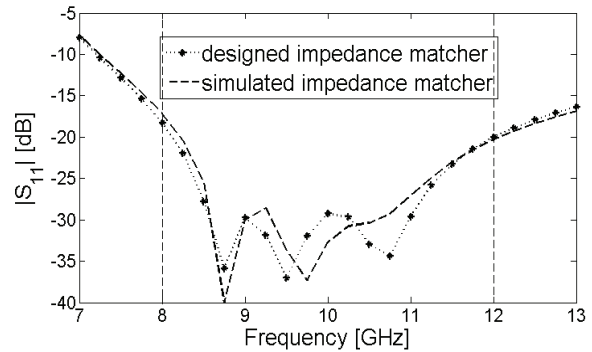
Fig. 3. The return loss of designed, and simulated impedance matching structure.
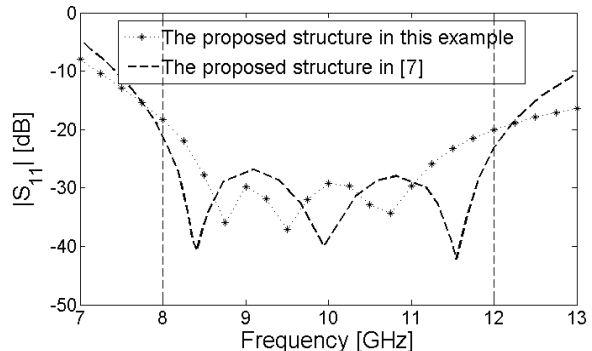
Fig. 4. The return loss of the proposed impedance matcher in this example versus the proposed one in [7].

B. Example II

In the second example, impedance matching network for a frequency dependent load impedance, whose reflection coefficient is varying from 0.64×exp (1.97i) to 0.43×exp (1.4i) in X-band, is proposed. All specification of the network is the same as previous example, except the pattern of the conducting plane. We

considered 8×12 subsections for the quarter of conductive plane and M=27 frequency samples with equal distance of 150 MHz.

Figure 5 illustrates the designed geometry of conductive plane. Figure 6 compares the return loss of the designed impedance matching network obtained by MATLAB with the simulated one obtained by HFSS. As it shows, this approach is effective to obtain a good impedance matching condition in desired frequency range.
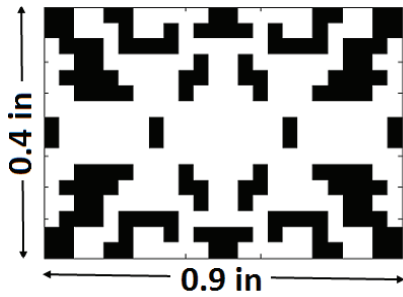
Fig. 5. The designed geometry of patterned conducting plane of impedance matching structure.
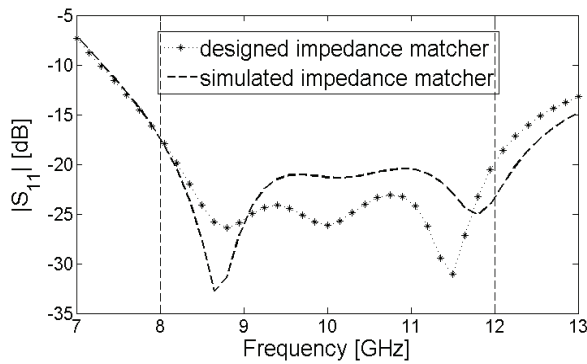
Fig. 6. The return loss of designed and simulated impedance matching structure.

C. Example III

In the third example, impedance matching network for a frequency dependent load impedance, whose reflection coefficient is varying from 0.43×exp (3.14i) to 0.3×exp (3.14i) in X-band, using the same WR-90 is designed. For given reflection coefficient, we have to utilize more than one patterned conducting plane to realize impedance matching structure. In this example, three patterned conducting plane is considered; also, the first and the last planes are the same. The space between them is assumed to be 2.5 mm, and all are selected with relative permittivity of 3.55 and thickness of 0.4 mm. So the total length of impedance matching structure is 6.2 mm. Its three dimensional view is shown in Fig. 7. In this design procedure, coupled magnetic field integral equations are used, which has been obtained in [14]. It is

assumed that the number of subsections is 8×12, also, M=17 frequencies with equal distance of 250 MHz, is considered in the optimization process. Also, Fig. 8 illustrates the designed geometry of patterned conducting planes.
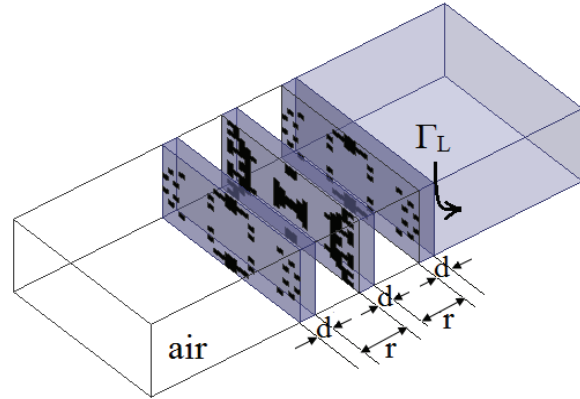
Fig. 7. Three dimensional view of impedance matching structure for $\Gamma_L=1/3\exp$ $(j\pi)$, based on 8-12 GHz optimization frequency range.

(a)

(b)
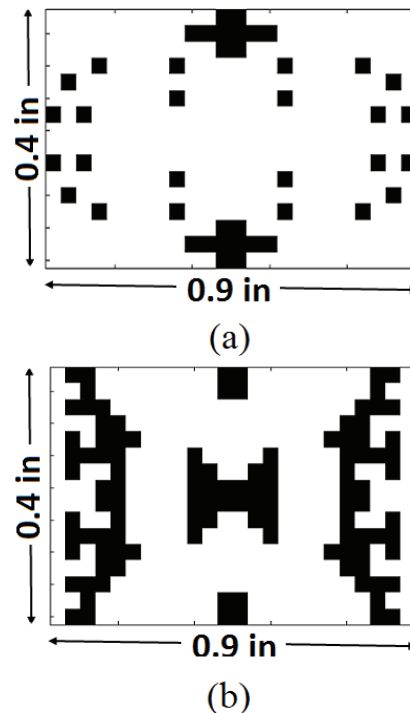
Fig. 8. The designed geometry of three FSSs: (a) geometry of first and third FSS, and (b) geometry of second FSS.

Figure 9 compares the return loss of the designed impedance matcher with the simulated one. It can be deduced that the designed structure has yielded a good impedance matching in the desired frequency band.
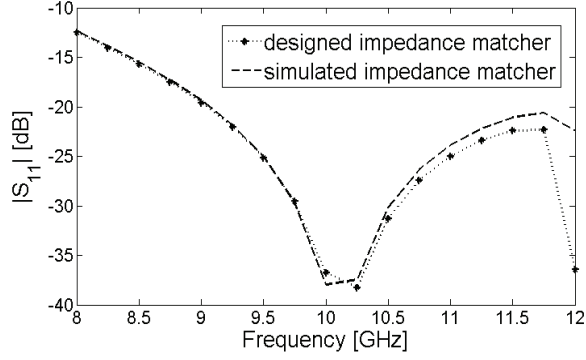
Fig. 9. The return loss of the designed impedance matcher, and that of the simulated one.

IV. CONCLUSION

In this paper, the idea of using dielectric backed patterned conducting planes in a waveguide for impedance matching was confirmed. A designing approach for finding suitable pattern of patterned conducting planes (PCPs) was introduced. The results of simulation show using only one dielectric backed PCP with inconsiderable thickness about 0.4 mm, adjust some loads to air filled waveguides. Matching condition was good about -25 dB return loss in a wide frequency band about 40 percent. Also, for other loads, which one dielectric backed PCP was not sufficient for their matching, we could use more than one dielectric backed PCPs. The usefulness and performance of the proposed structure was verified by testing three extended frequency dependent loads. The proposed method can be applied to any realizable and practical loads in desired frequency range, and for each given loads there is a specified patterned plane which can match the given load to the air-filled waveguide in the desired frequency range.

V. APPENDIX

In this appendix, we gave the matrices of third and fourth equation:Z

$$\left[\mathbf{Z}_1\right]_{kl} = \sum_{m=0}^{\infty}\sum_{n=0}^{\infty} \tilde{B}_k^x \tilde{B}_l^x \left(\tilde{G}^1_{xx} + \tilde{G}^2_{xx}\right), \quad (A1)$$

$$\left[\mathbf{Z}_2\right]_{kl} = \sum_{m=0}^{\infty}\sum_{n=0}^{\infty} \tilde{B}_k^x \tilde{B}_l^y \left(\tilde{G}^1_{xy} + \tilde{G}^2_{xy}\right), \quad (A2)$$

$$\left[\mathbf{Z}_3\right]_{kl} = \left[\mathbf{Z}_2\right]_{lk}, \quad (A3)$$

$$\left[\mathbf{Z}_4\right]_{kl} = \sum_{m=0}^{\infty}\sum_{n=0}^{\infty} \tilde{B}_k^y \tilde{B}_l^y \left(\tilde{G}^1_{yy} + \tilde{G}^2_{yy}\right), \quad (A4)$$

where $\tilde{B}_l^x$ and $\tilde{B}_l^y$ are the Fourier transform of x-directed and y-directed triangular sub-domain basis functions, respectively; and $\tilde{B}_k^x$ and $\tilde{B}_k^y$ are the

Fourier transform of x-directed and y-directed triangular testing functions, respectively.

$$\mathbf{C}_x = \begin{bmatrix} c_{1,1}^x \\ c_{1,2}^x \\ . \\ . \\ . \\ c_{R-1,C}^x \end{bmatrix}, \quad (A5)$$

$$\mathbf{C}_y = \begin{bmatrix} c_{1,1}^y \\ c_{1,2}^y \\ . \\ . \\ . \\ c_{R,C-1}^y \end{bmatrix}, \quad (A6)$$

$$\left[\mathbf{U}_x^{inc}\right]_k = 2Y_a^{TE10}(ab)^{0.5}\, \tilde{B}_k^x\ (m=1, n=0), \quad (A7)$$

$$\left[\mathbf{U}_y^{inc}\right]_k = 0, \quad (A8)$$

$$\tilde{G}_{xx}^i = Y^{i,h}\sin^2\theta + Y^{i,e}\cos^2\theta, \quad (A9)$$

$$\tilde{G}_{xy}^i = (Y^{i,h} - Y^{i,e})\sin\theta\cos\theta, \quad (A10)$$

$$\tilde{G}_{yx}^i = \tilde{G}_{xy}^i, \quad (A11)$$

$$\tilde{G}_{yy}^i = Y^{i,h}\cos^2\theta + Y^{i,e}\sin^2\theta, \quad (A12)$$

$$Y^{1e,h} = Y_a^{TM,TE}, \quad (A13)$$

$$Y^{2e,h} = Y_d^{TM,TE}\frac{Y_L^{TM,TE} + Y_d^{TM,TE}\tanh(\gamma_d d)}{Y_d^{TM,TE} + Y_L^{TM,TE}\tanh(\gamma_d d)}, \quad (A14)$$

$$\Gamma_L = (Y_a^{TE_{10}} - Y_L^{TE_{10}})/(Y_a^{TE_{10}} + Y_L^{TE_{10}}), \quad (A15)$$

where Y_a, Y_L and Y_d are wave admittance, in air, load and dielectric layer, respectively.

$$\sin\theta = \frac{k_x}{\sqrt{k_x^2 + k_y^2}}, \quad (A16)$$

$$\cos\theta = \frac{k_y}{\sqrt{k_x^2 + k_y^2}}, \quad (A17)$$

$$k_x = \frac{m\pi}{a}, k_y = \frac{n\pi}{b}. \quad (A18)$$

REFERENCES

[1] D. M. Pozar, *Microwave Engineering*, 4th ed., John Wiley & Sons, 2011.

[2] J. D. Kraus, *Antennas*, McGraw-Hill, 1988.

[3] R. E. Collin, *Foundations for Microwave Engineering*, McGraw-Hill, Singapore, 1996.

[4] P. J. B. Clarricoats, "A broad-band waveguide junction containing dielectric," *The Institution of Electrical Engineers*, monograph no. 437 E, Apr.

1961.

[5] F. Arndt, J. Borenmann, and R. Vahldieck, "Design of multi-section impedance-matched dielectric-slab filled waveguide phase shifters," *IEEE Trans. Microwave Theory Tech.*, pp. 34-39, 1984.

[6] F. Arndt, J. A. Frye, M. Wellnitz, and R. Wirsing, "Double dielectric-slab-filled waveguide phase shifter," *IEEE Trans. Microw. Theory Tech.*, pp. 373-381, 1985.

[7] M. Khalaj-Amirhosseini and H. Ghorbaninezhad, "Microwave impedance matching using waveguides filled by inhomogeneous dielectrics," *Wiley Periodicals, Inc., International Journal of RF and Microw. Computer-Aided Engineering*, pp. 69-74, 2008.

[8] F. E. Goodwin and G. E. Moss, "Broad band impedance matching into dielectric filled waveguides," *IEEE Trans. Microw. Theory Tech.*, pp. 36-39, Jan. 1963.

[9] K. Pengthaisong, P. Krachodnok, and R. Wongsan, "Design of a dual-band antenna using a patch and frequency selective surface for WLAN and WiMAX," *10th Int. Conf. on Electrical Eng., Electronics, Comp, Telecom and IT*, 2013.

[10] B. Yan, Y. Zhang, and L. Li, "Design of a dual-band shared-aperture antenna based on frequency selective surface," *Antennas & Propagation (ISAP)*, vol. 1, pp. 496-499, 2013.

[11] M. Sazegar, Y. Zheng, C. Kohler, H. Maune, M. Nikfalazar, R. Binder, and R. Jakoby, "Beam steering transmitarray using tunable frequency selective surface with integrated ferroelectric varactors," *IEEE Trans. Antenna Propag.*, vol. 60, no. 12, pp. 5690-5699, 2012.

[12] Y. Ranga, L. Matekovits, K. P. Esselle, and A. R. Weily, "Multioctave frequency selective surface reflector for ultrawideband antennas," *IEEE Antennas and Wireless Propag.*, vol. 10, pp. 219-222, 2011.

[13] I. L. Morrow and P. Thomas, "Compact frequency selective surface for polarisation transform," *Electronics Letters*, vol. 50, no. 2, pp. 64-65, 2014.

[14] M. Khalaj-Amirhosseini and H. Ghorbaninezhad, "Compact spatial band-pass filters using frequency selective surfaces," *Progress in Electromagnetics Research C*, vol. 21, pp. 59-73, 2011.

[15] P. S. Taylor, E. A. Parker, and J. C. Batchelor, "An active annular ring frequency selective surface," *IEEE Trans. Antenna Propag.*, vol. 59, no. 9, pp. 3265-3271, 2011.

[16] T. Itoh, "Spectral domain immitance approach for dispersion characteristics of generalized printed transmission lines," *IEEE Trans. Microw. Theory Tech.*, vol. 28, no. 7, pp. 733-736, 1980.

[17] L. P. Schmidt and T. Itoh, "Spectral domain analysis of dominant and higher order modes in fin-lines," *IEEE Trans. Microw. Theory Tech.*, vol. 28, no. 9, pp. 981-985, 1980.

A. Ghajar was born in Qazvin, Iran. He received his B.Sc. degree from Imam Khomeini International University (IKIU) in 2012 in Telecommunication Engineering. Now he is a M.Sc. student at University of Guilan in Telecommunication Engineering. His scientific fields of interest are electromagnetic problems and designing microwave components.

H. Ghorbaninejad-Foumani was born in Guilan, Iran. He received his B.Sc. degree from University of Guilan in 2003 and his M.Sc. and Ph.D. degrees from Iran University of Science and Technology (IUST) in 2005 and 2010 respectively, all in Telecommunication Engineering. He is currently Assistant Professor with the Department of Electrical Engineering of University of Guilan. His scientific fields of interest are electromagnetic problems including microwave filter design, compact microwave devices and Green's function of microwave structures.

Compact and Planar Monopole Antenna for WLAN and WiMAX Applications

S. C. Basaran [1] and K. Sertel [2]

[1] Department of Electrical-Electronics Engineering
Akdeniz University, Antalya, 07058, Turkey
cbasaran@akdeniz.edu.tr

[2] Department of Electrical and Computer Engineering
The Ohio State University, Columbus, OH. 43212, USA
sertel.1@osu.edu

Abstract ─ A novel compact dual-band monopole antenna for WLAN and WiMAX applications is presented. The antenna is fed by a microstrip feed line and consists of two side-by-side split-ring structure as the radiating element. The proposed antenna is compact in size and provides 25.5% and 11.8% dual band performance covering 2.4/5.2 GHz WLAN and 2.5/2.7 GHz WiMAX bands, respectively. Also, the antenna exhibits uniform radiation patterns at each frequency band in both *E*- and *H*-planes. Comparison of simulated and measured results of return losses, radiation patterns and gains of the antenna are provided.

Index Terms ─ Dual-band antenna, monopole antenna, split-ring elements, WiMAX, WLAN.

I. INTRODUCTION

The explosive growth in the number and variety of mobile communication devices, such as cell phones, laptops, and wireless modems, necessitates design of adaptable, miniature, multi-functional antennas. In this context, several frequency bands and signaling standards are typically exploited by means of a single antenna that must either support multiband or wideband operation. Conventional microstrip antennas have been the preferred choice for mobile devices due to their low-profile and high efficiency; however, they are inherently narrowband. It is, thus, necessary to tailor either the feed structure or the antenna element or both to achieve acceptable performance. Moreover, due to limited RF real-estate on mobile devices, antenna sizes must be kept to a minimum. In an effort to address the aforementioned requirements, monopole type printed antennas have played an increasingly important role. As they exhibit wide impedance bandwidth, compact and simple structure and ease-of-fabrication. Also, the omni-directional radiation pattern characteristics of monopole antenna make them very suitable for indoor applications such as airplane, shopping center, hospital, etc. Thus, the monopole structure has received much attention in the design of small antennas having wideband or multiband operation in recent years, as reported in literature.

For example, a monopole antenna can be designed to generate multiple resonant modes for size reduction and bandwidth improvement. In [1], an antenna with an L-shaped strip is designed for this purpose. There are many reported antenna designs for wireless systems such as coplanar waveguide (CPW)-fed monopole antenna with embedded slots [2], meandered split-ring (SR) slot [3], and slot monopole antenna with rectangular parasitic elements [4]. A dual-band back-to-back printed monopole antenna operating at UMTS and 2.4 GHz WLAN is reported in [5]. In [6], a dual-band orthogonal C-shaped printed monopole antenna with protruding T-shaped ground plane for 2.4 and 5.2 GHz WLAN operation is reported. In addition, miniature dual-band or multiband monopole antennas based on SR elements [7] and complementary-SR elements are reported in [8,9]. The antenna presented in [7] using concentric split-ring elements and metallic loadings appropriately placed between the rings provides dual-wideband performance. The dual-band antenna in [8] is formed by concentric complementary-SR resonators and slot elements inserted between the rings, and the antenna in [9] consists of two side-by-side complementary SR elements generating multiband performance.

In this paper, a novel SR antenna fed by a microstrip feed line is proposed. Unlike the designs in [7-9], two side-by-side split-ring elements are used as the main radiator in the new design as shown in Fig. 1. Furthermore, in order to achieve desired antenna performance, several ground plane geometrics were investigated and compared (also depicted in Fig. 1). In addition, dimensions of the microstrip feed line were optimized to obtain a very wide bandwidth. Based on this analysis, a dual-wideband antenna was fabricated and

characterized. The measurement results are in good agreement with the simulations (carried out using Ansoft HFSS v.14). The proposed antenna provides dual-band operation covering an impedance bandwidth of 25.5% at 2.75 GHz and 11.8% at 5.27 GHz, with a compact size of 28 mm by 32 mm. We also demonstrate that this antenna exhibits well-behaved radiation patterns in the respective bands.
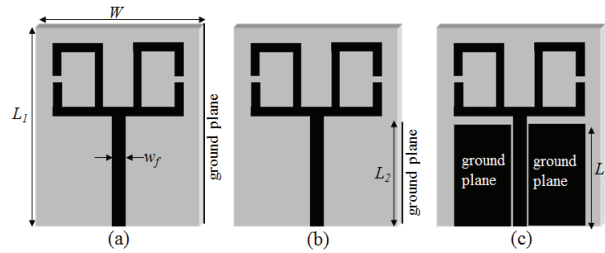
Fig. 1. Geometry of the printed SR-antenna: (a) full-covered ground plane, (b) half-covered ground plane, and (c) CPW-type ground plane. L_1=32, L_2=16, W=28, w_f=2.5.

II. NUMERICAL DESIGN OF THE ANTENNA

Figures 1 (a)-(c) shows three versions of the proposed antenna with two side-by-side SR elements and microstrip feed line. All antennas shown in Fig. 1 have same geometric dimensions apart from the difference in the ground plane metallization. In Fig. 1, while L_1 and L_2 are the lengths of ground planes, w_f is the width of microstrip feed line for three cases. The analysis of the three configurations shown in Fig. 1 reveals that the antenna with full-covered ground plane doesn't exhibit any resonances (as shown in Fig. 2). While the antenna with CPW-type ground plane provides single band performance at 3 GHz, a dual-band performance at 2.9 GHz and 5.2 GHz can be achieved using half-covered ground plane.

On the other hand, in order to enhance the bandwidths of the design with half-covered ground plane and achieve desired dual-wideband operation, the width of microstrip feed line are varied and compared as shown in Fig. 3. When width of the microstrip feed line is 1.5 mm, the antenna provides a single band operation about 3 GHz. When it is 3.5 mm, a single band operation about 5 GHz is observed. When the width of the feed line is 2.5 mm, a dual band operation about 2.9 and 5.2 GHz is obtained. Finally, in order to obtain broader bandwidth, two stage microstrip feed line is introduced as shown in the inset of Fig. 3. As seen, when the first stage of the feed line (W_1) is 3.5 mm and the second stage (W_2) is 1.5 mm, the antenna provides dual-wide band performance at 2 and 5 GHz bands.
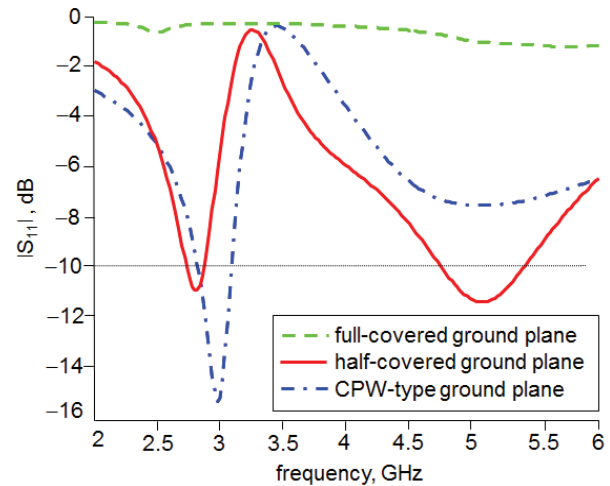
Fig. 2. Simulated return loss characteristics for different geometrical ground planes.
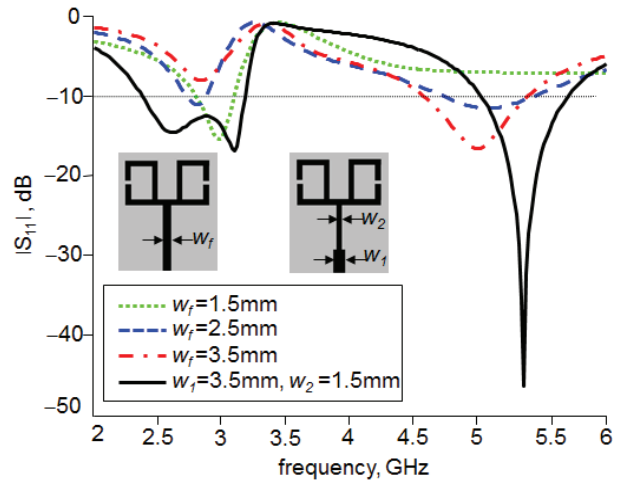
Fig. 3. Simulated return loss characteristics for different widths of microstrip feed line.

The optimum split-ring antenna (SRA) configuration with its design parameters is shown in Fig. 4. Here, the compact SRA is composed of two side-by-side split-ring elements fed by a two-stage microstrip feed line. The first stage of the feed line is 6 mm in length and 3.5 mm in width, while the second stage has a size of 12×1.5 mm². The split-ring resonators with microstrip feed-line are placed on a half grounded Rogers TMM4 substrate with 0.76 mm thickness and dielectric constant of ε_r=4.4. On the back side of the dielectric substrate, a half ground plane is printed below the microstrip feed-line. In order to tune first frequency band, a small patch (3.5×1 mm) is implemented into the top of the ground plane as shown in Fig. 4 (b). The design of the proposed antenna was carried out by means of Ansoft HFSS v.14,

and the final dimensions of the antenna are recorded as follows (in millimeters): $W=28$, $L=32$, $L_1=8.5$, $L_2=12$, $w_1=1.5$, $w_2=5$, $f_1=6$, $f_2=12$, $g=1$, $g_1=17$, $g_2=22$, $g_3=16.5$, $h=0.76$.

(a)   (b)
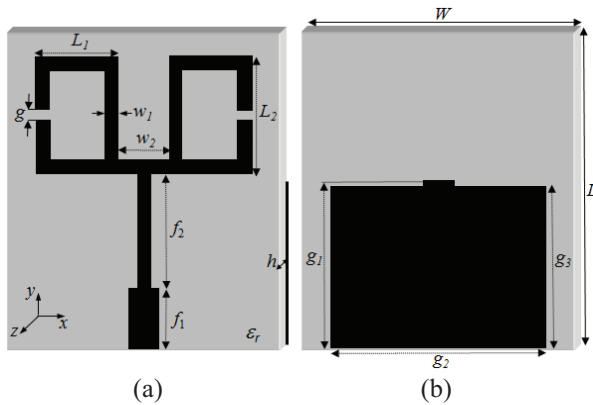
Fig. 4. Configuration of proposed SRA with its design parameters: (a) top view, and (b) bottom view.

III. SIMULATION AND MEASURMENT RESULTS AND DISCUSSION

Based on the design parameters shown in Fig. 4, a prototype antenna was fabricated, and the return loss, radiation pattern and gain measurements were carried out at The Ohio State University ElectroScience Laboratory. The return loss characteristics of the simulated as well as measured designs are shown in Fig. 5. As seen, for the simulated design dual-band coverage is achieved at 2.75 GHz and 5.27 GHz with corresponding 25.5% and 11.8% bandwidths, respectively. This modular design achieves coverage of WLAN bands in 2.4 (2.4–2.84 GHz), 5.2 (5.15–5.35 GHz) and WiMAX band in 2.6 GHz (2.5–2.7 GHz) and 2.8 GHZ (2.7–2.9 GHz).

The radiation patterns and gain of the proposed antenna were also measured. The simulated and measured radiation patterns on the $y-z$ plane and $x-y$ plane for 2.4, 2.6 and 5.3 GHz are shown in Fig. 6 (a), (b) and (c), respectively. As seen, the simulation and measurement results are in excellent agreement, and show that the proposed antenna exhibits omnidirectional radiation pattern in the H-plane ($y-z$ plane) and dipole-like radiation pattern in the E-plane ($x-y$ plane) at the respective bands. In addition, simulated and measured gains of the antenna are shown in Fig. 7 for the H-plane.

The measured gain at the frequencies 2.4 GHz, 2.6 GHz and 5.25 GHz are approximately 1.5, 1 and 2 dBi, respectively.
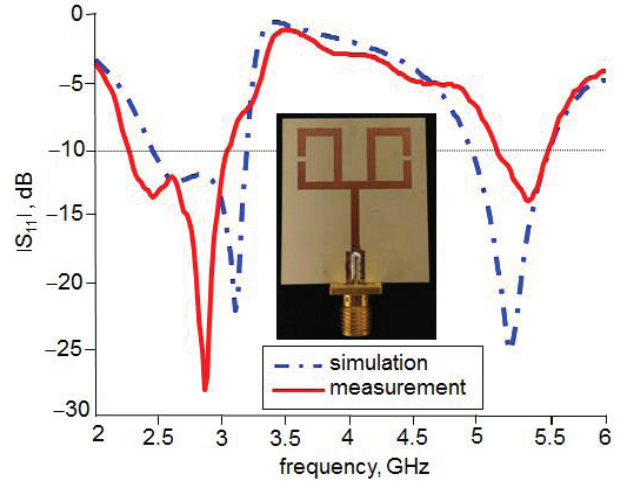
Fig. 5. Simulated and measured return loss (S_{11}) characteristics for the proposed SRA and the prototype of the antenna.
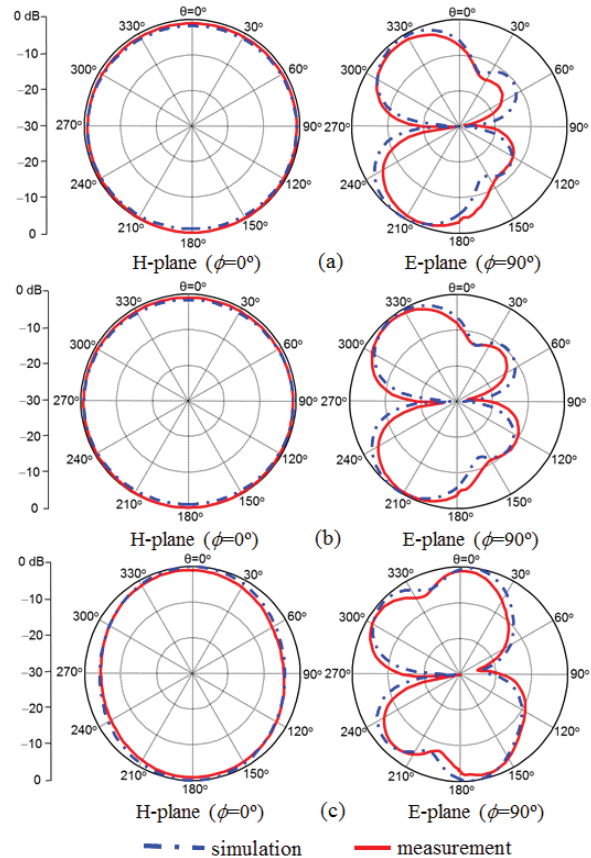
Fig. 6. Measured and simulated radiation patterns of proposed antenna at: (a) 2.4, (b) 2.6, and (c) 5.3 GHz.
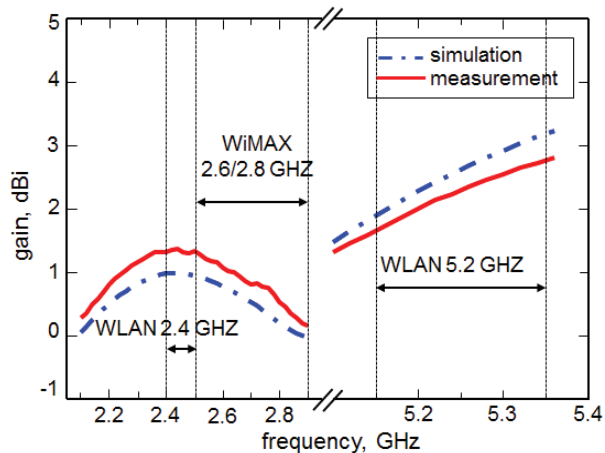
Fig. 7. Simulated and measured gain of the proposed antenna for the 2 GHz and 5 GHz band.

IV. CONCLUSION

A new dual-band monopole antenna for 2.4/5.2 GHz band WLAN and 2.6/2.8 GHz band WiMAX applications was presented. In order to keep the antenna size small, side-by-side split-ring elements are used as the main radiator of the antenna. The two-stage microstrip feed line and a partial ground plane provides to enhance bandwidth of the antenna at the dual respective bands. In addition, a good radiation pattern as well as gain performance is achieved for the frequency bands considered.

REFERENCES

[1] W. Hu, Y. Z. Yin, P. Fei, and X. Yang, "Compact triband square-slot antenna with symmetrical L-strips for WLAN/WiMAX applications," *IEEE Antennas Wireless Propag. Lett*., vol. 10, pp. 462-465, 2011.

[2] W. C. Liu, C. M. Wu, and N. C. Chu, "A compact CPW-fed slotted patch antenna for dual-band operation," *IEEE Antennas Wireless Propag. Lett*., vol. 9, pp. 110-113, 2010.

[3] P. Liu, Y. Zou, B. Xie, X. Liu, and B. Sun, "Compact CPW-fed tri-band printed antenna with meandering split-ring slot for WLAN/WiMAX applications," *IEEE Antennas Wireless Propag. Lett*., vol. 11, pp. 1242-1244, 2012.

[4] C.-Y. Huang and E.-Z. Yu, "A slot-monopole antenna for dual-band WLAN applications," *IEEE Antennas Wireless Propag. Lett*., vol. 10, pp. 500-502, 2011.

[5] Y. Ding, Z. Du, K. Gong, and Z. Feng, "A novel dual-band printed diversity antenna mobile terminals," *IEEE Trans. Antennas Propag*., vol. 55, no. 7, pp. 2088-2096, Jul. 2007.

[6] G. Chi, B. Li, and D. Qi, "Dual-band printed diversity antenna for 2.4/5.2 GHz WLAN application," *Microw. Opt. Technol. Lett*., vol. 45, no. 6, pp. 561-563, Jun. 2005.

[7] S. C. Basaran and K. Sertel, "Dual wideband CPW-fed split-ring monopole antenna with split-ring resonators," *Microw. Opt. Technol. Lett*., vol. 55, no. 9, pp. 2088-2092, 2013.

[8] S. C. Basaran, "A compact dual-wideband antenna based on complementary split-ring resonator," *Microw. Opt. Technol. Lett*., vol. 54, no. 8, pp. 1917-1920, 2012.

[9] S. C. Basaran, U. Olgun, and K. Sertel, "Multiband monopole antenna with complementary split-ring resonators for WLAN and WiMAX applications," *Electron. Lett*., vol. 49, no. 10, pp. 636-637, 2013.

S. Cumhur Basaran was born in Bayburt, Turkey, in 1975. He received the B.S., M.S. and Ph.D. degrees from the Kocaeli University, all in Electronics and Communication Engineering, in 1996, 2000 and 2008, respectively. During 2011-2012, he was a Visiting Scholar at the Ohio State University, ElectroScience Laboratory. He has been an Assistant Professor in the Department of Electrical-Electronics Engineering, Akdeniz University, Antalya, Turkey since 2010. His research interests include numerical analysis and design of conformal and reconfigurable antennas, implantable antennas for biomedical applications, and finite elements methods in electromagnetics.

Kubilay Sertel received his Ph.D. in 2003 from the Electrical Engineering and Computer Science Department at the University of Michigan-Ann Arbor. He is currently an Assistant Professor with the Electrical and Computer Engineering Department at the Ohio State University. He was a Research Scientist at the ElectroScience Laboratory and an Adjunct Professor with the Electrical and Computer Engineering Department at the Ohio State University during 2003-2012. His current research focuses on the analysis and design of THz and mmW sensors, antenna arrays and spectroscopy systems for biomedical and non-destructive imaging, His expertise also includes ultra wideband low-profile phased arrays for cognitive sensing and opportunistic wireless networks, reconfigurable antennas and arrays, applied electromagnetic theory and computational electromagnetics, particularly, curvilinear fast multipole

modeling of hybrid integral equation/finite element systems and efficient solution of large-scale, real-life problems on massively parallel supercomputing platforms.

Sertel is a Senior Member of IEEE, member of IEEE Antennas and Propagation and Microwave Theory and Techniques Societies and an Elected Member of URSI Commission B. He is also a Fellow of Applied Computational Electromagnetics Society and a Member of its Board of Directors. He co-authored two books: *Frequency Domain Hybrid Finite Element Methods in Electromagnetics* (Morgan & Claypool, 2006), and *Integral Equation Methods for Electromagnetics* (SciTech Publishing, 2012), and published 65 journal papers and over 200 conference articles.

Crosstalk Spectrum Predictions Considering Frequency-Dependent Parameters in Electric Vehicles

Yanjie Guo, Lifang Wang, and Chenglin Liao

Key Laboratory of Power Electronics and Electric Drive
Institute of Electrical Engineering, Chinese Academy of Sciences
No.6 Beiertiao, Zhongguancun, Beijing, 100190, China
yjguo@mail.iee.ac.cn, wlf@mail.iee.ac.cn, liaocl@mail.iee.ac.cn

Abstract ─ This paper presents a method which combines impedance measurements, calculations, and equivalent model together to predict crosstalk spectrums. It is simple for calculation and also has good accuracy, because frequency-dependent parameters of both cables and terminal loads are considered. So it has advantages in some complex situations such as electric vehicle (EV). Firstly, a model of single line and twisted-pair wires is established to describe the crosstalk system. In this model, crosstalk voltage expressions are given, and frequency-dependent parameters are obtained from impedance measurements and calculations. Then in order to verify the method, crosstalk spectrums are predicted under conditions of resistance load and frequency-dependent load. Furthermore, predictions and experiments are compared to assess the effectiveness of the method. Based on the predicted and experimental results, frequency domain characteristics of crosstalk are discussed and influence factors are analyzed.

Index Terms ─ Crosstalk, electromagnetic compatibility, frequency domain analysis, frequency estimation, impedance measurement.

I. INTRODUCTION

Crosstalk problems appear in many integrated electric or electrical systems [1]. Crosstalk among cables is the main interference propagation path when cables are banded together or placed closely [2]. High power interference sources and restricted spaces in electric vehicle (EV) make it even worse. Bus-connected units are usually vulnerable to these crosstalk interferences, which decline the stability and safety of the entire vehicle.

Some research on the transmission line can help to analyze this problem [3-6]. Also, the distributed parameters are used to analyze cables in the frequency domain or the complex frequency domain; for example, finite difference time domain (FDTD) [7,8] and methods of moments [9]. However, under some complicated conditions, such as EV applications, these methods are

not applicable because long simulation time and massive computing resources are required. Another method is lumped parameter descriptions [10,11]. But this method ignores the distributed parameters which affect the high frequency characteristics significantly. Furthermore, communication systems, such as controller area network (CAN) buses, have been tested to estimate the impacts of electromagnetic interferences [12]. Moreover, attempts of taking statistical results as input signals have been experimented to get crosstalk waveforms [13]. Though these methods can represent some interference characteristics clearly, they are not related to the mechanism of the crosstalk system and do little help to solve the problem fundamentally.

To the twisted-pair wires which are widely used in communication buses in EV, the typical method is to treat them as spiral lines, get distributed parameters of one twist and integrate all twists to parameter matrixes [14]. This will lead to substantial calculations and inaccuracy under the EV environment, where frequency-dependent parameters commonly exist.

Developments of impedance measurement technology provide a way to get frequency-dependent parameters [15-17]. Frequency-dependent parameters can be obtained from open-circuit and short-circuit impedance measurements. This technology can be extended to crosstalk analysis to obtain the frequency-dependent parameters of crosstalk systems. With the crosstalk equivalent model together, it can be used to predict the crosstalk interference spectrums.

The above discussions suggest traditional crosstalk calculation methods have limits in some complex situations, such as EV applications because of the following reasons: length of the cable is not meet the requirement of electric short; conductors and non-uniform dielectric objects around make non-uniform distributions of charge and flux in the cable; skin effect and proximity effect in high frequency range; irregular cable shape and inconsistent distances between cables, etc. These factors will significantly increase the calculation and bring the deviation.

So in this paper, we used cable parameters calculated from actual measurement results to make sure the above factors are considered. Furthermore, we established an approximate lumped parameter crosstalk model. Combined with the model and the frequency-dependent parameters, we proposed a crosstalk prediction method. It is simple for calculation because of the lumped parameters model. Also, it has good accuracy because the frequency-dependent parameters obtained from measurements are considered. At last, the proposed method is verified on conditions of both resistance load and frequency-dependent load.

II. SPECTRUM PREDICTION METHOD

The spectrum prediction method contains two stages: one is the crosstalk model expressing the cable system; the other is the impedance measurements and calculations from which frequency-dependent parameters of the crosstalk model obtain. To predict the spectrums, firstly, the input impedances among cables and the impedances of terminal loads are measured. Then, the frequency-dependent parameters of the crosstalk system are calculated. Finally, the parameters are taken into the frequency domain expressions which are obtained from the crosstalk model to get the crosstalk voltage spectrums.

A. Equivalent model

Figure 1 shows the equivalent model of single line and twisted-pair wires which is used to analyze crosstalk among cables in EV. The purpose of crosstalk analysis in this paper is to define the spectrums of the voltage on the near terminal $U_{t1}(j\omega)$ and the voltage on the remote terminal $U_{t2}(j\omega)$.
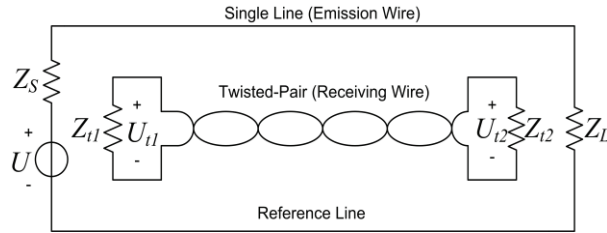
Fig. 1. Equivalent model of crosstalk system containing single line and twisted-pair wires.

Firstly, effect of twisted-pair wires on single line is approximately expressed in order to get the current and voltage in the single line. Because the inductive coupling between single line and twisted-pair wires is proportional to the difference of mutual-inductances between single line and the two twisted-pair wires; hence, an inductance L_{sf} is introduced to show twisted-pair wires' effect as shown in Fig. 2. And its value is approximately given by equation (1):

$$L_{sf} \approx L_s + \alpha(M_{st1} - M_{st2}),\qquad(1)$$

where L_s is the self-inductance of the single line; M_{st1} and M_{st2} are mutual-inductances between single line and twisted-pair wires; α is the coefficient related to the difference of power levels between single line and twisted-pair wires. Also, R_{sf} is used to express the resistance of the single line, which is frequency-dependent because of the skin effects.
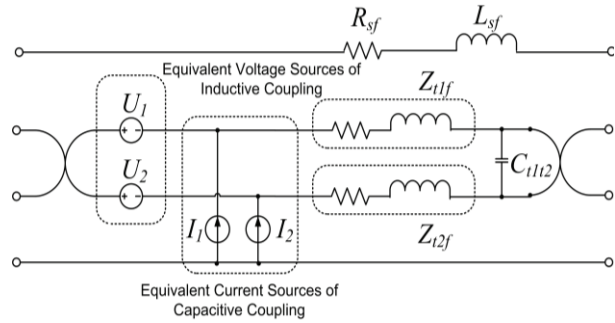
Fig. 2. Equivalent parameters and inductive, capacitive coupling equivalent sources.

So the current and voltage in single line are defined by equation (2):

$$I_s(j\omega) = \frac{U(j\omega)}{Z_S(j\omega) + Z_L(j\omega) + R_{sf}(j\omega) + j\omega L_{sf}(j\omega)},$$

$$U_s(j\omega) = \frac{Z_L(j\omega)U(j\omega)}{Z_S(j\omega) + Z_L(j\omega) + R_{sf}(j\omega) + j\omega L_{sf}(j\omega)}.\qquad(2)$$

Then treating $U_s(j\omega)$ and $I_s(j\omega)$ as interference sources, effects of inductive and capacitive couplings can be equivalent to voltage and current sources given by equation (3) [18] and shown in Fig. 2:

$$U_1(j\omega) = M_{st1}j\omega I_s(j\omega),$$
$$U_2(j\omega) = M_{st2}j\omega I_s(j\omega),$$
$$I_1(j\omega) = C_{st1}j\omega U_s(j\omega),$$
$$I_2(j\omega) = C_{st2}j\omega U_s(j\omega),\qquad(3)$$

where C_{st1} and C_{st2} are coupling capacitances between the single line and the two twisted-pair wires.

Finally, crosstalk voltages on the near and the remote terminal are calculated. And their frequency domain forms are given by equation (4) and equation (5). Where,

$$U_{t1}(j\omega) = \Big(\frac{Z_{t1}(j\omega)}{Z_{t1}(j\omega) + Z_{t2}(j\omega) + Z_{t1f}(j\omega) + Z_{t2f}(j\omega)}$$

$$\times (U_1(j\omega) - U_2(j\omega))$$

$$+ \frac{Z_{t1}(j\omega)(Z_{t2}(j\omega)//C_{t1t2} + Z_{t1f}(j\omega) + Z_{t2f}(j\omega))}{Z_{t1}(j\omega) + Z_{t2}(j\omega)//C_{t1t2} + Z_{t1f}(j\omega) + Z_{t2f}(j\omega)}\qquad(4)$$

$$\times \frac{Z_{t1}(j\omega)}{Z_{t1}(j\omega) + Z_{t1f}(j\omega) + Z_{t2f}(j\omega)}$$

$$\times (I_1(j\omega) + I_2(j\omega)).$$

$$U_{t2}(j\omega) = (-\frac{Z_{t2}(j\omega)}{Z_{t1}(j\omega) + Z_{t2}(j\omega) + Z_{t1f}(j\omega) + Z_{t2f}(j\omega)}$$
$$\times (U_1(j\omega) - U_2(j\omega))$$
$$+\frac{Z_{t1}(j\omega)(Z_{t2}(j\omega)//C_{t1t2} + Z_{t1f}(j\omega) + Z_{t2f}(j\omega))}{Z_{t1}(j\omega) + Z_{t2}(j\omega)//C_{t1t2} + Z_{t1f}(j\omega) + Z_{t2f}(j\omega)}$$
$$\times\frac{Z_{t2}(j\omega)//C_{t1t2}}{Z_{t2}(j\omega)//C_{t1t2} + Z_{t1f}(j\omega) + Z_{t2f}(j\omega)}$$
$$\times (I_1(j\omega) + I_2(j\omega)). \tag{5}$$

"//" means the two impedance variables are in parallel; Z_{t1f} and Z_{t2f} are the equivalent self-impedances of the twisted-pair wires, which contain the self-resistances, self-inductances of the twisted-pair wires.

B. Frequency-dependent parameter calculation

Equation (4) and (5) indicate that there are two kinds of frequency-dependent parameters. One is terminal loads, such as Z_S, Z_L, Z_{t1}, and Z_{t2}. The other is the parameters of the cables, including the equivalent impedances L_{sf}, Z_{t1f}, Z_{t2f}; mutual inductances M_{st1}, M_{st2} and coupling capacitances C_{st1}, C_{st2}, C_{t1t2}. The former can be directly measured by an impedance analyzer. The latter can be calculated through the following steps.

Firstly, the elements of impedance matrixes Z_{sc} and Z_{oc} can be expressed by input measurement impedances as follows:

$$Z_{sc}(i,i) = Z_{in}^{sc}(i,i),$$
$$Z_{sc}(i,j) = [Z_{in}^{sc}(i,i) + Z_{in}^{sc}(j,j) - Z_{in}^{sc}(i,j)]/2, \tag{6}$$
$$Z_{oc}(i,i) = Z_{in}^{oc}(i,i),$$
$$Z_{oc}(i,j) = [Z_{in}^{oc}(i,i) + Z_{in}^{oc}(j,j) - Z_{in}^{oc}(i,j)]/2,$$

where $Z_{sc}(i,i)$, $Z_{sc}(i,j)$ and $Z_{oc}(i,i)$, $Z_{oc}(i,j)$ are diagonal, non-diagonal elements of the short-circuit impedance matrix Z_{sc} and the open-circuit impedance matrix Z_{oc}; $Z_{in}^{sc}(i,i)$ and $Z_{in}^{oc}(i,i)$ are short-circuit and open-circuit input measurement impedances between conductor i and the reference conductor; $Z_{in}^{sc}(i,j)$ and $Z_{in}^{oc}(i,j)$ are short-circuit and open-circuit input measurement impedances between conductor i and conductor j; $i, j = 1, 2, \cdots N$ and $i \neq j$, N is the number of the conductors.

Then, series impedance matrix Z and parallel admittance matrix Y are obtained from Z_{sc} and Z_{oc} through equation (7). Where l is the lengths of the cables; Γ and Z_c are the propagation constant matrix and the characteristic impedance matrix:

$$\Gamma = arctan h\left[\left(Z_{sc}Z_{oc}^{-1}\right)^{1/2}\right]/l,$$
$$Z_c = \left(Z_{sc}Z_{oc}^{-1}\right)^{1/2} Z_{oc}, \tag{7}$$
$$Z = \Gamma Z_c, \quad Y = \left(Z_c\right)^{-1}\Gamma.$$

Finally, frequency-dependent resistance matrix R, inductance matrix L, admittance matrix G and capacitance matrix C are given by equation (8):

$$R = Re[Z(j\omega)], \quad L = Im[Z(j\omega)]/\omega,$$
$$G = Re[Y(j\omega)], \quad C = Im[Y(j\omega)]/\omega. \tag{8}$$

So, the parameters of the cables can be found or calculated in the elements of R, G, L and C. Combining with the directly measurement results of Z_S, Z_L, Z_{t1}, and Z_{t2}, spectrums of crosstalk voltage $U_{t1}(j\omega)$ and $U_{t2}(j\omega)$ can be got through equation (4) and equation (5).

III. PREDICTIONS CONSIDERING RESISTANCE LOAD

In order to verify the model and prediction method, single line and twisted-pair wires are lying in parallel in an experimental platform. They are bounded together with the length of 1 m and 30 mm high from the grounded plane. The cables are multi strand of copper wires with conductor cross sectional area 0.75 mm², and their gauge is 227 IEC 06(RV). A series of rectangular pulses are used as an interference source to imitate the crystal oscillator signals. They have a frequency of 8 MHz, which is the frequency of the crystal oscillators used in electric control units (ECUs) in the experimental EV. Under this condition, 51 Ohm resistors are connected as terminal loads of both single line and twisted-pair wires.

A. Parameter measurement results

Short-circuit and open-circuit input impedances between different cables are measured by an impedance analyzer. The sweeping frequency is 0 Hz - 300 MHz. Part of the results are shown in Fig. 3 and Fig. 4. Where Z_{S11} is the short-circuit impedances between the single line and the reference plane; Z_{O11} is the open-circuit impedances between the single line and the reference plane; Z_{S12} is the short-circuit impedances between the single line and one of the twisted-pair wires; Z_{O12} is the open-circuit impedances between the single line and one of the twisted-pair wires.
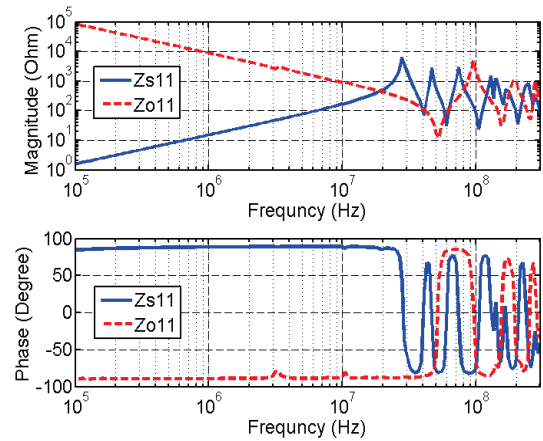
Fig. 3. Self-impedance measurement results of the single line.
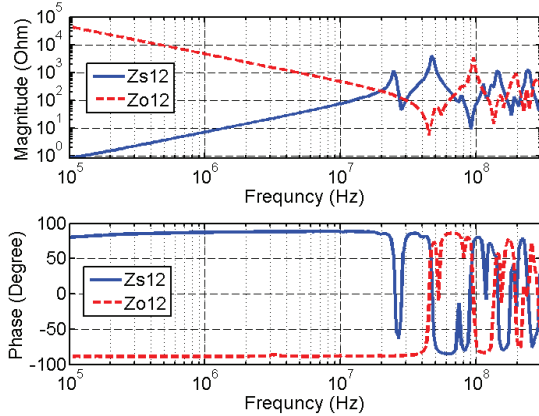
Fig. 4. Mutual-impedance measurement results between single line and one of twisted-pair wires.

Figures 3 and Fig. 4 suggest that, the open-circuit and short-circuit impedances change linearly in the low frequency range. While, there are oscillations in the high frequency range, because the inductances and capacitances of the crosstalk system are usually very small. These stray parameters will significantly affect the measured impedances among cables.

B. Predictions and experiments

Based on the parameter measurement results and the prediction algorithm, crosstalk spectrums can be predicted. In this paper, the terminal of twisted-pair wires close to the interference source is designated as the near terminal and the other is defined as the remote terminal. It is in consistent with the equivalent model in Fig. 1. Simulation study has been conducted in MATLAB in order to verify the performance of the proposed prediction method.

Considering 8 MHz pulse interference source, the predicted crosstalk spectrum of U_{t1} on the near terminal of twisted-pair wires is shown in Fig. 5, and the experimental result is given for comparison. In the same way, predicted spectrums and experimental results of U_{t2} on the remote terminal of twisted-pair wires are shown in Fig. 6.

Figure 7 shows the deviations between predicted and experimental spectrums for resistance loads. It suggests the predicted results have some differences with the experimental ones. Especially in a few frequencies, the deviation is bigger than 10 dBmV. This may be caused by the approximation of modeling process and measure deviations. However, average deviation in the whole frequency range up to 300 MHz is very small. Considering the main interference frequencies which have amplitudes higher than -65 dBmV, average deviation of the spectrum on the near terminal is 1.06 dBmV and average deviation of the spectrum on the remote terminal is 0.99 dBmV. Compared with the traditional crosstalk calculation method [18], deviations

of the proposed method are much smaller. So the proposed crosstalk predicted method has advantages in EV applications.
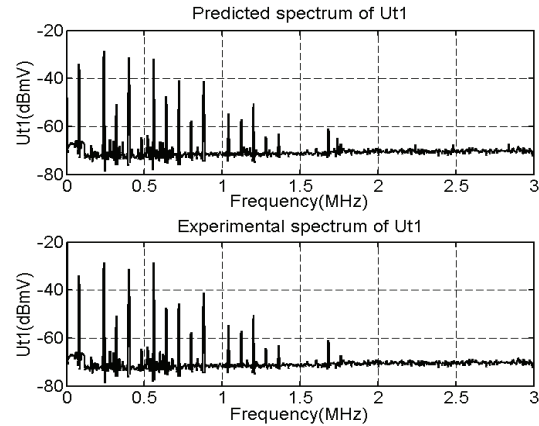
Fig. 5. Crosstalk spectrum predicted and experimental results on the near terminal for resistance loads.
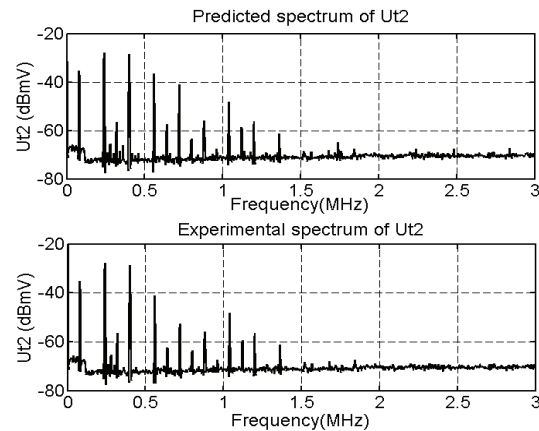
Fig. 6. Crosstalk spectrum predicted and experimental results on the remote terminal for resistance loads.
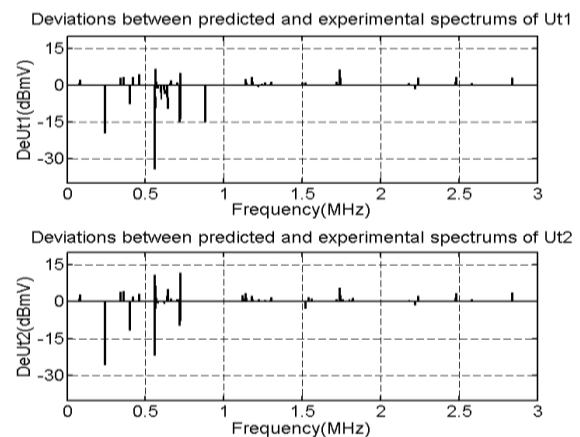
Fig. 7. Deviations between spectrum predicted and experimental results for resistance loads.

The predicted and experimental results not only prove the effectiveness of the method, but also provide materials for the frequency domain characteristics analysis of crosstalk in EV. They can be used to analyze the influence of the interference source. The interference source is a series of rectangular pulses, and the envelope curve of its spectrum is given by equation (9). Where A is the amplitude of the rectangular pulses, and τ is the width of the pulses:

$$F(j\omega) = A\tau \sin(\frac{\omega\tau}{2}) / \frac{\omega\tau}{2}. \qquad (9)$$

So the amplitude of the interference source spectrum is decided by equation (9). The frequencies of the spectrum are the frequency of the pulses and its multiples. Figure 5 and Fig. 6 indicate that the interference frequencies of crosstalk voltages are basically the same as the source. However, there are some new interference frequencies appeared, which are caused by the non-linear factors, such as small deformations of the cables, non-uniform distances between cables and so on. Also, they have different amplitudes because of the influence of the frequency-dependent parameters. Besides, the amplitude of the crosstalk spectrum on the remote terminal is a little smaller than that on the near terminal. That is because the inductive coupling is positive on the near terminal but negative on the remote terminal as expressed in equation (4) and equation (5).

IV. PREDICTIONS CONSIDERING FREQUENCY-DEPENDENT LOAD

Many ECUs in EV have frequency-dependent characteristics. These ECUs are wildly used as loads of communication buses and their frequency-dependent impedances have effects on crosstalk interferences. So it is more appropriate to consider them for interference simulation and estimation.

Considering the experimental platform above, an ECU used for battery management system (BMS) in Fig. 8 is connected on the remote terminal of twisted-pair wires instead of the 51 Ohm resistor. The impedance is measured between the positive terminal and the negative terminal of the BMS without power. The measurement result is shown in Fig. 9.

The measured impedances can be described as a series of complex numbers, which change with frequencies. These complex numbers are used as $Z_{t2}(j\omega)$ in equation (4) and equation (5), so crosstalk spectrums can be calculated. Predicted and experimental results on the near and the remote terminal of twisted-pair wires are shown in Fig. 10 and Fig. 11. Also, the deviations between predicted and experimental spectrums for a frequency-dependent load are shown in Fig. 12.

Fig. 8. Photo of the battery management system.
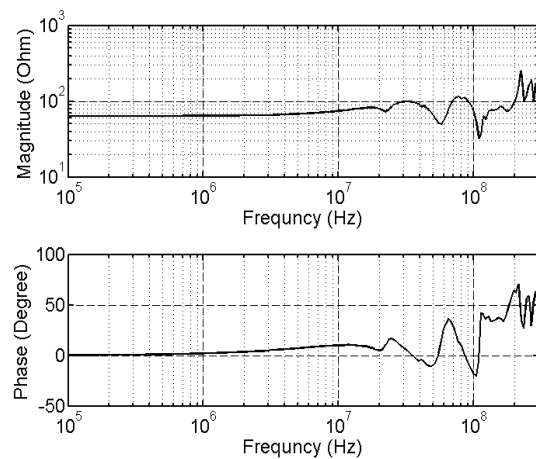
Fig. 9. Measurement impedance of the BMS.
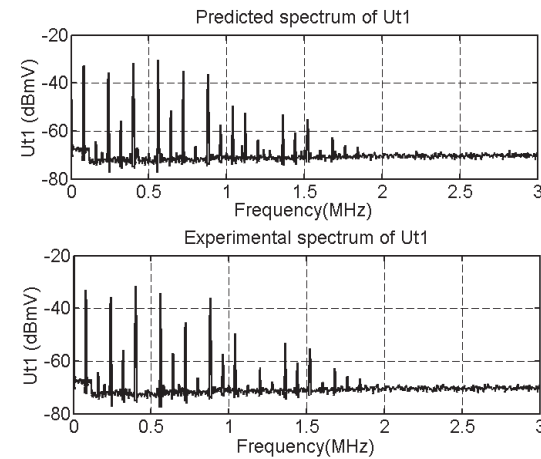
Fig. 10. Crosstalk spectrum predicted and experimental results on near terminal for a frequency-dependent load.
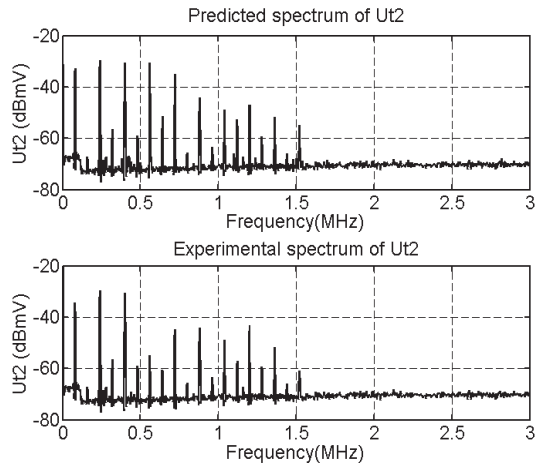
Fig. 11. Crosstalk spectrum predicted and experimental results on the remote terminal for a frequency-dependent load.
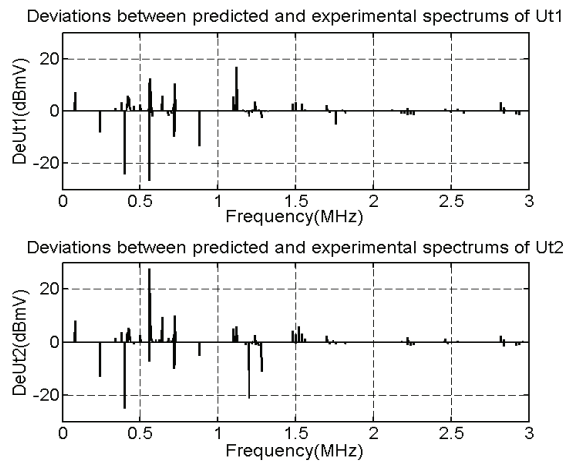
Fig. 12. Deviations between spectrum predicted and experimental results for a frequency-dependent load.

Similar with the results of resistance loads, predicted results have some differences with the experimental ones, especially in a few frequencies. However, considering the main interference frequencies which have amplitudes higher than -65 dBmV, average deviation of the spectrum on the near terminal is 1.92 dBmV, and average deviation of the spectrum on the remote terminal is 2.02 dBmV. Average deviation in the whole frequency range up to 300 MHz is also very small. So the proposed crosstalk prediction method is effective and has the advantage under the condition of frequency-dependent load.

These predicted and experimental results can be used to discuss the effects of the frequency-dependent load. The average deviations of a frequency-dependent load are only a little larger than the ones of resistance loads. It is caused by the following reason: Fig. 9 infers

that the impedance differences between a BMS and a 51 Ohm resistor are mostly in the high frequency range. In this range, amplitude of the interference source spectrum is even smaller than the background noises in the environment of electric vehicles. So the effects of BMS on the crosstalk spectrums are not very apparent as shown in Fig. 10 and Fig. 11. However, if the interference source has a higher frequency or the frequency-dependent loads have more complex inductive and capacitive impedances in the low frequency range, the effects will be significant.

So we believe that crosstalk spectrums are decided by the frequency characteristics of the interference source, the frequency-dependent parameters of the cables, and the terminal loads. Crosstalk spectrums can be predicted through the frequency-dependent parameter measurements, calculations, and the crosstalk equivalent model.

V. CONCLUSION

A simple method to predict crosstalk spectrums is discussed in this paper. It does not require long simulation time and substantial computing resources. Good accuracy has been achieved because frequency-dependent impedances of cables and terminal loads, which are obtained from measurements, are considered. So it is practical in some complex situations such as EV applications. This has been verified by experiments under the conditions of both resistance load and frequency-dependent load. The deviation analysis indicates the proposed method can provide more precise results than traditional crosstalk calculation method. Based on the simulations and experiments, the interference source, frequency-dependent parameters of cables and loads are analyzed to get the crosstalk frequency domain characteristics.

Although this method is proposed in the particular EV environment, it can be used in much more applications where conductors are put closely and their impedances can be measured easily. Also, this method will help interference suppression and electromagnetic compatibility (EMC) design.

REFERENCES

[1] K. Prachumrasee, A. Siritaratiwat, and V. Ungvichian, "A methodology to identify crosstalk contributor from 6-line suspension assembly interconnect of ultra-high capacity hard disk drives," *Appl. Comput. Electromagn. Soc. J.*, vol. 27, no. 1, pp.22-27, Jan. 2012.

[2] S. Weber, S. Guttowski, E. Hoene, *et al.*, "EMI coupling from automotive traction systems," *IEEE Int. Electromagn. Compat. Symp.*, Istanbul, Turkey, pp. 591-594, May, 2003.

[3] M. Rajabi, and N. Komjani, "Improvement of transmission line matrix method algorithm

frequency response based on modification of cell impedance," *Appl. Comput. Electromag. Soc. J.*, vol. 26, no. 4, pp.319-324, Apr. 2011.

[4] M. Khodier, "Design and optimization of single, dual, and triple band transmission line matching transformers for frequency-dependent loads," *Appl. Comput. Electromag. Soc. J.*, vol. 24, no. 5, pp.446-452, Oct. 2009.

[5] H. Jwaied, F. Muwanes, and N. Dib, "Analysis and design of quad-band four-section transmission line impedance transformer," *Appl. Comput. Electromagn. Soc. J.*, vol. 22, no. 3, pp.381-387, Nov. 2007.

[6] Y. W. Liu, D. S. Zhao, and K. K. Mei, "Implementation of generalized transmission-line equations to transmission line parameter extraction," *Appl. Comput. Electromagn. Soc. J.*, vol. 18, no. 1, pp.58-64, Mar. 2003.

[7] G. Ala, M. C. Di Piazza, G. Tine, *et al*., "Evaluation of radiated EMI in 42-V vehicle electrical systems by FDTD simulation," *IEEE Trans. Veh. Technol.*, vol. 56, no. 4, pp. 1477-1484, Jul. 2007.

[8] O. M. Ramahi, "Analysis of conventional and novel delay lines: A numerical study," *Appl. Comput. Electromagn. Soc. J.*, vol. 18, no. 3, pp.181-190, Nov. 2003.

[9] K. Chamberlin, K. Komisarek, and K. Sivaprasad, "A method-of-moments solution to the twisted-pair transmission line," *IEEE Trans. Electromagn. Compat.*, vol.37, no. 1, pp. 121-126, Feb. 1995.

[10] X. P. Dong, H. X. Weng, D. G. Beetner, *et al.*, "A preliminary study of maximum system-level crosstalk at high frequencies for coupled transmission lines," *IEEE Int. Electromagn. Compat. Symp.*, Silicon Valley, CA, pp. 419- 423, Aug. 2004.

[11] W. T. Smith, C. R. Paul, and J. S. Savageetc, "Crosstalk modeling for automotive harnesses," *IEEE Int. Electromagn. Compat. Symp.*, Chicago, IL, pp. 447-452, Aug. 1994.

[12] F. M. Ruan, S. Y. Sun, T. Dlugosz, *et al*., "Some consideration on electromagnetic compatibility in CAN bus design of automobile," *Asia-Pacific Int. Electromagn. Compat. Symp.,* Beijing, China, pp. 1431- 1434, Apr. 2010.

[13] W. Li, S. F. Yu, B. Zhang, *et al*., "High frequency conducted disturbance analysis of driving system in fuel cell vehicle," *The 4th Asia-Pacific Environmental Electromagnetics Conf.,* Dalian, China, pp. 724-727, Aug. 2006.

[14] C. Buccella, M. Feliziani, G. Manzi, *et al*., "Prediction of voltage and current propagation in twisted wire pairs (TWPs) by a circuit model," *IEEE Int. Electromagn. Compat. Symp.*, Chicago, IL, pp. 51-55, Aug. 2005.

[15] W. R. Zimmerman, and L. D. Wellems, "Measuring the transfer impedance and admittance of a cylindrical shield using a single triaxial or quadraxial fixture," *IEEE Trans. Electromagn. Compat.,* vol.35, no. 4, pp.445-450, Nov. 1993.

[16] B. Vanlandschoot, and L. Martens, "New method for measuring transfer impedance and transfer admittance of shields using a triaxial cell," *IEEE Trans. Electromagn. Compat.,* vol.39, no. 2, pp.180-185, May. 1997.

[17] S. Sali, "Cable shielding measurements at microwave frequencies," *IEEE Trans. Electromagn. Compat.,* vol.46, no. 2, pp.178-188, May. 2004.

[18] C. R. Paul, *Introduction to Electromagnetic Compatibility, 2nd ed.* Hoboken, NJ, John Wiley & Sons, Inc., 2006.

Yanjie Guo received the Ph.D degree in 2013 from Institute of Electrical Engineering, Chinese Academy of Sciences (IEECAS). Now he is an assistant professor in the Key Laboratory of Power Electronics and Electric Drive, Chinese Academy of Sciences. His research interest is mainly focus on electromagnetic compatibility (EMC), wireless power transfer, electric vehicles and power electronics.

Lifang Wang received the Ph.D degree in 1997 from Jilin University. She is currently the director of Department of Vehicle Energy System and Control Technology at IEECAS. She is also the vice director of Key Laboratory of Power Electronics and Electric Drive, Chinese Academy of Sciences. Her research interest is mainly focus on EMC, wireless power transfer, electric vehicles, vehicle control, power electronics, and power battery charging and management.

Chenglin Liao received the Ph.D. degree in 2001 from Beijing Institute of Technology and then spent 2 years as a postdoctoral researcher in Tsinghua University. Now he is a professor in the Key Laboratory of Power Electronics and Electric Drive, Chinese Academy of Sciences. His research interest is mainly focus on wireless power transfer, EMC, electric vehicles, and power battery.

Elliptical Slot Antenna with Dual Band-Notched Characteristics for UWB Applications

M. Naser-Moghadasi [1] and A. A. Kalteh [2]

[1] Faculty of Engineering
Science and Research Branch, Islamic Azad University, Tehran-Iran
mn.moghaddasi@srbiau.ac.ir

[2] Department of Electrical Engineering
Aliabad Katoul Branch, Islamic Azad University, Aliabad Katoul, Iran
Aziz_kalteh@yahoo.com

Abstract ─ A novel elliptical slot antenna with band-notched characteristics is presented for ultra-wideband (UWB) applications. The proposed antenna is fed via a microstrip-line that is connected to an elliptically shaped patch. Dual band-notched characteristic is achieved by utilizing an L-shaped strip and an inverted U-shaped slot incorporated within the antenna's structure. This antenna configuration enables the notch band to be finely tuned by simply adjusting the parameters of notch function components, the L-shaped slot and the inverted U-shaped slot. The antenna with optimal parameters was fabricated on RT/Duroid 6006 that has a thickness of 1.27 mm and a relative permittivity of 6.15. The size of the actual antenna is 50×50 mm^2. The measured VSWR, gain, impedance and radiation characteristics of the proposed antenna confirm it satisfies UWB system requirements.

Index Terms ─ Dual band notched, elliptical slot antenna, UWB.

I. INTRODUCTION

Ever since the Federal Communications Commission (FCC) first approved the regulations for the commercial use of ultra-wideband (UWB) in 2002 [1], the design and implementation of feasible UWB systems has become a highly competitive topic in both academic and industry communities of telecommunications. Antennas are the particularly challenging aspect of UWB technology. To satisfy such a requirement, various wideband antennas have been studied [2]-[4]. The design of UWB systems is further complicated as other radio systems co-exist within the 3.1–10.6 GHz UWB frequency band. These systems include the IEEE802.16 WiMAX system with an operating band of 3.3–3.7 GHz,

the C-band (3.7–4.2 GHz) satellite communication systems, and IEEE802.11a WLAN systems operating between 5.15–5.825 GHz. Inevitably UWB communication systems are likely to experience unwanted electromagnetic interference with such communication systems. To overcome this interference, various UWB antennas with single or multiple notch functions have been investigated for UWB communication systems [5]-[9].

In this paper, a novel elliptical slot antenna with dual band-notched characteristics is described for UWB applications. The proposed antenna comprises of an elliptical shaped patch etched on the front side of the substrate which is excited via a microstrip-line, and an elliptical shaped slot etched in the ground-plane on the back side of the substrate. To achieve dual band-notched characteristics at the frequency band of WLAN and C-band satellite communication systems, an inverted U-shaped slot and an L-shaped stub are included within the antenna structure. The bandwidth and center frequency of the notched bands can be finely controllable by adjusting the parameters of the inverted-U slot and an L-shaped stub. The proposed antenna is shown to operate over the commercial UWB frequency range (3.1–10.6 GHz) and also effectively suppresses interference with wireless local area network (WLAN) and C-band satellite communication systems. Effects of the notch function parameters on the performance of antenna have been investigated using Ansoft HFSS software [10]. A conceptual circuit model, which is based on the measured impedance of the proposed antenna, is presented to explain the dual band-notched characteristics. The prototype of the proposed antenna with optimal dimensions was fabricated and its characteristics are measured to confirm the validity of

the design. Comparison between experimental and simulation results demonstrate good agreement over virtually the entire UWB operating range. The remaining part of the article is organized as follows: Section 2 presents the configuration of proposed antenna, and parametric study of antenna is investigated in Section 3. The simulated and measured results are discussed in Section 4, and finally the conclusion is provided in Section 5.

II. ANTENNA GEOMETRY

The configuration of the proposed UWB elliptical slot antenna possessing two band-notched functions is depicted in Fig. 1, where the parameters of the geometry are defined. The antenna is located on the x–y plane and the normal direction is parallel to z-axis. The antenna consists of an elliptical slot with axial dimensions of A and B. The elliptical slot is located directly below an elliptical radiating patch with axial dimensions of a and b, and is feed via a 50 Ω microstrip-line of width $W_f = 2$ mm. The band-notching characteristics of antenna are achieved by creating an inverted-U slot within the elliptical patch and by connecting a thin L-shaped strip to the feed line. The proposed antenna is constructed on a dielectric substrate RT/duroid 6006 with relative permittivity (ε_r) of 6.15 and thickness of 1.27 mm. The antenna has a ground-plane size of $L_g \times W_g = 50 \times 50$ mm^2.
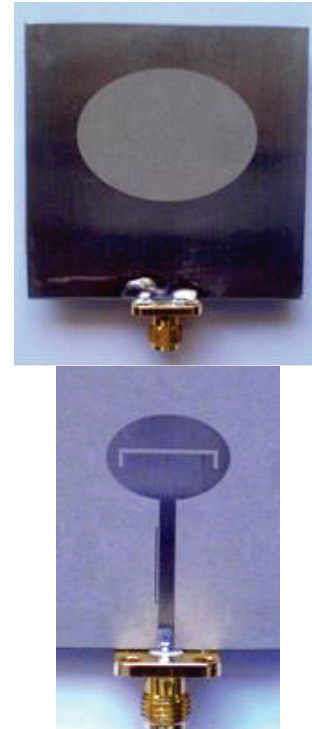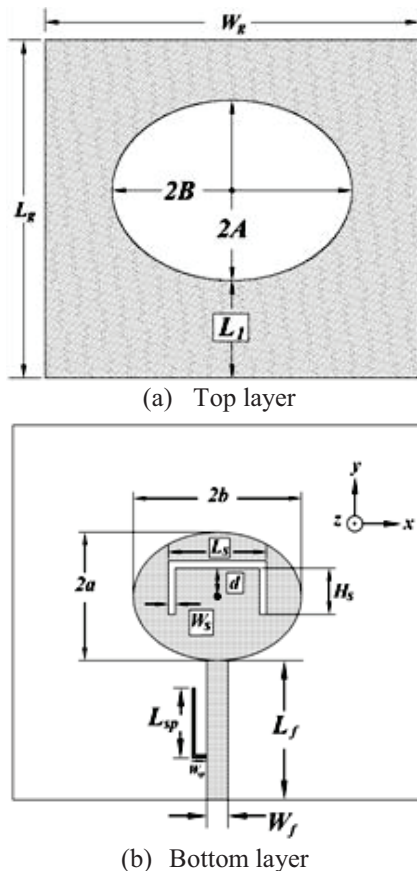
(c) Top and bottom layers of fabricated antenna

Fig. 1. Geometry of proposed UWB antenna.

III. PARAMETRIC STUDY OF ANTENNA

To achieve the desired band-notched characteristic, the effect of the L-shaped stub and inverted U-shaped slot parameters on the antenna's overall performance was studied. The simulated VSWR of the antenna for different values of L_{SP} is plotted in Fig. 2. This figure shows that by increasing the length of L_{SP} the first notch's frequency shifts towards lower frequencies. In this case, the values of L_s and H_s are fixed at 12 mm and 2.25 mm respectively.

(a) Top layer

(b) Bottom layer
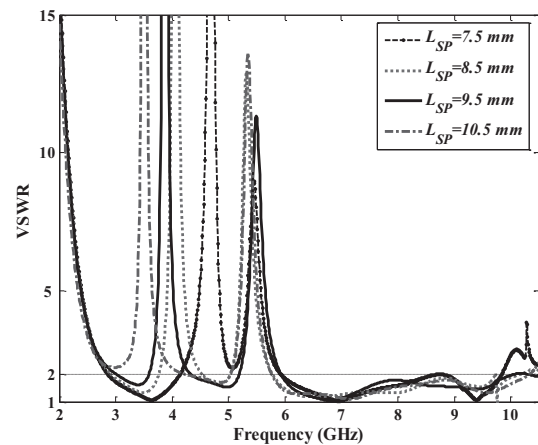
Fig. 2. Effect of L_{SP} on the antenna's band-notching characteristics.

Figure 3 shows the VSWR curve of the proposed antenna for L_{sp}=9.5 mm, H_s=2.25 mm and for different values of L_S. It can be observed that, in this case the second notch's center frequency decreases with the increase of the length L_S. Also, we can see that when the length of L_S increases to 13 mm, the first notch's center frequency shifts towards higher frequencies.

Figure 4 shows the simulated VSWR response of antenna for different values of H_S and fixed values of L_s and L_{sp}. It can be observed in that, in this case the second notch's center frequency decreases with the increase of H_S length.
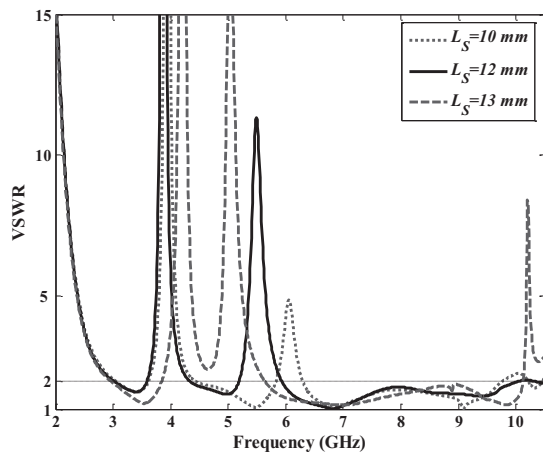
Fig. 3. Effect of L_S on the antenna's band-notching characteristics.
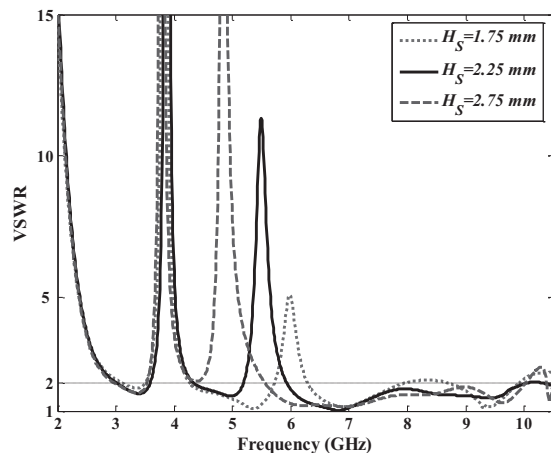
Fig. 4. Effect of parameter H_S of inverted-U slot on the antenna's band-notching characteristics.

As observed in Figs. 2 to 4, the filtering property of the antenna can be tuned by varying the principal parameters of L-shaped stub and inverted U-shaped slot.

IV. RESULTS AND DISCUSSIONS

The simulated and measured results of VSWR, radiation patterns, gain, and input impedance of the proposed antenna are presented in this section. The simulations were performed using Ansoft HFSS and CST Microwave Studio, which utilize numerical methods for electromagnetic computations. The VSWR and input impedance of antenna was measured by the Agilent 8722ES network analyzer and radiation characteristics measurements were performed in anechoic chamber at the antenna laboratory of Iran Research Institute for ICT (ITRC).

A. VSWR

The simulated and measured VSWR curves of the proposed dual band-notched UWB antenna, whose dimensions are given in Table 1, are shown in Fig. 5. This figure shows the simulated bandwidth of the proposed antenna for which VSWR≤2 is from 3 GHz to greater than 11 GHz, and it includes two notched frequency bands between 3.6–4.35 GHz (consistent with the C-band satellite communication system) and between 5.2–6 GHz (frequency band of WLAN systems) for VSWR≥2. The measured 3-dB bandwidth of fabricated antenna is from 2.5 GHz to greater than 11 GHz with VSWR≤2, and the notched bandwidths are over 3.65–4.35 and over 4.85–5.9 GHz for VSWR≥2. The measured frequency range encompasses the commercial UWB band (3.1–10.6 GHz), and the notch functions reject the frequency bands of C-band satellite communication and IEEE 802.11a to overcome EMI problems of UWB systems with WLAN and C-band satellite communication systems. The correlation between the numerical and experimental results is considered to be excellent.
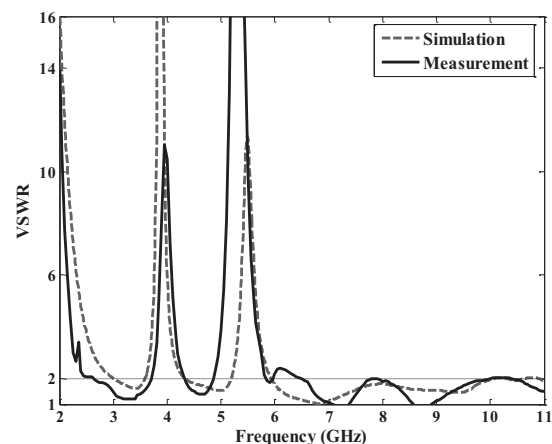
Fig. 5. The VSWR response of the proposed UWB antenna with dimensions given in Table 1.

B. Input impedance

The input impedance curve of the proposed dual band-notched UWB antenna is shown in Fig. 6. In the notched-bands, the imaginary component curve shows parallel resonance characteristics and the real component presents high resistance characteristics. As a result of impedance curve of proposed antenna, the input impedance of the notched antenna is equivalent to the input impedance R_a of the un-notched reference antenna connected with two parallel LC-resonant circuits in series. The conceptual circuit model is shown in Fig. 7.
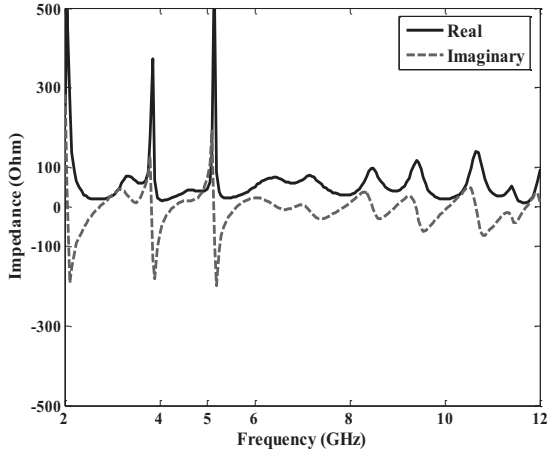
Fig. 6. The measured input impedance of proposed dual band-notched antenna.
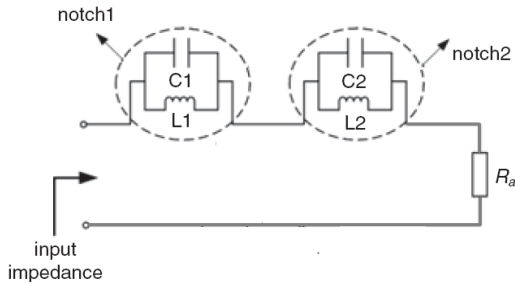
Fig. 7. Conceptual circuit model for proposed dual band-notched antenna.

When the proposed antenna is operating at the two desired notched frequencies, the two corresponding LC-resonant circuits lead to the input impedance to be opened-circuited. Therefore, proposed band-notched UWB antenna presents high impedance characteristics at notched frequencies.

C. Radiation patterns and gain

The simulated and measured antenna gain over the entire UWB band is shown in Fig. 8. This graph shows a sharp drop in gain occurring over the bands 3.6–4.2 and 5–6 GHz. However, for other frequencies outside the reject bands, the antenna gain variation is steady and is less than 2 dBi across the UWB band.

The measured and simulated radiation patterns of proposed dual band-notched UWB antenna in the E-plane (yz-plane) and H-plane (xz-plane) for three different spot frequencies of 4.5, 7.5, and 10 GHz are shown in Fig. 9. As shown in the H-plane, the antenna design exhibits an omni-directional profile at low and high frequencies and quasi bidirectional in the mid-range frequencies. However in the E-plane, the radiation pattern is bidirectional at low frequencies and quasi bidirectional at mid and high frequencies. The agreement between the measured and simulated radiation patterns is very good. However at 10 GHz a discrepancy is occurred.
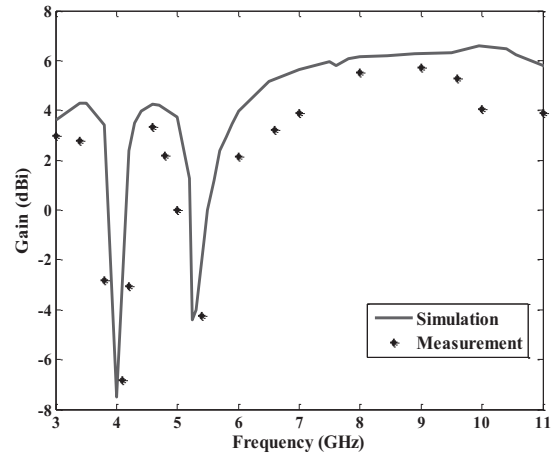
Fig. 8. The calculated and measured gain of the proposed UWB antenna.

Table 1: Dimensions of the proposed UWB antenna

Parameter	W_g	L_g	A	B	L_1	a	b	W_f	L_f	W_s	L_s	H_s	d	L_{sp}	W_{sp}
Value (mm)	50	50	12	16	13	5.25	7.5	2	13.3	0.5	12	2.25	0.5	9.5	0.4

(a) *f* = 4.5 GHz

(b) *f* = 7.5 GHz

(c) *f* = 10 GHz
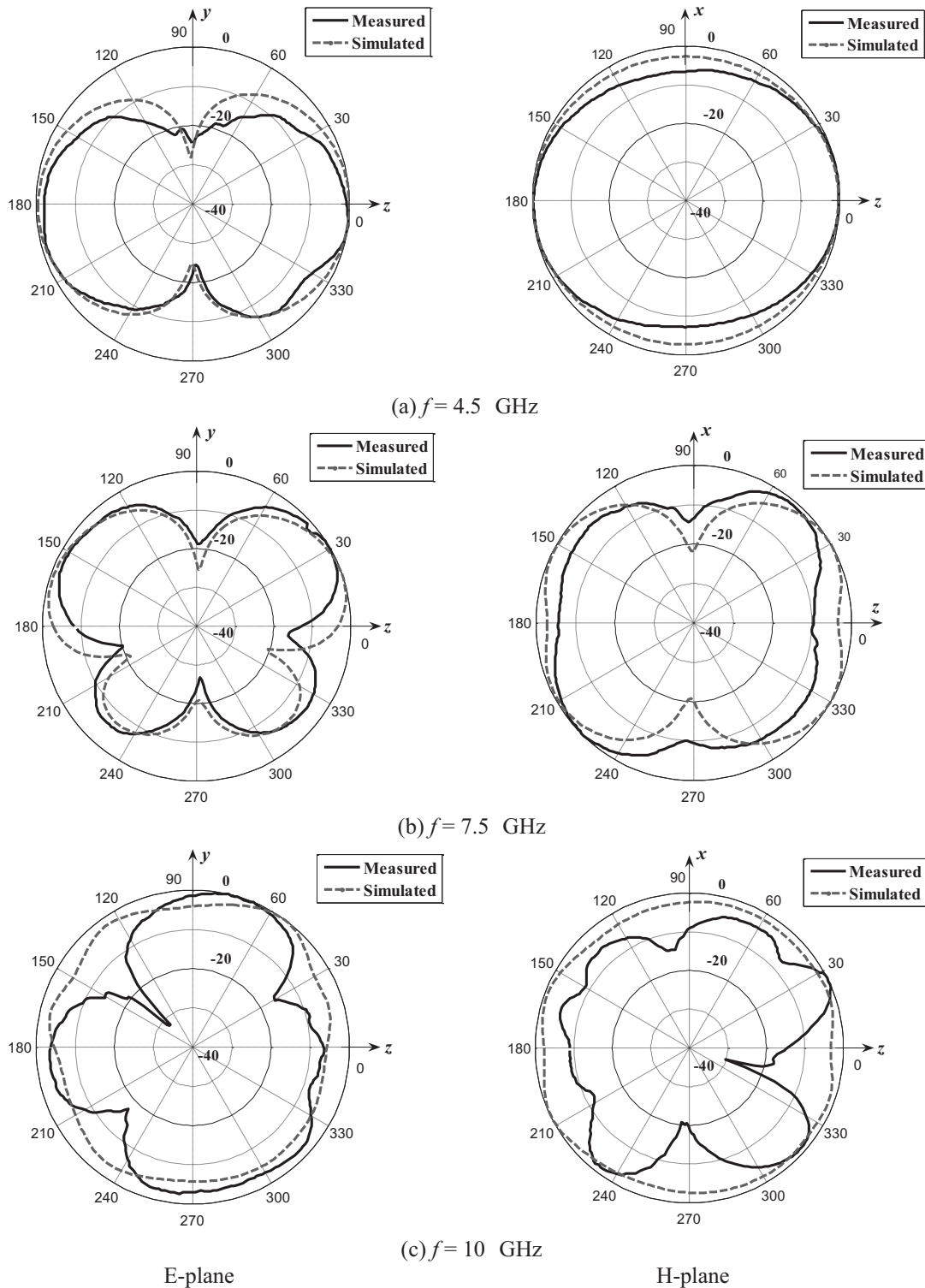
E-plane   H-plane

Fig. 9. Measured and simulated E-plane and H-plane radiation patterns for proposed antenna at: (a) 4.5 GHz, (b) 7.5 GHz, and (c) 10 GHz.

V. CONCLUSION

An UWB elliptical slot antenna with dual band-notched characteristics at C-band (3.7–4.2 GHz)

satellite communication systems and WLAN frequencies has been proposed and fabricated. The measurements show that VSWR is below 2 within the

desired UWB frequency bandwidth from 2.5 to greater than 11 GHz, and two notched frequency bands obtained where VSWR≥2 are 3.65–4.35 and 4.85–5.9 GHz. Stable radiation patterns and approximately constant gain in the UWB band, with the exception of notched bands, are obtained. The mechanism of the antenna's filtering properties was represented by a conceptual circuit model based on the dual band-notched phenomenon. The proposed antenna is compact and is considered to be a very candidate for use in various UWB systems.

REFERENCES

[1] First Report and Order, Revision of Part 15 of the Commission's Rule Regarding Ultra-Wideband Transmission System FCC 02-48, Federal Communications Commission, 2002.

[2] J. Liang, C. C. Chiau, X. D. Chen, and C. G. Parini, "Study of a printed circular disc monopole antenna for UWB systems," *IEEE Trans. Antennas Propag.*, 53, 3500-3504, 2005.

[3] S. Angelopoulos, A. Z. Anastopoulos, D. I. Kaklamani, A. A. Alexandridis, F. Lazarakis, and K. Dangakis, "Circular and elliptical CPW-fed slot and microstrip-fed antennas for ultra wideband applications," *IEEE Antennas Wireless Propag. Lett.*, 5, 294-297, 2006.

[4] K. P. Ray and Y. Rang, "Ultra wideband printed elliptical monopole antennas," *IEEE Trans. Antennas Propag.*, 55, 1189-1192, 2007.

[5] M. Naser-Moghadasi, G. R. Dadashzadeh, A.-A. Kalteh, and B. S. Virdee, "Design of a novel band-notched slot patch antenna for UWB communication systems," *Microwave and Optical Technology Letters*, 52 (7), 1599-1603, 2010.

[6] X. L. Ma, W. Shao, and G. Q. He, "A novel dual narrow band-notched CPW-fed UWB slot antenna with parasitic strips," *Applied Computational Electromagnetics Society (ACES) Journal*, vol. 27, no. 7, pp. 581-586, July 2012.

[7] M. Naser-Moghadasi, R. A. Sadeghzadeh, M. Katouli, and B. S. Virdee, "Ultra-wideband microstrip antenna with enhances impedance bandwidth," *Microwave and Optical Technology Lett.*, 52, 870-873, 2010.

[8] M. Naser-Moghadasi, R. Bayderkhani, G. Dadashzadeh, and B. S. Virdee, "Printed wide-slot antenna with high polarization purity for wideband applications," *Microwave and Optical Technology Lett.*, 52 (5), 2010.

[9] Q.-X. Chu and Y.-Y. Yang, "A compact ultrawideband antenna with 3.4/5.5 GHz dual band-notched characteristics," *IEEE Trans. Antennas Propagat.*, 56, 3637-3644, 2008.

[10] Ansoft High Frequency Structure Simulation (HFSS), Version 10 (Ansoft Corporation, 2005).

Inspired Metamaterial Quad-Band Printed Inverted-F (IFA) Antenna for USB Applications

Ahmed M. Soliman [1], Dalia M. Elsheakh [2], Esmat A. Abdallah [2], and Hadia M. El-Hennawy [1]

[1] Electronics and Communication Engineering Department
Faculty of Engineering, Ain Shams University, Cairo, 11517, Egypt
ahmed.soliman2020@yahoo.com

[2] Electronics Research Institute
Cairo, 12622, Egypt
daliaelsheakh@eri.sci.eg

Abstract ─ This paper presents quad-band printed inverted-F antenna that employs transmission-line based on inspired metamaterials for USB applications. The reactive loading of the printed IFA is inspired by transmission-line based metamaterials (TL-MTM), which is exploited to create a new resonant frequency while maintaining the antenna's small form-factor. The proposed USB antenna structure consists of two arms printed IFA CPW-fed loaded with two TL-MTM unit cells to achieve two operating bands with the same antenna size in addition to the two fundamental resonant frequencies of IFA arms themselves. The structure is designed to operate at LTE 11 0.9 GHz, Bluetooth 2.4 GHz, WIMAX 3.5 GHz, and WLAN 5.2 GHz. The component interaction including housing case, USB connector, and laptop device are also characterized. The design concept, a parametric study of the proposed antenna is carried out using HFSS ver. 14 and CST ver. 2014, and general design guidelines are provided. Experimental results are presented to validate the new design concept. Measurements and EM simulations are in a good agreement.

Index Terms ─ High frequency structure simulator (HFSS), inspired metamaterials, inverted-F antenna (IFA), transmission-line based metamaterials (TL-MTM), universal serial bus (USB).

I. INTRODUCTION

Universal serial bus device (USB) [1] is a good candidate for data transmission in most digital devices. The challenge in designing a USB antenna is to design compact, low cost and multiband antenna to support multi standards as much as possible. Generally, the monopole antenna applied to a wireless USB dongle has dual resonances including 2.4 GHz and 5.2 GHz bands

only [2-3]. A new research paper [4] supports triple band operation. These designs use traditional approach such as meander shaped slots [2], [4], and fractal shapes [3]; however, there is tradeoff between design complexity, and fabrication cost associated with multiband extension. On the other hand, the printed-F antenna offers an attractive solution for modern wireless communication systems because it has a low profile, can be etched on a single substrate and can provide the feature of broadband or multiband operation. Recently, the combination of inspired metamaterial and printed IFA has proven to be a good candidate for the design of compact multiband USB antennas [5]. Also, the transmission-line metamaterials (TL-MTM) provide a conceptual route for implementing small resonant antennas [6]-[9]. TL-MTM structures operating at resonance are first proposed in order to implement small printed antennas in [7].

In this paper, quad-band CPW fed printed IFA antenna is proposed using reactive loading, that is inspired by using the negative-refractive-index (NRI) transmission line metamaterial π unit cell [9], in order to meet the specifications of the long term evaluation LTE900 (0.9–0.96) GHz, the Wi-Fi bands (lower Wi-Fi band) of (2.4–2.48) GHz and upper Wi-Fi band of (5.2–5.25) GHz, and the WiMAX (3.5–3.6) GHz band while maintaining a small form factor for USB applications. All simulations are carried out using the EM commercial simulator, HFSS which is based on finite element method.

The rest of the paper is organized as follows: in Section II, the design and simulation of the proposed antenna is described. Section III discussed the components interaction. Section IV explains the experimental results and discussion. Section V concludes and summarized the features of the proposed

antenna.

II. ANTENNA DESIGN AND SIMULATION

Figure 1 shows the geometry of the 2D and 3D antenna, resonating at four frequency bands at 0.9, 1.8, 3.5, and 5.2 GHz, respectively. Table 1 shows the optimized dimensions of the proposed antenna. The antenna is designed on a low-cost FR4 substrate with height $h = 0.8$ mm, dielectric constant $\varepsilon_r = 4.7$ and loss tangent $tan\ \delta = 0.025$. The antenna is fed by a CPW transmission-line, which can be easily integrated with other CPW-based microwave circuits printed on the same substrate. The CPW feed is connected to the coaxial cable through a standard 50 Ω SMA connector. The overall size of the antenna including the ground plane is $50 \times 20 \times 0.8$ mm^3. The proposed design is via-free and can therefore be easily fabricated. The design steps and their responses are shown in Fig. 2. The reactive loading of the CPW fed IFA is inspired by transmission-line metamaterials, specifically the concept of a zero-index of refraction.

(a)　(b)　(c)

(d)
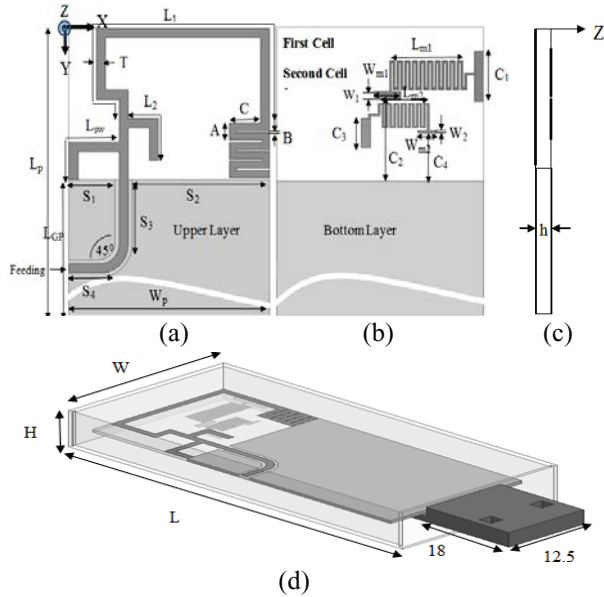
Fig. 1. Quad-band CPW fed printed IFA antenna with two metamaterial inspired unit cells: (a) top view, (b) bottom view, (c) side view, and (d) 3D schematic with housing case and USB connector.

Table 1: The dimensions of the proposed antenna (all dimensions in mm)

W_p	L_p	L_1	L_2	S_1	S_2	S_3	S_4	L_{sw}
20	50	39	6.75	4.5	14.1	7.3	3.8	9.5
L_{GP}	A	B	W_{m1}	W_{m2}	L_{m1}	L_{m2}	C_1	T
34	1.8	0.2	0.8	0.3	7.7	5.4	5.2	1
C_2	C_3	C_4	C	W	W_1	W_2	L	H
8.5	3	5	3.4	26	1	0.3	55.5	10

In order to maintain the antenna's small form-factor while achieving more operating frequencies, the CPW two IFA arms were loaded with a dual asymmetric negative-refractive-index transmission line (NRI-TL) metamaterial-based π unit cell, as shown in Fig. 3 (a). The matched dispersion characteristics of the proposed π unit cell is shown in Fig. 3 (b) [8]-[14-16] around 2.4 GHz. The structure consists of a host TL medium periodically loaded with discrete lumped element components. The unit cell was implemented at 2.4 GHz using the advanced design system (ADS) microwave circuit simulator. The impedance matching condition [8]-[14-15] has been satisfied and, therefore, the stop band has been closed. It can also be observed that at 2.4 GHz, the phase shift is 0 (balanced case).

The design flow can be described with the aid of Figs. 2 (a) to (d), and its corresponding reflection coefficient $|S_{11}|$ less than -6 dB is shown in Fig. 2 (e) as follows.

First step starts by designing the conventional CPW fed printed IFA as shown in Fig. 2 (a) to operate at 0.9 GHz, with L_1=39 mm. $|S_{11}|$ is shown as blue dashed dotted line in Fig. 2 (e).

Second step is to add the IFA second arm with $L_2 = $ 6.75 mm as shown in Fig. 2 (b), to operate at WLAN 5.2 GHz, shown as red dashed line in Fig. 2 (e).

The resonant frequencies of first and second IFA arms can be approximately determined by [10]:

$$F \approx \frac{c}{4\sqrt{\varepsilon_{reff}}(L_i)},\qquad(1)$$

where C, L_i and ε_{reff} are the speed of light, *the IFA 1st, 2nd arm lengths and the effective dielectric constant, respectively.

Third step of design, shown in Fig. 2 (c), is to load the first cell to operate at 2.7 GHz, shown as dotted green line in Fig. 2 (e).

Fourth step of design, shown in Fig. 2 (d), is adding the second cell with different size to operate at WIMAX 3.5 GHz, shown as gray solid line in Fig. 2 (e). It is noticed that the resonant frequency at 2.7 GHz is reduced to be at Bluetooth 2.4 GHz, due to the coupling effect of the nearby elements. All dimensions are listed in Table 1. The two capacitors formed between the first cell, the first IFA arm and ground plane, are represented by the two lengths C_1 and C_2, respectively. The same with the second cell, the lengths C_3 and C_4 represent the two capacitors between the second cell, the first IFA arm and ground plane while the two inductors of first and second cells are represented by the two lengths meander lines, L_{m1} and L_{m2}, respectively. The length L_{m1} is represented by ten turns of 8.8 mm one turn length. The length L_{m2} is represented by seven turns of 8.8 mm one turn length. With decreasing the capacitor C_1 between the first cell and the IFA first arm, the three resonant 3.5 GHz, 2.5 GHz, and 5.2 GHz are affected, while all other parameters remain constant. The first cell is coupled to

the second cell and the IFA second arm. The same happens when decreasing the number of meander line length as shown in Fig. 4. The parameters C_1 and C_2 represent the capacitive loading (distance to ground plane), therefore the most significant effect will be capacitive. While the length L_{m1} and L_{m2} represent the inductive loading (the parameter's lengths are increased right and left without moving toward the ground plane), therefore the most significant effect will be inductive.

(a)   (b)   (c)   (d)

(e)
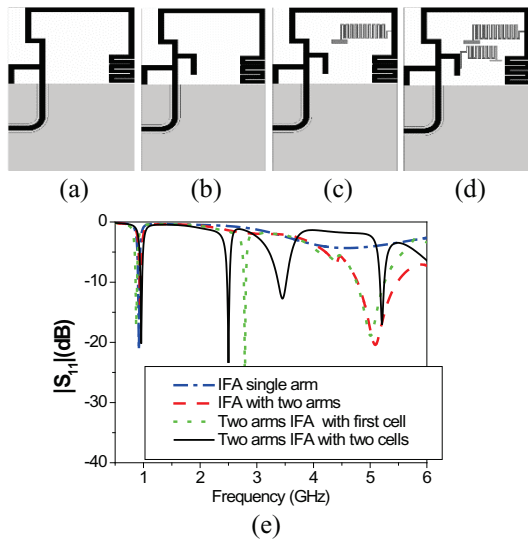
Fig. 2. (a)-(d) Design steps of the proposed quad printed-IFA, and (e) the $|S_{11}|$ design procedures of the proposed antenna.

(a)   (b)
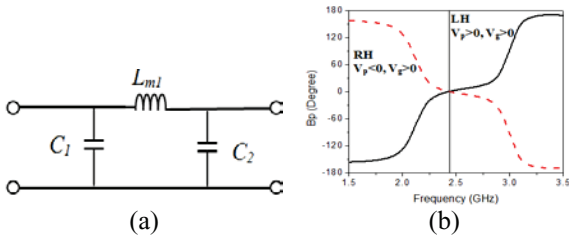
Fig. 3. (a) The equivalent circuit when the proposed antenna operates at the first arm IFA, and (b) dispersion relation calculated for the balanced first π unit cell.

(a)   (b)
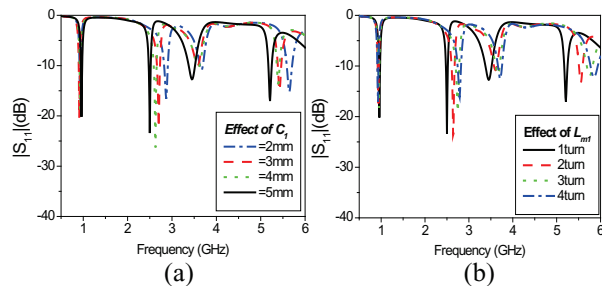
Fig. 4. Variation of $|S_{11}|$ against first cell parameters: (a) C_1, and (b) L_{m1}.

On the other hand, with decreasing the number of meander line turns and length C_3 between the second cell and IFA second arm, the resonant frequency is increased for wireless communication applications, as shown in Figs. 5 (a) and (b), while all other parameters almost remain unchanged. The same happens when increasing the length C_4 between the second cell and the IFA second arm, as shown in Fig. 5 (c). The second cell has independent tuning due to free space zone to the ground plane

Otherwise, the first cell has dependent tuning due to coupling effect with second cell and IFA second arm loading. The operations of the antenna at the four resonant frequencies are further studied using the surface current distribution, as shown in Fig. 6. In addition to the two fundamental resonant frequencies of the two IFA arms, at 0.9 GHz and 5.2 GHz, the two TL-MTM reactive loading unit cells introduce new two resonances around Bluetooth 2.4 GHz and WIMAX 3.5 GHz. At these frequencies, the antenna no longer acts as a printed IFA mode, but rather as dipole mode along the x-axis [7], as shown in Figs. 6 (b) and (c). The highest current densities mainly flow around each element that corresponds to its resonant frequency, and so is responsible for the corresponding radiations.

(a)   (b)

(c)
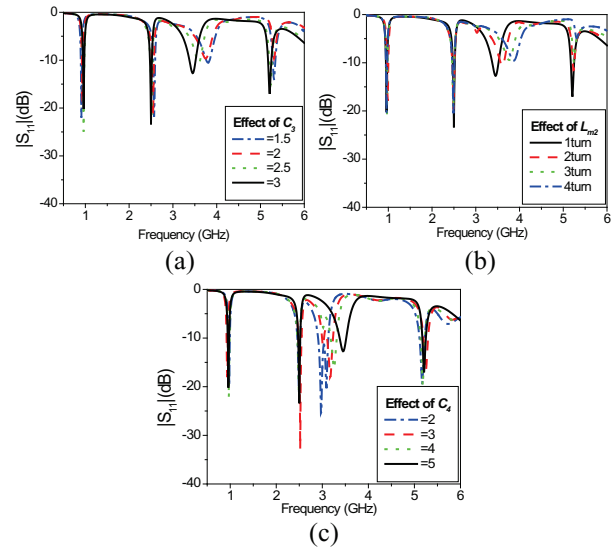
Fig. 5. Variation of $|S_{11}|$ against second cell parameters: (a) C_3, (b) L_{m2}, and (c) C_4.

(a)   (b)   (c)   (d)
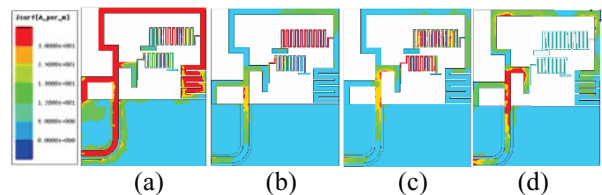
Fig. 6. The surface current distribution at: (a) 0.9 GHz, (b) 2.4 GHz, (c) 3.5 GHz, and (d) 5.2 GHz, respectively.

III. COMPONENTS INTERACTION

The whole USB structure has dimensions of $0.8 \times 20 \times 50$ mm^3, while the USB antenna has dimensions of $0.8 \times 20 \times 16$ mm^3. The rest of this space is used to mount the other components of the USB. Therefore, component interaction is an issue to take into account as for mobile handset [11]. This section deals with the effect of the housing case, USB connector and laptop device on the antenna performance.

Figure 7 (a) shows the geometry of the USB antenna with housing case, USB connector, and laptop device. The antenna is packaged with PVC (Polyvinyl chloride) casing materials of permittivity 4.5. The permittivity of screen, keyboard, laptop housing are 3.5, 2.25 and 3, respectively. Figure 7 (b) shows the effect on antenna reflection coefficient of the proposed antenna. To validate our results we are using another simulator, microwave studio transient solver (CST) ver. 2013, which is based on finite integral technique.

It is noticed that loading the antenna with PVC housing case, USB connector, and laptop device causes a slight shift on the frequencies at 0.9 GHz, 3.5 GHz and 5.2 GHz, but still covers the channel bandwidth of LTE, WIMAX and upper WLAN.

(a)

(b)
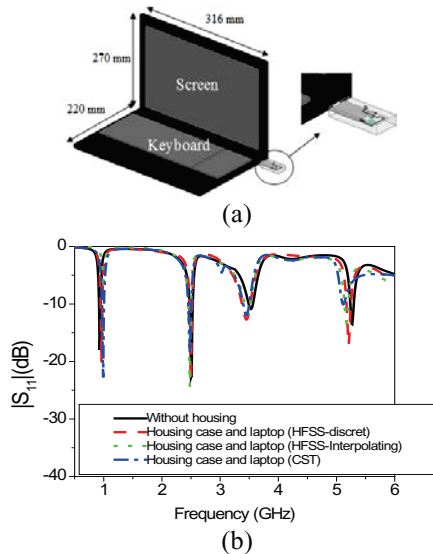
Fig. 7 (a). The HFSS proposed antenna with housing case, USB connector and laptop device, and (b) simulated |S$_{11}$| of the proposed antenna with housing case, connector and laptop using different simulators.

In the simulation, it seems that the proposed antenna is too small with respect to the laptop. The simulation results are performed using HFSS, both solver discreet and interpolating setup solution and CST microwave studio time domain solver. HFSS and CST programs have automatic and manual adaptive meshing options. The number of mesh cells could be controlled in the

antenna's area than the other areas (laptop), as shown in Table 2. As expected, there is a slight difference between both results due to different methods of meshing, as shown in Fig. 7 (b).

Table 2: Different simulator parameters

Simulator	HFSS Interpolating	HFSS Discreet	CST
Start F$_o$ (GHz)	0.1	0.1	0.1
Stop F$_o$ (GHz)	6	6	6
Step F$_o$ (GHz)	0.01	0.01	0.01
No. of points	551	551	551
No. of tetra hydras	95391	195244	-
No. of mesh cells	-	-	24200079

IV. EXPERIMENTAL RESULTS AND DISCUSSION

To verify the simulated results, two proposed antennas are fabricated at C_4=5 mm and C_4=2 mm, as shown in Figs. 8 (a) and (b). The antennas are fabricated using photolithographic technique and were measured using Rohde and Schwarz ZVA67. A 50 Ω CPW feed line with a metal strip width W_s=1 mm and a gap distance W_{ss}=0.2 mm is used to excite the designed antenna. Figure 9 (a) shows the comparison between the simulated and measured reflection coefficient of the antenna. The experimental result shows good agreement with the simulated one at the target operating frequencies. Figure 9 (b) shows that the unbalanced case between the right and left handed regions [8] are appeared when decreasing the length C_4 to 2 mm, which broaden the bandwidth of the original resonant frequency of the second cell itself, covering wide bandwidth at 3 GHz.

Figure 8 (c) and Fig. 9 (c) show the fabricated USB antenna with the PVC case material and comparison between measured and simulated |S$_{11}$|, respectively. It is noticed that matching is improved by increasing the permittivity of the casing material, while the radiation efficiency is worsened. The simulated gains, radiation efficiency at each operating frequency are summarized in Table 3. The radiation efficiency was measured by using wheeler-cap method [12-13]. The average radiation efficiency is more than 75% over operating frequencies. The measured -6 dB impedance bandwidths for each resonance are suitable for the channel bandwidth of the LTE band 11 (0.9-0.96 GHz), Bluetooth (2.4-2.45 GHz), WIMAX (3.5-3.6 GHz), and upper WLAN (5.2-5.25 GHz).

(a)   (b)   (c)
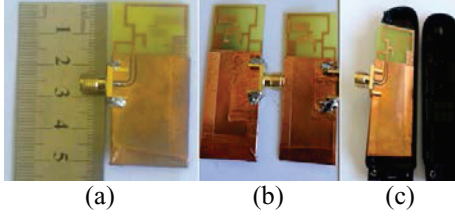
Fig. 8. Photos of proposed antennas (C_4=2 mm & 5 mm): (a) upper layer, (b) bottom layer, and (c) with casing material.

(a)

(b)

(c)
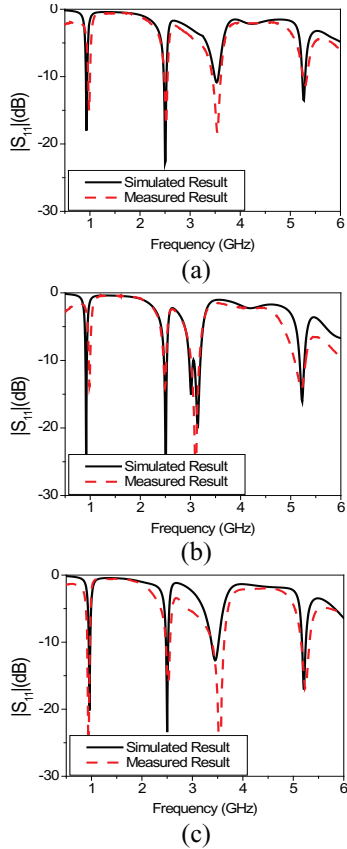
Fig. 9. Simulated and measured |S_{11}| of the proposed antenna: (a) C_4=5 mm, (b) C_4=2 mm, and (c) with package of PVC casing material.

Table 3: The simulated and measured antenna parameters

Parameter \ F_o (GHz)	0.9	2.4	3.5	5.2
Sim. Gain (dBi)	2.2	2.5	2.6	2.9
Sim. Effi. (%)	65	79	85	88
Measu. Effi. (wheeler) (%)	68	81	84	86
Sim. BW (MHz) (-6 dB)	70	80	95	80
Measu. BW (MHz) (-6 dB)	70	80	90	120

The radiation patterns of the proposed antenna are measured in a Star-Lab 18 anechoic chamber, and the walls inside the chamber are covered with absorbing materials to mitigate signal reflections. The simulated and measured radiation patterns of the proposed antenna are listed in Table 4 in E-plane ($\Phi = 0^0$) and H-Plane ($\theta = 90^0$), with normalized co- and cross-polarization (E_Φ and E_θ), respectively. For almost all frequency bands, the normalized co-polarized (co-pol) patterns show nearly omni-directional radiations and their corresponding cross-polarized (x-pol) patterns exhibit monopole-like. The average difference between the co and cross levels in the main plane for most of the frequencies is higher than 10 dB, which is accepted for wireless communication. Some discrepancies between the simulated and measured results appear at certain frequencies that may be attributed to the inadequate size of the absorbers in addition to normalization error.

Table 4: Radiation patterns, simulated: black lines; measured: red lines; E_Φ: solid lines; E_θ: dotted lines at each resonant frequency; axes are shown in Fig. 1

Fo (GHz)	XZ	XY
0.9		
2.4		
3.5		
5.2		
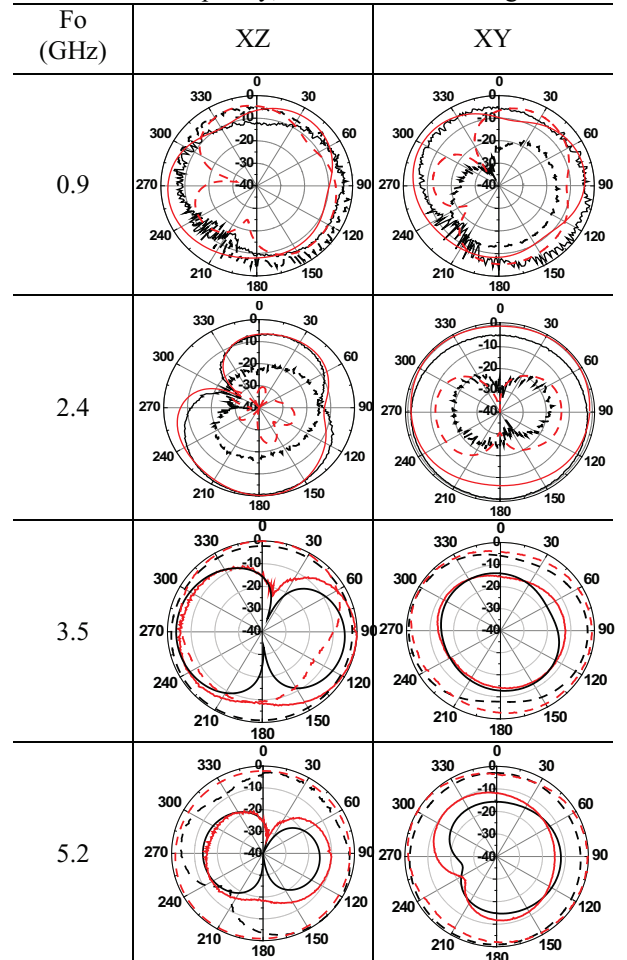
V. CONCLUSION

New quad-band USB antenna was presented in this paper. A metamaterial inspired reactive loading was used to create multiband for wireless USB applications. The theory of the proposed antenna was verified by using EM simulator and measurements. The antenna was designed to have quad-band operation covering LTE 0.9 GHz, Bluetooth 2.4 GHz, WIMAX (3.5 GHz), and upper WLAN (5.2 GHz) bands. The effect of the laptop, housing case, and USB connector is studied using different simulation programs. The results show that these components have no significant effect on the performance of the proposed antenna. The measured and simulated results were in good agreement. The proposed antenna demonstrates good gain and radiation efficiency. The radiation patterns approximate an omnidirectional pattern. These features make the antenna a good candidate for a multiband USB dongle antenna.

ACKNOWLEDGEMENTS

REFERENCES

[1] http://en.wikipedia.org/wiki/Universal_Serial_Bus
[2] S. Lee and Y. Sung, "Multiband antenna for wireless USB dongle applications," *IEEE Antennas and Wireless Propagation Letters*, vol. 10, pp. 25-28, 2003.
[3] S. Chaimool, C. Chokchal, and P. Akkrak, "Multiband loaded fractal loop monopole antenna for USB dongle applications," *IET Electronics Letters*, vol. 48, pp. 388-390, 2012.
[4] Y. Park, D. Kang, and Y. Sung, "Compact folded tri-band monopole antenna for USB dongle applications," *IEEE Antennas and Wireless Propagation Letters*, vol. 11. pp. 228-231, 2012.
[5] A. Soliman, D. E-Sheakh, and E. A. Abdallah, "Compact independent tri-band printed-IFA loaded with inspired metamaterial for wireless communication applications," *17ᵗʰ European Conference on antenna and Propagation (EUCAP) Conference*, pp. 931-934, 2013.
[6] G. Eleftriades, A. Lyar, and P. Kamar, "A compact tri-band monopole antenna with single-cell metamaterial loading," *IEEE Trans. Antennas Propagat.*, vol. 58, pp. 1031-1038, Apr. 2010.
[7] G. Eleftriades and K. Balmain, *Negative-Refraction Metamaterials: Fundamental Principles and Applications*, Hoboken/Piscataway, NJ: Wiley/IEEE Press, 2005.
[8] G. Eleftriades, A. Grbica, and M. Antoniades, "Compact linear lead/lag metamaterial phase shifters for broadband applications," *IEEE Antennas and Wireless Propagation Letters*, vol. 2, pp. 104-107, 2003.
[9] M. Antoniades and G. Eleftriades, "A folded-monopole model for electrically small NRI-TL metamaterial antennas," *IEEE Antennas and Wireless Propagation Letters*, vol. 7, pp. 425-428, 2008.
[10] D. Elesheakh, H. Elsadek, and H. Ghali, "Single feed compact quad-band PIFA antenna for wireless communication applications," *IEEE Trans. Antennas Propagat.*, vol. 53, pp. 36-43, 2005.
[11] K. Wong and H. Chang, "Surface-mountable EMC monopole chip antenna for WLAN operation," *IEEE Trans. Antennas Propagat.*, vol. 54, pp. 1100-1104, 2006.
[12] H. Wheeler, "The radian sphere around a small antenna," *Proceedings of the IRE*, vol. 47, pp. 1325-1331, 1959.
[13] W. Mckinzie, "A modified wheeler cap method for measuring antenna efficiency," *Proceedings of the IEEE Symp. Antennas and Propag.*, pp. 542-545, 1997.
[14] T. Zvolensky, J. A. Laurinaho, C. R. Simovski, and A. V. Räisänen, "A systematic design method for CRLH periodic structures in the microwave to millimeter-wave range," *IEEE Trans. Antennas Propagat.*, vol. 62, no. 8, pp. 4153-4161, Aug. 2014.
[15] A. Lai, T. Itoh, and C. Caloz, "Composite right/left-handed transmission line metamaterials," *IEEE Microw. Mag.*, vol. 5, no. 3, pp. 34-50, Sep. 2004.
[16] C. Caloz and T. Itoh, *Electromagnetic Metamaterials: Transmission Line Theory and Microwave Applications*, Hoboken, NJ, USA: Wiley, ch. 3, 5, and 6, 2006.

Ahmed M. Soliman was born in Cairo in 1987. He received the B.Sc. degree (with honors) in Electrical and Communication Engineering from Shoubra Faculty of Engineering, Zagazig University, Cairo, Egypt, in 2009. Currently, he is working towards the M.Sc. degree at the Faculty of Engineering, Ain Shams University. Since his graduation, he was appointed as an R.A. by the Electronics Research Institute, Microstrip Department, Giza, Egypt. His graduation project was to design a communication system for cube satellite under the supervision of the National Authority for Remote Sensing and Space Sciences (NARRS). He and his graduation projects team received the Information

Technology Industry Development Agency Award, the 2009 Young Investigator Award, and Giza Systems School of Technology scholarship Award.

Dalia M. Elsheakh born in Giza, Egypt, in 1976. She received the B.S., M.S., and Ph.D. degrees in Electrical and Communication Engineering from Ain Shams University, Cairo, Egypt, in May 1998, 2004 and 2010 respectively. M.Sc. title, "The Design of Microstrip PIFA Antennas for Mobile Handsets" and Ph.D. entitled, "Electromagnetic Band-Gap (EBG) Structure for Microstrip Antenna Systems (Analysis and Design)". From 2000 to 2004 she was a Research Assistant and from 2004 to 2010 she has been an Assistant Researcher with the Microstrip Department, Electronic Research Institute. She has been an Assistant Professor with the Microstrip Department. 2014 she has been an international visitor in Hawaii Center for Advanced Communications (HCAC).

Esmat A. Abdallah graduated from the Faculty of Engineering and received the M.Sc. and Ph.D. degrees from Cairo University, Giza, Egypt, in 1968, 1972, and 1975, respectively. She was nominated as Assistant Professor, Associate Professor and Professor in 1975, 1980 and 1985, respectively. In 1989, she was appointed President of the Electronics Research Institute ERI, Cairo, Egypt, a position she held for about ten years. She became the Head of the Microstrip Department, ERI, from 1999 to 2006. She has focused her research on microwave circuit designs, planar antenna systems and nonreciprocal ferrite devices, and recently on EBG structures, UWB components and antenna and RFID systems.

Hadia M. El Hennawy received the B.Sc. and the M.Sc. degrees from Ain Shams University, Cairo, Egypt, in 1972 and 1976, respectively, and the Ph.D. degree from the Technische Universitat Braunschweig, Germany, in 1982. In 1982, she returned to Egypt and joined the Electronics and Communications Engineering Department, Ain Shams University, as an Assistant Professor. She was nominated an Associate Professor in 1987 and then a Professor in 1992. In 2004, she was appointed as the Vice-Dean for Graduate Study and Research. In 2005, she was appointed as the Dean of the Faculty of Engineering, Ain Shams University. She has focused her research on microwave circuit design, antennas, microwave communication and recently wireless communication. She has been the Head of the Microwave Research Lab since 1982.

Optimization of the Auxiliary Sources Method for 2D Arbitrary-Shaped Scattering Problems

A. Bouzidi and T. Aguili

Department of Information Technology and Communication
Tunis El Manar University, Tunisia, B. P. 37, Le Belvedere, Tunis 1002
afif.bouzidi@gmail.com, taoufik.aguili@gmail.com

Abstract ─ The distribution of radiation centers plays an important role in the auxiliary sources method. It has a decisive influence on the accuracy of solutions, the convergence rate and the computation cost. The optimal selection of the MAS (method of auxiliary sources) parameters (auxiliary surface, position of radiation centers) is considered an open issue. This work presents a systematic optimization framework to achieve the optimal configuration of the MAS for scattering by an infinite arbitrary-shaped cylinder.

Index Terms ─ Auxiliary sources method, level set method, radar cross-section.

I. INTRODUCTION

The method of auxiliary sources presents an auspicious alternative to standard integral equation techniques (such as the moment method) to solve scattering problems with an optimal compromise between accuracy and computational resources. Previous researches [1,2] have shown that the rigorous location of the auxiliary sources (AS) is imperative to achieve efficiency of the MAS, the distribution of the AS strongly affects the convergence rate and the accuracy of the solution. It is shown that to guarantee the optimality of the MAS, the auxiliary surface should encircle the scattered field singularities as tightly as possible [3]. The standard allocation of the auxiliary sources is based on empirical rules and on the caustic hypothesis. Consequently, the appropriate distribution of the auxiliary sources, for a predesigned accuracy is achieved by try-and-error processes or by searching the corresponding caustic surfaces [4,5,6]. These approaches are applicable only for problems with simple canonical geometries. The obscurity associated with the location of the auxiliary sources for arbitrary-shaped objects is the prevailing breakdown point of the MAS.

The salient feature of the proposed technique is the replacement of laborious trial and error procedure of the standard MAS by a systematic and fully automated one. The outline of the paper is as follows. First we go over 2D scattering problem with perfectly conducting boundary conditions, we present the formulation of the MAS and we discuss the impact of the singularities localization on its efficiency. Secondly, we review the level set method and we adapt it to our purpose. Proceeding from this, we set up a numerical framework to automatically carry out the optimal auxiliary sources distribution. Finally, we report some numerical experiments to clearly demonstrate the accuracy and the robustness of the optimized MAS compared to the standard one.

II. AUXILIARY SOURCES METHOD FORMULATION

Let us consider a two-dimensional object having an arbitrary cross-section Ω as shown in Fig. 1. The object is assumed to be uniform in the z direction and a perfectly conducting boundary condition is held on its contour Γ. The polarization of the incident wave is assumed to be transverse magnetic (TM) with respect to the cylinder axis z. It is obvious that the scattered field is z directed too, which reduces the scattering problem to a bidirectional one.

On the boundary Γ the scattered electric field satisfies:

$$E_z^s = -E_z^i \quad \forall \vec{r} \in \Gamma. \qquad (1)$$
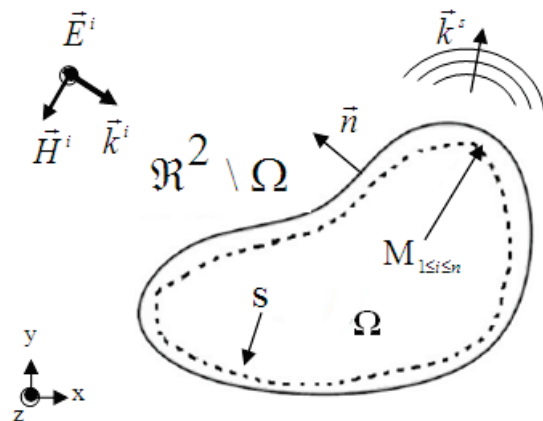
Fig. 1. MAS geometry.

According to the auxiliary sources method, let S designates the auxiliary surface, $M_{1\le i\le n}$ the radiation centers located at points $\vec{r}_{i\le n}$ as shown in Fig. 1, and $H_0^{(2)}(k|\vec{r}_i-\vec{r}|)_{1\le i\le n}$ the Hankel functions of zero order and second kind associated with elementary sources. Kupradze [2] proved that the set of functions $H_0^{(2)}(k|\vec{r}_i-\vec{r}|)_{1\le i\le\infty}$ is complete and linearly independent on the surface Γ. So, there are coefficients $a_{1\le i\le n}$ such that, using the n first functions of the aforementioned system, the scattered electric field can be approximated as follows:

$$E_z^s \approx \sum_{i=1}^{n} a_i H_0^{(2)}(k|\vec{r}_i-\vec{r}|). \qquad (2)$$

This will approach exact solution as $n \mapsto \infty$ It has been proved that any scattered field that transfers energy to infinity must have areas of irregular sources within finite volume, otherwise the scattered field is null everywhere [7]. So, it is obvious that E_z^s certainly has irregular domains that could be in form of isolated points, lines or surfaces. S should enclose the singularities as tightly as possible. Ignoring this point leads to a weakening of convergence and even diverging of the equation (2) when n increases. By matching the boundary condition at m collocation points $\vec{r}_{1\le p\le m}$, the problem can be formulated as follows. Find $a_{1\le i\le n}$ such that:

$$\sum_{i=1}^{n} a_i H_0^{(2)}(k|\vec{r}_i-\vec{r}_p|) = -E_z^i(\vec{r}_p)\ \ 1\le p\le m. \qquad (3)$$

The stability and the size of the obtained algebraic system depend on the proper choice of auxiliary parameters that are the shape of the auxiliary surface S and the distribution of the radiation centers $\vec{r}_{1\le i\le n}$.

The necessary number of terms of the series (2) strongly depends on the relative distance between the real surface and the auxiliary surface S on which the auxiliary sources are placed. When the auxiliary surface moves away from the real one the number of terms in (2) decreases strongly and consequently, the computational cost decreases, but it should be noted that if the scattered field singularities appear outside the auxiliary surface, the computing process might diverge. Therefore a good description of singularities is an essential part of the method to carry out the optimal solution.

III. THE LEVEL SET METHOD
A. An overview of level set method
The level set method was introduced by Osher and Sethian [8] in the field of fluid dynamics, to trace interfaces between different phases of fluid flows. Later, it has been used for many different kinds of physical problems. The main idea behind this method is to represent the interface at each time t as the zero level set

of a function $\varphi(\vec{r},t)$. Thus, given a contour S bounding an open region D in $\mathfrak{R}^2$, we wish to study its motion under a velocity field v. The level set idea consists in defining a smooth function to implicitly represent S as the set of points where $\varphi(\vec{r},t)$ vanishes. That is $S = \{\vec{r}\in\mathfrak{R}^2\ /\ \varphi(\vec{r},t)=0\}$. The function $\varphi(\vec{r},t)$ is called the level set function, and it has the following properties:

$$\varphi < 0\ for\ \vec{r}\in D$$
$$\varphi > 0\ for\ \vec{r}\notin D \cdot \qquad (3)$$
$$\varphi = 0\ for\ \vec{r}\in S$$

This concept is illustrated by the Fig. 2.
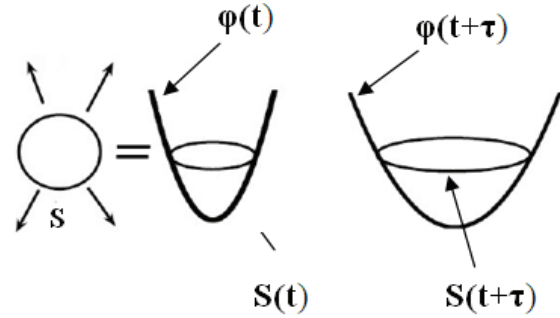
Fig. 2. Level set function.

The Fig. 2 shows a propagating contour and the accompanying function φ, S moves along its forwards pointing normal at a fixed speed v. We remark that the evolution of S is perfectly described by the zero level set of φ. The evolution of the implicit function φ can be described by the following partial differential equation, known as Hamilton-Jacobi equation [8]:

$$\frac{\partial\varphi}{\partial t} + v\|\nabla\varphi\| = 0,\ \varphi(\vec{r},0)=\varphi_0, \qquad (4)$$

where, $\frac{\partial}{\partial t}$ denotes a partial derivative to the temporal variable t and ∇ denotes the gradient operator. The function φ_0 embeds the initial position of the moving contour S.

B. The level set dictionary
Once the level set function φ is defined, most of the geometrical quantities of the contour S can be represented in terms of the function φ:
The normal vector is given by:

$$\vec{n} = \frac{\nabla\varphi}{\|\nabla\varphi\|}. \qquad (5)$$

The mean curvature:

$$\kappa = \nabla\cdot\vec{n} = \nabla\cdot\frac{\nabla\varphi}{\|\nabla\varphi\|}. \qquad (6)$$

The length of S:

$$L(\varphi) = \int_\Omega \delta(\varphi) \|\nabla \varphi\| dS, \qquad (7)$$

where $\delta(\varphi)$ denotes the Dirac function:

$$\delta(\varphi) = \begin{cases} 1 & \text{if } \varphi = 0 \\ 0 & \text{if } \varphi \neq 0 \end{cases}. \qquad (8)$$

Moreover, the integral of a function f along S can be writing in function of φ:

$$\int_S f(r) dS = \int_\Omega f(r) \delta(\varphi) \|\nabla \varphi\| dr. \qquad (9)$$

IV. OPTIMIZATION METHOD

The algebraic system (3) can be written in the following form:

$$\int_S A(\vec{r}') H_0^{(2)}(k|\vec{r}' - \vec{r}_p|) dS = -E_z^i(\vec{r}_p) \ 1 \leq p \leq m, \ (10)$$

where $A(\vec{r})$ represents the distribution of the auxiliary sources over S. Let's consider D an open subset of Ω enclosed by the auxiliary surface S as shown in Fig. 3.

We define φ as level set function of S by:

$$\varphi(\vec{r}, t) = \begin{cases} -\operatorname{distance}(\vec{r}, S) & \text{if } \vec{r} \in D \\ \operatorname{distance}(\vec{r}, S) & \text{if } \vec{r} \notin D \end{cases}. \qquad (11)$$

S divides the domain D into two parts, and then the level set function φ is negative inside and positive outside,

$$S = \{\vec{r} \in \mathfrak{R}^2 / \varphi(\vec{r}, t) = 0\}. \qquad (12)$$

By using the property (9) of the level set method, the equation (10) can be writing as:

$$\int_\Omega A(\vec{r}') H_0^{(2)}(k|\vec{r}' - \vec{r}_p|) \|\nabla \varphi\| \delta(\varphi) dr' \\ = -E_z^i(\vec{r}_p) \ 1 \leq p \leq m \qquad (13)$$

The problem can be formulated as an optimization one:

$$(A^*, \varphi^*) = \underset{A, \varphi}{\operatorname{argmin}} J(A, \varphi). \qquad (14)$$

Find distribution A^* and the level set function φ^* which minimize the cost function J:

$$J(A, \varphi) = \\ \frac{1}{m} \sum_{p=1}^m \left\| \int_\Omega A(\vec{r}') H_0^{(2)}(k|\vec{r}' - \vec{r}_p|) \|\nabla \varphi\| \delta(\varphi) dr' \right. \\ \left. + E_z^i(\vec{r}_p) \right\|^2 \qquad (15)$$

The optimal distribution of the radiation centers strongly depends on the area of the auxiliary surface. By shifting the sources into the conducting body the scattered field function becomes smoother on the surface of the body and the fulfillment of the boundary conditions in the region between collocation points is improved. However, the shift of the auxiliary surface is restricted by the location of the scattered field singularities. So, the area of the auxiliary surface should

be added to the cost functional J as regularization term. Therefore, we force the algorithm to search the best-suited auxiliary surface that encloses the singularities:

$$J(A, \varphi) = \\ \frac{1}{m} \sum_{p=1}^m \left\| \int_\Omega A(\vec{r}') H_0^{(2)}(k|\vec{r}' - \vec{r}_p|) \|\nabla \varphi\| \delta(\varphi) dr' \right. \qquad (16) \\ \left. + E_z^i(\vec{r}_p) \right\|^2 + \beta L(\varphi)$$

where β is a real-valued regularization coefficient.
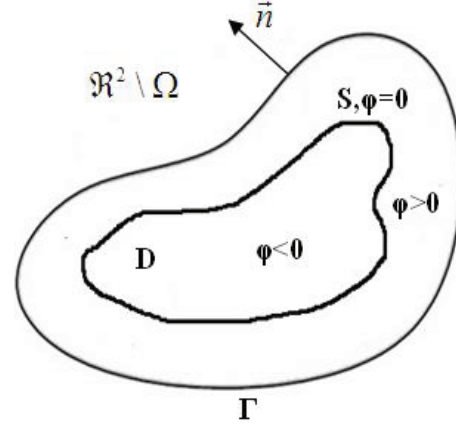
Fig. 3. Level-set representation of the auxiliary surface.

A. Localization of the auxiliary surface

The evolution of φ is described by the following Hamilton-Jacobi equation (4). In this differential form t stands for not actual time, but instead optimization steps. We want to choose an evolution law v such $\frac{\partial J}{\partial t} < 0$, J will decrease with the artificial time evolution during a sufficient small time interval, $[0, \tau]$ $\frac{\partial J}{\partial t}$ is given by: (by applying the chain's rule and the definition of Gateaux differential):

$$\frac{\partial J}{\partial t} = \int_S v \left[\alpha \kappa + \frac{\partial \alpha}{\partial \vec{n}} \right] dS, \qquad (17)$$

where $\vec{n}$ denotes the unit normal to the auxiliary surface S and

$$\alpha = \left[\beta + \right. \\ \frac{1}{m} \sum_{p=1}^m real(< 2(\int_S A(\vec{r}') H_0^{(2)}(k|\vec{r}' - \vec{r}_p|) dS - E_Z(\vec{r}_p)), \qquad (18) \\ A(\vec{r}) H_0^{(2)}(k|\vec{r} - \vec{r}_p|) >)$$

$\langle, \rangle$ denotes the dot product. An obvious selection for v is:

$$v = -\left(\beta \kappa + \frac{\partial \alpha}{\partial \vec{n}} \right). \qquad (19)$$

After substituting v into (4), the differential equation can

be solved numerically using the upwind scheme.

B. Calculation of the radiation center positions

Suppose φ is perturbed by a small variation $\delta\varphi$ and let δr be the resulting variation of the point r as shown in Fig. 4. By taking the variations of the equation (4) between $t = 0$ and $t = \tau$, we get:

$$\delta\varphi + v\tau \|\nabla\varphi\| = 0 . \qquad (20)$$

We have $v\tau = \delta r$. We find the relation between δr and $\delta\varphi$:

$$\delta r = -\frac{\delta\varphi}{\|\nabla\varphi\|} . \qquad (21)$$

So, the radiation center positions $r_{1 \leq i \leq n}$ are updated as follows:

$$r_i(t + \tau) = r_i(t) - \frac{\delta\varphi}{\|\nabla\varphi\|} . \qquad (22)$$
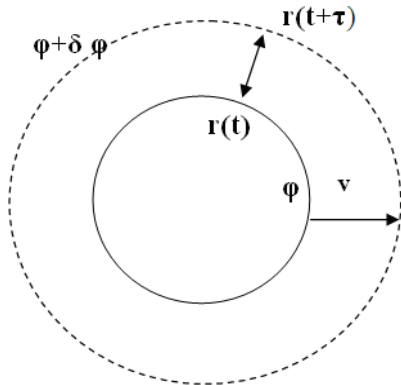
Fig. 4. Deformation of shapes by the level set formulation

C. Calculation of the auxiliary sources' amplitudes

To find the optimal auxiliary sources' amplitudes, we should update $a_{1 \leq i \leq n}$ by following the descent direction of the cost function J. The descent direction is given by the negative derivative of J with respect to $a_{1 \leq i \leq n}$. So, we just need to compute $\frac{\partial J}{\partial a_i}_{1 \leq i \leq n}$ and updating a_i as follows. Choose the step size $\alpha > 0$:

$$a_i(t + \tau) = a_i(t) - \alpha \frac{\partial J}{\partial a_i} . \qquad (23)$$

$\frac{\partial J}{\partial a_i}$ is given by: (by applying the chain's rule and the definition of Gateaux differential):

$$\frac{\partial J}{\partial a_i} = \frac{1}{m}\sum_{p=1}^{m} real(< 2(\sum_{k=1}^{n} a_k H_0^{(2)}(k|\vec{r}_k - \vec{r}_p|) - E_Z^i(\vec{r}_p)), \quad (24)$$

$$H_0^{(2)}(k|\vec{r}_i - \vec{r}_p|) >)$$

D. Numerical scheme

To summarize we can list the optimization steps as below:

1- Choose the initial level set function φ_0 that represents the initial auxiliary surface S_0.

2- Choose the initial positions and amplitudes of the radiation centers ($r_{1 \leq i \leq n}, a_{1 \leq i \leq n}$).

3- For $j \geq 0$:

-   Choose the regularization coefficient β and calculate v (equation (19)).

-   Determine the level set function φ^j by resolving the Hamilton-Jacobi equation in the time interval $[0, \tau]$ with the initial condition $\varphi = \varphi^{j-1}$ (equation (4)).

-   Update r_i^j (equation (22)).

-   Update a_i^j (equation (23)).

-   Go to the next iteration if not converged.

The error of the boundary condition is used for convergence criterion:

$$e_{1 \leq p \leq m} = \frac{\left\| \int A(\vec{r}')H_0^{(2)}(k|\vec{r}'-\vec{r}_p|)dS - E_Z^i \right\|}{\|E_Z^i\|} .$$

Iterations continue until the stop criterion will be satisfied, typically when the errors $e_{1 \leq p \leq m}$ exhibit, between two iterations, become smaller than a predefined threshold. The proposed optimization procedure provides three degrees of freedom (auxiliary surface, positions and amplitudes of the radiation centers) to achieve any boundary condition error, which is a great advantage over classical MAS implementations. Indeed, in the classical MAS implementations, the auxiliary surface and the radiation center positions are fixed beforehand. So, the accuracy is not automatically adjustable, the only degree of freedom is the auxiliary sources' amplitudes. Generally, the standard MAS is based on empirical rules and on the caustic concept leading to the following recommendations [9,10,11,12,13]. The distance d between the physical surface Γ and the auxiliary surface S should satisfy the condition d<Rmin, where Rmin is the minimal radius of positive curvature of the surface Γ. Several numerical methods have been proposed to overcome these constraints such as [6,14,15]. By using level set technique, the proposed method shows a great potential to determine the optimal MAS parameters that satisfy any accuracy.

V. NUMERICAL EXPERIMENTS

We present two experiments. The aim of the first one is showing the aptitude of the optimized method to trace scattered field singularities. The second numerical example is about RCS (radar cross-section) calculating,

we compare the accuracy and the computational cost obtained by the proposed method and those obtained by the standard MAS.

A. Singularities localization

We consider an elliptical cylinder illuminated by an incident plane wave at 100 MHz. It is well-known that the singularities of the wave field in this problem are located at focal points [16]. The auxiliary surface evolution at 0, 23, 50 and 70 iterations is shown at Fig. 5. The angle α (Figs. 5 and 6) is used to indicate the positions of the radiation centers on the auxiliary surface.

When the boundary condition error does not exceed 1% (iteration 70), the distribution of the sources' amplitudes for different angle α is shown in Fig. 5. The obtained surface passes through the foci's region and for particular angles $\alpha \in \{0, \pi, 2\pi\}$ the sharpest amplitude is observed. These angles correspond to focal points F1 and F2, which is consistent with the analytic result.
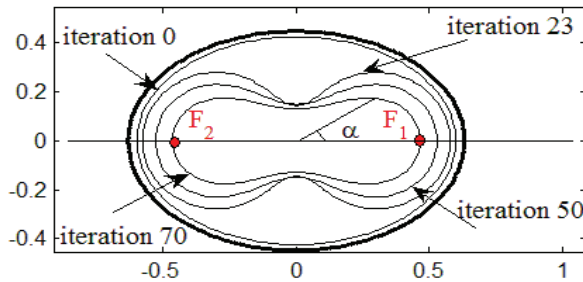
Fig. 5. Singularities location.
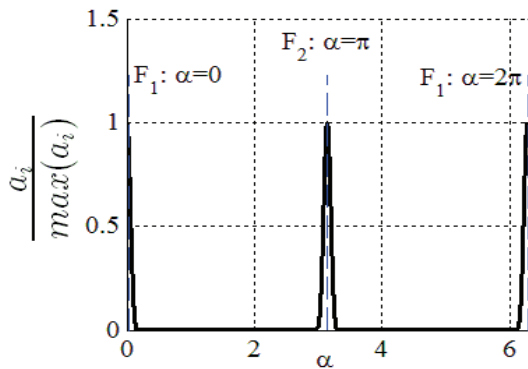
Fig. 6. The distribution of the auxiliary sources amplitudes.

B. Accuracy and computational cost evaluation

We present numerical experiments for some canonical geometries: infinite cylinders with square cross-section, circular cross-section, star-shaped cross-section and dumbbell-shaped cross-section. All these obstacles are illuminated by an incident plane wave at f = 300 Mhz. Figures 7, 8, 9 and 10 show a comparison between the bistatic RCS values obtained from the

optimized MAS and those obtained by the standard implementation, the result from FEKO electromagnetic simulation software is taken as reference. Tables 1 and 2 show comparison between the optimized and the standard MAS method, the following criteria are taken into account: achieved accuracy (error on the boundary condition), number of auxiliary sources and number of collocation points.
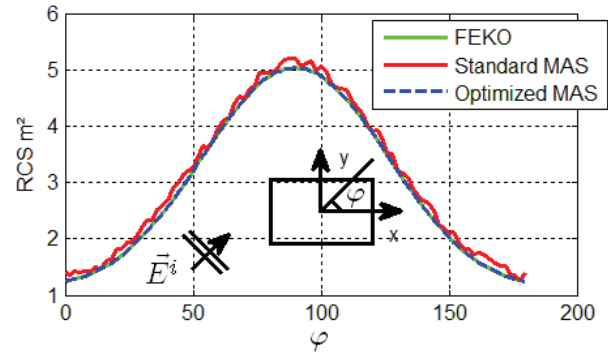
Fig. 7. RCS of an infinite length cylinder with square cross-section.
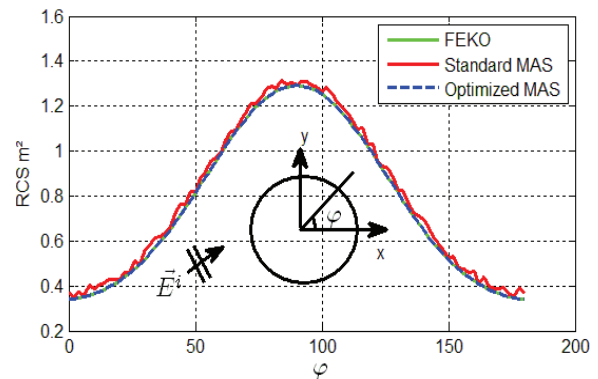
Fig. 8. RCS of an infinite length cylinder with circular cross-section.
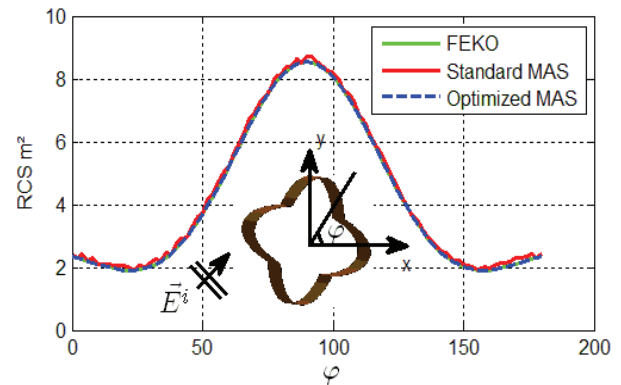
Fig. 9. RCS of an infinite length cylinder with star-shaped cross-section.
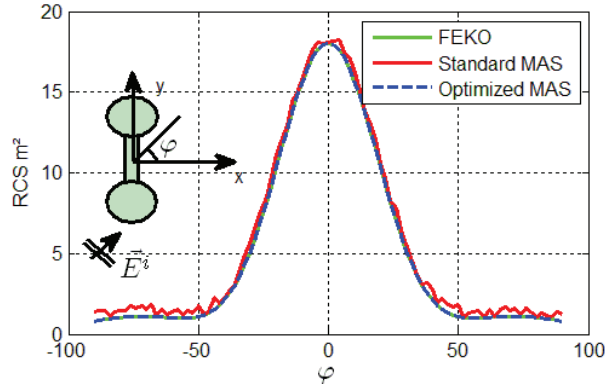
Fig. 10. RCS of an infinite length cylinder with dumbbell-shaped cross-section

Table 1: Results obtained by the standard MAS implementation

	Accuracy	Auxiliary Sources	Collocation Points
Circular cross-section	5%	300	300
Square cross-section	7%	400	400
Star-shaped cross-section	5%	400	400
Dumbbell shaped cross-section	6%	400	400

Table 2: Results obtained by the optimized MAS

	Accuracy	Auxiliary Sources	Collocation Points
Circular cross-section	0.1%	50	300
Square cross-section	0.2%	90	400
Star-shaped cross-section	0.1%	50	400
Dumbbell shaped cross-section	0.1%	50	400

As a conclusion of these numerical experiments, it appears clearly that the optimized method is able to achieve high accuracy with less implementation cost than the standard MAS implementation.

VI. CONCLUSION

We have reported a numerical scheme for determining the optimal MAS parameters for two-dimensional scattering problem by using the level set method. The comparison between RCS obtained from the proposed framework and those obtained from the standard MAS implementation shows that the proposed method can achieve high accuracy with less implementation cost. We have restricted our study to perfect electric cylinders, but the optimized method can be easily extended to study partially or fully penetrable ones.

REFERENCES

[1] R. S. Popovidi-Zaridze and Z. S. Tsverikmazashvili, "Numerical study of a diffraction problems by a modified method of nonorthogonal series," (in Russian, English translation available, translated and reprinted by Scientific Translation Editor, Oxford), *Zurnal. Vichislit. Mat. Mat Fiz.*, vol. 17, no. 2, 1977.

[2] V. Kupradze, "About approximates solution mathematical physics problem," *Success Math. Sci.*, vol. 22, no. N2, pp. 59107, 1967.

[3] R. Zaridze, G. Bit-Babik, K. Tavzarashvili, N. Uzunoglu, and D. Economou. "Wave field singularity aspects large-size scatterers and inverse problems," *IEEE Transactions on AP*, vol. 50, no. 1, pp. 50-58, Jan. 2002.

[4] N. Hichem and T. Aguili, "Scattering by multilayered structures using the extended method of auxiliary sources emas," *Progress In Electromagnetics Research B*, vol. 15, 133-150, 2009.

[5] N. Hichem and T. Aguili, "Analysis of two-dimensional scattering by a periodic array of conducting cylinders using the method of auxiliary sources," *PIERS Online*, vol. 4, no. 5, 521-525, 2008.

[6] A. Bouzidi and T. Aguili, "Numerical optimization of the method of auxiliary sources by using level set technique," *Progress In Electromagnetics Research B*, vol. 33, 203-219, 2011.

[7] V. Kupradze, *Method of Integral Equations in the Theory of Diffraction*, Moscow-Leningrad, 1935.

[8] S. Osher and J. A. Sethian, "Fronts propagating with curvature-dependent speed: algorithms based on Hamilton-Jacobi formulations," *Journal of Computational Physics*, vol. 79, pp. 1249, 1988.

[9] R. Popovidi-Zaridze, D. Karkashadze, G. Ahvlediani, and J. Khatiashvili, "Investigation of possibilities of the method of auxiliary sources in solution of two-dimensional electrodynamics problems," *Radiotech. Electron.*, vol. 22, no. 2, 1978.

[10] M. A. Aleksidze, *Solution of Boundary Problems by Expansion into a Nonorthogonal Series*, Nauka, Moscow, 1978.

[11] M. A. Aleksidze, *Fundamental Functions in Approximate Solutions of the Boundary Problems*, Nauka, Moscow, 1991.

[12] V. D. Kupradze and M. A. Aleksidze, "On one approximate method for solving boundary

problems," *The Bulletin of the Georgian Academy of Sciences*, 529-536, 1963.

[13] D. Karkashadze and R. Zaridze, "The method of auxiliary sources in applied electrodynamics," *in LATSIS Symp.*, Zurich, 1995.

[14] N. L. Tsitsas, E. G. Alivizatos, H. T. Anastassiu, and D. I. Kaklamani, "Optimization of the method of auxiliary sources (MAS) for scattering by an infinite cylinder under oblique incidence," *Electromagnetics*, vol. 25, iss. 1, 2006.

[15] H. T. Anastassiu and D. I. Kaklamani, "Error estimation and optimization of the method of auxiliary sources (MAS) applied to TE scattering by a perfectly conducting circular cylinder," *Journal of Electromagnetic Waves and Applications*, vol. 18, no. 10, 1283-1294, 2004.

[16] A. G Kyurkchan, B. Y. Sternin, and V. E. Shatalov, "Singularities of continuation of wave fields," *Usp. Fiz. Nauk*, vol. 166, pp. 1221-1242, Dec. 1996.